Department of Mechanical Engineering

Friction of Textured Surfaces in Elastohydrodynamic Regime: Experimental and Numerical Investigations

Thomas Gaston Léon Touche

This thesis is presented for the Degree of
Doctor of Philosophy
of
Curtin University

September 2016

Declaration

To the best of my knowledge and belief this thesis contains no material previously published by any other person except where due acknowledgment has been made.

This thesis contains no material which has been accepted for the award of any other degree or diploma in any university.

Signature: …….

Date: 18/09/2016…...

Abstract

This thesis investigates friction in Elasto-Hydrodynamic Lubrication (EHL), which occurs for example, in roller bearings or gear wheels. In particular, this study focuses on controlling the friction coefficient in EHL thanks to surface texturing. The development of surface texturing with LASER irradiations allows one to sculpt various types of micro and/or nano topographic patterns on steel surfaces. Previous studies demonstrated the ability of such surfaces to strongly modify the lubrication efficiency of mechanical contacts in EHL. Nevertheless, few dealt with the friction consequences of surface texturing lubrication and the coupling between the modification of the film thickness, the pressure and the friction.

The objective of this thesis is to provide friction laws, which predict the friction coefficient in EHL with surface texturing. It will answer the two following questions: what are the governing phenomena responsible for the friction in EHL and how can surface texturing control them? Two complementary approaches were used: experimental and numerical. On one hand, experiments between a textured ball and a smooth disc were carried out and compared with experimental smooth EHL results. Film thickness distribution and friction were simultaneously measured for three textures: groove, ripple and cavity. On the other hand, an EHL line contact numerical simulation was developed to provide further understanding of the friction coefficient, the film thickness and the pressure distribution as a function of the geometrical parameters of the textures.

Experimental, theoretical and numerical results showed that the friction in EHL is the consequence of a Cross-like fluid shearing under pressure and that the mean contact pressure and the average central film thickness are the key control parameters. The mixed/EHL transition is governed by local film thickness reductions induced by the texture. Asperity contacts happen at higher $\eta_0 u_e$ and shift the mixed/EHL transition.

In comparison with a smooth contact, the groove and ripple textures did not change much the average central film thickness, the mean contact pressure and thus the friction in EHL. Nevertheless, they significantly reduced locally the film thickness which leads to asperity contacts. This was accentuated with shallow and/or deep periodic grooves and large ripple amplitudes. The orientation of the

groove and ripple textures had no significant influence except that only transverse groove textures were able to form a film thickness dimples on their tops.

The cavity disturbances in the inlet were responsible for the film thickness reductions and led to the onset of asperity contacts. Despite the large depth of the cavities, the upper envelope of their bottom roughness caused local film thickness enhancements. The intensity and the spreading of the film thickness modifications were governed by the sliding-rolling ratio absolute value and sign, respectively. Finally, the mean contact pressure of the fluid inside the contact, but outside the cavity, increased as the pressure inside the cavity dropped. Then, the lubricant viscosity rose and so the friction coefficient.

Contents

Nomenclature

a	Hertzian contact radius
A	amplitude
A_d	deformed amplitude
A_i	initial amplitude
$A_\%$	asperity contact ratio
d	depth
E'	reduced Young modulus
G	dimensionless material parameter
h	film thickness
h_{av}	central average film thickness
h_c	central film thickness
$h_{c,H\&D}$	Hamrock and Dowson central film thickness
$h_{c,m}$	minimum film thickness on the central line
$h_{c,s}$	smooth central film thickness
h_m	minimum film thickness
$h_{m,H\&D}$	Hamrock and Dowson minimum film thickness
$h_{m,s}$	smooth minimum film thickness
h_+	maximum film thickness induced by the cavity
h_-	minimum film thickness induced by the cavity
H	dimensionless film thickness
H_{Moes}	Moes' dimensionless film thickness
$\mathcal{H}$	Hersey number
$\tilde{\mathcal{H}}$	modified Hersey number
M_1	Moes' dimensionless load parameter (line contact)
M_2	Moes' dimensionless load parameter (point contact)
n	Cross exponent
L	Moes' dimensionless materials parameter
p	pressure
p_h	maximum Hertzian pressure
p_m	mean contact pressure
P	dimensionless pressure

q	reduced pressure
r	roughness
R	dimensionless roughness
R_q	RMS roughness
R_x	reduced radius of curvature in the x direction
R_y	reduced radius of curvature in the y direction
S	generalized Sommerfeld number
S_q	RMS surface
t	time
T	dimensionless time
u_1	smooth surface velocity
u_2	rough surface velocity
u_e	entrainment velocity
u_s	sliding velocity
U	dimensionless speed parameter
v_{groove}	volume of a groove
v_{ripple}	volume of a ripple
w	width
w_{top}	groove top width
w_L	load (line contact)
W_1	dimensionless load parameter (line contact)
W_2	dimensionless load parameter (point contact)
W_L	load (point contact)
x	coordinate
x_c	location of the cavity front
X	dimensionless coordinate
y	coordinate
z	coordinate
z_α	pressure viscosity index
α	piezo-viscosity coefficient
$\dot{\gamma}$	shear rate
$\dot{\gamma}_c$	critical shear rate
δ_e	elastic deformation
ϵ	penalty parameter
η	viscosity
$\bar{\eta}$	dimensionless viscosity
η_0	viscosity at atmospheric pressure
$\eta_{0/P}$	viscosity under pressure at zero shear stress
$\eta_{\infty/P}$	viscosity under pressure at infinite shear stress
λ	wavelength

Λ	dimensionless wavelength
Λ_T	Tallian parameter
μ	friction coefficient
ν	Poisson ratio
ρ	density
$\bar{\rho}$	dimensionless density
ρ_0	density at atmospheric pressure
σ	composite RMS roughness
Σ	sliding-rolling ratio
τ	shear stress
τ_c	Couette shear stress
τ_p	Poiseuille shear stress
θ_s	ripple orientation
$\varnothing$	cavity diameter

Introduction

Presently, the automotive industry aims at reducing petrol consumption in their motor-vehicles, targeting 2 liters per 100 km by 2020 to reduce their impact on the environment. 33% of combustion energy is wasted due to friction, among which 50% is lost in the engine and transmission [1]. Hence, friction reduction in motor-vehicles is a key point of interest for the industry.

In 1966, Hamilton et al. [2] demonstrated the potential tribological improvement by the introduction of surface texturing. In the late 90s, Etsion et al. [3] achieved tribological improvement by applying LASER to produce surface textures. For the past years, experimental PhD studies conducted at the Laboratoire de Tribologie et Dynamique des Systèmes (LTDS), Ecole Centrale de Lyon, France, have successfully demonstrated benefits of surface texturing in the Elasto-Hydrodynamic Lubrication (EHL) regime [4, 5]. In particular, the cavity textures were experimentally observed to increase the film thickness and affect the friction in EHL [6]. The magnitude of the film thickness and friction changes strongly depended on the cavity geometry.

In late 70s, Patir and Cheng [7] developed a numerical model for rough hydrodynamic lubricated contacts. A breakthrough in algorithm efficiency was achieved ten years later with the implementation of multi-grid method for the solution of the EHL equations [8, 9]. Recently at the Tribology Laboratory, Curtin University, Australia, Stachowiak's group [10, 11, 12] showed that the optimization of surface textures might be achievable in two-dimensional hydrodynamic lubrication.

The present work aims at developing friction laws to predict the friction coefficient in EHL with surface texturing. These laws will provide tools to control and optimize the EHL contacts in terms of friction. The originality of this study relies on the combination of experimental and numerical methods in order to understand the physical mechanisms responsible for the EHL friction. In particular, the coupling between the film thickness, the pressure and the friction was investigated.

The present work is the result of the collaboration between two laboratories and one industrial partner:

- Laboratoire de Tribologie et Dynamique des Systèmes (LTDS), UMR CNRS 5513, ECL/ENISE/ENTPE, France,
- Tribology Laboratory, Department of Mechanical Engineering, Curtin University, Australia,
- IREIS, Hydromécanique Et Frottement (HEF) company, France.

The laboratories (LTDS at Ecole Centrale de Lyon and the Tribology Laboratory at Curtin University) have developed solid knowledge and background in experimental and theoretical tribology, together providing expertise in both fields. Surface textures were manufactured using a femtosecond pulse LASER. The HEF company located in Saint Etienne, France, assisted in production of the textured surfaces. Three types of surface textures were chosen:

- periodic groove texture (one-dimensional),
- periodic ripple texture (one-dimensional and non-elastically deformed),
- single cavity texture, (two-dimensional).

EHL experiments with textured surfaces were carried out at LTDS which has extensive experience with physics and experimentation of EHL contacts. The numerical simulations were performed under the supervision of the Tribology Laboratory. Experimental data supported the development of a full numerical solution of EHL equations with textured surfaces under transient conditions.

The organization of the thesis is as follows. In Chapter 1, general description of the elastohydrodynamic lubrication mechanism is presented. The details of the EHL regime for smooth surfaces are explained, including the limitations of such contacts in friction optimization. Then, a review on surface texturing in EHL is given and possible challenges are identified. The strategy followed during this work is presented.

The description of the EHL equations, the literature review on numerical methods and the numerical model chosen are given in Chapter 2. The model is based on a line contact model coupled with an equivalent line contact description of point contacts. Tribological tests conducted at the LTDS according to the robust and well-recognized test procedures in lubrication studies on the IRIS tribometer, i.e. a home-developed tribometer, are described. Tribological responses

of experimental smooth surfaces in EHL contacts are compared to the tribological behavior of numerical smooth surfaces to validate the numerical model.

The investigations on groove, ripple and cavity textures are reported in Chapters 3, 4 and 5, respectively. First, a multi-scale surface roughness characterization of these manufactured textured surfaces was conducted using Atomic Force Microscopy (AFM) and optical interferometry at the LTDS. Second, the tribological response of each texture was experimentally measured following similar procedures as for the smooth surfaces. Numerical simulations provided complementary data such as the pressure in the textured EHL contacts. The effect of each texture geometry is then analyzed in terms of film forming capability, pressure distribution and friction.

Chapter 1

Elastohydrodynamic lubrication regime

Contents

Two basic concepts in tribology are first introduced: the lubrication regimes and the Stribeck curve. The focus is then made on the Elasto-Hydrodynamic Lubrication (EHL) regime with smooth surfaces. The analytical model of Ertel-Grubin is presented and compared to the work of Hamrock and Dowson. Standard numerical methods in EHL are detailed and the origin of the smooth EHL friction is developed considering the rheology of the lubricant. Next, a literature review of surface texturing in EHL is reported to emphasize its potential in terms of lubrication efficiency and friction reduction. Finally, the objectives and strategy of the present work are presented.

1.1 Lubrication overview

1.1.1 Definition

Tribology is the science of the interface between two moving surfaces that are typically in contact with a third body, the lubricant. This lubricant can be a solid, a liquid or a gas. The choice depends on the conditions of the mechanical contact. Solid lubricants are preferred to ensure the surface separation in extreme conditions (high loads) whereas gas lubrication suits mechanical contacts with low load and very high velocities. Most contacts are lubricated with liquids where the surface separation is directly driven by the hydrodynamic effects. In this thesis, the lubricant is considered to be a liquid at room temperature.

The main purpose of the lubricant is to avoid the severe conditions that would have occurred in dry contact by easing or preventing the asperity contacts. The lubrication strongly reduces adhesive and abrasive wear in the contact as well as the friction coefficient (ratio of the tangential force and the normal force). In addition, the lubricant may provide others advantages: in severe conditions, the contact heats up and the lubricant contributes to the heat dissipation. The lubricant also prevents any material debris from remaining in the contact. Therefore, the lubricant increases the lifetime of a mechanical contact and decreases the force required to set and keep the motion of solids in mechanical components.

1.1.2 Lubrication regimes

The intimacy of the two surfaces, i.e. the film thickness, can range from the full separation (no asperity contact) to the contact of all surface asperities. This is illustrated in Fig. 1.1. To describe these different states, three regimes of lubrication are defined.

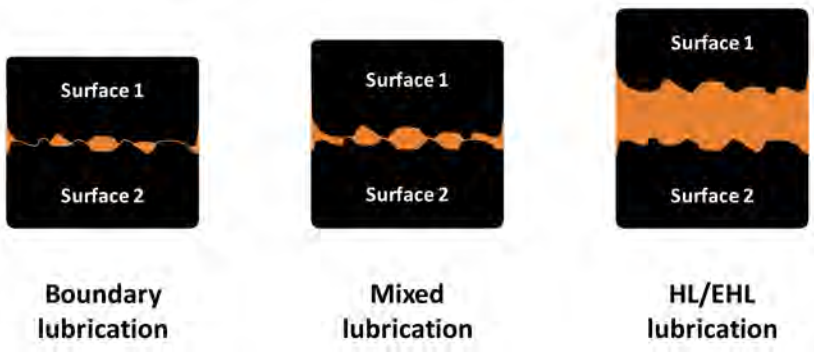

Figure 1.1: Intimacy of two surfaces separated by a lubricant in three different lubrication regimes: boundary, mixed and HL/EHL.

Hydrodynamic and elastohydrodynamic lubrication regimes

When the lubricant fully separates the two surfaces (no asperity contact), the contact is in Hydrodynamic Lubrication (HL) regime. The fluid mechanics equations govern the pressure generation in the lubricant. The ability to separate the surfaces relies on the pressure applied by the fluid on the surfaces, compensating the load. The presence of a convergent wedge in the contact is necessary to obtain the fluid pressurization to promote the hydrodynamic lift. Yet, the latter also requires high enough mean surface velocity u_e and lubricant viscosity at atmospheric pressure η_0.

When the load reaches about 100 MPa and the lubricant is piezo-viscous (the viscosity increases with the pressure), the lubricant carries enough pressure in the contact to elastically deform the surfaces. This case refers to the Elasto-Hydrodynamic Lubrication (EHL) regime. In HL, the film thickness varies between hundreds of nm and tens of μm whereas in EHL, the film thickness can reach down to few nm and is much lower than the elastic deflection of the contact.

Since the lubricant velocity must accommodate to the surface velocities, it experiences shearing responsible for the Couette friction. The Couette shear stress is the product of the viscosity η and the shear rate $\dot{\gamma}$. Usually, the friction increases with the viscosity and the mean velocity u_e ($\propto \dot{\gamma}$). In addition, pressure gradients generate Poiseuille friction. However, the viscosity increase in the EHL contact is high enough so that the Poiseuille shear stress is in general negligible compared to the Couette shear stress.

In summary, the HL and EHL regimes strongly depend on the viscous properties of the lubricant, on the surface velocities and on the solid shape.

Mixed lubrication regime

An increasing load and/or decreasing viscosity and surface velocities in HL and EHL regimes weaken the hydrodynamic lift. The surface separation keeps reducing until the first asperity contacts: this is the onset of the mixed lubrication regime. In this regime, the load carried by the fluid is progressively transferred to the asperities in the contact; slight wear may occur. The contact is split into two regions: one in HL or EHL (full separation) and the other in boundary lubrication (asperity contacts). Thus, the mixed friction is the sum of the fluid shear stress and the asperity contact shear stress contributions. The increasing number of asperity contacts will raise the friction.

Boundary lubrication regime

In boundary lubrication, the film thickness resulting in the surface separation, is only of few lubricant molecules adsorbed on the two surfaces. In this regime, the load entirely bears on the asperity contacts: there is no more hydrodynamic lift. The wear is severe and the friction can be a constant equal to the value reached at the boundary/mixed regime transition. Since the film thickness is of few molecules, the boundary friction is directly related to the physics-chemistry of the lubricant and the two surfaces. In that case, lubricant additives become of prime importance.

1.1.3 Stribeck curve

The friction coefficient is the ratio of the tangential force F_T, i.e. the friction force, over the normal force F_N, i.e. the load. The friction force is equal to the integral of the shear stress τ over the whole lubricated contact. In his works, Stribeck plotted the eponymous curve in which the friction coefficient is reported versus the generalized Sommerfeld number S:

$$S = \frac{\eta_0 \omega}{p_m} \ , \tag{1.1}$$

with ω the rotation velocity and p_m the mean contact pressure which depends of the load. The general shape of this curve is, to a certain extend, the same regardless of the mechanical contact and is reported in Fig. 1.2. Three regions are distinguished:

- at high S, the friction follows a positive slope,
- at low S, the friction is constant,

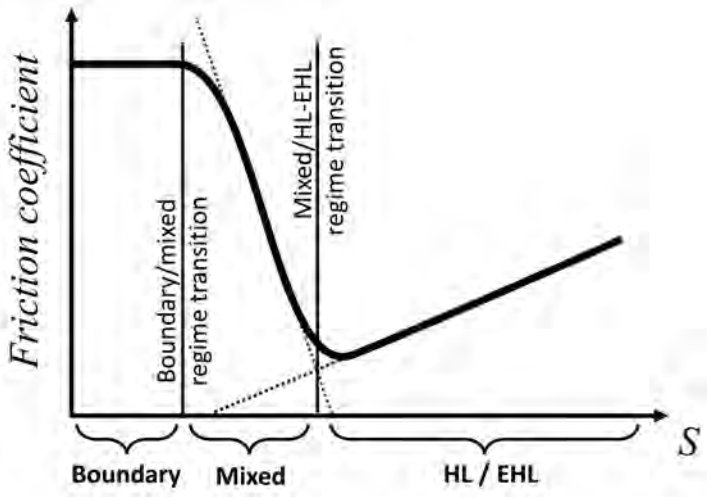

Figure 1.2: Example of a Stribeck curve plotting the friction coefficient versus the generalized Sommerfeld number S. The three lubrication regimes are highlighted: boundary, mixed and HD/EHL regimes.

- and in between, the friction is a decreasing function of S with a minimum.

These three parts of the Stribeck curve respectively correspond to the EHL (or HL), boundary and mixed regimes. The position of the minimum usually indicates the mixed/EHL transition. Hence, the Stribeck curves are a precious tool to identify the lubrication regimes and the transitions between these regimes. Nonetheless, the definition of the mixed/EHL transition, may be source of confusion if associated to the S value below which the friction is no more purely viscous. Actually, Poon et al. [13] pointed out that local viscosity increases induced by micro-EHL effects, can occur and raise the friction without asperity contact. In the following, the general definition of the mixed/EHL transition given by Schipper [14] is used: the mixed/EHL transition is the abscissa of the slope intersect at the inflection point of the Stribeck curve and of the positive slope at high S (dash lines in Fig. 1.2). The physical origin of this transition, asperity contact or micro-EHL, is not presupposed.

1.2 Smooth EHL contacts

This section describes the fundamental physical principle in EHL regime for smooth surfaces. An EHL point contact is divided into three regions as illustrated in Fig. 1.3, the *inlet* where the lubricant is pressurized before entering the

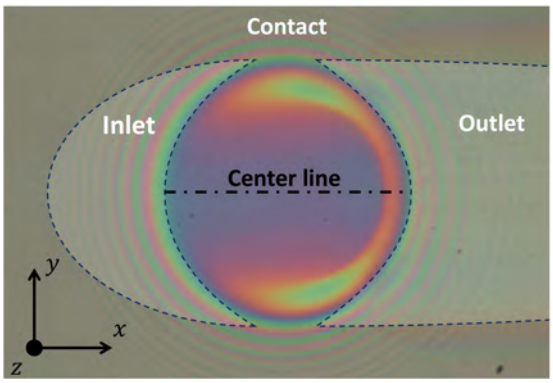

Figure 1.3: Contact interferogram of an EHL point contact highlighting the inlet, contact and outlet regions and the center line. The fluid goes from left to right. Each color corresponds to a film thickness separating the surfaces.

contact region where the sheared lubricant separates the two surfaces and the *outlet* where the lubricant exits the contact and cavitates. The contact width is twice the Hertzian contact radius a.

The physics of smooth EHL contacts is well described by the two-dimensional Reynolds equation and presented in more details in Chapter 2:

$$\frac{\partial}{\partial x}\left(\frac{\rho h^3}{12\eta}\frac{\partial p}{\partial x}\right)+\frac{\partial}{\partial y}\left(\frac{\rho h^3}{12\eta}\frac{\partial p}{\partial y}\right)=u_e\frac{\partial \rho h}{\partial x}+\frac{\partial \rho h}{\partial t}\ . \tag{1.2}$$

Eq. 1.2 emphasizes the coupling between the lubricant pressure p and the lubricant film thickness h; the lubricant viscosity η and density ρ are pressure-dependent. Also, the film thickness and the pressure are coupled through the elastic deformation of the surfaces. To predict the film thickness and pressure inside an EHL contact various approaches - analytical, empirical or numerical - have been proposed.

1.2.1 Ertel-Grubin model

An analytical model to solve the Reynolds equation (Eq. 1.2) was proposed for the first time by Ertel and Grubin [15]. The EHL contact was reduced to an EHL line contact (one-dimensional Reynolds equation) with an incompressible fluid. Under steady-state conditions, Eq. 1.2 becomes:

$$\frac{\partial}{\partial x}\left(\frac{h^3}{12\eta}\frac{\partial p}{\partial x}\right)=u_e\frac{\partial h}{\partial x}\ . \tag{1.3}$$

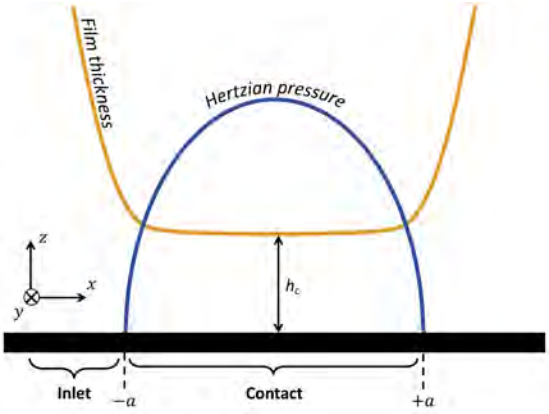

Figure 1.4: Film thickness and pressure profiles in the Ertel-Grubin model.

The viscosity η was assumed to follow the Barus law:

$$\eta = \eta_0 \exp(\alpha p) \ , \tag{1.4}$$

with η_0 the viscosity at atmospheric pressure and α the piezo-viscosity coefficient. Introducing the 'reduced' pressure q given by:

$$q = \frac{1 - \exp(-\alpha p)}{\alpha} \ , \tag{1.5}$$

Eq. 1.3 yields:

$$\frac{\partial}{\partial x}\left(h^3 \frac{\partial q}{\partial x}\right) = 12\eta_0 u_e \frac{\partial h}{\partial x} \ . \tag{1.6}$$

In Ertel-Grubin model, the surfaces were assumed to be parallel inside the contact region. The film thickness is constant in the whole contact region, equal to the central film thickness h_c. The contact interferogram from Fig. 1.3 shows that the color is homogeneous on the center line except at the contact end, close to the constriction region. Therefore, the previous approximation makes sense. In addition, the pressure distribution was supposed to be equal to the Hertzian one. Fig. 1.4 illustrates the film thickness and pressure profiles according to Ertel-Grubin's assumptions.

To estimate h_c, Ertel-Grubin solved Eq. 1.6 in the inlet region, $x \in]-\infty, -a]$. h_c was the value of h in $x = -a$. The shape of the inlet film thickness was approximated by the inlet Hertzian deformed contact shape. However, Wolveridge et al. suggested later a more accurate approximation originally proposed by Crook [15]:

$$h(x) = h_c + C|x + a|^{3/2} \ , \tag{1.7}$$

with C a constant. The film thickness h in Eq. 1.6 was substituted by its expression in Eq. 1.7. Eq. 1.6 was then integrated twice. The second integration was evaluated from $-\infty$ to $-a$, given the following approximations:

- in $x = -a$, $q = 1/\alpha$ as the pressure is very high in the contact, i.e. $\exp(-\alpha p) \ll 1$,
- for $x \to -\infty$, $q = 0$ as the pressure is almost null.

Finally, the Ertel-Grubin model gave the following relation for h_c:

$$\frac{h_c}{R_x} = 2.2081\ U^{3/4} G^{3/4} W_1^{-1/8}\ , \tag{1.8}$$

where U, G, and W_1 are speed, material and load dimensionless numbers introduced by Dowson and Higginson (see Eq. 2.35, 2.36 and 2.37). It yields that h_c is a function of:

- the viscosity at atmospheric pressure η_0,
- the entrainment velocity u_e,
- the piezo-viscosity coefficient α,
- the curvature radius R_x,
- the material properties (Young modulus, Poisson ratio),
- the applied load.

For a given material and geometry, the Ertel-Grubin model indicates that the film thickness in EHL strongly depends on the inlet viscosity η_0, the mean velocity u_e and the piezo-viscous coefficient α. On the contrary, the load has only a slight influence on the lubrication performance. Moreover, the model emphasizes the fundamental role of the inlet in the film thickness formation in EHL.

1.2.2 Hamrock and Dowson formula

Later Hamrock and Dowson [16] proposed an empirical formula, based on their numerical and experimental results, of the central film thickness h_c in EHL line contacts:

$$\frac{h_c}{R_x} = 2.922\ U^{0.692} G^{0.470} W_1^{-0.166}\ . \tag{1.9}$$

As predicted with the analytical formula from the Ertel-Grubin model, the inlet viscosity and mean velocity play a major role in the formation of the central film thickness. However, Eq. 1.9 indicates that the piezo-viscosity coefficient has a lesser influence than estimated in the Ertel-Grubin model. Hamrock and Dowson confirmed that the load is not much significant in the lubrication process. Hamrock and Dowson also determined similar relation for EHL point contacts:

$$\frac{h_c}{R_x} = 2.69\ U^{0.67} G^{0.53} W_2^{-0.067} \left(1 - 0.61\mathrm{e}^{-0.73}\right)\ , \tag{1.10}$$

with W_2 (see Eq. 2.38) the load dimensionless number in point contact from Dowson and Higginson. It is remarkable that the exponents of the speed, material and load dimensionless numbers in Eq. 1.9 and 1.10 are very close. This means that the physics of te elastohydrodynamic lubrication is similar in line and point contacts.

Despite numerous simplifications, the analytical Ertel-Grubin model is also able to give a very good physical understanding of lubrication mechanisms in both line and point contacts. Nonetheless, the Ertel-Grubin model is not suitable for quantitative studies.

1.2.3 Numerical solutions

To calculate the pressure and film thickness distributions in a smooth EHL contact, several numerical methods have been used. The two most efficient ones are: the multigrid and the Newton-Raphson methods. They are both based on the resolution of the Reynolds equation instead of the Navier-Stokes equations used in the Computational Fluid Dynamics (CFD) methods [17, 18]. The convergence issues of the CFD methods do not currently make them appealing for EHL numerical simulations.

In the following, the basics of the multigrid and Newton-Raphson methods are presented. It should be mentioned that further numerical works have been developed to include non-Newtonian and/or thermal effects.

Multigrid method

The multi-grid method was introduced by Lubrecht et al. [19, 20, 8] to solve the EHL problem. The concept of this method bears on the resolution of discretized equations on various grid sizes. The EHL equations are solved on the finest grid leading to the approximated solution s_0. EHL equations are transposed to a coarser grid and the approximated error s_1 made in the approximated solution

s_0 is determined. On the next coarser grid, the approximated error s_2 made on approximated error s_1 is computed, etc. until reaching the coarsest grid. Then, the approximated errors s_i on coarse grids are used to improve the approximation s_{i-1} obtained on their corresponding finer grids. This process goes from the coarsest grid to the finest grid which gives the EHL solution, i.e. the film thickness and pressure distribution. At each step, the solution is obtained using the Gauss-Seidel iteration scheme, as first proposed by Hamrock and Dowson [21, 22, 23] in an EHL solver.

The advantage of the multigrid method is to overcome the long convergence time of the Gauss-Seidel scheme. Indeed, at each Gauss-Seidel iteration the error on the smaller wavelength components is reduced faster than that on the longer ones. This results in numerous iterations and very long computing time to get an accurate solution. The steps of the multigrid method are: (i) solving the governing equation on a coarser grid with Gauss-Seidel scheme, calculating the error s_i of an approximated solution s_{i-1} previously obtained on a finer grid with few Gauss-Seidel iterations, (ii) correcting s_{i-1} using s_i and (iii) performing additional few Gauss-Seidel iterations on the finer grid. Indeed, the passage through the coarser grid, artificially lower the wavelength component, improving the efficiency of the Gauss-Seidel iterations. Combining several steps of coarse grids leads to a very efficient and competitive EHL solver.

Major improvements to the multigrid method were then developed by Venner et al. [24, 9, 25, 26]. They added the Jacobi iteration scheme to overcome convergence issues at high load conditions. Moreover, they integrated the multi-integration technique presented by Brandt et al. [27]. This technique implements a new and lighter way to calculate the elastic deformation δ_e described by the half-space approach (here in point contact):

$$\delta_e(x,y) = \frac{2}{\pi E'} \int_{\mathbb{R}^2} \frac{p(x',y')dx'dy'}{\sqrt{(x-x')^2+(y-y')^2}} \ . \tag{1.11}$$

Once discretized, Eq. 1.11 takes the following form:

$$\delta_e(x_i,y_j) = \sum_{k,l} K_{k-i,l-j}\ p(x_k,y_l) \ , \tag{1.12}$$

where $\{K\}_{k,l}$ are constant coefficients. The computation of each $\delta_e(x_i,y_j)$ requires to sum all the pressures $p(x_k,y_l)$. For a problem with n nodes, the complexity rises to $O\left(n^2\right)$. With the multi-integration method, the calculus of the integral is added to the multigrid process, reducing the complexity to $O\left(n\ln(n)\right)$.

Newton-Raphson method

The Newton-Raphson was introduced before the multigrid method [28] to solve the EHL problem. This method bears on the Taylor series of a function f, restricted to the first order:

$$f(u + \Delta u) \approx f(u) + \Delta u f'(u) \ . \tag{1.13}$$

To find the solution $\tilde{u}$ to $f(\hat{u}) = 0$, the Newton-Raphson method starts from a chosen solution u_0. Then, the increment Δu needed to obtain $f(u_0 + \Delta u) = 0$ is approximated using Eq. 1.13:

$$\Delta u \approx -\frac{f(u_0)}{f'(u_0)} \ . \tag{1.14}$$

In the case of a system of equations, f and f' respectively correspond to the residual vector and the Jacobian matrix of this system. Eq. 1.14 shows that f'^{-1} must be calculated, i.e. the Jacobian must be inverted which represents currently the major limitation. n nodes lead to a n^2 Jacobian matrix. The matrix inversion requires a lot of time and memory, all the more so the Jacobian is a full matrix due to the half-space modeling the elastic deformation (Eq. 1.11). As Eq. 1.13 is an approximation, the above process needs to be repeated until reaching the solution with the desired accuracy: the previous approximated solution is used as the next 'chosen solution'.

To reduce the complexity of the Newton-Raphson algorithm, Holmes et al. [29, 30] developed the differential deflection method. They replaced the film thickness equation (see Eq. 2.20) with its differential form [31]:

$$\frac{\partial^2 h(x_i, y_j)}{\partial x^2} + \frac{\partial^2 h(x_i, y_j)}{\partial y^2} = \frac{1}{R_x} + \frac{1}{R_y} + \frac{2}{\pi E'} \sum_{k,l} c_{k-i,l-j} p_{k,l} \ , \tag{1.15}$$

where $\{c\}_{k,l}$ are coefficients that decay faster, as the indexes increase from zero, than the coefficients $\{K\}_{k,l}$ in the discretization form of the elastic deformation δ_e (see Eq. 1.12). This allows to reduce the density of the Jacobian matrix and thus to achieve time and memory savings.

Recently, Habchi et al. [32, 33] developed the *Full system approach*, using a full-body elasticity instead of the half-space approach. They solved solid mechanics equations inside the elastic body to calculate δ_e and the Reynolds equation at the contact surface. As a result, the Jacobian matrix becomes a band matrix but wider as the nodes inside the solid body are added. As a result, Habchi et al. reported memory storage reduction.

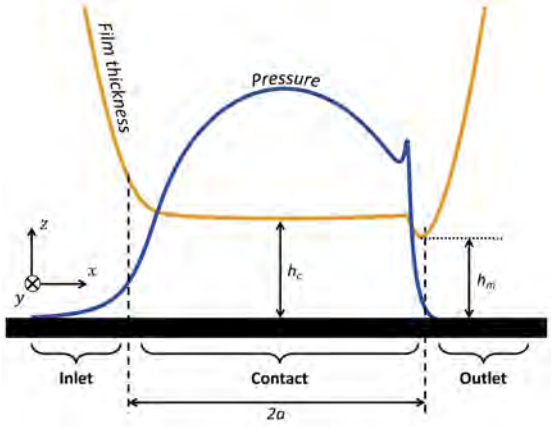

Figure 1.5: Typical shapes of film thickness and pressure in smooth EHL line contacts. The inlet, contact and outlet regions are emphasized as well as the central film thickness h_c and the minimum film thickness h_m.

Film thickness and pressure profiles

Typical shapes of the film thickness and the pressure in EHL line contacts obtained using the Newton-Raphson method (see Chapter 3 for details), are reported in Fig. 1.5. The film thickness and pressure profiles in the Ertel-Grubin model (see Fig. 1.4) are qualitatively in agreement with these numerical ones. Nevertheless, the pressure peak and the constriction are not modeled in the Ertel-Grubin model. Two film thicknesses are defined: (i) the central film thickness h_c at the contact center and the minimum film thickness h_m which occurs in the constriction region in smooth EHL.

1.2.4 Friction coefficient

Shear stress

In EHL, two flows, Couette and Poiseuille, are responsible for the EHL shear stress. The difference of the surface velocities causes the Couette flow whereas the pressure gradients generate the Poiseuille flow. The Couette shear stress is:

$$\tau_c = \eta\dot{\gamma} \ , \tag{1.16}$$

where $\dot{\gamma}$ is the shear rate defined as:

$$\dot{\gamma} = \frac{\partial u}{\partial z} \ , \tag{1.17}$$

with u the speed of the fluid. Considering the film thickness h, the sliding-rolling ratio Σ and the entrainment speed u_e, the shear rate can be approximate by:

$$\dot{\gamma}(x) \approx \frac{u_e \Sigma}{h(x)} \ . \tag{1.18}$$

The Poiseuille shear stress is given by:

$$\tau_p = \pm \frac{h}{2} \frac{\partial p}{\partial x} \ . \tag{1.19}$$

Due to its piezo-viscosity, the lubricant viscosity is very high in the contact and low in the inlet and the outlet. Therefore, the Couette shear stress is negligible in the inlet and outlet regions in comparison to that in the contact region. As Fig. 1.5 reports, the pressure does not vary sharply inside the EHL contact except at the narrow location of the pressure peak and at the inlet which cause high local pressure gradients. Yet, over the whole contact $\tau_p \ll \tau_c$ because of the very high viscosity. As a result, the EHL friction force depends mainly on the Couette shear stress in the contact region. The friction force is the integral of τ_c over the contact region: $\int_{-a}^{+a} \tau_c$. To sum up, the EHL friction is mainly caused by the lubricant piezo-viscosity and its shearing.

Lubricant rheology

Many lubricants have a non-Newtonian rheology which must be taken into account to model their viscosity and thus their friction in EHL. Theories on non-Newtonian viscosities assume that the fluid characteristics are associated with structural changes such as molecule or particle organization [34], flocculation state [35], formation and rupture of structural links [36], rearrangement of polymer chain network [37].

Eyring first introduced the partition state chemical reaction rate theory, to model the viscosity of simple liquids made of spherical molecules. He modeled the flow as a monomolecular 'chemical' reaction. The elementary process (flow unit) is the displacement of one molecule from an equilibrium position to another over a potential energy barrier, disrupted by the fluid shearing. The expression of viscosity η versus the shear rate $\dot{\gamma}$ yields:

$$\eta = \frac{\tau_0}{\dot{\gamma}} \sinh^{-1}\left(\eta_0 \frac{\dot{\gamma}}{\tau_0}\right) \ , \tag{1.20}$$

with η_0 the zero shear rate (and atmospheric pressure) viscosity and τ_0 the shear stress above which the fluid is no more Newtonian. The energy barrier can also

be viewed as the energy required to create a volume large enough to receive a molecule [38]. This required energy increases when a pressure is applied, leading to a viscosity rising. Ree and Eyring [39] extended the previous model to a wider range of materials and shear rates. They considered the fluid as a multimolecular material, made of different flow unit types.

From works of Goodeve [40] on the viscosity impulse theory, Gillespie [35] proposed a similar kinetics approach. During shearing, links between the particles stretch, break and reform. An impulse is transmitted from a fast-moving layer to a slower adjacent one. The non-Newtonian behavior is the consequence of the shear effect on the number and average lifetime of links and any change in interacting particle size. This was used as a starting point to derive a $\tau(\dot{\gamma})$-relationship for colloidal materials, calculating the number of links per particles and their rupture probability due to the shearing. At high shear rate, the viscosity rate becomes:

$$\eta = \eta^* + \frac{\tau_L}{\dot{\gamma}_c + \dot{\gamma}} \ , \tag{1.21}$$

with η^* a plastic viscosity, τ_L the yield shear stress and $\dot{\gamma}_c$ a critical shear rate.

Later, Cross proposed a similar viscosity model for colloidal liquids. His model was based on the equilibrium between the formation and the rupture of linkages between dispersed or dissolved particles [41]. Assuming that linkages are the result of the Brownian movement, it yielded the viscosity expression:

$$\eta = \eta_\infty + \frac{\eta_0 - \eta_\infty}{1 + (\dot{\gamma}/\dot{\gamma}_c)^n} \ , \tag{1.22}$$

with η_0 and η_∞ the viscosities at zero and infinite shear rates, respectively, and $1/\dot{\gamma}_c$ a relaxation time. The Gillespie's theory (Eq. 1.21) can be interpreted as a particular case of Cross' theory (Eq. 1.22) with $n = 1$. Cross first derived the value 2/3 for n. Presently, the shear rate exponent is often considered as a constant, less than the unity. Nevertheless, several authors showed that $n > 1$ may occur which strongly depends on the colloidal fluid polydispersity [41, 42]. In further works, Cross [43] generalized the kinetics treatment allowing to consider shear thickening fluid.

Meanwhile, Lodge [44] derived a polymer-rheology model based on molecular network theory. As the fluid flows, temporary links are created and lost between randomly arranged polymer chains. Later, Carreau [37] provided the following mathematical solution to this model:

$$\eta = \eta_\infty + \frac{\eta_0 - \eta_\infty}{\left[1 + \left(\frac{\dot{\gamma}}{\dot{\gamma}_c}\right)^2\right]^{\frac{1-m}{2}}} \ . \tag{1.23}$$

Interfacial friction and rheology

To describe the friction in EHL, models based on the previous non-Newtonian rheological works were used to predict the shear stress. Johnson and Tevaarwerk [45, 46] used the Eyring model (Eq. 1.20) to describe the non-linear viscous response of the lubricant. However, this approach did not explain the transition from shear thinning flow to limiting plastic shear [47]. Then, Bair and Winer [48, 49, 50, 51] proposed an alternative approach based on the glass transition property of amorphous polymers to introduce the limiting shear stress of the lubricant. The $\tau(\dot{\gamma})$-relationship yielded:

$$\dot{\gamma} = -\frac{\tau_L}{\eta} \ln\left(1 - \frac{\tau}{\tau_L}\right) \ , \tag{1.24}$$

with τ_L the limiting shear stress which is proportional to the pressure.

Few works have considered other approaches [52]. Lee and Hamrock [53] used a 'circular' non-Newtonian model bearing on the following law:

$$\dot{\gamma} = \frac{\tau}{\eta}\sqrt{1 - \left(\frac{\tau}{\tau_L}\right)} \ . \tag{1.25}$$

Then, Elsharkawy and Hamrock [54] proposed a generalization of the limiting shear stress models leading to the expression:

$$\dot{\gamma} = \frac{\tau}{\eta}\left[1 - \left(\frac{\tau}{\tau_L}\right)^n\right]^{-1/n} \ , \tag{1.26}$$

with $n = 1$ and 2 with linear and circular models, respectively.

Jacobson [55, 56] calculated the film thickness and pressure distributions in EHL, modeling the lubricant as a combination of (i) a Newtonian liquid at low pressure with (ii) a plastic solid at high pressure and shear stress. With Hamrock [56, 57], Jacobson also introduced a model in which the slip at the surfaces was used to describe the limiting shear stress behavior of the lubricant. Ehret [58] also implemented slip boundary conditions in EHL, re-addressing the flow conditions and rheological behavior of the lubricant.

Recently, Spikes et al. [59] fitted the parameters of Eyring (Eq. 1.20) and Carreau (Eq. 1.23) rheological models with under pressure viscosity experiments. These rheological laws were then able to accurately predict the experimental EHL friction. Using a similar approach with the under pressure Cross-like fluid rheology (Eq. 1.22), Diew et al. [60] and Ernesto et al. [61] also well predicted the experimental EHL friction in traction, Stribeck experiments and for transient

kinematics at moderate pressures and shear rates. Even if various rheological laws have been used to model the EHL friction, all the works in the literature prone that the latter is mainly governed by the viscosity of the lubricant in the contact and its dependence on pressure and shear rate.

1.3 Textured EHL contacts

In smooth EHL, the shape of the inlet region is mainly given by the Hertz theory. Thus, the optimization of the film thickness is only achievable through the choice of the lubricant properties (η_0, α) which govern the shear rate ($\propto 1/h$), the under pressure viscosity and thus the friction.

It has been shown that surface texturing, i.e. the introduction of micro patterns on the surface, can significantly modify the inlet and contact shapes and thus the EHL film thickness and friction. The surface texturing introduces new geometrical parameters (depth, width, wavelength, roughness, etc.) to be tweaked. Understanding the relationship between these topographic parameters and the EHL physics open p a possibility to control the film thickness and friction in EHL. A review of surface texturing (groove and cavity texture) in both experimental and numerical EHL studies is presented to highlight the main knowledge in this field.

1.3.1 Groove-like textures

A groove is a one directional feature described by its depth d, width w and wavelength λ when periodic. Usually, d ranges from 100 nm to 1-2 μm, w is about 10-100 μm and λ is between 10 and 500 μm. In this review, EHL experimental works on grooves are combined with EHL numerical studies on sinusoidal waviness. Both topographic features have similar wavelength and amplitude and are also a one directional texture. Therefore, the tribological response of grooves and sinusoidal waviness in the EHL contact is comparable.

On one hand, the studies on the film thickness are reported. As a starting point, the analytical model of the transient solution in EHL and the amplitude reduction model are presented. Then, experiments dealing with the comparison of transverse (to the entrainment direction) grooves with longitudinal ones are reported. The measurements were made in pure rolling conditions ($\Sigma = 0\%$), or in sliding fixing either the smooth surface ($\Sigma = -200\%$) or the rough surface ($\Sigma = +200\%$). Results with other groove orientations are also described. Next, the influence of the groove geometry (depth, width) is emphasized. Finally, the

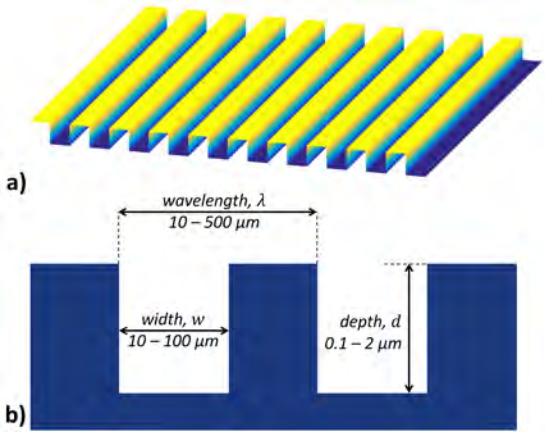

Figure 1.6: Scheme of a periodic groove (a) with a transverse profile (b) highlighting the geometrical parameters and their range.

effects of the SRR is presented. On the other hand, results on the EHL friction with grooves are highlighted.

Analytical transient solution

Greenwood and Morales-Espejel [62] analytically obtained the exact solution for an 'infinite EHL contact' with transverse sinusoidal waviness for $\Sigma = +200\%$. Introducing transient conditions [63], they showed that the pressure and film thickness of the transient solution are the sum of two components (see Fig. 1.7):

- the particular integral traveling at u_2 (velocity of the rough surface) and corresponding to the moving steady state solution,
- a complementary function traveling at u_e (velocity of the fluid) and representing the inlet disturbance on the film thickness and pressure due to the partially deformed roughness at the inlet.

This decomposition allows to physical understand the effects induced by the texture on the film thickness distribution and particularly the coupling between the perturbation in the inlet and that inside the contact.

Based on this analytical transient solution, Morales-Espejel et al. [64] proposed a fast and efficient model to predict the film thickness and pressure in transient EHL line contacts for any kind of roughness with low amplitude. This work also bore on the amplitude reduction theory described below and applied to the Fourier decomposition of the roughness. Later, Morales-Espejel et al. [65]

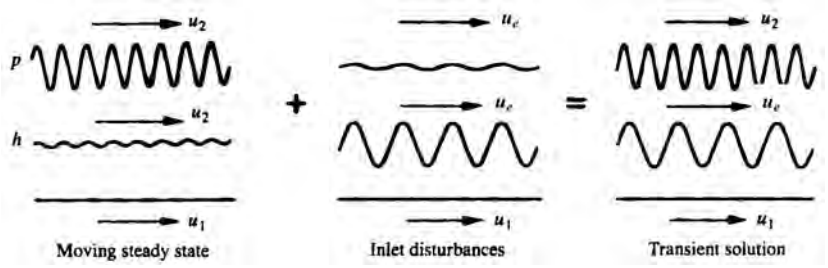

Figure 1.7: Transient pressure and film thickness in EHL line contact according the model of Greenwood and Morales-Espejel [63], for transverse sinusoidal waviness.

extended the Greenwood and Morales-Espejel model to take into account longitudinal waviness. This allowed them to develop a rapid calculations of the pressure and film thickness in pure rolling EHL point contacts. Hooke et al. [66] extended it to wider SRR conditions.

Amplitude reduction - wavelength effect

For $\Sigma = +200\%$, Kweh et al. [67] observed for numerical transverse waviness ($62.5 < d < 250$ nm, $\lambda = 200$ μm), that the waviness is almost flattened in the EHL contact. Later, Venner et al. [68] carried out several numerical simulations with transverse sinusoidal waviness to determine the dimensionless parameter governing the amplitude reduction in EHL line contact. The amplitude reduction was defined as the ratio of the elastically deformed amplitude A_d over the initial amplitude A_i. They demonstrated in pure rolling $\Sigma = 0\%$ and pure sliding $\Sigma = +200\%$ that the amplitude reduction is only a function of the dimensionless parameter ∇ defined as:

$$\nabla = \frac{\lambda}{a} M_1^{3/4} L^{1/2} \ . \tag{1.27}$$

Lubrecht et al. [69] extended the amplitude reduction theory to wider SRR conditions introducing the new dimensionless parameter $\bar{\nabla}$ given by:

$$\bar{\nabla} = \nabla \left(1 - \Sigma/2\right)^{-1/2} = \nabla \sqrt{\frac{u_e}{u_2}} \ . \tag{1.28}$$

When the Moes parameters M_1 and L are substituting by their definition in $\bar{\nabla}$, it yields, in terms of velocity, that $\bar{\nabla}$ depends only on the wavy surface velocity u_2 and not on u_e. This explains why at low SRR $-15\% < \Sigma < 10\%$ ($u_2 \approx u_e$), Sperka et al. [70] showed that the amplitude reduction is almost equal to that of pure rolling conditions.

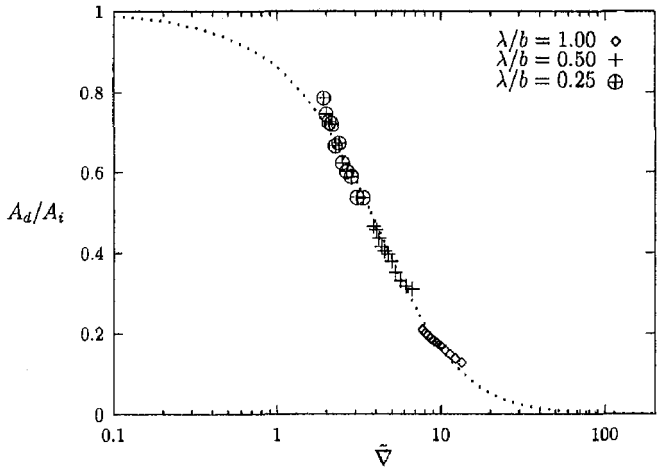

Figure 1.8: Amplitude reduction versus the dimensionless parameter $\bar{\nabla}$ from [69]. The numerical simulations and the fit (Eq. 1.29) are respectively reported with dots and a dash line.

Fitting the results on a single master curve (see Fig. 1.8), Lubrecht et al. [69] obtained the following expression of the amplitude reduction as a function of $\bar{\nabla}$:

$$\frac{A_d}{A_i} = \frac{1}{1 + 0.125\bar{\nabla} + 0.04\bar{\nabla}^2} \ . \tag{1.29}$$

The longer the wavelength, the stronger the amplitude reduction. The amplitude reduction theory allows a better understanding of previous observations reporting flattened surface with large surface wavelength components [71, 72, 73, 74]. Therefore, the tribological response of a periodic texture with a long wavelength will be similar to that of a smooth surface.

Transverse and longitudinal grooves

Jackson et al. [75] first reported EHL results with a groove-like texture: a surface with parallel artificially-produced cuts. The maximum peak-to-valley height was equal to $d = 380$ nm and the average periodicity was $\lambda = 51$ µm. Fixing these cuts either perpendicular or parallel to the entrainment direction allowed them to simulate either transverse or longitudinal grooves. At $\Sigma = +200\%$, with both transverse and longitudinal grooves, they reported a reduction of the minimum film thickness in comparison with the smooth case. The thickness reduction was stronger with longitudinal grooves.

At $\Sigma = 0\%$, Wedeven and Cusano [76] investigated transverse and longitudinal single grooves. The grooves had a depth $d = 500$ nm and a width $w = 40$

μm. Both transverse and longitudinal grooves (contact interferograms in Fig. 1.9a,c) reduced the nominal film thickness in comparison with smooth EHL case. However, the transverse groove decreased it to a lesser degree. Wedeven and Cusano also experimented these two grooves at $\Sigma = -200\%$. For the transverse groove (contact interferogram in Fig. 1.9b), the film thickness distribution was comparable to that of the rolling case, but with a film thickness reinforcement was generated at the groove rear. This thicker film lagged behind when the transverse groove passed through the EHL contact. For the longitudinal groove (contact interferogram in Fig. 1.9d), the same film thickness distribution as $\Sigma = 0\%$ was measured. For transverse grooves in sliding, Wedeven and Cusano stated that micro-EHL effects happened not only in the inlet (like in the three other cases) but also inside the EHL contact, leading to a local film thickness reinforcement. These works [75, 76] first highlighted thicker film thickness with transverse grooves than longitudinal ones. However, the surface clearance was lower than in smooth EHL.

Later, Lubrecht et al. [77] carried out research on numerical transverse and longitudinal waviness ($d \in [0.05a^2/R_x, 0.4a^2/R_x]$, $\lambda \in [0.5a, 8a]$) at $\Sigma = +200\%$. As groove, transverse waviness reduced to a lesser degree the minimum film thickness than the longitudinal grooves. The influence of both orientated waviness upon the minimum film thickness was one order larger than their effects on the average film thickness. Moreover, for large wavelengths $\lambda > a$, the longitudinal waviness reduced the average film thickness while the transverse waviness enhanced it. Venner et al. [78] also showed that the minimum film thickness remained in the side lobe of the constriction region for numerical transverse waviness ($d = 80$ nm, $\lambda = 59$ μm) at $\Sigma = -100$, 0 and $+100\%$.

Seabra et al. [79] showed that small waviness amplitudes were flattened whereas larger ones were not completely deformed. These ones formed leakage channels that reduced the film thickness. Holmes et al. [80] drew similar conclusion: the film thickness failure at the contact sides was due to side leakage inside the groove valley. This was also analytically pointed out by Evans et al. [81] with single transverse groove-like features. They adapted the Ertel-Grubin model, supposing that the pressure was infinite ($q = 1/\alpha$) at the front edge of the groove, i.e. at the "inlet" of the next downstream micro contact, located after the EHL inlet contact.

Transverse and longitudinal grooves reduce the minimum film thickness, i.e. the surface clearance due to the side leakage. Therefore, grooves will cause asperity contacts at operating conditions where smooth surfaces still ensure a full surface separation. In the Stribeck curve, the grooves are expected to increase the generalized Sommerfeld number S corresponding to the mixed/EHL transition.

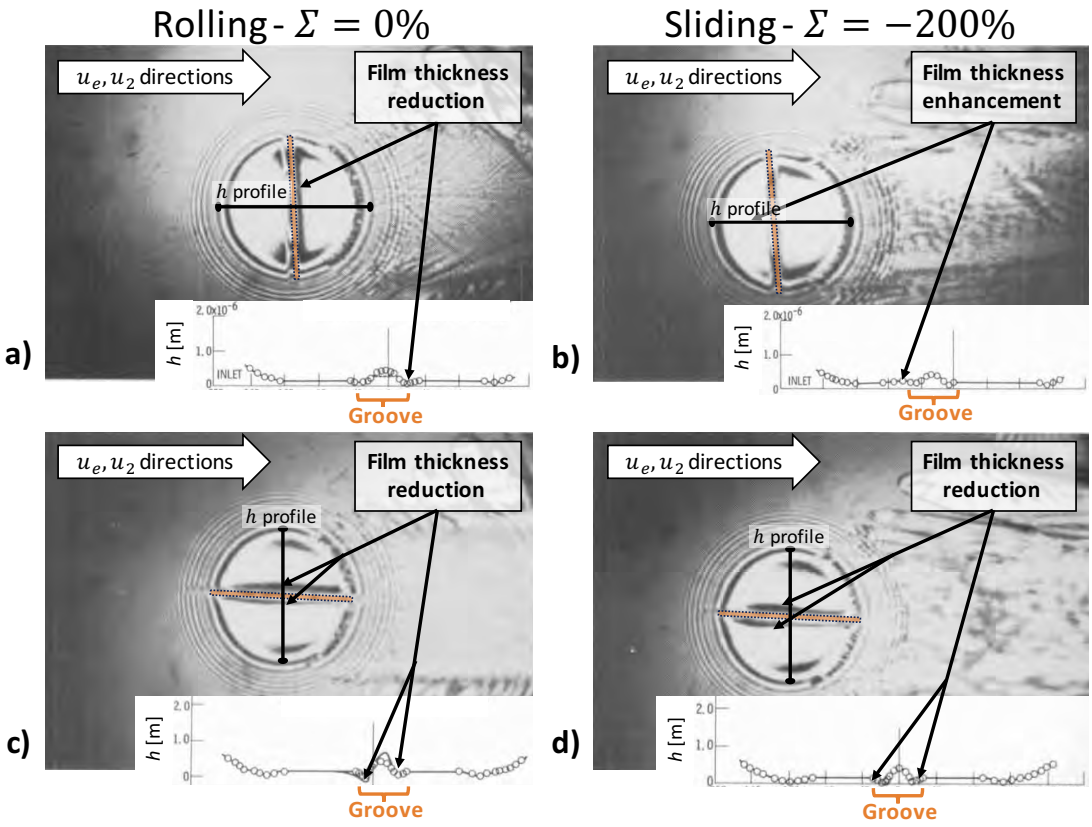

Figure 1.9: Interferograms of single transverse (a-b) and longitudinal (c-d) grooves passing through the EHL contact at $\Sigma = 0$ (a,c) and -200% (b,d) with their corresponding film thickness profile from [76]. The groove texture is highlighted in orange and the location of film thickness reduction and enhancement is indicated.

Other groove orientations

Further orientations ranging from 0° (longitudinal) to 90° (transverse), with numerical sinusoidal waviness, were simulated at $\Sigma = +200\%$ by Erhet et al. [82]. Two surfaces were modeled: $d = 495$ nm, $\lambda = 250$ μm and $d = 125$ nm, $\lambda = 125$ μm. The thickest nominal film thickness happened with the transverse configuration, confirming that transverse texture better lubricates than longitudinal one. The lowest minimum film thickness was obtained at the 60° orientation. For orientation between 0° and 90°, Erhet et al. numerically observed that the film thickness distribution was no more homogeneous in the EHL contact. In one half of the contact, the lubricant was deviated toward the outside. This side leakage resulted in poorer lubrication, leading to severe reduction of the surface clearance such as for the 60° oriented waviness. Kaneta et al. [83] got similar numerical results with $d = 200$ nm and $\lambda = \{80, 160\}$ μm. Nonetheless, at $\Sigma = 0\%$, Erhet et al. [84] found no significant influence of the orientation upon the minimum film thickness with numerical sinusoidal waviness ($d = 120$ nm, $\lambda/a \in [0.32, 0.68]$).

Groove geometry

For $\Sigma = -200\%$, Wedeven and Cusano [76] experimented a twice as deep as the transverse groove presented in the above part: *Transverse and longitudinal grooves*. When passing through the contact, this deeper ($d = 1$ μm) transverse single groove decreased the film thickness in the groove rear region (see Fig. 1.10a). They suspected the groove depth to cause a pressure drop, weakening the repressurization of the fluid at the cavity rear. Increasing groove depths leading to a thinner film was also reported by Krupka et al. [85]. They experimented longitudinal roughness with a root mean square of 90 nm amongst which a deep longitudinal groove ($d = 800$ nm, $w = 10$ μm) was located (see Fig. 1.10b).

From numerical simulations of transverse sinusoidal waviness ($0 < d < 1$ μm, $\lambda = 250$ μm), Venner et al. [86] demonstrated, in pure rolling, that the increasing amplitude d resulted in the reduction of the minimum film thickness but the rising of the average film thickness. The average film thickness was even thicker than the reference numerical smooth results. Nevertheless, with longitudinal grooves ($490 < d < 970$ nm) and shorter wavelength ($19 < \lambda < 45$ μm), Guegan et al. [87] experimentally found that the average film thickness was equal to the smooth surface one at both $\Sigma = 0$ and 50%. The groove wavelength $\lambda = 0.5a$ studied by Venner may be the reason of this difference with Guegan ($\lambda < a/3$).

Recently, Sperka et al. [88] introduced the groove influence ratio R_{GI} defined as the minimum film thickness induced by the groove on the center line (outside the constriction region) over the smooth film thickness. Experimenting transverse

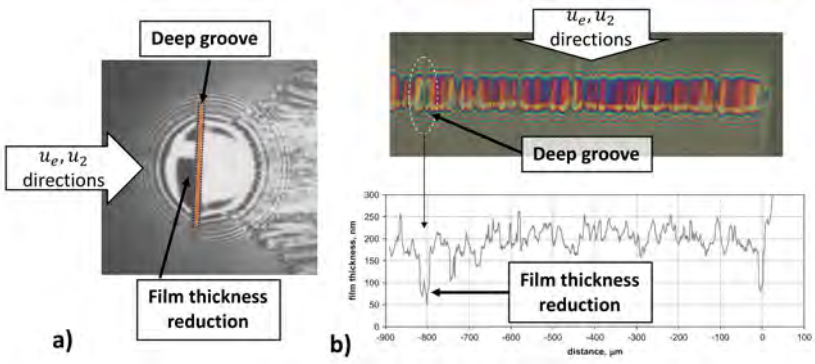

Figure 1.10: Influence of a deep groove on the local film thickness with transverse groove from [76] (a) and longitudinal groove from [85] (b).

single grooves ($80 < d < 1790$ nm, $8 < w < 63$ μm) at $\Sigma = +100\%$, they plotted the groove influence ratio R_{GI} versus the entrainment speed u_e for each groove geometry. From each of these curves, they calculated the velocity at which $R_{GI} = 50\%$ and referred it to u_{RGi50}. Then, they drew the u_{RGi50} values versus the depth d and width w of the grooves. Fitting their curve, they obtained the following expression:

$$u_{RGi50} = 0.0125\ d^{1.8} w^{0.576}\ . \tag{1.30}$$

Thus, they pointed out that the groove depth affects the speed u_{Rgi50} and the film thickness reduction to a much greater degree than the groove width.

In addition, Hirayama et al. [89] experimented complex groove patterns described in Fig. 1.11a. The groove depth ranged from 100 to 200 nm, the step depth was equal to 100 or 500 nm, the groove distance was between 100 and 500 μm, the groove angle was equal to 0°, 45° or 135° and the 'groove width' was set to 1 mm. When located in the side region of the contact (groove distance of 200 μm), the best central film thickness enhancement (+99%) was achieved thanks to a longitudinal groove (groove angle = 0°) with $d = 200$ nm and a step depth of 100 nm. Hirayama et al. attributed the film thickness reinforcement to the reduction of side leakage thanks to the presence of groove in the side regions. The groove depth was more effective than the groove angle in the film thickness reinforcement as reported in Fig. 1.11b.

When grooves are long enough to link the contact center to the contact edges, the valleys may provide a preferential channel for the leakage toward the outside thanks to the Poiseuille flow. This phenomenon is increased as the valley is deeper. Deep grooves decrease the local film thickness. However, when the grooves are only located at the contact edges with no connexion to the contact center, the central film thickness is reinforced.

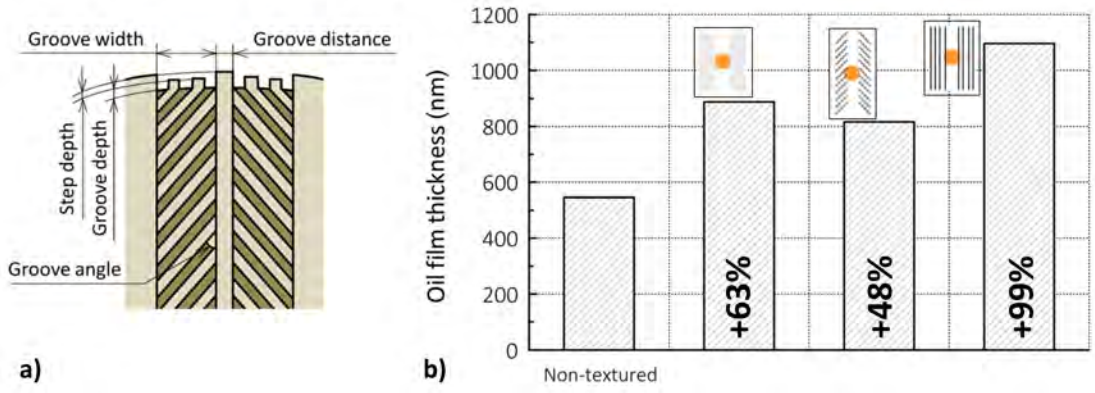

Figure 1.11: Geometrical characteristic of complex groove pattern (a) and the induced film thickness enhancement in comparison with the non-textured surface (b), adapted from [89].

Sliding Rolling ratio (SRR) value

Kaneta et al. [90] investigated EHL with grooves ($d = 500$ nm, $\lambda = 60$ μm) over $\Sigma \in [-100\%, +100\%]$. They reported the significant influence of the SRR with transverse groove on the film thickness distribution. This was later confirmed numerically in the above amplitude reduction formula (see Eq. 1.29). However, with longitudinal grooves, Kaneta reported no influence of the SRR on the film thickness distribution.

Venner et al. [78] showed that the central film thickness increased at $\Sigma = -100\%$ and decreased at $\Sigma = 0$ and $+100\%$. For negative SRR, they explained that the inlet perturbations are propagated slower than the original wave. The slower induced wave tends to limit the reduction generated by the original wave and enhances the total flow through the contact. Kaneta et al. [91] also observed different behavior between positive ($\Sigma = +100\%$) and negative ($\Sigma = -100\%$) SRR. With transverse grooves, $300 < d < 580$ nm and $\lambda = 60$ μm, they reported significant (insignificant) influence of the grooves in the downstream direction for positive (negative) SRR. Indeed, the Greenwood and Morales-Espejel model [62, 63] showed that the modification of the ratio $u_2/u_e = 1 - \Sigma/2$ directly influences the phasing between the two components of the transverse transient solutions and thus on the resulting film thickness distribution.

Groove friction

Contrary to the film thickness, fewer studies carried out the influence of groove upon the friction in EHL. Wedeven and Cusano [92] also studied the influence of single transverse and longitudinal grooves upon the friction ($d = 500$ nm and $w = 40$ µm) at $\Sigma = +200\%$. They reported an increase of the friction in both cases, regardless of the location of the groove inside the EHL contact. The transverse groove increased the friction to a larger degree than the longitudinal groove. Wedeven and Cusano suspected the friction increase to result from the inlet shape modifications and micro-EHL effects inside the EHL contact. These change the film thickness and pressure and thus the friction. Studying longitudinal roughness, Jacod et al. [93] pointed out the relation between the viscosity and friction through a dimensionless parameter representing the measure of the pressure-induced viscosity variations. This allowed them to predict the possible friction change in case of longitudinal roughness.

With transverse grooves shorter than the contact diameter (200 µm length $< 2a$, $d = 600$ nm and $w = 60$ µm), Ali et al. [94] observed an increase in the film thickness. They also obtained a reduction in the friction in EHL up to 20% in sliding-rolling conditions. They explained the friction reduction by the increase of film thickness generated by the grooves and thus the reduction of the shear rate. The pressure at the groove location was low and thus considered as not significant in the friction decrease.

Suh et al. [95] investigated the friction with crosshatched grooves as illustrated in Fig. 1.12a-b ($d = 5$ µm, $w \in \{40, 70, 100\}$ µm). The angle ranged from 20° to 60°. At $\Sigma = +200\%$, they observed a friction reduction which depended on both the crosshatch angle (θ_R) and the groove width (w). They introduced the sliding length G_l of the fluid inside the groove as illustrated in Fig. 1.12b and the trigonometrical relation between G_l, w and θ_R is:

$$G_l = \frac{w}{\cos\theta_R} \ . \tag{1.31}$$

As illustrated in Fig. 1.12c, the friction reduction occurred when the sliding length G_l increased, i.e. when the width and/or the angle increased (from 0° to 90°), regardless of the surface velocity. Hence, wide crosshatched grooves close to longitudinal ones tend to reduce the friction in EHL.

1.3.2 Cavity textures

A cavity texture is a two dimensional pattern as illustrated in Fig. 1.13a-b. Its depth d and diameter $\varnothing$ respectively range from 1 to 100 µm and from 10 nm

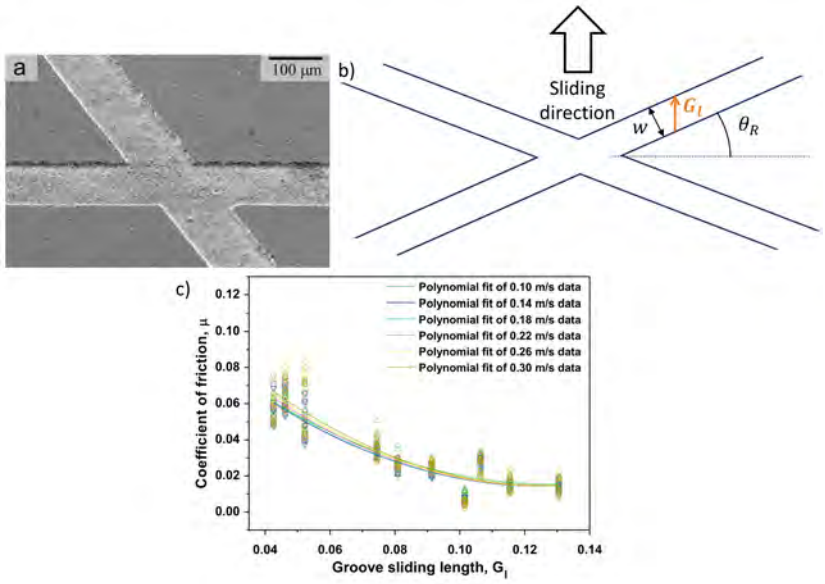

Figure 1.12: SEM image of a crosshatched groove from [95] (a). Scheme of a crosshatched groove illustrating the width w, the angle θ_R and the sliding length G_l (b). Friction coefficient versus the groove sliding length G_l at various velocities (c).

to 10 µm. In 1979, Wedeven and Cusano [76] investigated the effects of a single cavity ($d = 1$ µm, $\varnothing = 10$ µm). At $\Sigma = 0\%$, in pure rolling conditions, the cavity locally decreased the film thickness at its front. Wedeven and Cusano attributed the decrease to the pressure disturbances which had occurred when the cavity had passed through the contact inlet. At $\Sigma = -200\%$, a film thickness reduction was still observed at the cavity front but to a lesser degree than previously. In addition, a local film thickness enhancement - twice the smooth film thickness - happened at the cavity rear (see Fig. 1.14a). As the cavity passed through the contact, this thicker film lagged behind the cavity (see Fig. 1.14a-c).

Wedeven and Cusano also measured the friction [92] for $\Sigma = +200\%$ fixing the cavity at various location in the contact. When the cavity was located at the contact entrance (in the inlet region), the friction decreased. Wedeven and Cusano explained that the cavity in the inlet increased the fluid pressurization leading to a thicker film downstream. Therefore, the friction decreased. On the contrary, the friction increased when the cavity was inside the contact region. When the cavity was placed elsewhere in the contact, the film thickness was reduced in the cavity vicinity and local pressure increase was likely to occur, leading to the friction rising.

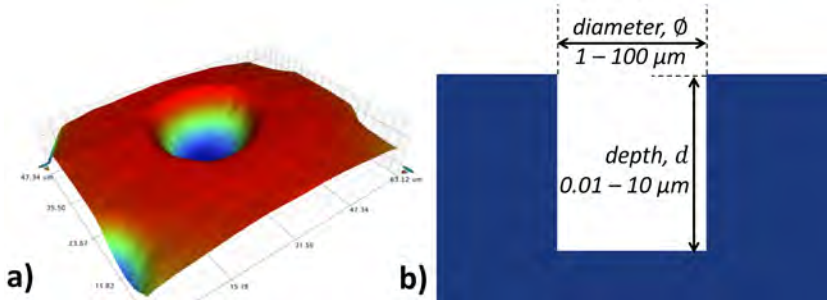

Figure 1.13: Topographic image of a cavity obtained with femtosecond LASER (a) and a schematic profile of the cavity highlighting its depth and diameter (b).

Cavity geometry and film thickness

Later, Mourier et al. [4, 96, 97], with both experimental and numerical approaches, investigated the influence of the cavity geometry on the film thickness. At $\Sigma = 0\%$ with a cavity with $d = 180$ nm and $\varnothing = 56$ µm, Mourier et al. experimentally observed and numerically predicted a small local decrease of film thickness located at the cavity front as previously noticed by Wedeven and Cusano. Elsewhere, the cavity did not induce a significant film thickness variation for pure rolling condition. Introducing sliding, Mourier et al. reported significant film thickness variations. For $\Sigma = +100\%$, the same cavity generated a film thickness enhancement which spread from the cavity front toward the downstream direction.

Keeping $\Sigma = +100\%$, Mourier et al. investigated with different cavity depths, 29 nm $< d <$ 10.5 µm, with constant diameter $\varnothing = 56$ µm. Except for $d = 29$ nm, all their contact interferograms (see Fig. 1.15a) showed a film thickness modification at the cavity front. There, the film thickness enhancement Δ_h, equal to the maximal film thickness induced by the cavity minus the smooth central film thickness, was measured. The ratio of Δ_h over the smooth film thickness h is plotted versus the cavity depth d in Fig. 1.15b. Mourier et al. emphasized the existence of an optimal cavity depth value, around 400 nm, which maximizes the film thickness reinforcement. For either too shallow cavities (e.g.: $d = 29$ nm) or too deep cavities (e.g.: $d = 2.1$ and 10.5 µm) no film thickness increase was observed. Krupka and Hartl [98] carried out experiments with cavities with 513 nm $< d <$ 1.453 µm and confirmed the depth dependency of the film thickness reinforcement for positive SRR. With cavity depth of 200-300 nm, Krupka et al. [99] were able to lift off the surfaces in mixed lubrication regime at Σ = -50 and + 50%, confirming the good lubrication behavior of such cavity depth (hundreds of nm).

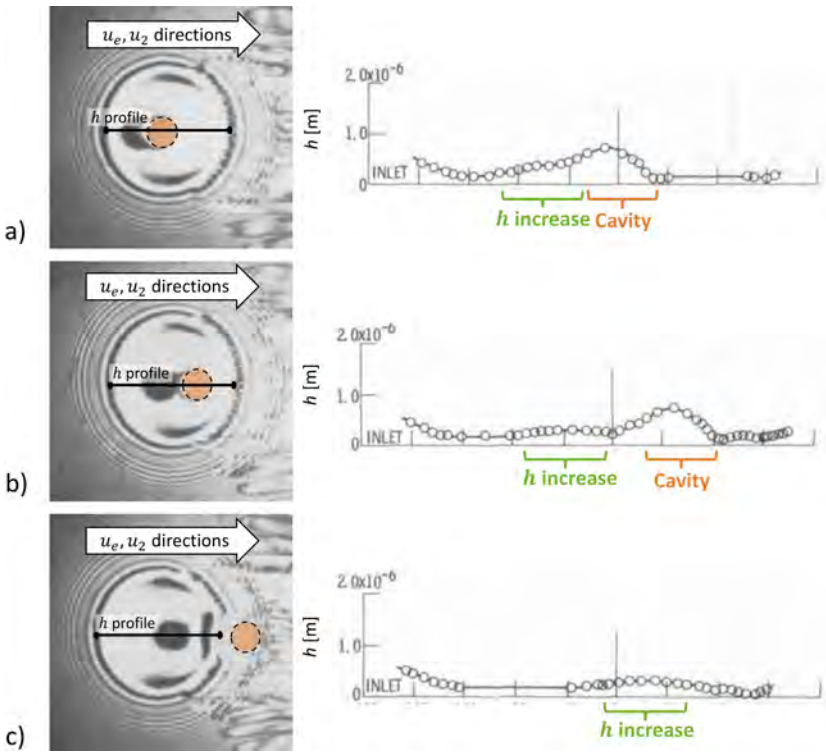

Figure 1.14: Contact interferograms and film thickness profiles on the center line when a single cavity passes through the EHL contact at $\Sigma = -200\%$ from [76]. The cavity is at the contact center (a), near the rear of the Hertzian contact (b) and in the outlet zone of the contact (c).

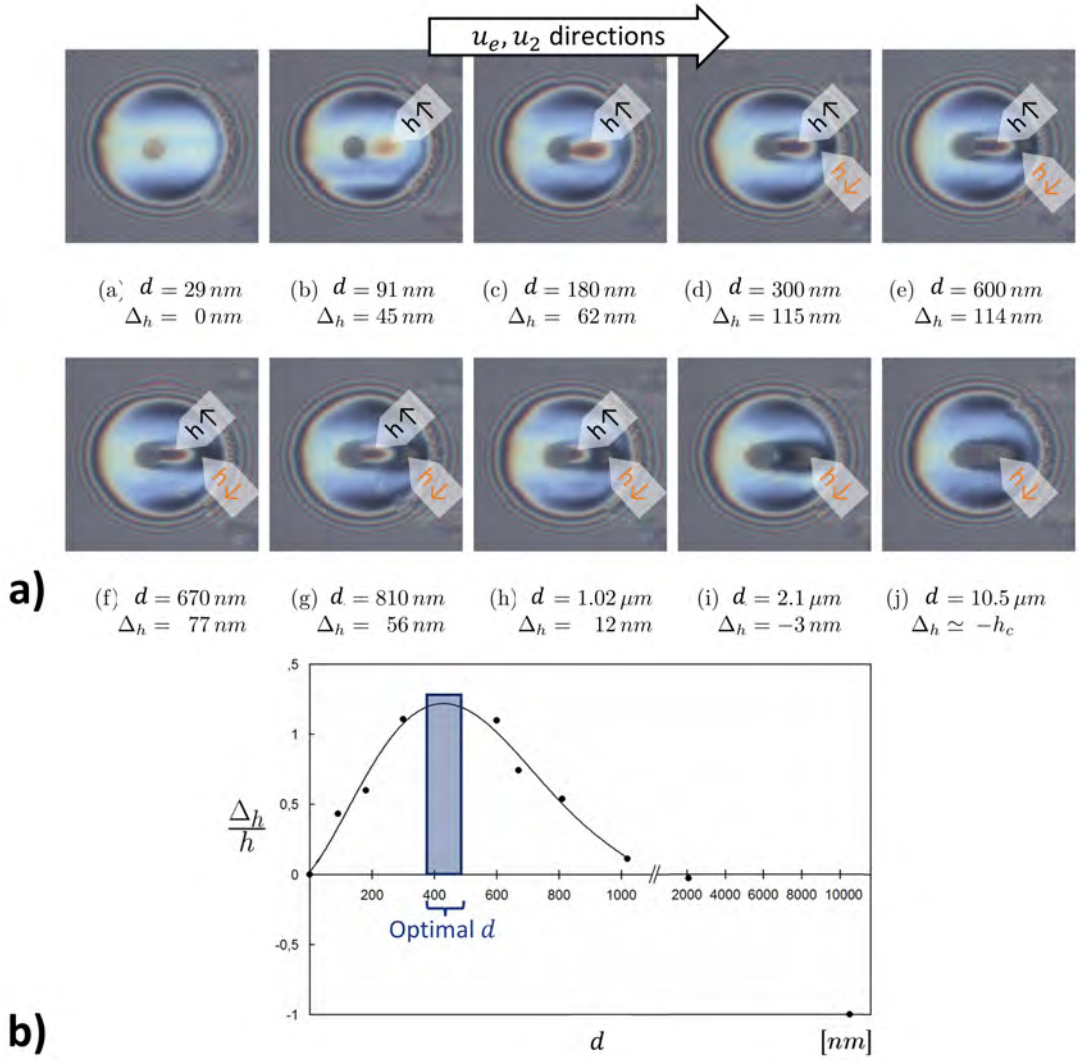

Figure 1.15: Contact interferograms of the EHL point contact involving cavities with a given diameter ($\varnothing = 56$ μm) and varying depth ($0.029 < d < 10.5$ μm) located at the contact center for $\Sigma = +100\%$ (a). Ratio δ_h/h of the film enhancement over the smooth film thickness versus the groove depth for $\Sigma = 100\%$ (b). Data adapted from [4].

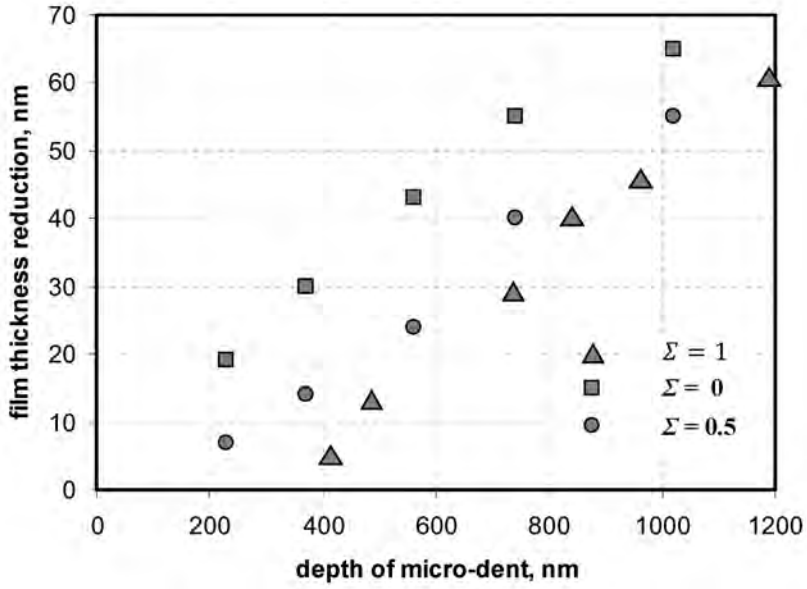

Figure 1.16: Film thickness reduction versus the cavity depth for $\Sigma = +100$, $+50$ and 0% from [100, 101].

Mourier et al. attributed the film thickness reinforcement to the shear-induced extraction of the highly viscous fluid trapped inside the cavity. For $\Sigma = 0\%$, there is no shearing, therefore, the fluid remains inside the cavity. At $\Sigma = +100\%$, the fluid is able to exit the cavity. The piezo-viscosity of the fluid exiting the cavity is directly related to the pressure peaks induced by the cavity depth d. Shallower cavities generate not enough pressure variations while deeper cavities reduce too much the absolute pressure. Both cases prevent the viscosity from rising and reinforcing the film thickness.

In addition to the film thickness reinforcement, the cavity can reduce locally the film thickness as illustrated in Fig. 1.15a. Krupka and Hartl [100, 101] highlighted the depth dependency of the film thickness reduction. In the contact interferograms from Fig. 1.15a, cavities with $d \geq 300$ nm induce a film thickness reduction (gray and dark colors) downstream the film thickness enhancement (yellow and brown colors). Cavities with 230 nm $< d <$ 1.36 µm and almost constant diameter ($\varnothing \in [90, 120]$ µm) were experimented at $\Sigma = +100$, 50 and 0%. The maximal film thickness reduction generated by the cavity decreased when (see Fig. 1.16) the cavity depth d decreased. Below a certain depth (few hundreds of nm), the cavity caused no more film thickness reduction.

In addition, Mourier et al. pointed out the influence of the cavity diameter comparing two cavities with respectively $d = 300$ nm, $\varnothing = 57$ µm and $d = 305$ nm

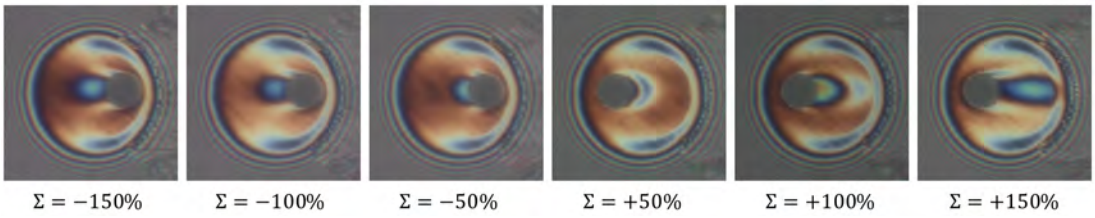

Figure 1.17: Contact interferograms of a single cavity with $d = 305$ nm and $\varnothing = 95$ μm for $-150\% < \Sigma < +150\%$ from [4].

and $\varnothing = 95$ μm. The larger diameter increased the film thickness enhancement yet delayed the time when this reinforcement started to appear. The cavity had to completely enter the contact before any film thickness enhancement happened.

SRR and film thickness

Finally, Mourier et al. carried out the influence of the SRR upon the film thickness enhancement. As Fig. 1.17 points out, the propagation direction and the length of the film thickness reinforcement depends, respectively, on the SRR sign and on its absolute value $|\Sigma|$. Krupka et al. [102] also observed this SRR sign dependency with a single cavity ($d = 700$ nm, $\varnothing = 73$ μm). When $\Sigma < 0$, the ball moves faster than the lubricant ($u_2 > u_e$). Therefore, the fluid trapped in the cavity lags behind the cavity and exits at its rear. When $\Sigma > 0$, the opposite happens; the fluid is faster than the cavity ($u_2 < u_e$). Krupka et al. [100, 101] also showed that the sliding rolling ratio Σ accentuates the film thickness reduction (see Fig. 1.16). Yet for negative SRR, they observed no film thickness reduction regardless of d.

Friction of cavity textured surfaces

Ninove et al. [6] studied the EHL friction with cavity networks. They focused on the geometrical parameters such as the depth $d \in \{0.5, 3\}$ μm, the diameter $\varnothing \in \{20, 60\}$ μm and the cavity coverage ratio or cavity density $5\% < T_s < 30\%$. Depending on the SRR sign, they pointed out two different optimal cavity depth (see Fig. 1.18). When $\Sigma < 0$, the friction was reduced up to 12% for deep cavities ($d = 3$ μm). On the contrary, for shallow cavities ($d = 500$ nm) the friction was reduced by 7% for $\Sigma > 0$. In each case, cavities had the same diameter $\varnothing = 20$ μm and a low coverage ratio $T_s = 6$-7%. Ninove et al. linked the SRR dependency to the dwell time of the cavities in the EHL contact. When the SRR increases

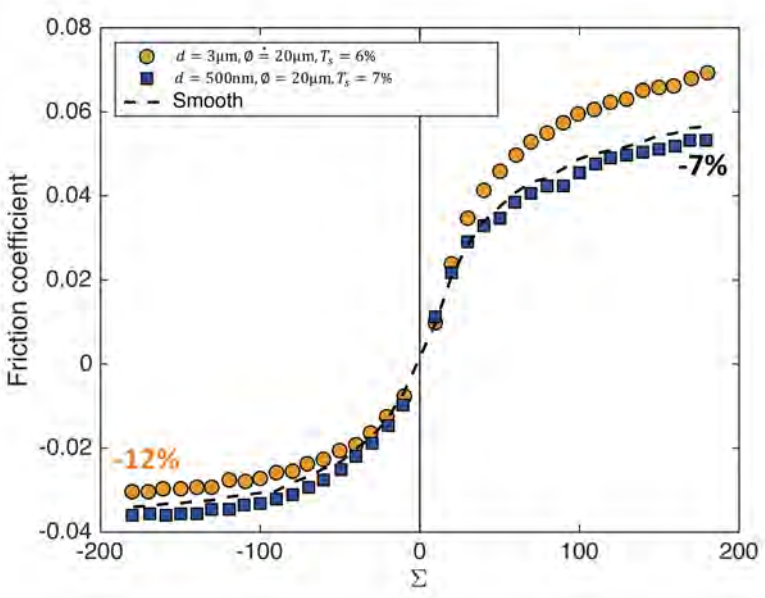

Figure 1.18: Friction coefficient versus the SRR for two cavity array patterns, adapted from [6]. The smooth surface friction coefficient is reminded in full line.

from negative to positive values, the dwell time increases. Moreover, the density T_s also appeared to be a significant parameter. Indeed, high coverage ratios with deep cavities increased the friction even when $\Sigma < 0$.

In addition, Ninove et al. [6] carried out experiments with single cavities at $\Sigma = -200\%$. They emphasized the influence of the trapped volume ratio T_v defined the ratio of the fluid trapped inside the cavity over the total volume of fluid inside the contact. Cavities with $d = 5$ µm corresponded to $T_v = 61\%$ which led to a friction reduction of 22% whereas cavity depth of 300-400 nm, i.e. $T_v = 7$-8% raised the friction. Ninove et al. explained that in the deep cavities, the pressure is so low that the fluid is almost isoviscous (very low viscosity) and therefore, the friction decreases. Ninove et al. also investigated cavity networks at $\Sigma = -200\%$. Experiments pointed out the possible coupling between successive cavities in an array. The film thickness exiting at a cavity rear will affect the following one, etc. To summarize, Ninove et al. explained that the friction is a complex coupling between:

- the operating conditions (surface kinematics, contact pressure and dwell time),
- the geometrical parameters of the cavities (depth d, diameter $\varnothing$, density T_s and trapped volume ratio T_v),

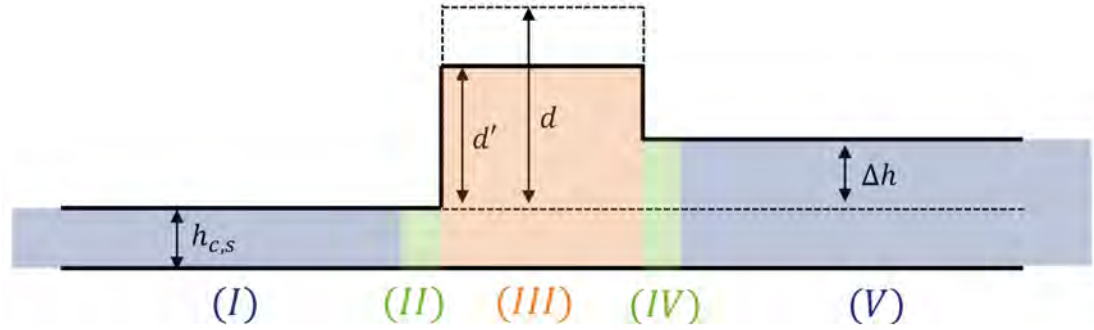

Figure 1.19: Simplified film thickness profile when an elastically deformed cavity ($d \to d'$) is in an EHL contact. The fluid goes from the left to the right and the film thickness modification Δh can be either positive or negative.

- lubricant properties (piezo-viscosity).

Finally, Ninove et al. [6] proposed an analytical approach to model the friction by using a simplified geometry of the deformed cavity (see Fig. 1.19). Introducing the variable $s = x - u_2 t$, the incompressible line contact Reynolds equation yields:

$$\frac{\partial}{\partial s}\left(\frac{h^3}{12\eta}\frac{\partial p}{\partial s}\right) = u_e\frac{\partial h}{\partial s} - u_2\frac{\partial h}{\partial s} = u_e\Sigma\frac{\partial h}{\partial s}\ . \tag{1.32}$$

The contact with one cavity is split into five parts as illustrated in Fig. 1.19 which presents a simplified film thickness profile of a cavity inside an EHL contact. The cavity is elastically deformed: its deformed depth is d'. The fluid goes from the left to the right. The film thickness entering the cavity is equal to $h_{c,s}$ (smooth central film thickness) while the exiting one is equal to $h_{c,s} + \Delta h$, Δh being either positive or negative. The different part of the EHL contact with a cavity are:

- the cavity upstream region (I) with a length $L_1(t)$ where the film thickness h_I is equal to the smooth central film thickness $h_{c,s}$,
- the upstream cavity edge (II) with a length $\epsilon_L \ll 2a$ where $h_{II} = h_{c,s}$,
- the central part of the cavity (III), with a length of $\varnothing - 2\epsilon_L$, where $h_{III} = d' + h_{c,s}$, with d' the depth of the deformed cavity,
- the downstream cavity edge (IV), with a length of ϵ_L where $h_{IV} = h_{c,s} + \Delta h$, Δh could be either positive or negative,
- the downstream cavity region (V) with a length of $L_2(t)$ where $h_V = h_{c,s} + \Delta h$.

The pressure is equal to the mean contact pressure p_m and $\partial p/\partial s = 0$ everywhere excepted at the cavity edges, i.e. in the parts II and IV. The piezo-viscosity of the lubricant is modeled with the Barus law for mathematical convenience. Finally it yields that the friction force $F(t)$ is:

$$F(t) = 2a\tau_{c,s}\left(1 - \frac{\varnothing}{2a} - L_2(t)\frac{r(t)}{1+r(t)}\right) + \frac{r(t)h\Delta p}{2} \ , \tag{1.33}$$

with $r(t) = \Delta h/h$, Δp the pressure drop inside the cavity and $\tau_{c,s}$ the Couette shear stress in smooth EHL. From Eq. 1.33, Ninove et al. drew the following trends:

- since Δh depends on the cavity depth, so does the friction $F(t)$,
- if the fluid is reinforced by the cavity ($\Delta h > 0$), then $\left(1 - \frac{\varnothing}{2a} - L_2(t)\frac{r(t)}{1+r(t)}\right) < 1$. The Couette shear stress with a cavity is then lower than $\tau_{c,s}$. Therefore, if the friction increases in such case, it is due to the Poiseuille shear stress.

The model was then extended for multiple cavities in the contact, highlighting the influence of the dwell time and the cavity density T_s. This analytical model confirms the above mentioned experimental observations and interpretations.

1.4 Thesis objectives and strategy

Previous studies have shown that surface texturing affects the EHL film thickness. However, no studies have thoroughly and systematically investigated the relationship between the EHL friction, film thickness and pressure. This also applies to a possible relationship between the friction and a shift in the mixed/EHL lubrication regime transition. The latter could be caused by surface texturing through the generation of asperity contacts or local increase in viscosity (micro-EHL effect).

Based on the above, the following two objectives were set for this thesis: 1) to provide further understandings of the film thickness and pressure disturbances and on the onset of asperity contacts induced by the surface texture. Relationships between the texture geometries and the induced film thickness, pressure and asperity contact onset need to be defined, 2) to link these couplings to the friction response characterized with Stribeck curves. Friction laws will be established and the mixed/EHL transition which depend on the texture geometrical parameters will be described. This study will address the two following questions: what are

the governing phenomena responsible for the friction in EHL and how can this surface texturing control them?

To achieve these goals, the smooth surfaces are experimentally characterized and will be the reference levels in this study. Surface texturing is performed with femtosecond LASER. First, periodic grooves are investigated, focusing on their geometrical parameters: depth and width. As mentioned in the literature, the tribological behavior of the groove may significantly change whether they are transverse or longitudinal. Thus, experiments for both orientations are investigated. The wavelength of the grooves is such that they can be elastically deformed, according to the amplitude reduction theory. Then, to highlight the effect of the elastic deformation on the lubrication and friction, a texture with a theoretical zero amplitude reduction is also carried out. This is a ripple surface, i.e. a sinusoidal surface with a very small wavelength (lower than the micron). At constant wavelength, the influence of its amplitude and orientation are investigated. Finally, cavity textures are studied. As experiments have largely dealt with the influence of its depth and width, a waviness is introduced at the cavity bottom to account for the effects of the cavity roughness. In addition, a new way to characterize the cavity film thickness is introduced.

The tribological response of each surface is characterized on a ball-on-disc tribometer by performing Stribeck curve measurements. Time, cost and technical limitations of the manufacturing process (femtosecond LASER ablation) reduce the total number of surface textures considered. Moreover, the experimental apparatus used does not measure the pressure distribution, which is an important in situ data to drive the friction force (lubricant piezo-viscosity). To overcome these limitations, numerical simulations are carried out. This complementary tool enriches the experimental data and lead to further analyses and interpretations of the experimental findings such as the detection of micro-EHL effects or the determination of the physical nature of the mixed/EHL transition.

The development of this numerical strategy bears on two main requirements. First, the numerical simulations must work regardless of the input surface topographies: measured topographic profiles or mathematical functions obtained from experimental characterizations. Second, the time requirement to develop and run the numerical code must be competitive with the experimental way. An EHL line contact model is then developed and validated with both numerical and experimental results. Based on the literature review, the EHL line contact was chosen to model equivalent point contacts which allowed thethe comparison against the experimental measurements made on EHL point contacts.

Chapter 2

EHL numerical model

Contents

In this chapter, the physics of an EHL contact and the governing equations are first described. Then, from the review of numerical methods, the choice of an equivalent line contact using the Newton-Raphson method is made. Last, this model is validated using with both numerical and experimental data to determine its strengths and possible limitations.

2.1 EHL equations

The experiments and simulations were carried out for a point contact between a rough ball and a rough disc. This is equivalent to a contact between a smooth rigid plane (solid 1) and a rough elastic sphere (solid 2) as illustrated in Fig. 2.1.

The roughness of the sphere is $r(x, y, t)$, which is the sum of the ball roughness r_1 and the disc roughness r_2:

$$r(x, y, t) = r_1(x, y, t) + r_2(x, y, t) \ . \tag{2.1}$$

The reduced curvature radii R_x and R_y of the elastic sphere are:

$$R_x^{-1} = R_{x,1}^{-1} + R_{x,2}^{-1} \ , \tag{2.2}$$

$$R_y^{-1} = R_{y,1}^{-1} + R_{y,2}^{-1} \ , \tag{2.3}$$

and its reduced Young modulus E' is:

$$\frac{2}{E'} = \frac{1 - \nu_1^2}{E_1} + \frac{1 - \nu_2^2}{E_2} \ . \tag{2.4}$$

Three equations describe the physics of EHL contacts between the smooth rigid plane and the rough elastic sphere:

- the Reynolds equation,
- the film thickness equation,
- the force balance equation.

2.1.1 Reynolds equation

Consider a fluid with the density ρ, the dynamic viscosity η, the second viscosity η', the velocity $\mathbf{U} = u_x\mathbf{x} + u_y\mathbf{y} + u_z\mathbf{z}$ and subject to the pressure p and an

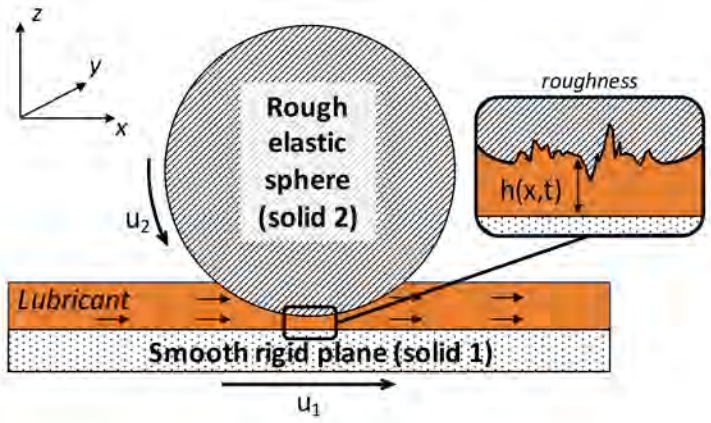

Figure 2.1: Scheme of the equivalent lubricated contact between a ball and a disc. $h(x,t)$ is the film thickness, i.e. the distance between the rough elastic deformed sphere and the smooth rigid plane.

external density force $\mathbf{F}$. The behavior of this fluid is described by the Navier-Stokes Equations (NSE):

$$\begin{cases} \rho\dfrac{D\mathbf{U}}{Dt} = \rho\left(\dfrac{\partial\mathbf{U}}{\partial t} + \mathbf{U}\cdot\nabla\mathbf{U}\right) = -\nabla p + \nabla\cdot\left[\eta' I\nabla\cdot\mathbf{U} + \eta\left(\nabla\mathbf{U} + \nabla\mathbf{U}^{\mathrm{T}}\right)\right] + \rho\mathbf{F}\ , \\ \dfrac{\partial\rho}{\partial t} + \nabla.(\rho\mathbf{U}) = 0\ . \end{cases} \tag{2.5}$$

In EHL, the following assumptions can be made:

- The clearance between the ball and the disc (z direction) is far smaller than the contact radius (x and y directions), thus variations of pressure through z are negligible:

$$\frac{\partial p}{\partial z} = 0\ . \tag{2.6}$$

  Moreover the velocity $u_x \gg u_y, u_z$:

$$\frac{\partial u_x}{\partial x}, \frac{\partial u_y}{\partial x}, \frac{\partial u_z}{\partial x}, ..., \frac{\partial u_y}{\partial z}, \frac{\partial u_z}{\partial z} \ll \frac{\partial u_x}{\partial z}\ . \tag{2.7}$$

- The fluid inertia is negligible compared to viscous shear; inertia forces consist of fluid acceleration, centrifugal forces and gravity. In EHL, the Reynolds number is less than 1.0×10^{-2}: the flow is laminar (neither turbulence nor vortex):

$$\mathbf{U}\cdot\nabla\mathbf{U} = \mathbf{0}\ . \tag{2.8}$$

- There is no external force:

$$\mathbf{F} = \mathbf{0} \ . \tag{2.9}$$

- The fluid flow is Newtonian:

$$\frac{\partial}{\partial z}\left(\eta \frac{\partial u_x}{\partial z}\right) = \eta \frac{\partial^2 u_x}{\partial z^2} \ , \tag{2.10}$$

$$\eta' = -\frac{2}{3}\eta \ . \tag{2.11}$$

- There is no slip at the wall and both disc and ball velocities are constant, respectively equal to:

$$\begin{cases} \mathbf{U_1} = u_1 \mathbf{x} \ , \\ \mathbf{U_2} = u_2 \mathbf{x} \ . \end{cases} \tag{2.12}$$

From these velocities along the x-direction, the mean entrainment speed u_e, the sliding speed u_s and the sliding-rolling ratio Σ are defined as:

$$u_e = (u_1 + u_2)/2 \ , \tag{2.13}$$

$$u_s = u_1 - u_2 \ , \tag{2.14}$$

$$\Sigma = u_e/u_s \ . \tag{2.15}$$

The above assumptions applied to the NSE (Eq. 2.5) yields the Reynolds equation for point contacts:

$$\frac{\partial}{\partial x}\left(\frac{\rho h^3}{12\eta}\frac{\partial p}{\partial x}\right) + \frac{\partial}{\partial y}\left(\frac{\rho h^3}{12\eta}\frac{\partial p}{\partial y}\right) = u_e \frac{\partial \rho h}{\partial x} + \frac{\partial \rho h}{\partial t} \ . \tag{2.16}$$

The first two terms on the left-hand side of Eq. 2.16 represent the Poiseuille flow in the x and y-directions. The right-hand side of Eq. 2.16 corresponds to the Couette flow and the transient squeeze term, respectively.

The viscosity of the fluid η is assumed to depend on the pressure according to the Roelands' equation [103]:

$$\begin{cases} \eta = \eta_0 \exp\left\{(\ln(\eta_0) + 9.67)\left(-1 + \left(1 + \dfrac{p}{p_0}\right)^{z_\alpha}\right)\right\} \ , \\ z_\alpha = \dfrac{\alpha}{\ln(\eta_0) + 9.67} \ , \end{cases} \tag{2.17}$$

where η_0 is the viscosity at ambient pressure, α is the piezo-viscosity coefficient, p_0 is a constant equal to 1.98×10^8 Pa and z_α is the pressure viscosity index.

The density of the fluid ρ is determined according to the relation of Dowson and Higginson [104]:

$$\rho = \rho_0 \frac{0.59 \times 10^9 + 1.34p}{0.59 \times 10^9 + p} \ , \tag{2.18}$$

where ρ_0 is the density at atmospheric pressure.

For EHL line contacts there is no Poiseuille flow in the y direction, Eq. 2.16 becomes:

$$\frac{\partial}{\partial x}\left(\frac{\rho h^3}{12\eta}\frac{\partial p}{\partial x}\right) = u_e \frac{\partial \rho h}{\partial x} + \frac{\partial \rho h}{\partial t} \ . \tag{2.19}$$

2.1.2 Film thickness equation

The second governing equation describes the film thickness h in the EHL contact:

$$h(x,y,t) = h_0(t) + \frac{x^2}{2R_x} + \frac{y^2}{2R_y} - r(x,y,t) + \frac{2}{\pi E'}\int_{\mathbb{R}^2} \frac{p(x',y',t)dx'dy'}{\sqrt{(x-x')^2+(y-y')^2}} \ . \tag{2.20}$$

It is the sum of:

- the clearance between the undeformed ball and the disc $h_0(t)$,
- the curvature of the ball $x^2/2R_x + y^2/2R_y$,
- the roughness $r(x,y,t)$
- and the elastic deformation based on Boussinesq's theory.

For EHL line contacts, the film thickness equation is written as:

$$h(x,t) = h_0(t) + \frac{x^2}{2R_x} - r(x,t) - \frac{4}{\pi E'}\int_{\mathbb{R}} \ln|x-x'|p(x')dx' \ . \tag{2.21}$$

2.1.3 Force balance equation

The third governing equation ensures force balance between the applied load and the force generated by the pressure of the fluid in the EHL contact. For EHL point contacts, the equation is given by:

$$\int_{\mathbb{R}^2} p(x,y,t)dxdy = W_L \ , \tag{2.22}$$

and for EHL line contacts it is:

$$\int_{\mathbb{R}} p(x,t)dx = w_L \ , \tag{2.23}$$

where W_L and w_L are the loads.

2.2 EHL line contact model

To obtain the pressure and the film thickness inside the EHL contact, Eq. 2.20 is substituted into Eq. 2.16 for EHL point contacts. For EHL line contacts, Eq. 2.21 is substituted into Eq. 2.19. The unknowns of the EHL problem are the pressure distribution $p(x, y, t)$ and the clearance $h_0(t)$. They can be calculated by solving the Reynolds and the load balance equations. Since the film thickness, viscosity and density are pressure-dependent, the EHL problem is non-linear.

2.2.1 Method review

To solve the EHL problem, the Gauss-Seidel iteration scheme was first used by Hamrock and Dowson [21, 22, 23]. Later, Okamura [28] introduced the Newton-Raphson method in numerical EHL. It is based on the inversion of the Jacobian matrix obtained from the equations of the problem. Then Lubrecht proposed the multi-grid method [19, 20, 8], which speeds up the convergence of the Gauss-Seidel iteration scheme. This method was later improved by Venner [24, 9, 25, 26] by adding Jacobi iteration scheme and implementing the multi-integration technique [27].

To reduce the complexity of the Newton-Raphson algorithm, Holmes et al. [29, 30] developed the differential deflection method. They replaced the film thickness equation with its differential form [31]. More recently, Habchi et al. [32, 33] used a full-body elasticity instead of the half-space approach, which also reduces the complexity of the algorithm. The method was called the full system approach. In addition, numerous articles deal with the optimization and improvements of the methods to reduce memory and computational time. Some of these works implemented other rheological laws in the Reynolds equation and thermal effects inside the EHL contact.

The Computational Fluid Dynamics (CFD) techniques can also be used to solve directly the Navier-Stokes equations [17, 18]. Nevertheless, convergence issues limit the CFD techniques to low load conditions.

2.2.2 Method selection

The selection was based on the following criteria. First, the numerical simulations have to converge whatever the input surface roughness. The convergence of the Newton-Raphson method is independent of the choice of the roughness [4] unlike the multi-grid method which is very sensitive to under-relaxation factors in the iterative schemes (Gauss-Seidel and Jacobi). These under-relaxation factors cannot be analytically determined.

Second, the computational time required to develop and run the simulations should be reasonably fast. The Newton-Raphson method needs to inverse a full Jacobian matrix, which size is the square power of mesh size. In EHL transient line contacts (1D) the needed time remains competitive: a couple of seconds with a 512 mesh size. However, in EHL transient point contact (2D), a 512×512 mesh size requires a huge amount of computational time and memory which slows down the process. The use of either the differential deflection method or the half-space approach would be recommended in such case as they sparse the Jacobian matrix. Yet their implementation is expected to require extra-time compared to the "classical" Newton-Raphson method, not to forget that point contact simulations will still be slower than line contact simulations. A compromise has to be done given our aim to build, in a short time, a fast simulation that enriches experimental data.

Both criteria are satisfied by the Newton-Raphson method. The choice bore on implementing a model, which simulates the same physics as our experiments. Nijenbanning et al. [105] proposed an equivalence between an EHL line contact and an EHL point contact, with good agreement in terms of central film thickness. As a consequence, we decided to implement a transient line contact. The equivalent line contact description will be used for 2D simulations to get pressure and film thickness on the central line in the contact ($y = 0$). Thereby this model choice satisfies both roughness and time requirements.

2.2.3 Dimensionless equations of the EHL line contact

The EHL line contact equations are solved in dimensionless form. The following dimensionless variables are defined:

$$\bar{\rho} = \rho/\rho_0 \ , \tag{2.24}$$
$$\bar{\eta} = \eta/\eta_0 \ , \tag{2.25}$$
$$X = x/a \ , \tag{2.26}$$
$$P = p/p_h \ , \tag{2.27}$$
$$H = hR_x/a^2 \ , \tag{2.28}$$
$$T = tu_e/a \ , \tag{2.29}$$

where a is the Hertzian half-width and p_h is the maximum Hertzian pressure defined as:

$$a = \sqrt{\frac{8w_L R_x}{\pi E'}} \ , \tag{2.30}$$
$$p_h = \frac{2w_L}{\pi a} \ . \tag{2.31}$$

The Reynolds equation in dimensionless form becomes:

$$\begin{cases} \dfrac{\partial}{\partial X}\left(\dfrac{\bar{\rho}H^3}{\bar{\eta}}\dfrac{\partial P}{\partial X}\right) = \lambda_0 \dfrac{\partial \bar{\rho}H}{\partial X} + \lambda_0 \dfrac{\partial \bar{\rho}H}{\partial T} \ , \\ \lambda_0 = \dfrac{12\eta_0 u_e R_x^2}{a^3 p_h} \ . \end{cases} \tag{2.32}$$

The dimensionless film thickness equation is:

$$H(X,T) = H_0 + \frac{X^2}{2} - R(X,T) - \frac{1}{\pi}\int_{\mathbb{R}} \ln|X - X'|P(X')dX' \ . \tag{2.33}$$

And the dimensionless force balance equation is:

$$\int_{\mathbb{R}} P(X)dX = \frac{\pi}{2} \ . \tag{2.34}$$

2.2.4 Equivalent EHL line contact description

Dowson and Higginson [104] introduced a set of three dimensionless parameters G, U and W to describe EHL line and point contacts:

$$G = \alpha E' \ , \tag{2.35}$$

$$U = \frac{\eta_0 u_e}{E' R_x} \ , \tag{2.36}$$

$$W_1 = \frac{w}{E' R_x} \text{ in line contact,} \tag{2.37}$$

$$W_2 = \frac{W}{E' R_x^2} \text{ in point contact.} \tag{2.38}$$

Later, Moes [106] introduced two dimensionless parameters M and L to describe EHL point and line contacts based on those of Dowson and Higginson:

$$M_1 = W_1 (2U)^{-1/2} \text{ in line contact,} \tag{2.39}$$

$$M_2 = W_2 (2U)^{-3/4} \text{ in point contact,} \tag{2.40}$$

$$L = G(2U)^{1/4} \ . \tag{2.41}$$

Nijenbanning et al. [105] proposed that for a given EHL point contact, an equivalent EHL line contact can be obtained. They stated that the two contacts must have the same half-width a, curvature radius R_x and maximum Hertzian contact pressure p_h, yielding:

$$M_{1,\text{eq}} = \frac{1}{2} \left(\frac{3}{2} M_2 \right)^{2/3} \ . \tag{2.42}$$

Therefore, to simulate an EHL point contact, the parameters M_2 and L are first calculated given the operating conditions. Then, the equivalent $M_{1,\text{eq}}$ is determined and the developed EHL line contact model is used to solve the EHL line contact for $M_{1,\text{eq}}$ and L.

2.2.5 Cavitation model

Cavitation pressures for typical lubricants are of the order kPa while pressures inside the EHL contacts exceed hundreds of MPa. Therefore, the cavitation pressure is set to 0 in the numerical simulations without much loss of accuracy.

In smooth EHL line contacts, cavitation occurs in the outlet of the contact due to the sudden pressure drop below the cavitation pressure. For some rough EHL

contacts, it was shown that cavitation may occur inside the contact [75, 81]. The present numerical model was developed to simulate the experimental conditions of the IRIS tribometer (see section 2.4). For these conditions, no evidence of any cavitation inside the contact was observed on the contact interferograms. After each simulation, the existence of cavitation in the contact zone is always checked. No cavitation was observed inside the contact during simulations.

If cavitation occurs at the contact outlet, the cavitation problem consists of finding the moving boundary x_c where the fluid starts cavitating and then solving the EHL problem in the upstream region of the contact ($x < x_c$). In addition, the pressure gradient has to be continuous along the contact (Swift-Stieber boundary conditions):

$$\left.\frac{\partial p}{\partial x}\right|_{x=x_c} = 0 \ . \tag{2.43}$$

To satisfy these conditions, Wu [107] proposed the Penalty method: a penalty term is added to the Reynolds equation:

$$P_{-}(X,T) = \frac{1}{\epsilon}\min\left(P(X,T),0\right) \ , \tag{2.44}$$

where ϵ is a small number. In the region where the fluid is not cavitating, P is positive and so the penalty term P_{-} is null. Elsewhere, i.e. in the cavitation region ($P < 0$), the penalty term forces the pressure solution to be close to zero. The magnitude of ϵ monitors this numerical effect.

2.2.6 Model implementation

The EHL line contact model is written in MATLAB. The solution scheme used in the solver is displayed in Fig. 2.2. The discretization proposed by Venner [9] is used and multiplied by the spatial pitch to obtain a finite volume scheme, ensuring the fluid mass conservation. The pressure is discretized on a homogeneous mesh with ΔX spacing, over the domain $[X_0, X_{end}]$. In the Newton-Raphson method, the initial values for P and H_0 are:

$$\begin{cases} P(X) = \sqrt{1-X^2} \text{ Hertzian pressure,} \\ H_0 = 0 \ . \end{cases} \tag{2.45}$$

The film thickness equation (Eq. 2.33) is substituted in the Reynolds equation (Eq. 2.32). Based on the initial solution, the residual and the Jacobian matrix of both the steady-state Reynolds and the force balance (Eq. 2.34) equations are discretized using finite-volume method in a way proposed by Venner. An updated

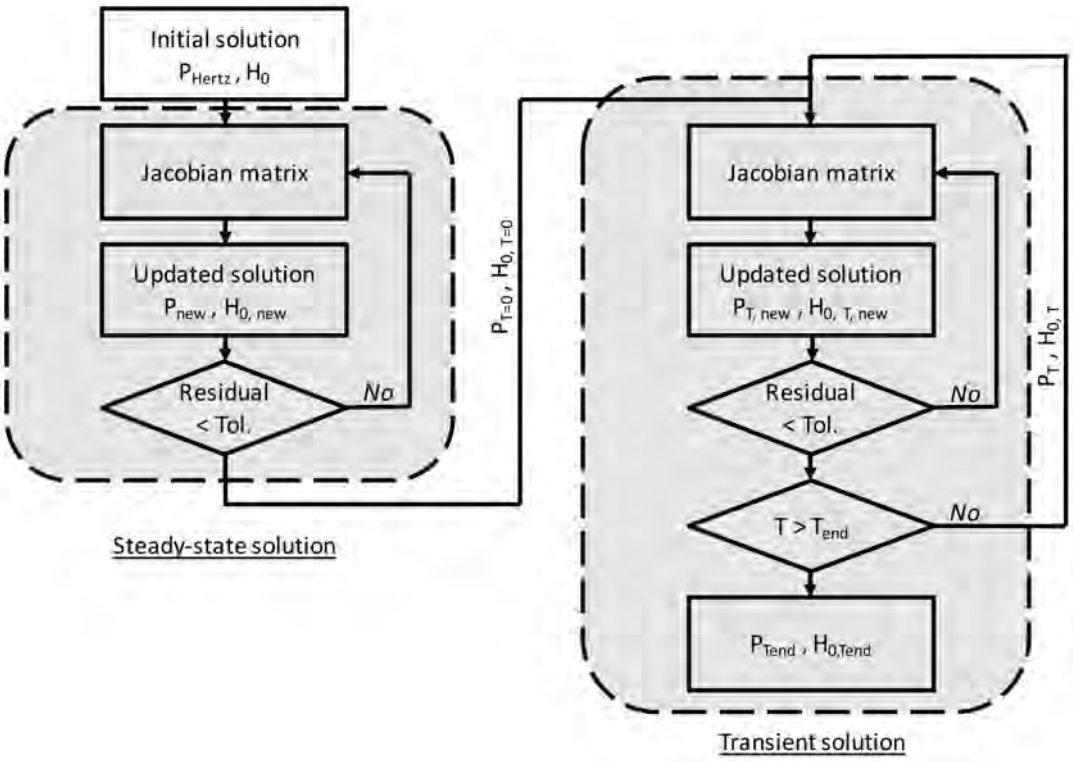

Figure 2.2: Numerical scheme of the EHL line contact model.

solution is obtained with the Newton-Raphson method. While the residual of this new solution is higher than the tolerance, the previous process is repeated.

Once the steady-state solution has converged, the transient solution is solved at $T = 0$ using the previous solution as the solution at $T = -\Delta T$. Then the algorithm is repeated until $T = T_{end}$ with a spatial pitch $\Delta T = \Delta X$ to avoid numerical artifact [4].

2.2.7 Model convergence

The convergence of the minimum film thickness H_m was investigated as a function of the mesh size 2^N over the domain $X \in [-2.5, 1.5]$. The case of $M_1 = 20$ and $L = 10$ for a smooth contact was used. The tolerance and the penalty parameter ϵ were set to 1.0×10^{-10} and 1.0×10^{-8}, respectively. Fig. 2.3 shows the relative

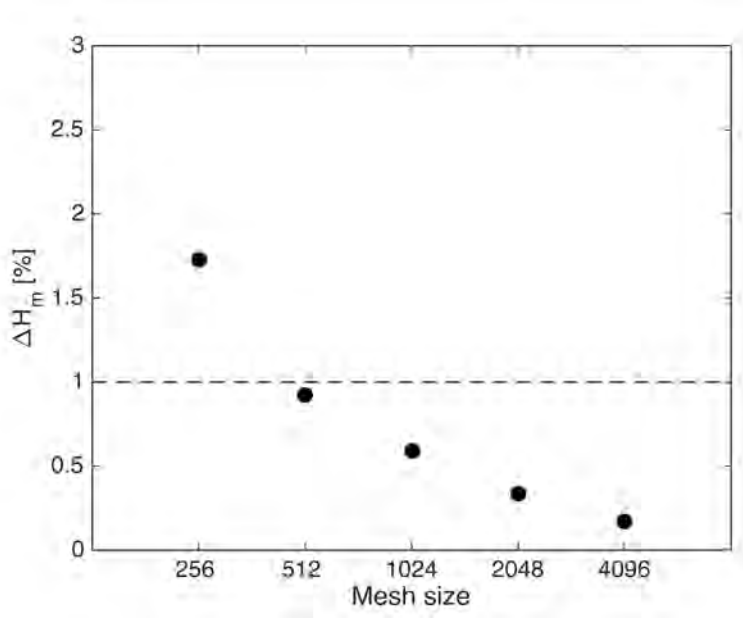

Figure 2.3: Convergence of the EHL line contact model versus the mesh size.

variation of the minimum film thickness ΔH_m defined as:

$$\Delta H_m = \frac{|H_{m,2^N} - H_{m,2^{N-1}}|}{H_{m,N}} \ , \tag{2.46}$$

versus the mesh size. ΔH_m converges rapidly with the increasing mesh size. For meshes with 512 or more nodes, ΔH_m is below 1%. For other values of M_1 and L similar convergence patterns were observed. A mesh with 512 nodes was chosen in the following numerical comparison. The EHL problem will be solved over the domain $X \in [-2.5, 1.5]$ with the tolerance of 1.0×10^{-10}.

In the contact $-1 \leq X \leq 1$, the magnitude order of the dimensionless pressure is of 1 as $P = p/p_h$, with p_h the maximal Hertzian pressure. For $\epsilon = 1.0 \times 10^{-8}$, the penalty method leads to negative dimensionless pressures between -1.1×10^{-8} and 0 Pa in the cavitation region, i.e. 1.0×10^{-9} times lower than in the contact. Yet the lower ϵ, the slower the simulation. Indeed, small ϵ increases the residual leading to more Newton iterations. The influence of ϵ is then investigated for a 512 node mesh with ϵ ranging in $[1.0 \times 10^{-8}, 1.0 \times 10^{-2}]$. As a result, the variation of H_m is less than 1% in comparison with the minimum film thickness for $\epsilon = 1.0 \times 10^{-8}$. The negative pressures range from $-\epsilon$ to 0.

For $\epsilon = 1.0 \times 10^{-2}$, the penalty method leads to a negative pressure 1000 times lower than the pressure in the contact. Moreover, the film thickness is correctly determined in a very short time: less than 2s on an i7 2.9GHz, 8GB

RAM workstation. Thus in the following, the penalty parameter is set to 1.0×10^{-2}.

2.3 Numerical comparisons

First, the EHL line contact model is compared to numerical data in EHL line contacts, from Venner et al. [24, 9]. Second, the equivalent line contact description is validated with numerical EHL point contact results, from Venner et al. [9, 25, 26] and Ali et al. [94]. These comparisons are performed for smooth, stationary rough and moving rough surfaces.

2.3.1 EHL line contacts

Smooth surface

The surfaces are smooth: $r(x,t) = 0$. Venner only provides values of the Moes dimensionless minimum film thickness, H_{min}, for several couples of Moes parameters (M_1, L). The Moes dimensionless film thickness is defined as:

$$H_{Moes} = \frac{h}{R_x\sqrt{2U}} \ . \tag{2.47}$$

Results from the present model ($\times$) are reported in Fig. 2.4 beside Venner's data ($+$). They are plotted versus the dimensionless Moes parameter M_1. Very good agreement is found except for (large M_1, small L) and for (small M_1, large L). These two cases correspond respectively to elastic isoviscous and rigid piezoviscous EHL contacts, respectively.

Stationary rough surface

The ball is stationary and has an indentation feature located at the center of the contact, $X = 0$. The roughness $R(X)$ is defined as:

$$R(X) = A.10^{-10\left(\frac{X}{\Lambda}\right)^2} \cos\left(\frac{2\pi X}{\Lambda}\right) \ , \tag{2.48}$$

where A is the dimensionless amplitude and Λ is the dimensionless wavelength. In the following, data from Venner [9] are plotted in dash line whereas results from our EHL line contact model are in full line. For $M_1 = 100$, $L = 11.08$, $A = -0.11$ and $\Lambda = 1$, the dimensionless pressure P and film thickness H profiles

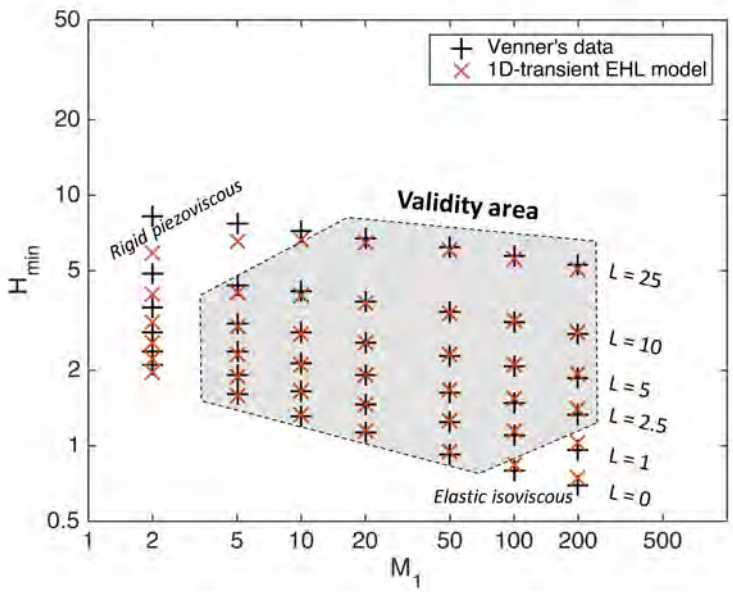

Figure 2.4: Comparison of the minimum Moes dimensionless film thickness in smooth EHL line contacts from [24, 9] and the EHL line contact model.

are plotted in Fig. 2.5a-b. The pressure and film thickness profiles are in very good agreement for this steady-state case.

Moving rough surface

The ball is then moving and has a single indentation feature. The roughness $R(X,T)$ is:

$$R(X,T) = A.10^{-10\left(\frac{X-X_s-T}{\Lambda}\right)^2} \cos\left(2\pi\frac{X-X_s-T}{\Lambda}\right) \ , \tag{2.49}$$

where X_s is the location of the feature at $T=0$. Fig. 2.6a-b report the dimensionless pressure P and film thickness H profiles when $X_s+T=0$, for $M_1=100$, $L=11.08$, $A=-0.11$ and $\Lambda=1$. The pressure and the film thickness are also in very good agreement with Venner's data for this transient case.

2.3.2 EHL point contacts

The EHL line contact model has shown its ability to model EHL line contact in various operating conditions. In the following, the robustness of the equivalent

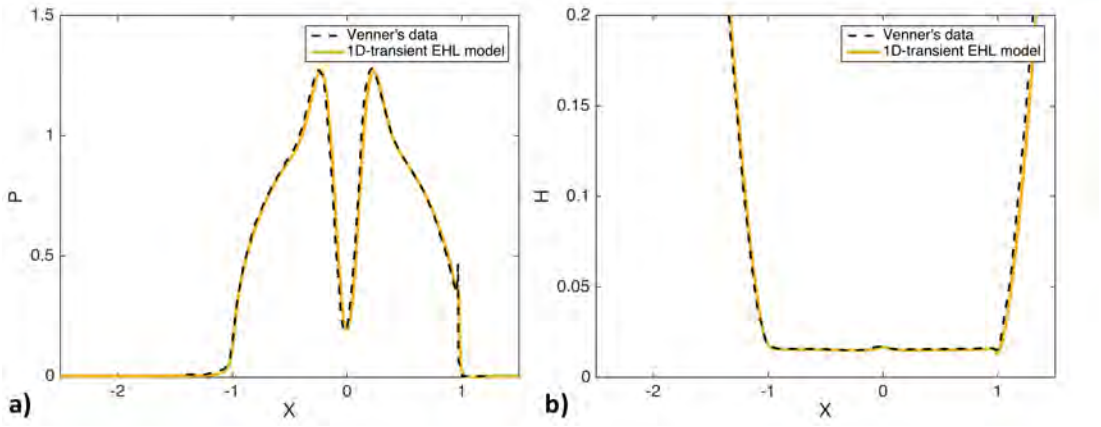

Figure 2.5: Comparison of the dimensionless pressure (a) and film thickness (b) in steady-state rough EHL line contact from [9] and the EHL line contact model.

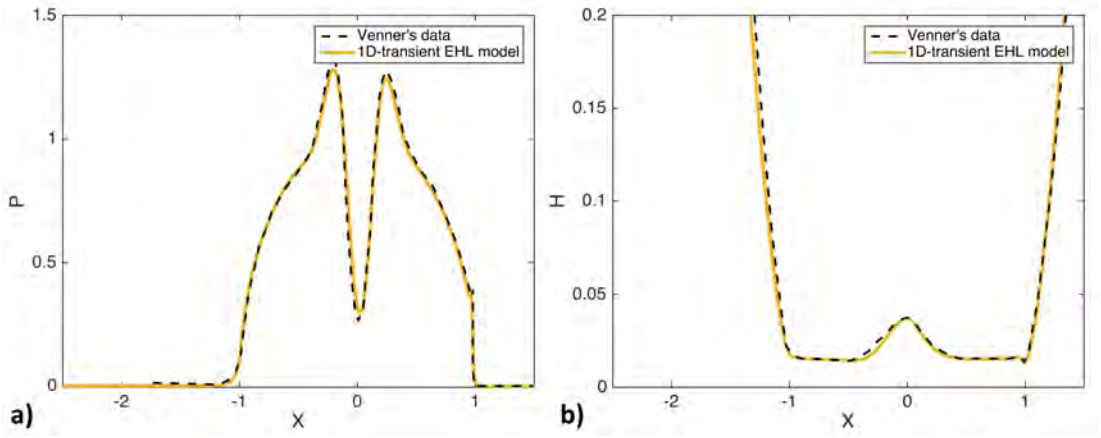

Figure 2.6: Dimensionless pressure P (a) and film thickness H (b) in transient rough EHL line contact from [9] and from the EHL line contact model.

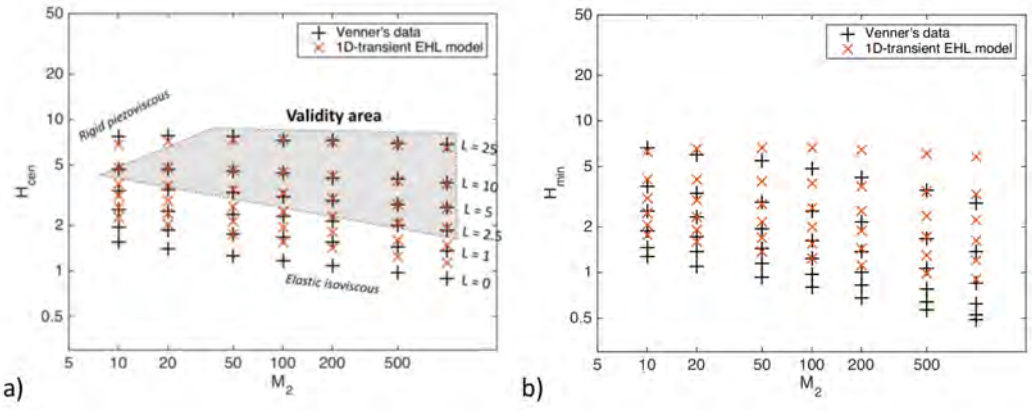

Figure 2.7: Central (a) and minimum (b) Moes dimensionless film thicknesses in smooth EHL point contact from [9] and from the EHL line contact model results using the equivalent line contact description.

line contact description is tested with numerical point contact results from the literature.

Smooth surface

The model is now compared to multi-grid data obtained by Venner [9, 25, 26] for various couples of (M_2, L) in smooth point contact. The Moes dimensionless central H_{cen} and minimum H_{min} film thicknesses from Venner ($\times$) are plotted in Fig. 2.7 versus M_2 and compared to results of EHL line contact model ($+$) using the equivalent line contact description.

Fig. 2.7.a shows that the equivalent line contact description allows to successfully predict the Moes dimensionless central film thickness of smooth EHL point contacts. Yet there are two limitations: for small L and for large L, small M_2. These two cases correspond respectively to isoviscous and rigid piezoviscous EHL contacts.

Fig. 2.7.b illustrates that the equivalent EHL line contact cannot accurately determine the minimal film thickness. This was previously stated by Nijenbanning et al. [105]. Indeed, the Poiseuille flow in the y-direction is neglected with the line contact model. Thus, the side leakage occurring in EHL point contact is not taken into account although it strongly influences the minimal film thickness in the side constriction regions.

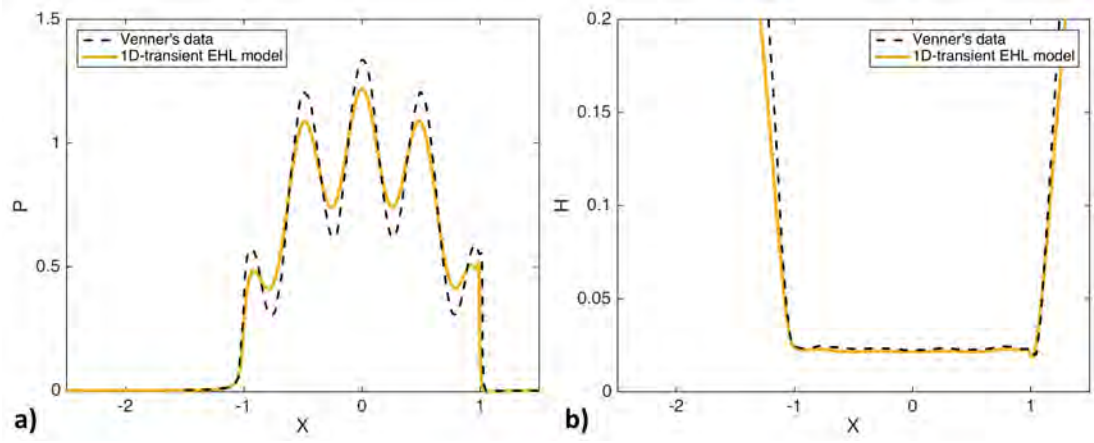

Figure 2.8: Dimensionless profiles of the pressure (a) and film thickness (b) on the central line for a rough steady-state EHL point contact from [9] and the EHL line contact model results using the equivalence description.

Stationary rough surface

The equivalent line contact description is then tested for a stationary wavy surface in an EHL point contact. Its roughness is defined as:

$$R(X,Y) = A\cos\left(\frac{2\pi X}{\Lambda}\right) \ . \tag{2.50}$$

In Fig. 2.8a-b, the dimensionless profiles of the pressure and the film thickness on the central line ($y = 0$) are plotted for $M_2 = 1007.6$, $L = 12.05$, $A = 0.018$ and $\Lambda = 0.5$. The EHL line contact model well predicts the general shape of both the pressure and the film thickness. The equivalent line contact description correctly predicts the central film thickness. Yet the pressure fluctuations are underestimated, probably due to the absence of the point contact side leakage effects in the equivalent line contact model.

Moving rough surface

For comparison with numerical transient point contacts, data from Ali et al. [94] are used. In Venner's work this case was not investigated. And Ali et al. used the multigrid method to numerically simulate it. The equivalent line contact description is tested in the case of a single limited groove passing through the EHL contact and given by the equation:

$$R(X,T) = A \times 10^{-12.5(X/\Lambda)^2}\cos(2\pi X/\Lambda) \ , \tag{2.51}$$

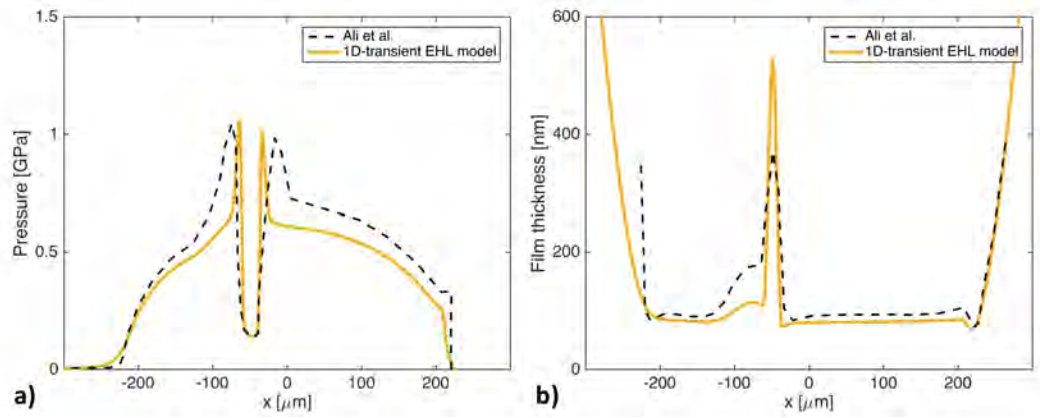

Figure 2.9: The pressure (a) and the film thickness (b) on the central line for a limited groove passing through the contact from calculation from the EHL line contact model and data from [94].

where $A = -0.15$ and $\Lambda = 0.27$. The pressure and film thickness on the central line are plotted in Fig. 2.9 versus $\eta_0 u_e$ for $M_1 = 50$ and $L = 4.7$. The model gives a good idea of the general shape of the pressure and film thickness: occurrence of the pressure drop and elastic deformation at the groove rear. However, the magnitude of pressure outside the limited groove and the elastic deformation at the groove rear are underestimated. These differences probably bear on the side leakage effects occurring at the limited groove edge in the y-direction.

2.4 Experimental comparisons

The EHL line contact model using the equivalent line contact description is compared to our EHL point contact experiments. Experimental procedure is first described, then the comparisons in terms of film thickness and friction are discussed.

2.4.1 Experimental procedure

Tribometer

Tribological experiments were carried out on the home-developed IRIS tribometer whose principle is detailed in [108, 109]. This tribometer creates an EHL point contact between a ball and a transparent disc, for which both kinematics are pre-

cisely controlled. While the surfaces are in motion, the normal load, the friction torque and the film thickness distribution inside the contact are simultaneously measured. The film thickness distribution was obtained using optical interferometry technique and recorded with either a Phantom® v7 camera, a high-speed camera (up to 4000fps) with a resolution of 2.19 μm/px, to capture continuously the film thickness evolution along one ball rotation (acquisition time from 0.1 to 10 s) or a Kappa® camera to capture with higher definition (resolution of 0.9 μm/px) selected instants over the ball rotation.

Stribeck curve experiments were performed on this tribometer to measure simultaneously both the friction and the film thickness distribution at constant SRR for various entrainment speeds. During measurements, the entrainment speed is gradually decreased from 0.5 m/s to 0.005 m/s and then reversely increased to 0.5 m/s. For each investigated entrainment speed, the tangential force was measured at $+\Sigma$ and $-\Sigma$, respectively during a 30-second step. The tangential force, F_t for each entrainment speed was then calculated as the average Couette tangential force (mean of the force at $+\Sigma$ and $-\Sigma$) over the two-ways:

$$F_{t,Couette} = \frac{1}{2}\left[\frac{F_{t,+\Sigma} - F_{t,-\Sigma}}{2}\right]_{one-way} + \frac{1}{2}\left[\frac{F_{t,+\Sigma} - F_{t,-\Sigma}}{2}\right]_{wayback} . \quad (2.52)$$

At each entrainment speed, the friction coefficient was then determined as the ratio of $F_{t,Couette}$ over the mean load. Various SRR were tested: 8, 25, 50 and 100%.

Traction experiments were also performed to determine the viscous friction in the case of smooth surfaces. In these experiments, the entrainment speed was set constant while the SRR varied. During measurements, the SRR is gradually increased from 0% to 150% and decreased reversely. For each $|\Sigma|$ value, the shear stress was measured over a 30-s step at Σ and another at $-\Sigma$. For each $|\Sigma|$ value, the tangential force was measured as previously described. Then the shear stress was determined as the ratio of $F_{t,Couette}$ over the contact area, i.e. πa^2 which is measured during the experiment or calculated with Hertz' theory. The entrainment speeds were set to 0.2 and 0.4 m/s to remain in fully flooded EHL. Experiments were carried out at room temperature, between 19°C and 24°C.

Surface topography

The ball was made of AISI 52100-drilled steel with a radius of 9.525 mm. It was polished to reduce its RMS roughness until $S_q < 10$ nm. The disc surface was smooth. Its topography was measured with an AFM, which gives 5 nm $< S_q <$ 10 nm. The transparent disc was made of quartz with two coatings, a 6-nanometer-thick chromium layer plus a 200-nanometer-thick silica layer. When in contact

Surfaces	R_x *(mm)*	E *(GPa)*	ν
Ball	9.525	210	0.30
Disc	∞	70	0.17

Table 2.1: Material and geometrical characteristics of the surfaces.

with a reflective surface, here the ball, optical interferences are generated. After appropriate calibration, the local film thickness that separates the ball and the disc, and its distribution were measured with a resolution of 2 nm. The material and geometrical characteristics of the disc and the ball are summarized in Table 2.4.1.

Lubricant

The 330 Neutral Solvent (330NS) mineral oil was used as lubricant. Using an AR2000 rheometer in a cone/plane configuration, the lubricant viscosity at ambient pressure, η_0, under constant shear rate $\dot{\gamma} = 0.1$ s^{-1}, was measured as a function of temperature and is plotted in Fig. 2.10a. The temperature range of the Stribeck experiments is also indicated. Data were well fitted with the Vogel viscosity law,

$$\eta_0 = c_1 e^{\frac{c_2}{T - c_3}} \ , \tag{2.53}$$

where $c_1 = 2.44 \times 10^{-5}$ Pa.s, $c_2 = 1285$ °C and $c_3 = -124$ °C.

Several traction experiments were performed at $u_e = 0.2$ and 0.4 m/s with a smooth contact. The load was set to 15 N, leading to a Hertzian contact radius a equal to 125 μm. The same contact radius value was measured in the experiments. It yielded an average Hertzian contact pressure equal to 305 MPa. As explained in [60], from the simultaneous measurements of film thickness and shear stress in smooth contacts under moderate conditions, the apparent viscosity of the 330NS was measured at 305 MPa, i.e. the mean contact pressure according the shear rate. The value of the viscosity under 305 MPa is reported in Fig. 2.10b. Cross rheology was used to fit the data since this model showed accurate rheological description of the under-pressure lubricant and shear rates in previous works [60, 61]. It yields,

$$\eta = \eta_{\infty/P} + \frac{\eta_{0/P} - \eta_{\infty/P}}{1 + \left(\frac{\dot{\gamma}}{\dot{\gamma}_s}\right)^n} \ , \tag{2.54}$$

where $\eta_{0/P} = 160$ Pa.s, $\eta_{\infty/P} = 1$ Pa.s, $\dot{\gamma_s} = 1.1 \times 10^5$ s^{-1} and n = 1.1. As shown in recent works [59, 60], the value of $\eta_{0/P}$ is in good agreement with the under-

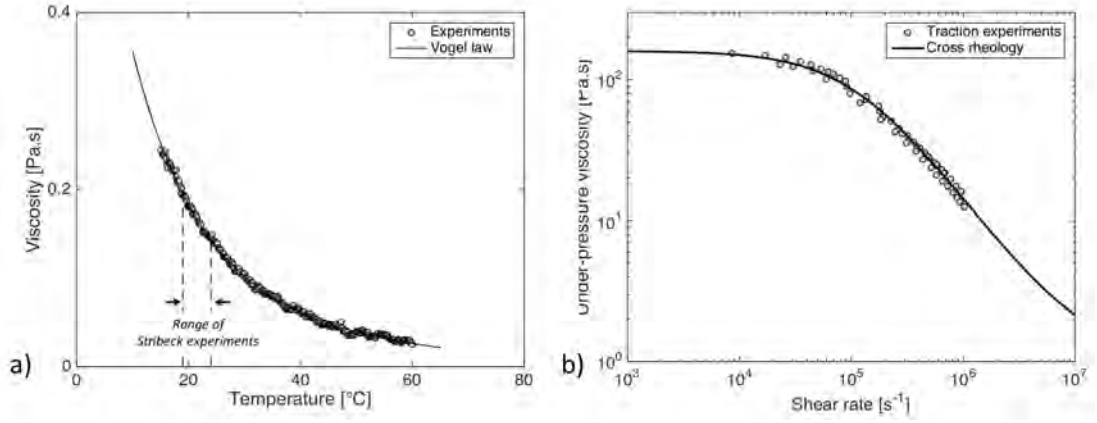

Figure 2.10: 330NS rheology at atmospheric pressure vs. temperature (a) and under pressure vs. the shear rate (b). Experimental data are respectively fitted with the Vogel viscosity law (a) and the Cross law (b).

pressure viscosity of the lubricant at low shear rate calculated with Roelands' equation at 305 MPa.

2.4.2 EHL point contacts

Several Stribeck experiments were performed with a smooth ball and a smooth disc, for a contact pressure of 305 MPa and at various SRR: 8%, 25%, 50% and 100%. In the generalized Sommerfeld number S, used in the Stribeck curve, the numerator depends on the product of the viscosity times the velocity and the denominator is equal to the pressure. In the experiments, the pressure is a constant therefore the data will be plotted versus the viscosity η_0 times the entrainment velocity u_e. The experimental film thickness and Couette friction measurements are compared to the results of the EHL line contact model using the equivalent line contact description. In term of Moes parameters, the experiments belong to the domain $(M_2, L) \in [30, 1250] \times [3, 10]$.

In point numerical contact, the friction coefficient μ is calculated as the ratio of the tangential force F_t over the normal force F_n. F_t corresponds to the fluid shear stress τ over the EHL contact $\Omega = \{(x, y), x^2 + y^2 \leq a^2\}$ and F_n to the load W_L. It yields:

$$\mu = \frac{F_t}{F_n} = \frac{\int_\Omega \tau(x, y) dx dy}{W_L} \ . \tag{2.55}$$

For the equivalent line contact, the equivalent friction μ_{eq} is defined as:

$$\mu_{eq} = \frac{\int_{x=-a}^{a} \tau(x)dx}{w_L} \ , \tag{2.56}$$

where the line load w_L is equal to:

$$w = \frac{\pi p_h a}{2} \ . \tag{2.57}$$

The shear stress τ and the shear rate $\dot{\gamma}$ are defined as:

$$\begin{cases} \tau(x) = \eta(x)\dot{\gamma}(x) \ , \\ \dot{\gamma}(x) = \dfrac{\partial u_x}{\partial z} \approx \dfrac{u_s}{h(x)} \ . \end{cases} \tag{2.58}$$

If the Cross rheology is used, $\eta(x)$ is defined from Eq. 2.54 and if the Newtonian rheology is chosen, $\eta = \eta_{0/P}$. In both case, the under pressure viscosity $\eta_{0/P}$ at the mean contact pressure p_m has to be calculated with the Roelands' equation (Eq. 2.17). The mean contact pressure is obtained as:

$$p_m = \frac{1}{2a} \int_{-a}^{a} p(x)dx \ . \tag{2.59}$$

The EHL line contact model is run for $\eta_0 u_e \in [1.0\times10^{-4}, 1.0\times10^{-2}]$ Pa.m over the domain $X \in [-2.5, 1.5]$ with 512 nodes and a tolerance of 1.0×10^{-10}. Regarding the experimental Hertzian radius $a = 125$ µm, the spatial pitch is $\Delta x \approx 1$ µm.

In the following parts, the numerical results are reported in straight line whereas the experimental results are plotted with dots.

Smooth surfaces - $\Sigma = 8\%$

In Fig. 2.11a the central film thickness h_c from numerical and experimental results, is plotted versus $\eta_0 u_e$ for $\Sigma = 8\%$. Moreover the central film thickness prediction of Hamrock and Dowson, $h_{c,H\&D}$ [16] defined for point contact as:

$$\frac{h_{c,H\&D}}{R_x} = 2.69U^{0.67}G^{0.53}W_2^{-0.067}\left(1 - 0.61e^{-0.73}\right) \ , \tag{2.60}$$

is plotted in dash line in Fig. 2.11a as a reference. Good agreement between experimental and numerical data is found for the determination of the central film thickness in point contact. In addition, the Hamrock and Dowson formula is proved to be robust for our experiments although there is a slight difference. This may be due the empirical determination of the $h_{c,H\&D}$ formula.

In Fig. 2.11b, the numerical film thickness and the pressure on EHL central line are plotted at $\eta_0 u_e = 3.6 \times 10^{-2}$ Pa.m. The corresponding experimental central line film thickness profile is displayed. This figure confirms the ability of the equivalence method to well predict the film thickness profile on the central line.

Fig. 2.11c reports the numerical minimum film thickness, the experimental minimum film thickness ($\circ$), the experimental minimum film thickness on the central line of the same contact ($\diamond$) and the theoretical minimum film thickness from Hamrock and Dowson versus $\eta_0 u_e$. The minimum film thickness formula of Hamrock and Dowson [16] is:

$$\frac{h_{m,H\&D}}{R_x} = 3.68 U^{0.68} G^{0.49} W_2^{-0.073} \left(1 - e^{-0.68}\right) \ . \tag{2.61}$$

In our smooth contact the minimum film thickness is located in the side constriction regions, not modeled in EHL line contacts. Logically, the equivalent description can estimate the minimum film thickness on the central line (see also Fig. 2.11b) but is far from the overall minimum film thickness of the point contact. This minimum film thickness is mostly influenced by the side leakage. Besides, the Hamrock and Dowson formula also overestimates the minimum film thickness and is closer to the minimum film thickness on the central line.

With these numerical results, the friction is calculated using the Cross and the Newtonian rheology. The friction is reported in Fig. 2.11d versus $\eta_0 u_e$ as well as the experimental data. Excellent agreement is found here between experimental and Cross numerical friction whereas the Newtonian rheology predicts a higher friction. This seems to indicate that friction originate from the theory of a Cross-like fluid under pressure rheology in the contact. In the context of the actual debate over thermal effects, Newtonian friction with a warmer fluid in the contact, $x \in [-a, +a]$, is also calculated in Fig. 2.11d. Higher temperature is expected to decrease the viscosity of the shear fluid and the friction. To reduce the Newtonian friction to the experimental one, the fluid needs to be heated up to 30°C. Nonetheless, the shape of the friction versus $\eta_0 u_e$is not correctly described with this heated Newtonian fluid. On the contrary, this is perfectly achieved with a fluid having a Cross rheology without heating. This shows that Newtonian rheology does not correctly describe the EHL friction, even if fluid heating is considered.

Also, the friction is correctly predicted with the Cross friction although the minimum film thickness is overestimated. Indeed, at the location of minimum film thicknesses in Fig. 2.11b, the pressure is about a tenth of the mean contact pressure ($\approx$ 30 MPa). The viscosity is thus thousand times lower than the lubricant viscosity in the contact center. Therefore the local shear stress in the

constriction region is negligible compared to the friction contribution in the central zone. The correct simulation of the rheology is essential to determine the EHL friction under the contact conditions analyzed here.

Smooth case - Σ = 25%, 50% and 100%

Experiments were carried out at three other SRR: 25%, 50% and 100%. Numerical results (central film thickness and friction) from the EHL line contact model and the experimental point contact data are reported in Fig. 2.12 versus $\eta_0 u_e$. The central film thickness is again well predicted by the numerical model (see Fig. 2.12a,c,e). The increase of the SRR does not modify the central film thickness in smooth experiments. Indeed, the SRR does not appear in the smooth EHL equations (Eq. 2.19 and Eq. 2.21). Nonetheless, the SRR has a strong impact on fluid shearing and so on EHL friction. Fig. 2.12.b,d,f show an increasing friction when the SRR grows. For $\eta_0 u_e > 1.0 \times 10^{-2}$, the friction starts decreasing.

The Newtonian friction is determined at ambient temperature and respectively at T = 40, 50 and 100°C, for Σ = 25%, 50% and 100%. In Fig. 2.12b,d,f the Newtonian friction is higher as compared to experimental data. Taking into account the possible thermal effects leads to an incoherency, especially for Σ = 100% where a temperature of 100°C, of the sheared fluid, is not enough to reach the experimental values.

To highlight the origins of the friction reduction, the Cross friction is here calculated in two ways: using $\eta_{0/P}$ at the mean pressure p_m (calculated from numerical simulation) and at the theoretical mean Hertzian pressure $p_{m,Hertz}$. Only the Cross friction using p_m is able to predict the decrease of the friction at high $\eta_0 u_e$. This means that at high values of $\eta_0 u_e$, the shear flow of the lubricant in the inlet area contribute to the friction force.

Fig. 2.13a reports the mean pressure p_m over the mean Hertzian pressure $p_{m,Hertz}$ and $\eta_{0/P}$ at the pressure p_m versus $\eta_0 u_e$. As above-mentioned, EHL equation is independent of Σ for smooth contacts. Thereby, the pressure solutions are also independent and so do p_m values. Fig. 2.13 shows that the mean pressure p_m is a decreasing function of $\eta_0 u_e$. This means that at high $\eta_0 u_e$, the pressure profile expands toward the contact inlet. This phenomenon is illustrated in Fig. 2.13b which reports the pressure profile respectively at $\eta_0 u_e = 1.0 \times 10^{-4}$ Pa.m and $\eta_0 u_e = 1.0 \times 10^{-1}$ Pa.m. Thereby the under-pressure viscosity is lower when $\eta_0 u_e$ increases and so does the friction.

It is demonstrated here that the Newtonian friction cannot predict the EHL friction since it does not take into account fluid shear thinning. This phenomenon decreases the viscosity when the shear rate increases and so the viscous friction.

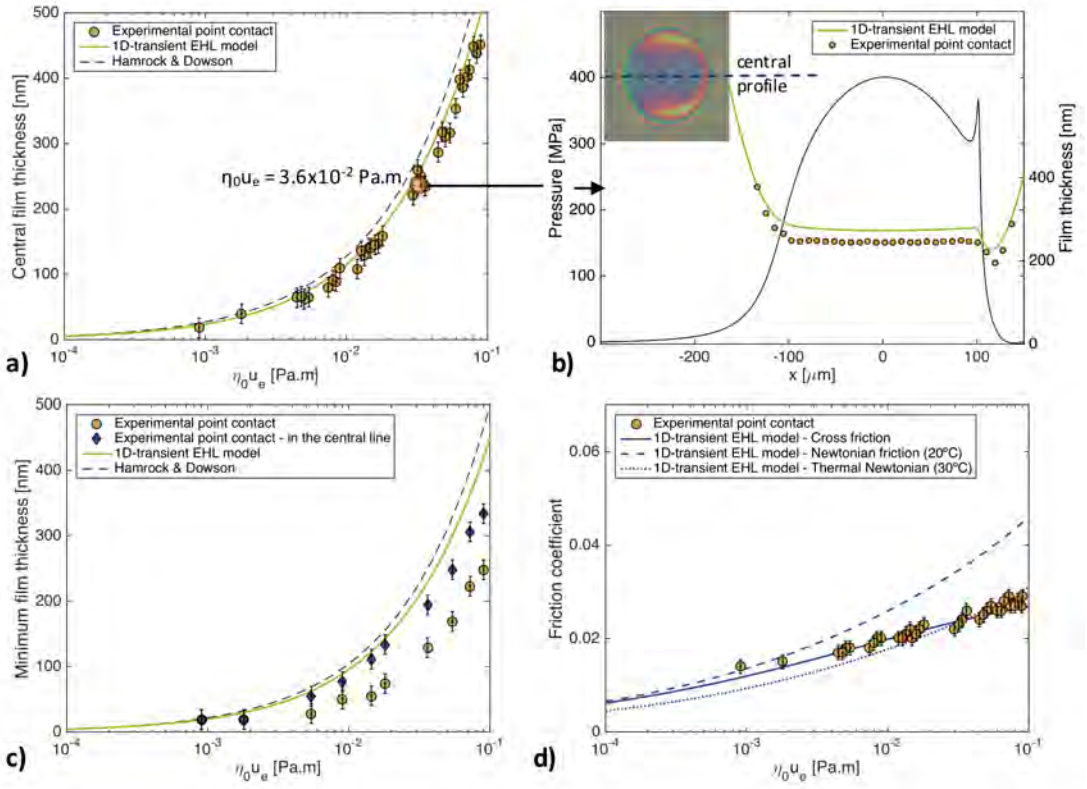

Figure 2.11: $\Sigma = 8\%$ - Numerical and experimental central film thickness are plotted versus $\eta_0 u_e$(a). The numerical pressure and film thickness at $\eta_0 u_e$ =3.6 $\times$ 10^{-2} Pa.m is reported in (b) as well as the corresponding experimental film thickness. The numerical and experimental minimum film thicknesses are shown in (c). The numerical (Cross, Newtonian) and experimental friction are plotted versus $\eta_0 u_e$in (d). Numerical data are obtained from the EHL line contact model using equivalent line contact description.

The Cross rheology is able to well describe this physical behavior. It is interesting to point out that the friction prediction does not require the resolution of non-Newtonian EHL equations but only the use of Cross rheology in the friction calculus. In fact, the non-Newtonian numerical simulations from Jacobson et al. [110] showed that the non-Newtonian effects had only few impact on the film thickness. This confirms that the line contact model correctly determine the central film thickness and thus the shear rate.

Moreover, in the determination of the Cross parameters, $\eta_{0/P}$ was physically linked to the under-pressure viscosity in the EHL contact. It has been shown that this under-pressure viscosity is a decreasing function of $\eta_0 u_e$. This dependency (see Fig. 2.13) explains that the friction starts decreasing at high $\eta_0 u_e$; the EHL friction is due to the Cross shearing of the lubricant inside the contact, i.e. from $-a$ to $+a$. This phenomenon is enhanced as the SRR increases. Therefore, the ratio of the Cross shear stress, τ calculated with p_m over the Cross shear stress τ_{Hertz} using $p_{m,Hertz}$ is investigated for a given $\eta_0 u_e$ and Σ. As the shear rate is the same in both cases:

$$\frac{\tau}{\tau_{Hertz}} = \frac{\eta\dot{\gamma}}{\eta_{Hertz}\dot{\gamma}} = \frac{\eta}{\eta_{Hertz}} \ . \tag{2.62}$$

In the Cross law (Eq. 2.54), $\eta_{\infty/P} \ll \eta_{0/P}$ so:

$$\eta \approx \frac{\eta_{0/P}}{1 + \left(\frac{\dot{\gamma}}{\dot{\gamma}_s}\right)^n} \ . \tag{2.63}$$

Thus Eq. 2.62 yields:

$$\frac{\tau}{\tau_{Hertz}} = \frac{\eta_{0/P}}{\eta_{0/P,Hertz}} \ , \tag{2.64}$$

which do not depend on the SRR but only on $\eta_0 u_e$. Thus, for $\eta_0 u_e = 1.0 \times 10^{-1}$ Pa.m, this ratio is about 95% according Fig. 2.13. Thereby, at low SRR the lower friction prevents to highlight such variation. In addition to the variations of $\eta_{0/P}$ as function of $\eta_0 u_e$, the other Cross parameters might also vary. However, the above calculations correctly predict the friction level in EHL. Therefore, these possible variations have far less impact on the EHL friction determination.

Hence the EHL friction results from the shearing of the Cross-like lubricant in the contact ($x \in [-a, +a]$), which under-pressure viscosity is governed by the spread of the pressure profile at the contact inlet.

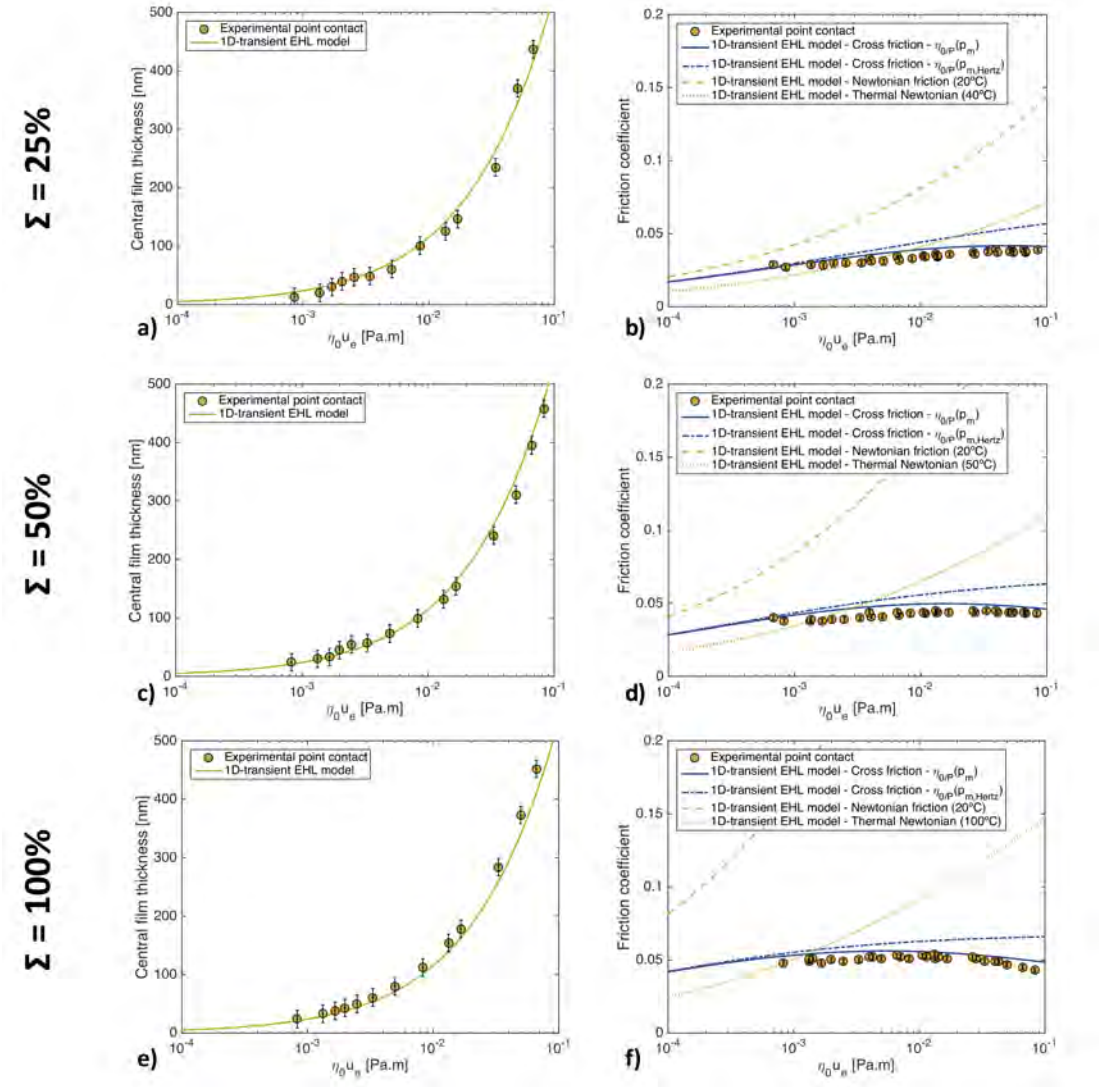

Figure 2.12: $\Sigma = 25\%$, 50% and 100% - Numerical and experimental central film thickness (a,c,e) and friction (b,d,f) versus $\eta_0 u_e$. Numerical data are obtained from the EHL line contact model using equivalent line contact description.

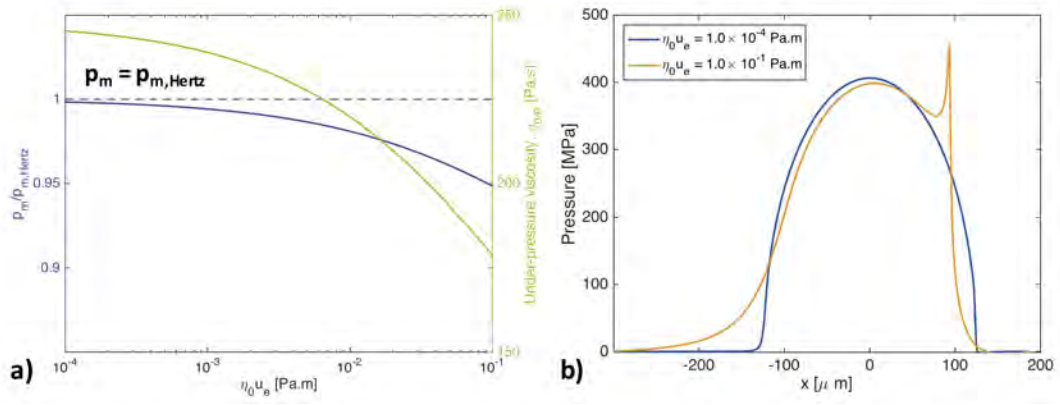

Figure 2.13: Ratio of p_m over the theoretical Hertzian pressure $p_{m,Hertz}$ versus $\eta_0 u_e$ and the corresponding $\eta_{0/P}$ (a). Pressure profiles at $\eta_0 u_e = 1.0 \times 10^{-4}$ and 1.0×10^{-1} Pa.m (b). Numerical data come from the EHL line contact model.

2.5 Conclusions

From the review literature, a line contact solver was developed: the EHL line contact model. Its efficiency in solving the EHL equations for steady-state and transient conditions has been proved for elastic piezoviscous fluids.

Combined with the equivalent line contact description, the EHL line contact model has correctly predicted the central film thickness for smooth surfaces. First, it has correctly determined the friction, highlighting the importance of shearing Cross-like fluid rheology and the variations of the mean pressure inside the contact, p_m, versus $\eta_0 u_e$. This emphasizes that EHL line and point contacts are physically very close. Therefore physical understandings in EHL point contacts can be achieved from numerical EHL line contacts. Yet the main difference remains the side leakage induced by the Poiseuille flow, that is neglected in the EHL line contact model. This hypothesis leads to an underestimation of the minimum lubricant film thickness.

This model has proved to correctly simulate our experiments with a very competitive and efficient time allocation (developing and running). But this was achieved by accepting some limitations: the minimum film thickness cannot be accurately determined in point contact and the elastic deformation of two-dimensional textures (limited grooves or cavities) is underestimated. However, our numerical strategy shows great potential in providing further understandings of the EHL point contact mechanisms, in a small time lapse and for any kind of roughness.

Chapter 3

Groove textures

Contents

The influence of the groove geometry on friction is analyzed according to the lubrication regimes. Two main characteristics of the friction are investigated: the onset of the mixed/EHL regime transition and the viscous shear stress responsible for the EHL friction. Both depend on the film thickness. First, the film thickness corresponds to the average clearance between surface asperities. Therefore, it governs the onset of asperity contacts through a direct interaction and/or micro-EHL between these surface asperities which both are expected to increase the friction. Second, the shear stress is a function of the shear rate which is proportional to the inverse of the film thickness.

Two groove orientations are investigated experimentally: transverse with grooves perpendicular to and longitudinal with grooves parallel to the entrainment direction. For each orientation, the effect of groove top width is studied more particularly. The originality of this work is in the experimental approach developed and on the comparison against the numerical simulation. Multiple contacts were studied to determine local friction and film thickness at precise instants over one cycle (millisecond-scale time and one contact area). This was made possible by the use of textured surfaces with geometrical features (groove top width for instance) which vary along one cycle.

The topography of the balls is first presented. The smooth surface is used as a reference surface in order to exhibit the possible difference between the friction transition, called mixed/EHL transition in the following, and the film thickness transition.

The EHL line contact model coupled with the equivalent line contact description is introduced to simulate a wider range of transverse grooves. A parametric study is carried out on the groove depth and highlight how the coupling of the latter with the groove top width modifies the EHL friction. Comparisons with the experimental results are performed and provide further understandings in terms of film thickness and pressure.

These complementary approaches give a clear description of the EHL friction through the film thickness modifications induced by the grooves. The transitions in terms of friction and film thickness, the viscous shear rate and the possible origins of the mixed friction are also discussed.

3.1 Groove topography

The balls were made of AISI 52100-drilled steel with a radius of 9.525 mm. They were polished to reduce their roughness until $S_q < 10$ nm. The smooth surface is referred to as B0. After polishing, three other balls (B1, B2 and B3) were treated

with femtosecond LASER irradiations to sculpt periodic grooves on their surface. The wavelength is constant along the ball track and equal for all surfaces to λ = 25 µm. The grooves of B1 are transverse regarding the entrainment direction whereas B2 and B3 present longitudinal grooves.

The groove top width was set to vary along each ball track as Fig. 3.1a schematically shows. Given the manufacturing process by LASER ablation, the creation of narrow tops, i.e. wide bottoms, required a larger amount of LASER passes and a more energetic beam than to sculpt wide tops, i.e. narrow bottoms. As a consequence, the narrower the groove, the more ablated the surface and so the deeper the groove (see Fig. 3.1a). Since the groove wavelength is constant and the groove depth is correlated to the top width, at each ball position the grooves are characterized by a single parameter: the top width.

Two techniques were used to quantify the variation of the groove top width along each ball track. First, the groove top width was measured for each groove contact interferograms at low entrainment speed (u_e = 0.005 m/s) to reduce image blur and in pure rolling ($\Sigma = 0\%$) to limit the elastic deformation of the grooves. The top width is measured as the average of the top widths present in the contact of diameter 250 µm at a fixed angular position of the ball. Thanks to this in-situ method, the bright-colored groove tops were easily distinguished from the gray groove bottoms. Direct topographic measurements would have imposed the definition of a threshold to distinguish the groove tops from the groove bottoms. This threshold would have been influenced by parameters such as the surface planarity or the small roughness on the grooves. In addition, the chosen methodology still kept top width measurement accurate compared to topographic measurements since the elastic deformation only affects the pattern amplitude but not its wavelength [86, 68, 69]. The evolution of the groove top width is then reported along the ball tracks, from 0° to 360°, in Fig.3.1b. For B1, the top widths range from 8 to 22 µm. The top width of B2 is between 3 and 15 µm. B3 top widths are smaller, beneath 5 µm.

Second, at the location of the widest ($\square$) and the narrowest ($\star$) tops as shown by the contact interferograms, the 2D-topography of the non-deformed ball was measured with a Brucker optical interferometer. Central 1D-profiles were extracted from these surface measurements and plotted in Fig.3.1c-d, respectively . They indicate a correlation between groove depth and groove top width. For wide tops, the depth is less than 100 nm whereas it reaches up to 250 nm with narrow tops. The depth remains of the same order of magnitude except for the wide tops of B1, which topography tends to a smooth surface. When the surface is nearly flat such as B1, the corresponding top width (here 22 µm) tends to the value of the wavelength, $\lambda = 25$ µm. On the contrary, the narrower the top width,

Label	*Orientation*	*Top width (μm)*
B0	-	-
B1	Transverse	8 - 22
B2	Longitudinal	3 - 15
B3	Longitudinal	0 - 5

Table 3.1: Texture characteristics of the surfaces.

the sharper the surface peaks (see B3 for instance). The surface characteristics are summarized in Table 3.1.

3.2 Reference smooth surface

3.2.1 Mixed/EHL transition

The Stribeck curve of the smooth surface B0 for $|\Sigma| = 8\%$ is reported in Fig. 3.2. The friction coefficient is plotted versus $\eta_0 u_e$ to take into account the effect of the viscosity variation induced by room temperature variation on the lubricant film thickness. From the rheology of the interfacial film under-pressure at 305 MPa (see chapter 2) and the measurements of the velocity, of the film thickness (cf. Fig. 3.3) and of the contact area, one can calculate and plot the viscous friction (see dashed curve in Fig. 3.2). For $\eta_0 u_e$ superior to 1.0×10^{-3} Pa.m, the measured friction coefficient collapses on the calculated viscous friction coefficient with an averaged error, $|\mu_{viscous} - \mu_{exp}|$, of 0.001 for B0; this is the EHL regime. For $\eta_0 u_e$ less than 1.0×10^{-3} Pa.m, the friction diverges from this predicted viscous law.

The mixed/EHL regime transition is defined as the friction slope breaks in the Stribeck curve. In Fig. 3.2, the smooth EHL regime occurs for $\eta_0 u_e > 1.0 \times 10^{-3}$ Pa.m. For values of $\eta_0 u_e$ lower than 1.0×10^{-3} Pa.m., B0 is in mixed lubrication regime. The left vertical line marks this regime transition in Fig. 3.2. This friction transition is commonly attributed to the moment when the first asperity contacts between the ball and the disc occur even though relatively little is known on the mixed regime [111]. For instance, Poon et al. [13] stressed that two transition regimes could be defined which do not share the same physical meaning: the primary one at the asperity contact onset and the secondary one, happening at a higher $\eta_0 u_e$ value, when micro-EHL effects increase the friction.

The transition determined from the friction response corresponds to the $\eta_0 u_e$ value below which the flow of the pressurized lubricant is not purely viscous anymore.

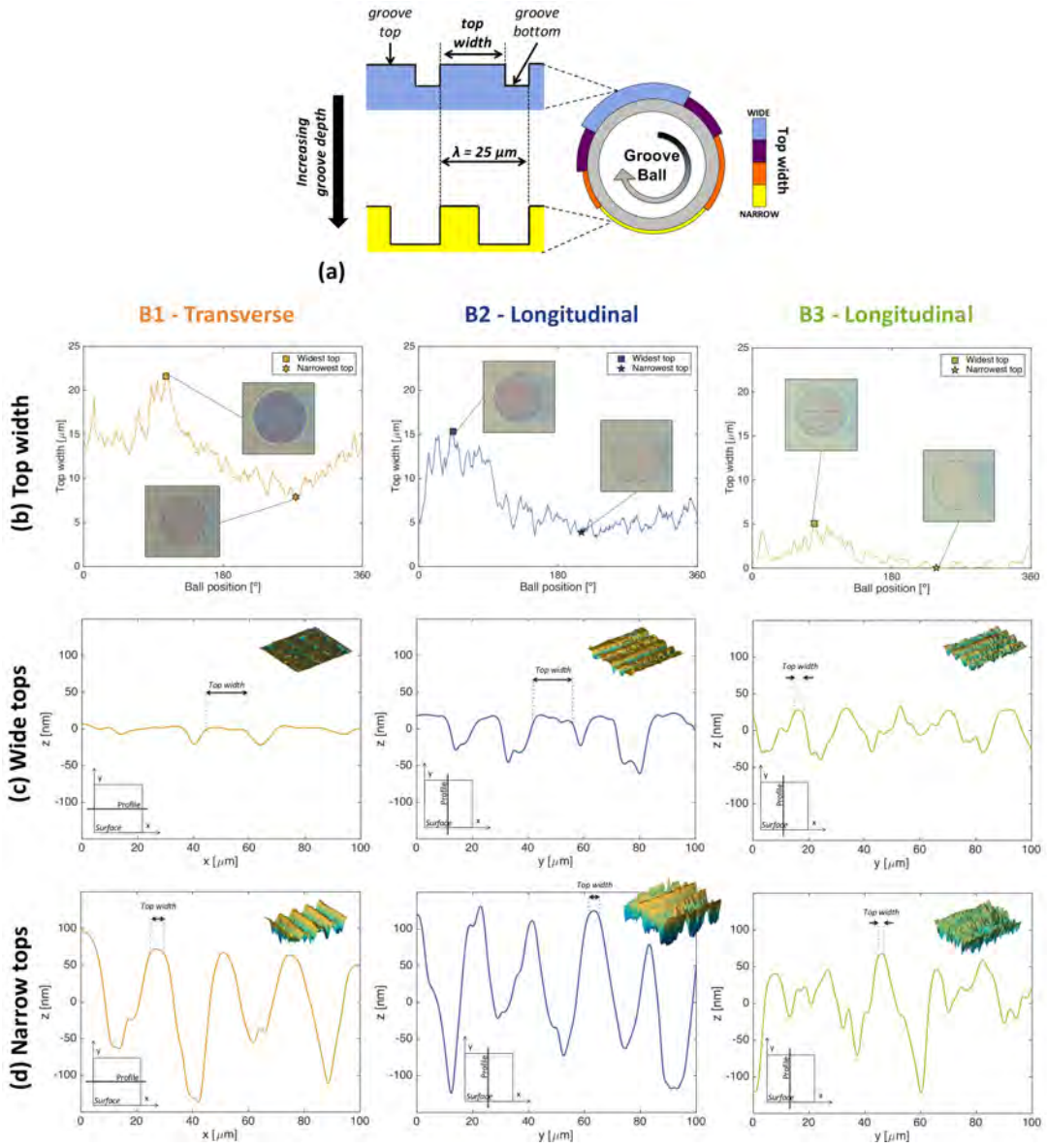

Figure 3.1: (a) Schematic evolution of the groove top width and the groove depth vs. the angular position, (b) morphological data for B1, B2 and B3 texturing using contact interferograms and 2D topography associated with 1D topographic profiles for wide (c) and narrow tops (d). The contact edges are stressed with a dash line in the contact interferograms.

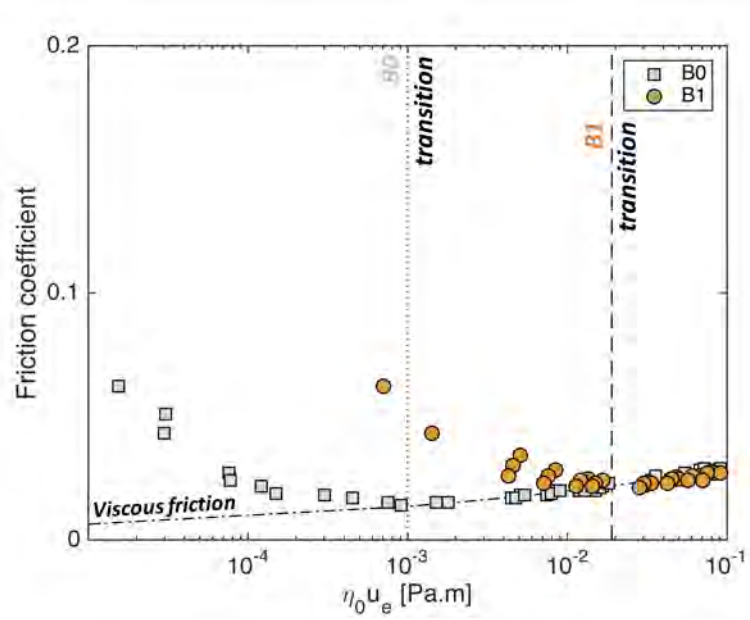

Figure 3.2: Stribeck curves of the smooth surface B0 and B1 at $|\Sigma| = 8\%$, highlighting the mixed/EHL regime transitions and pure viscous friction level.

This transition could be the result of either asperity contacts (local boundary lubrication) or a local increase of the lubricant viscosity (micro-EHL) or a change of the lubricant rheology due to local pressure variations. The transition from friction measurements is then expected to be higher or equal to the transition based on the film thickness analysis. The point where the first asperity contacts occur will be referred to the film thickness transition.

3.2.2 Film thickness transition

The film thicknesses evolution during the Stribeck experiments with ball B0 is presented in Fig. 3.3 as well as interferograms displayed for several operating conditions: $u_e = 0.005$, 0.03, 0.1, 0.2, 0.4 m/s. The contact radius is 125 μm and the fluid flow is entrained from left to right. A homogeneous film thickness is formed all over the contact except in the constriction zone. The square symbols (□) represent the central film thickness at various $\eta_0 u_e$. In practice, the latter is measured as the average value of the film thickness over a 2/3-Hertzian-radius square zone centered on the contact. The film thickness distribution in the contact, i.e. the whole range of values taken by the film thickness in the contact, is plotted in bold gray line for several $\eta_0 u_e$.

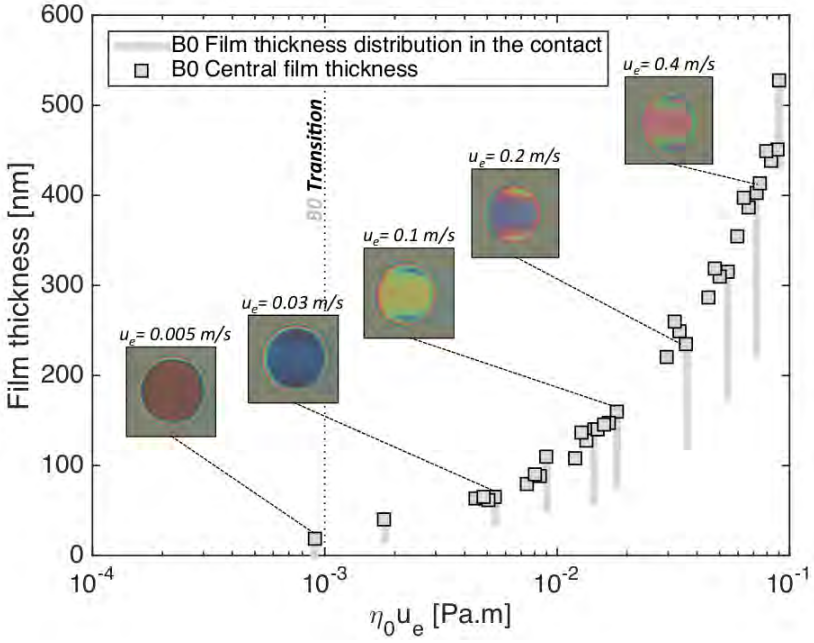

Figure 3.3: Contact film thickness measured during the Stribeck experiments performed on smooth ball B0 with related 125-µm-radius contact interferograms vs. $\eta_0 u_e$. The B0 mixed/EHL regime transition determined with the friction criteria is also indicated.

In smooth EHL contacts, the maximum film thickness is reached at the contact center. This is the reason why the central film thickness is the maximum of the film thickness distribution in Fig. 3.3. For $\eta_0 u_e \leq 1.8 \times 10^{-3}$ Pa.m, the minimum film thickness distribution is always superior to zero meaning that no contact occurs: it is the EHL regime. However at $\eta_0 u_e = 9.0 \times 10^{-4}$ Pa.m, the minimum film thickness reaches zero. The film thickness transition is then supposed to occur for values of $\eta_0 u_e$ between 9.0×10^{-4} and 1.8×10^{-3} Pa.m. So far, experimental results are in agreement with these definitions yet the resolutions in $\eta_0 u_e$ prevent from determining if the mixed/EHL transition measured on the Stribeck curve is indeed due to asperity contact or micro-EHL.

3.3 Experimental transverse grooves

3.3.1 Mixed/EHL transition

The Stribeck curve of the transversal groove ball B1 is reported in Fig. 3.2. When $\eta_0 u_e > 1.9 \times 10^{-2}$ Pa.m, the experimental friction coefficient collapses on the data measured for B0 and on the previous calculated smooth viscous friction: it is the EHL regime. Below this value, the friction diverges from the viscous one and increases as $\eta_0 u_e$ decreases: the contact with ball B1 works in mixed lubrication regime. The mixed/EHL regime transition of B1 is then shifted to higher $\eta_0 u_e$, 1.9×10^{-2} Pa.m, compared to B0.

3.3.2 Film thickness transition

Film thickness measurements corresponding to Stribeck curve obtained with ball B1 are reported in Fig. 3.4. Unfortunately, several limitations did not allow us to obtain the whole film thickness distribution of the contacts. First, in the case of ball B1, the grooves are perpendicular to the direction of the lubricant flow and even with the Phantom high-speed camera the image was blurred at high entrainment speed. The contact appears then homogeneous. Second, the bottom of the grooves does not reflect the light in the same way as the smooth surface and the groove tops do: the groove bottoms appear as gray stripes while the groove tops are bright stripes. They are only distinguishable on interferograms at low entrainment velocity. As an illustration of this effect, Fig. 3.1b displays interferograms at $u_e = 0.005$ m/s where consecutive gray and colored stripes are visible. This difference in light reflection results in the fact that the color of the tops predominates, especially at high speed. In addition, in the absence of appropriate calibration of the gap measurement for the groove bottom, the film thickness could only be measured accurately on the top of the grooves. As a consequence, the measurements of the film thickness at the groove tops were much more robust than at the groove bottom. Given these considerations, interferograms of the contact were treated to extract values of film thickness.

Maximal and minimal central film thicknesses

Fig. 3.4a reports the ratio $h_{c,B1}/h_{c,B0}$ of the central film thickness of B1 over the central film thickness of B0 at $\eta_0 u_e = 3.1 \times 10^{-2}$ Pa.m, in the EHL regime, versus the angular position of the ball. The central film thickness measured with ball B1 corresponds to the average separation between the groove tops and the disc

in the center of the contact. $h_{c,B1}/h_{c,B0}$ is constant around 100% except between 220° and 320° where it collapses to 65%. This leads us to define two central film thicknesses over a ball rotation: a maximum central film thickness (∘) and a minimum central film thickness (⋆).

In Fig. 3.4b, the film thickness distribution in the contact over a ball rotation is plotted in vertical continuous bold line versus $\eta_0 u_e$. The maximum and minimum central film thicknesses exhibited in Fig. 3.4a are also presented for the various operating conditions in Fig. 3.4b. A gray dash line shows the average tendency of the central film thickness measured for B0 for comparison and a vertical dashed line gives the B1 regime transition determined by Stribeck experiments. The film thickness transition corresponds to a $\eta_0 u_e$ value located between 1.4×10^{-2} and 2.8×10^{-2} Pa.m according to minimum-film-thickness-based technique described previously. This result is again in agreement with the mixed/EHL transition value, $\eta_0 u_e = 1.9 \times 10^{-2}$ Pa.m, detected from the friction coefficient measurements. In EHL regime, the maximal central film thickness formed with ball B1 is similar to that formed with the smooth ball B0. Meanwhile, the minimal central film thickness formed with B1 is lower than that formed with B0. On the contrary, in the mixed regime, the maximal central film thickness formed with B1 is higher than that formed with B0 and its minimal central film thickness is equal to the central film thickness of B0. An exception occurs for very low $\eta_0 u_e$ where the minimal central film thickness of B1 reaches almost zero and becomes lower than B0 central film thickness. In particular, the first asperity contacts detected at $\eta_0 u_e = 1.4 \times 10^{-2}$ Pa.m only occurred when the central film thickness is close to the minimal central film thickness.

In the mixed and EHL regimes, the distance between the maximal and minimal central film thickness seems random. It is equal in EHL to 60 ± 15 nm where the blur, generated by the texture velocity, increases the measurement error to a dozen of nm in the contact interferometer corresponding to the minimal central film thickness. In the mixed regime, asperity contacts are more numerous when the film thickness is minimal. Yet, the camera resolution does not allow to measure, with sufficient precision, the ratio of asperity contact over the contact for $\eta_0 u_e > 2.0 \times 10^{-3}$ Pa.m.

Influence of the groove top width in mixed lubrication

The origin of film thickness variation with the grooves of ball B1 is investigated into detail in Fig. 3.5. Contact interferograms, representative of both decreasing and increasing entrainment speeds (with 60s-step), are displayed for four entrainment speeds: 0.005 m/s ($\eta_0 u_e = 7.8 \times 10^{-4}$ Pa.m) (a), 0.03 m/s ($\eta_0 u_e = 4.7 \times$

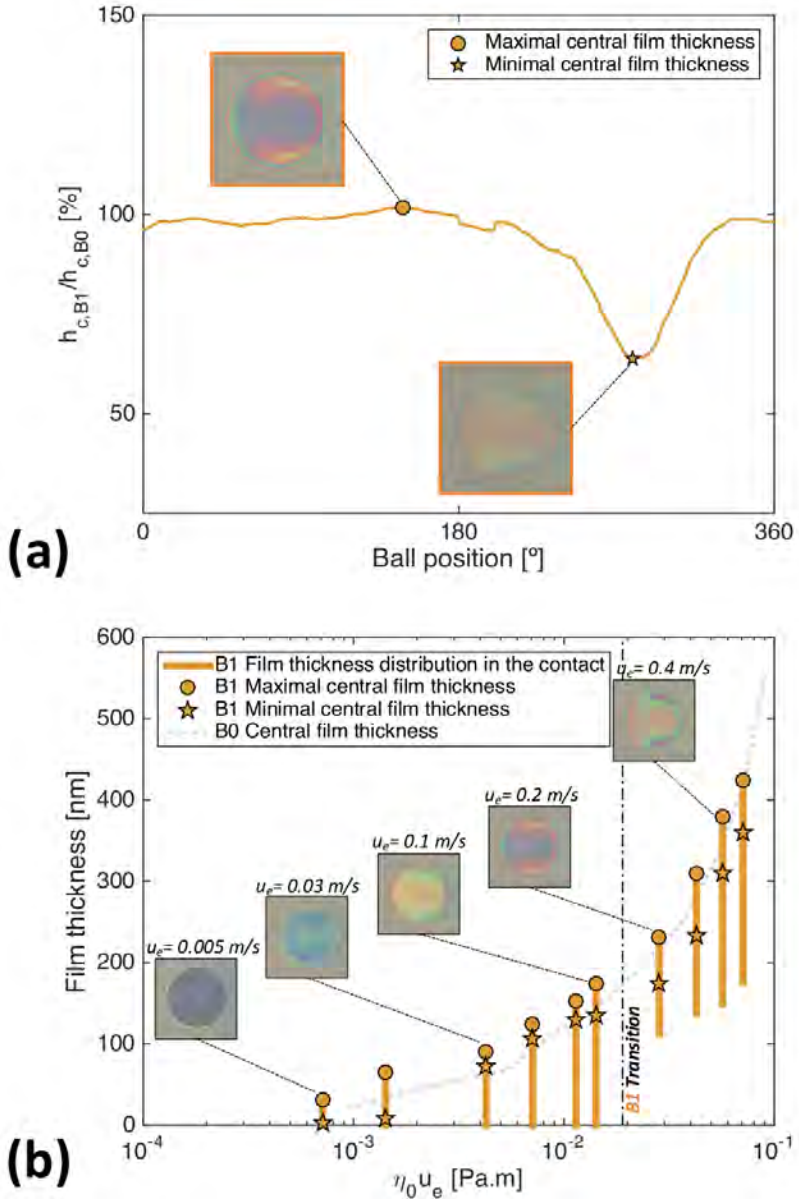

Figure 3.4: (a) Ratio of central film thickness measured for B1 over that measured for B0 at $\eta_0 u_e = 3.1 \times 10^{-2}$ Pa.m along the ball circumference. A maximal ($\circ$) and a minimal ($\star$) film thickness can be defined at the contact center. (b) Film thickness measured during Stribeck experiments performed on ball B1 with related 125-µm-radius contact interferograms vs. $\eta_0 u_e$. The $\eta_0 u_e$ value characteristic from the mixed/EHL transition with ball B1 is highlighted and the central film thickness measured for the smooth ball B0 is reported for comparison.

10^{-3} Pa.m) (b), 0.1 m/s ($\eta_0 u_e = 1.6 \times 10^{-2}$ Pa.m) (c) and 0.2 m/s ($\eta_0 u_e = 3.1 \times 10^{-2}$ Pa.m) (d). These interferograms show the passage through the contact of a 47-µm wide groove top (almost twice as the wavelength) located in the middle of narrower ones of 8-µm width. On each interferogram, the film thickness measured on the widest groove top (h_{thick}) is higher than the one measured on its neighboring groove tops (h_{thin}). $h_{c,B0}$ is also indicated for comparison.

In EHL regime, for $\eta_0 u_e = 3.1 \times 10^{-2}$ Pa.m, the value of h_{thick} is close to the maximal central film thickness of B1 and to the B0 central film thickness. However in mixed regime (see Fig3.5a-c), h_{thick} is higher than the B0 central film thickness. This situation is also illustrated in Fig. 3.5e, which shows the central 1D-profile of film thickness at $\eta_0 u_e = 7.8 \times 10^{-4}$ Pa.m (mixed regime − interferogram Fig. 3.5a). In this case, the B0 central film thickness is equal to 18 nm. The color-filled surface corresponds to the bulk of the ball and the disc is located at the zero altitude. This 1D-profile also points out the existence of two constriction zones at the front and at the rear of the widest top groove. These two constrictions entrap the fluid in the middle of the groove top, forming a dimple, i.e. a thicker film. Such a shape is typical of the squeeze effect induced by the transient term $\partial\rho h/\partial t$ in the Reynolds' equation generating a pressure peak at the constriction location. This dimple is equivalent to the smooth region located between a groove or a cavity, and the contact outlet. Indeed, the smooth region exhibits upstream a constriction directly linked to the presence of the texture (micro-EHL) and so does the dimple. Downstream the smooth region, a second constriction occurs corresponding to the constriction of the macro-EHL contact. Such cases have been reported in the literature. For example, Wedeven and Cusano [76] experimented a single transverse groove passing through the EHL contact in pure sliding (stationary smooth surface). Later Mourier et al. [96] investigated this phenomena, experimentally and numerically with a cavity at $\Sigma = 50\%$. They both reported an increased film thickness, between their surface feature and the constriction zone, suspecting pressure modifications to be the cause. This is in agreement with the observations shown in Fig. 3.5. Here, the squeeze contribution is local, occurring at the scale of the groove width. The physical principle of the dimple formation is a pressure collapse at the edges of the zone: such a pressure variation is probably caused here by the two groove bottoms, respectively at the front and at the rear of the wide top. The dimple can be explained by a micro-EHL effect similar to the pressure drop that leads to the constriction zone in EHL. The groove depth should then play a role in the dimple formation. No dimple occurs with neighboring grooves. Even if the groove depth induces sufficient pressure variations, the two constrictions are too close to each other on narrow groove tops to leave enough space for a dimple to be formed. The dimple formation at the widest tops persists in mixed regime

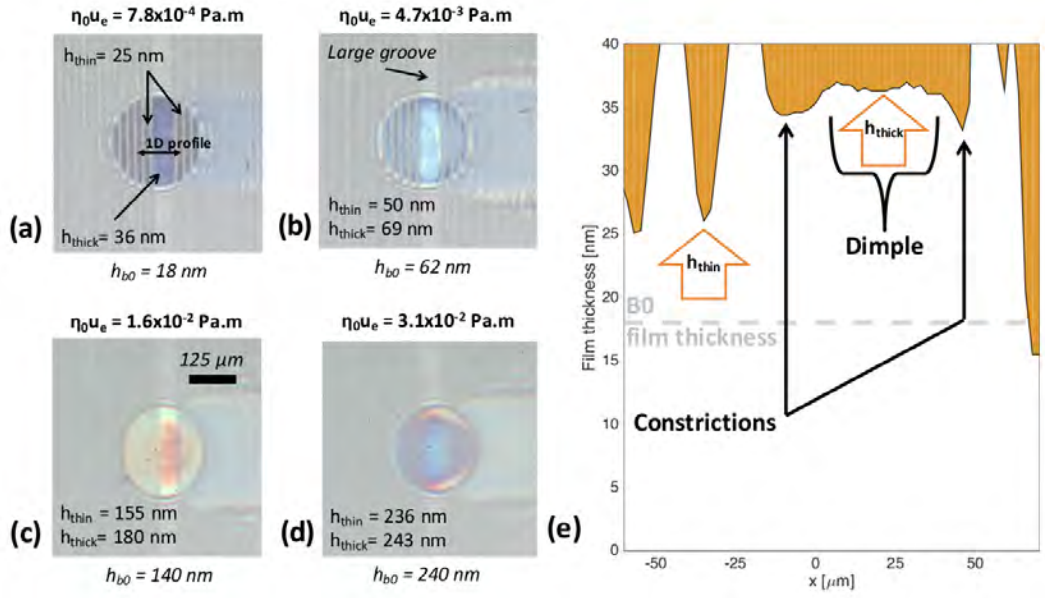

Figure 3.5: Interferograms of the lubricated contact formed between the disc and ball B1 with a wide groove top at several entrainment speeds (a-d) and 1D central profile of the film thickness at $\eta_0 u_e = 7.8 \times 10^{-4}$ Pa.m (e).

and allows a better separation of the surfaces resulting in a lubricant film locally thicker than that formed between smooth surfaces, as shown in Fig. 3.4b.

Combining Fig. 3.4a and Fig. 3.1b using the same origin of the ball position, the ratio $h_{c,B1}/h_{c,B0}$ in EHL at $\eta_0 u_e = 3.1 \times 10^{-2}$ Pa.m is plotted versus the groove top width in Fig. 3.6. The curve is split in two parts around the critical top width value of 12-13 μm emphasized by a vertical dash line. Below this critical width value, the ratio decreases when the top width decreases, meaning that the central film thickness formed with ball B1 diminishes compared to that formed with the smooth ball B0. Above, the ratio is constant and equal to 100%, meaning that the central film thickness of B1 is similar to that of B0 in EHL. Fig. 3.6 is also in agreement with the following physical tendency: when the top width tends to the wavelength, the groove surface tends to a smooth surface and so the ratio $h_{c,B1}/h_{c,B0}$ is expected to tend to 100%. In addition, the case illustrated in Fig. 3.5d is in agreement with the existence of a critical width of 12-13 μm since the widest groove top width is of 47 μm and the narrow groove tops are of 8 μm. It also points out the weak influence of dimple on the film formation capability in EHL regime, the maximum film thickness ratio remaining close to 100%.

To sum up, the passage of grooves with wide tops (wider than 12-13 μm) does

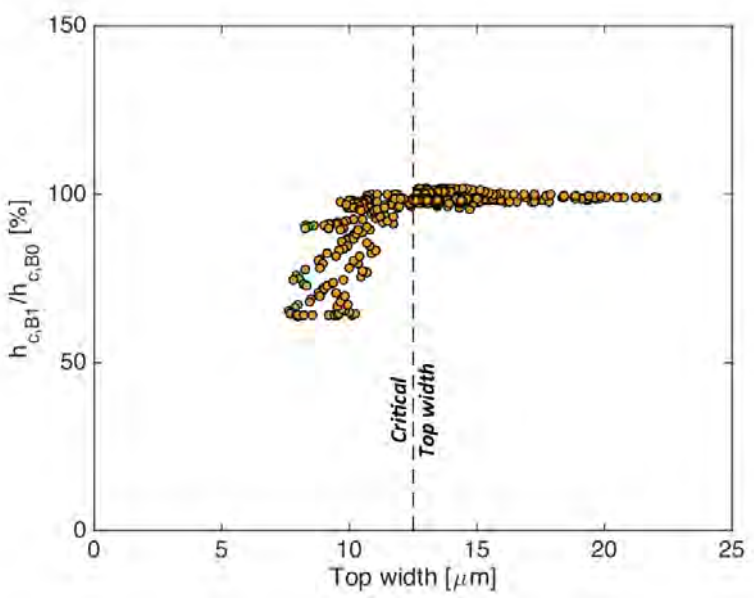

Figure 3.6: Ratio of the central film thickness formed in EHL regime with balls B1 and B0 at $\eta_0 u_e = 3.1 \times 10^{-2}$ Pa.m versus the groove top width. A critical top width below which the ratio starts decreasing, can be defined.

not modify the central film thickness in EHL. On the contrary, the passage of grooves with narrower than 12-13 μm decreases the central film thickness and significantly reduces the minimum film thickness, leading to asperity contacts. Several authors [77, 112, 79, 81, 80] reported that transverse roughness surfaces reduce the minimum film thickness to a larger degree because of side leakage. Moreover since the groove tops are narrower, i.e. the groove bottoms are wider, the fluid flow over the contact through these channels becomes easier. Finally, the ball B1 which surface texturing combines narrow and wide groove tops, leads to a film thickness transition shifted to higher $\eta_0 u_e$.

In mixed lubrication regime, transverse grooves with wide tops produce a dimple due to transient effects, in which the lubricant is trapped and forms locally a thicker film. Transverse grooves with narrow tops still decrease the film thickness.

3.3.3 EHL friction

The average viscous shear stress was determined over one ball rotation. The angular distribution of the shear rate was calculated from the angular distribution of the central film thickness in Fig. 3.4a. This gives the corresponding angular

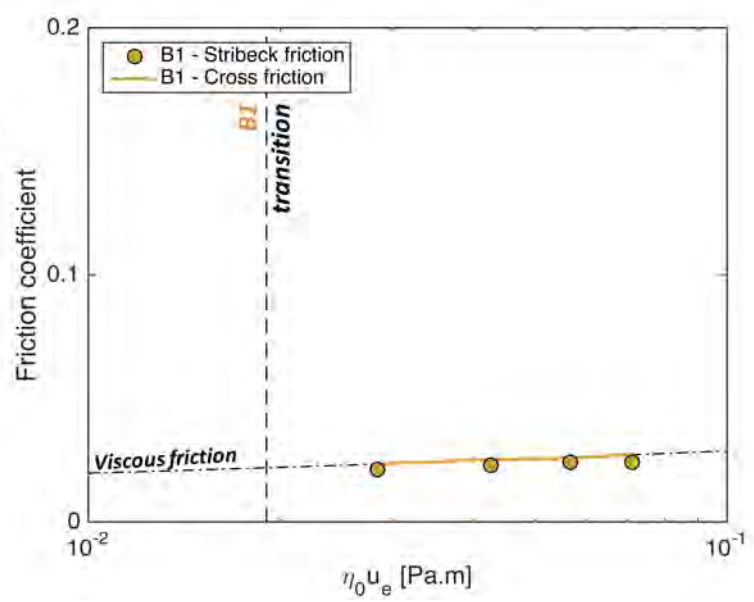

Figure 3.7: Viscous friction prediction for groove surface B1 assuming the lubricant under pressure follows a Cross law (see Eq. 2.54). These theoretical results are compared to friction measurements from Stribeck experiments in EHL.

distribution of the under-pressure fluid Cross-like rheology. These calculations were made for EHL entrainment speeds equal to 0.2, 0.3, 0.4 and 0.5 m/s. The contribution of the flow of the fluid trapped in the groove depth was neglected in the shear stress calculation. The film thickness evolution plotted in Fig. 3.4a ($h_{c,B1}/h_{c,B0}$) is supposed to remain valid over the EHL regime. Fig. 3.7 reports the viscous friction due to the shearing of the pressurized lubricant, which viscosity is given by a Cross law (continuous line) and the experimental data (dots) versus $\eta_0 u_e$ product. The friction error is of 0.002 for ball B1. The viscous friction calculated from B0 in Fig. 3.2 is reminded for comparison. The viscous model applied with B1 ball superimposes the smooth viscous friction and predicts accurately the friction for a transverse groove surface although the shear rate was determined from the film thickness between the groove tops and the disc. This confirms that the possible contribution of lubricant flow inside the groove bottoms can be neglected. The EHL friction due to fluid shearing averaged over multiple rotations is not impacted by the presence of transverse grooves

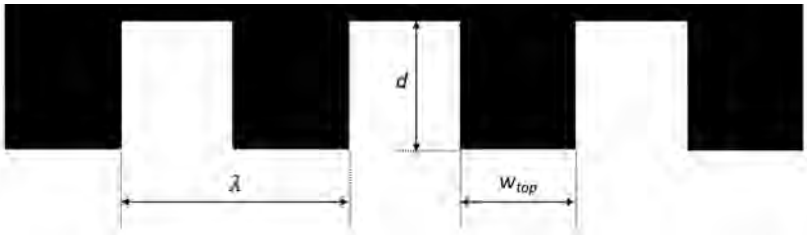

Figure 3.8: Scheme of the groove surface used in the numerical simulations.

3.4 Numerical transverse grooves

The numerical model presented in the previous chapter is used to simulate Stribeck curves at $\Sigma = 8\%$ for transverse periodic grooves in EHL. Fig. 3.8 shows the scheme of the grooves used in the numerical simulations. They are mathematically modeled with a λ-periodic step function:

$$r(x,t) = d.\Phi\left(x - u_2 t - w_{top} \mod \lambda\right) , \tag{3.1}$$

where Φ is the Heaviside function, w_{top} the groove top width, d the groove depth and λ the groove wavelength. Experiments have pointed out the key role of the groove top width and the possible influence of the groove depth. The goals of these numerical simulations are to investigate the effect of the coupling between the groove depth and the top width on the EHL friction, and to state upon the existence of micro-EHL friction, studying the pressure inside the contact. As the next chapter deals with lower wavelength textures (ripples), the effect of the wavelength is not studied here. The wavelength value is taken equal to that of the groove surfaces studied in the experiments: $\lambda = 25$ µm.

The EHL equations were solved over the domain $X \in [-2.5, 1.5]$ with a mesh of 512 nodes, $\Delta T = \Delta X$. The tolerance was set to 1.0×10^{-10} and $\xi = 1.0 \times 10^{-2}$. In addition, the operating conditions, the materials and lubricant properties were the same as those used in the groove experiments. Since $\lambda = 25$ µm, $w_{top} \in\ ]0, 25]$ µm. The groove depth varied from 50 nm to 200 nm. Thus, it remains of the same order of magnitude as the film thickness and the experimental grooves. Simulations were run for $d = \{50, 100, 150, 200\}$ nm and $w_{top} = \{5, 10, 20\}$ µm and for operating conditions such as: $\eta_0 u_e \in [1.0 \times 10^{-2}, 1.0 \times 10^{-1}]$, since the experimental groove transition occurred at $\eta_0 u_e = 1.9 \times 10^{-2}$ Pa.m. If asperity contact occurs, i.e. $\exists\ x, h(x) < 0$, the result is not taken into account.

First the convergence of the line contact model with groove surfaces is studied. Second, the experimental central film thickness is compared to numerical results. This validation allows us to discuss the onset of the film thickness transition, the EHL shear stress and the nature of the mixed/EHL regime transition.

3.4.1 Calculation convergence

The numerical model starts solving a steady-state solution from which a transient one is computed. According to Eq. 3.1, the grooves are already in the contact at $t = 0$. Thus, the first time steps of the code correspond to a transient state: from a stationary ball to a moving ball. Here, we focus on the steady-state reached when the ball moves at constant velocity (as experiments did). In Fig. 3.9, the evolution of the dimensionless film thickness is plotted versus the time steps. This simulation corresponds to $\eta_0 u_e = 1.0 \times 10^{-1}$ Pa.m with $d = 150$ nm and $w_{top} = 10$ µm. As expected, the simulation needs a number of time iterations (here ≈ 300) to converge to the mean final value displayed in dash line. The additional oscillation is due to the periodicity of the groove. Indeed, this signal has a periodicity of 28-29 time steps which corresponds to 0.05 ms. When the textured surface is moving at the velocity $u_2 = 0.5$ m/s, the dwell time of one groove defined as the period of the pattern shown in Fig. 3.8 is $\lambda/u_2 = 0.05$ ms. Similar trends were observed for other $\eta_0 u_e$ values and other geometries. As a conclusion, 500 time steps are run for the simulation of the lubrication of contacts involving groove surfaces in order to ensure this convergence. In the following, the calculated values will be an average over the last hundred time steps to take into account the oscillation due to the groove periodicity.

3.4.2 Central film thickness

Groove depth and top width influence

The central film thickness, as defined in experiments, is determined from the simulations: it corresponds to the average distance between the groove tops and the disc in the central zone of the contact. Results for various groove geometries are plotted versus $\eta_0 u_e$ in Fig. 3.10a-d. They respectively correspond to groove depths 50, 100, 150 and 200 nm. In each figure, the groove top width varies: $w_{top} = 20$, 10 and 5 µm. The lubricant film thickness calculated for the smooth ball B0 is highlighted in bold line. The wavelength λ of the groove surfaces being kept constant at 25 µm, the smooth ball can be regarded as a groove surface such as $w_{top} = \lambda = 25$ µm. The central film thickness measured for the transverse groove B1 is reported for comparison and its mixed/EHL transition is emphasized in dash line. Experimentally, the maximal central film thickness was obtained for shallow grooves (< 50 nm) according to Fig. 3.1b-d and 3.4 and these data are displayed in (a). Similarly, the minimal central film thickness is obtained for deeper grooves (≈ 200 nm) and it is plotted in (d).

Fig. 3.10a shows that the groove top width has a small influence on the central

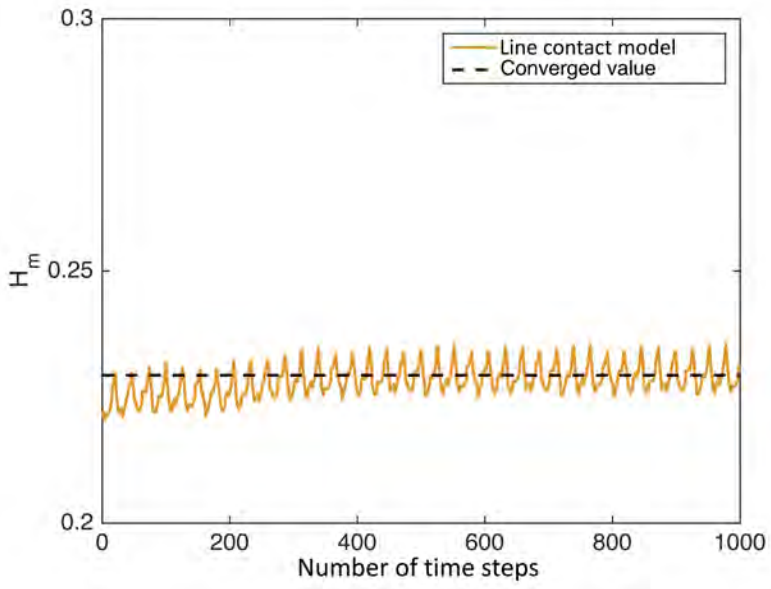

Figure 3.9: Dimensionless film thickness versus the number of time steps for $\eta_0 u_e = 1.0 \times 10^{-1}$ Pa.m, $d = 150$ nm and $w_{top} = 10$ µm. The mean converging value is highlighted (dotted line).

film thickness, for shallow grooves ($d = 50$ nm). Yet increasing, the groove depth enhances the influence of the groove top width as Fig. 3.10b-d illustrate. The central film thickness obtained with groove surfaces is always smaller than that calculated for a smooth surface and the wider the groove top, the closer to the smooth film thickness. In fact, when $w_d = 25$ µm, the groove surface is equivalent to a smooth surface. When $w_d \to 0$, the groove surface is made of very thin peaks. From Fig. 3.10a-d, the worst lubrication (i.e the lowest lubricant film thickness) occurs for $d = 200$ nm and $w_{top} = 5$ µm. Thus, textured surfaces with deep grooves having narrow tops have the worst lubrication efficiency.

In Fig. 3.10a the B1 maximal central film thickness is compared with the numerical simulations. A good agreement is found above the mixed/EHL transition: the shallow and large grooves do not modify significantly the central film thickness. In Fig. 3.10d, above the mixed/EHL transition, the B1 minimal central film thickness is located between the central film thickness calculated for grooves with $w_{top} = 5$ µm and that calculated for grooves with $w_{top} = 10$ µm. Fig. 3.1b shows that the narrowest groove top is around 10 µm wide and is about 200 nm deep (cf. Fig. 3.1d). Thus experiments and numerical simulations are in good agreement.

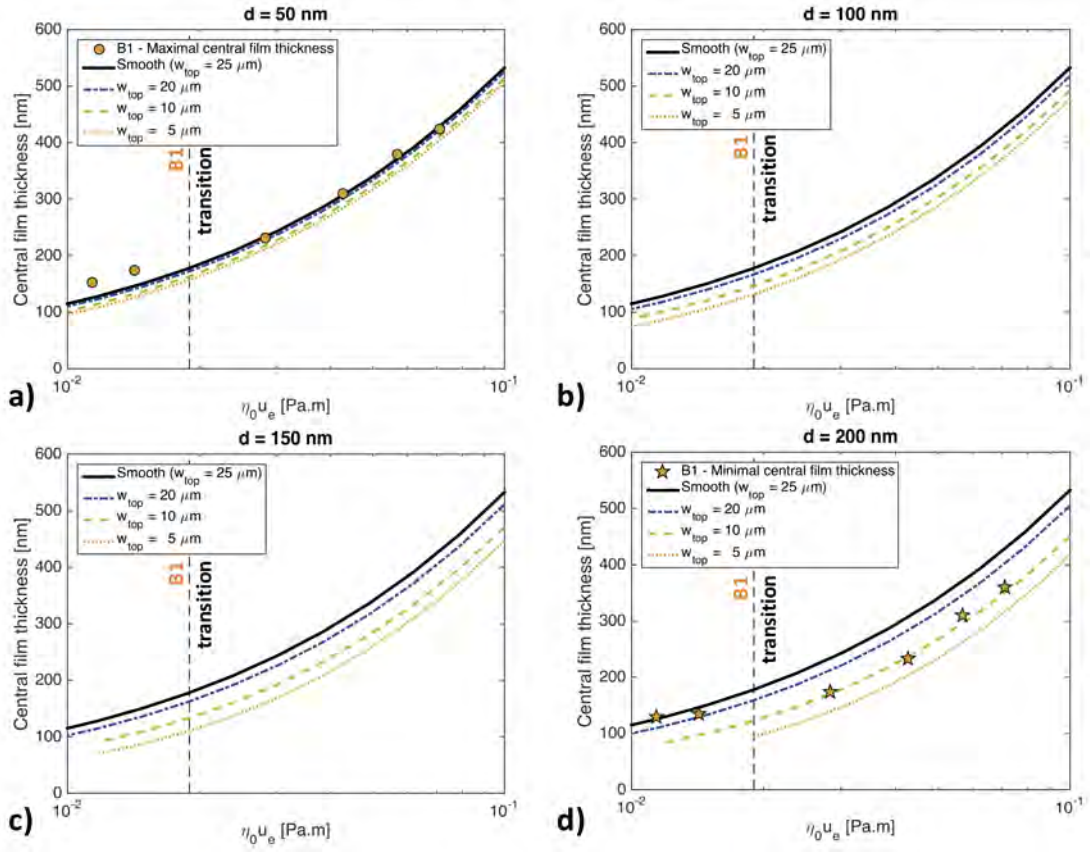

Figure 3.10: Central film thickness of groove surfaces versus $\eta_0 u_e$. The grooves have depths, $d = 50$ nm (a), 100 nm (b), 150 nm (c) and 200 nm (d). For each depth various top widths, $w_{top} = 20$ μm, 10 μm and 5 μm are analyzed. Smooth central film thickness is displayed in bold line. B1 experimental maximal and minimal film thickness results are respectively reported in (a) and (d) and its mixed/EHL transition is emphasized in dash line.

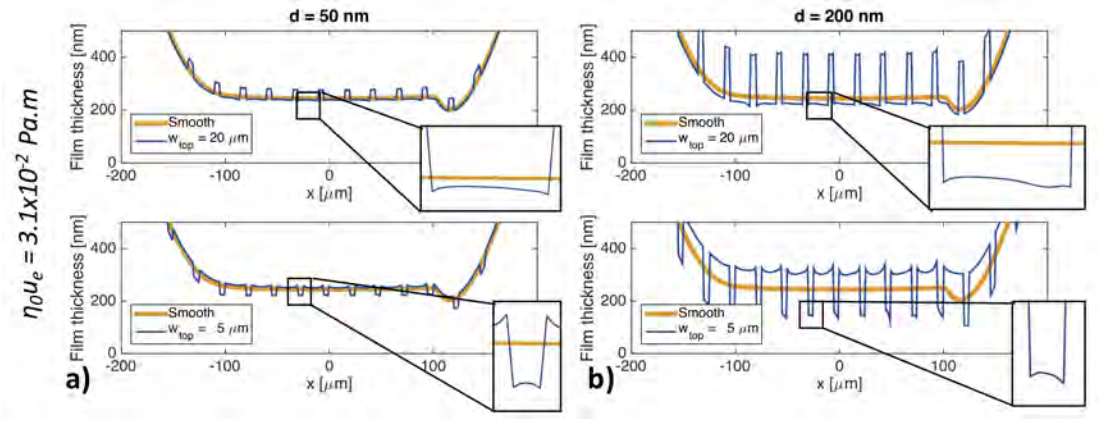

Figure 3.11: Film thickness profile of groove surfaces at 3.1×10^{-2} Pa.m. Two values of depth $d = 50$ nm (a) and 200 nm (b) were investigated. For each depth, two top widths $w_{top} = 20$ μm and 5 μm were studied. The smooth film thickness profile is displayed in bold line. A zoom of the film thickness at the groove tops illustrates the "dimple" effect.

Below the mixed/EHL transition, the experimental film thicknesses are higher than the numerical one, for the same groove geometry. For minimal central film thickness data, asperity contacts occur in the constriction region whereas the surfaces are fully separated for the maximal central film thickness data. This central film thickness difference may bear on the equivalent line contact description, which fluid mechanics neglects the contribution of the Poiseuille flow in the y direction. Under a certain film thickness, the pressure gradient $\partial p/\partial y$ may not be negligible in the film thickness calculation.

"Dimple" effect

The numerical film thickness profiles are reported for $\eta_0 u_e = 3.1 \times 10^{-2}$ Pa.m, i.e. in EHL regime Pa.m in Fig. 3.11a-b with groove depths respectively of 50 and 200 nm. In each plot, two top widths are displayed: $w_{top} = 20$ and 5 μm. The numerical smooth case is plotted for comparison.

Zooms of the film thickness profile at groove tops in Fig. 3.11a-d illustrate the "dimple" effect and emphasize a maximal film thickness at the center of the groove tops embraced by two constrictions at their edges. This confirms the occurrence of the "dimple" effect observed experimentally. Yet this does not lead to a film thicker than the one calculated for a smooth surface. For $\eta_0 u_e = 3.1 \times 10^{-2}$ Pa.m, the presence of grooves with wide tops do not modify much the central

	$d = 50$ nm	$d = 200$ nm
$w_{top} = 20$ µm	88%	91%
$w_{top} = 5$ µm	80%	96%

Table 3.2: Amplitude reduction of the grooves calculated from the film thickness profiles displayed in Fig. 3.11.

film thickness whereas grooves with narrow tops reduce it. This is in agreement with the experimental observations from Fig. 3.5d. Further comparison with Fig. 3.5a-c was not carried out as in the groove lubrication was in mixed regime.

In addition, the amplitude reduction defined as the ratio of the deformed groove amplitude A_d over the initial groove amplitude A_i, was measured and reported in Table 3.4.2. The model proposed by Lubrecht and Venner [86, 68, 69] predicts an amplitude reduction of 95% and underestimates the actual groove deformation. The difference may come from the fact that the amplitude reduction theory is based on sinusoidal surfaces.

Hence, the numerical model was able to correctly predict the central film thickness of the transverse grooves B1 at the locations of the widest and the narrowest groove, since the groove depth was known there. Elsewhere, the correlation between the top width and the groove depth is unknown. Thus, detailed comparisons between experimental and numerical central film thicknesses cannot be pushed further such as the existence of the groove top width critical value. Nonetheless, the influence of the groove top width on the lubricant film thickness experimentally observed is numerically confirmed, as well as the existence of a "dimple effect". The strong coupling between the groove depth and the groove top width has been pointed out.

3.4.3 Film thickness transition

As previously stated, the groove geometry strongly influences the central film thickness, i.e. the central clearance between the ball and the disc. In the following, the way it influences the minimum film thickness is investigated. As illustrated in the previous chapter, our model is not able to determine the minimum film thickness h_m in point contacts. Nevertheless, it provides a good approximation of the minimum film thickness on the central line $h_{c,m} = \min h(x, y = 0)$. The latter can then be used as an indicator of the absolute minimum film thickness since $h_m < h_{c,m}$. The minimum film thickness on the central line $h_{c.m}$ is then plotted in Fig. 3.12a-d versus $\eta_0 u_e$; the display is similar to Fig. 3.10a-d.

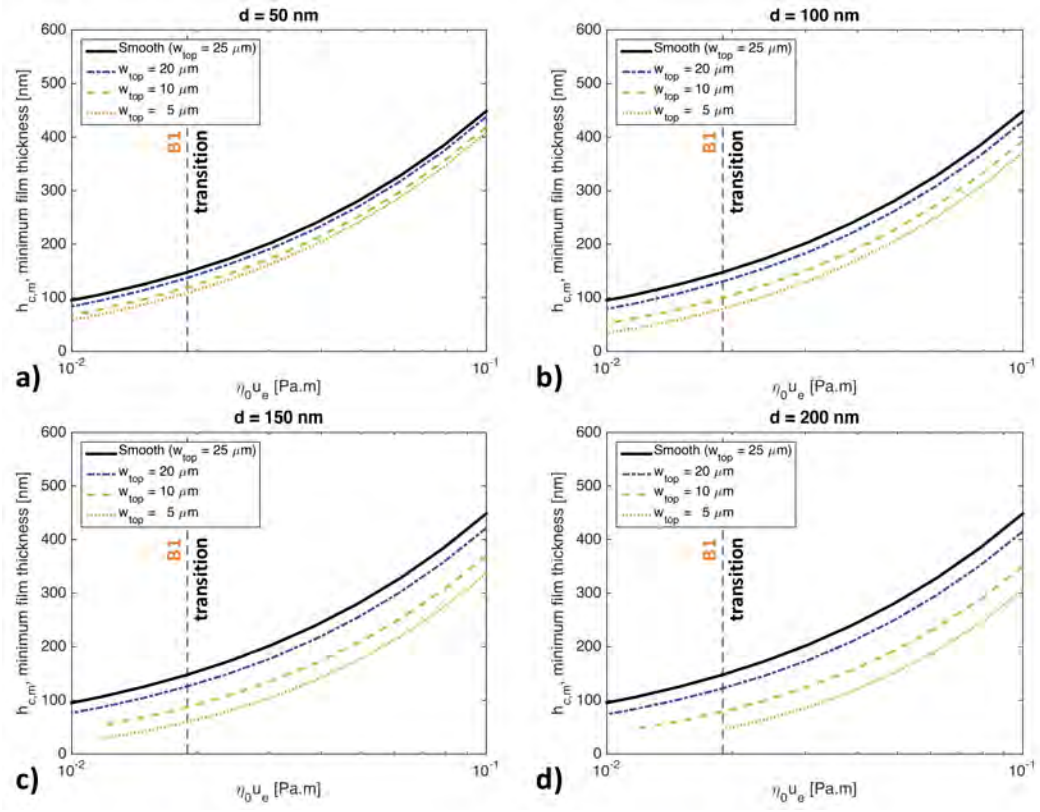

Figure 3.12: Minimal film thickness on the central line of groove surfaces versus $\eta_0 u_e$. The grooves have depths $d = 50$ nm (a), 100 nm (b), 150 nm (c) and 200 nm (d). For each depth various top widths, $w_{top} = 20$ μm, 10 μm and 5 μm are studied. The minimum film thickness for a smooth ball on the central line is displayed in bold line. The B1 mixed/EHL transition is emphasized in dash line.

As expected, Fig. 3.12a-d confirms that surfaces with narrow groove tops, reduce $h_{c,m}$ and so the minimum film thickness. This reduction is all the more important that the grooves are deep. Qualitatively, the groove geometry behaves similarly on h_c and h_m: deep grooves with narrow tops reduce their value. As a consequence, the onset of mixed regime determined from the film thickness transition is directly modified by the depth and the top width of the grooves. Since our model cannot determine quantitatively the minimum film thickness h_m, the $\eta_0 u_e$ value where the film thickness transition occur is not investigated.

3.4.4 Friction - Mixed/EHL transition

As the central film thickness strongly depends on the groove top width and depth, the EHL friction and the possible occurrence of micro-EHL was investigated regarding these parameters. Pressure profiles at $\eta_0 u_e = 1.9 \times 10^{-2}$ Pa.m (just above the mixed/EHL transition) are plotted in Fig. 3.13a-d, respectively for $d = 50$, 100, 150, and 200 nm. In each plot, two top widths are displayed: $w_{top} = 20$ and 5 µm. The numerical smooth pressure profile is reported in bold line for comparison.

Fig. 3.13 shows that the deep grooves with narrow top width increase the local pressure maxima reaching up to three time the maximal Hertzian pressure. Given the exponential relation in the Roelands' piezoviscosity law, one can expect that the important pressure variations induce huge viscosity modifications, synonymous of possible micro-EHL effects.

Therefore, the EHL friction coefficient was calculated (see Eq. 2.55) versus $\eta_0 u_e$ and plotted in Fig. 3.14a-d, following the display of Fig. 3.10a-d in terms of grooves geometry. The experimental friction coefficient of ball B1 is reported with dots (∘). The curves of Fig. 3.14 reveal that the EHL friction numerically calculated for grooves surface is always equal to that calculated for the smooth one, regardless of the groove geometries. As the texture of ball B1 is a combination of various groove geometries and as the latter do not influence the EHL friction, it is logical that the EHL friction, derived from numerical simulations, fits the experiments for $\eta_0 u_e$ values above the mixed/EHL transition.

In addition, the mean contact pressure p_m, i.e. the average pressure for $-a < x < +a$, was measured in each case: its difference between groove and smooth cases is around 0.1%. Thus, the pressure peaks observed in Fig. 3.13 have no substantial effect on the under-pressure viscosity: they are not responsible for the friction increase observed in the B1 experiments at the mixed/EHL regime transition.

Moreover it can be supposed that no micro-EHL phenomenon occurs in the

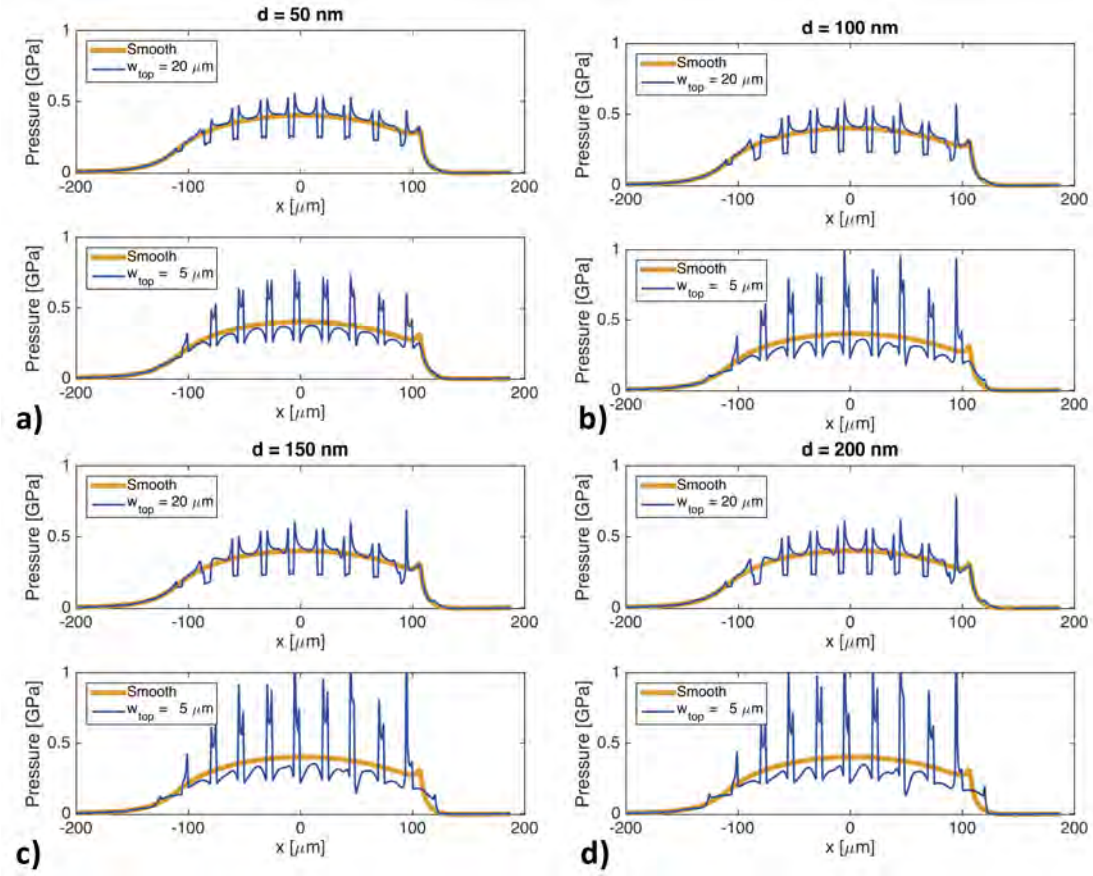

Figure 3.13: Pressure profile of groove surfaces at $\eta_0 u_e = 1.9 \times 10^{-2}$ Pa.m. i.e. in EHL regime. The grooves have various depths, $d = 50$ nm (a), 100 nm (b), 150 nm (c) and 200 nm (d). For each depth, two top widths, $w_{top} = 20$ μm and 5 μm were studied. The smooth pressure profile is displayed in bold line.

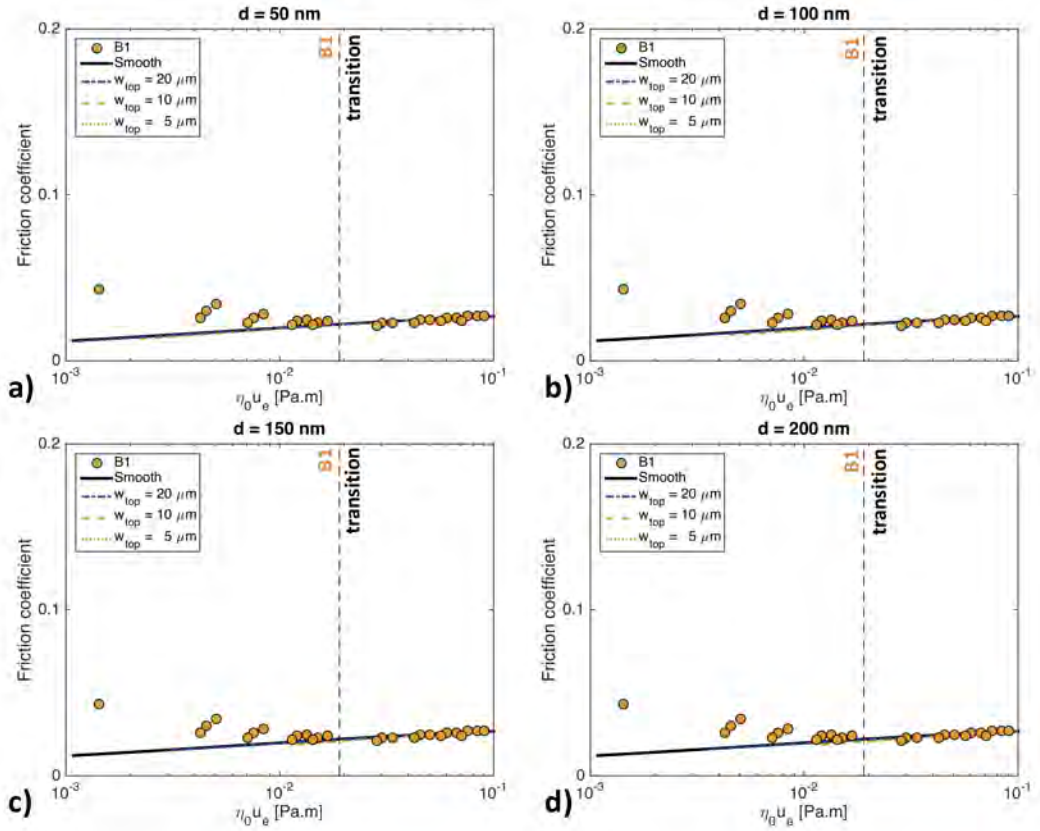

Figure 3.14: Calculated friction coefficient of groove surfaces versus $\eta_0 u_e$. The grooves have various depth, $d = 50$ nm (a), 100 nm (b), 150 nm (c) and 200 nm (d). For each depth, groove exhibit various top widths, $w_{top} = 20$ μm, 10 μm and 5 μm. Smooth friction is displayed in bold line. The experimental friction coefficient measured with ball B1 is plotted with (∘) symbols. The B1 mixed/EHL transition is emphasized in dash line.

contact since the friction of the grooved ball well superimposes the friction of the smooth regardless of $\eta_0 u_e$. The mixed/EHL transition is then due to the onset of asperity contacts. Thereby, the mixed/EHL regime transition is the same as the film thickness transition for transverse grooves. Below this mixed/EHL transition, the numerical results did not predict asperity contact. Thus the numerical friction is lower than that measured for ball B1 which increases.

In addition, the fluid flow inside the grooves is taken into account to compute the shear rate in the numerical simulation of the friction coefficient in EHL. On the contrary, the prediction of the viscous friction coefficient based upon the lubricant film thickness measurements and a Cross law to describe the lubricant viscosity (see Eq. 2.54), has neglected this contribution because it was not possible to measure the film thickness in the grooves. Yet good agreements were found between the measured EHL friction coefficient and the experimental EHL friction coefficient prediction. This would suggest that the lubricant shearing inside the groove does not contribute significantly to the overall friction in EHL regime. Nevertheless, this conclusion cannot be generalized without any caution, as will be shown in Fig. 3.15. The latter presents the evolution of the EHL friction coefficient calculated from numerical simulations, neglecting the lubricant flow inside the grooves, for $d = 50$ nm, $w_{top} = 20$ µm and for $d = 200$ nm, $w_{top} = 5$ µm. As above-mentioned, these two grooves geometries respectively correspond to the widest and narrowest tops of B1. The experimental friction of B1 is reported with dots (∘) in the same figure for comparison.

For $d = 50$ nm, $w_{top} = 20$ µm, neglecting the lubricant shearing inside the groove keeps providing the same friction prediction as in Fig. 3.14. However, this is not anymore valid for $d = 200$ nm, $w_{top} = 5$ µm, which friction prediction is higher in comparison to Fig. 3.14. In the latter case, as the wavelength of the grooved pattern is constant and equal to 25 µm, then the groove bottom is 20 µm wide. Thus, when w_{top} decreases from 20 µm to 5 µm, the area over which low shear rates occur is multiplied by 4. Besides, the oil film being thicker and the lubricant viscosity decreasing because of the decrease in pressure, the viscous shear stress is significantly lowered in the grooves. Therefore, the contribution of viscous flow of the lubricant inside the grooves is dominant. All these arguments qualitatively explain why the calculated EHL friction coefficient becomes higher than it should be, when the lubricant shearing in the grooves is neglected.

Moreover in the experiments, the B1 texture is a combination of wide and narrow tops, so does the associated experimental EHL friction coefficient. Wide grooves (i.e. shallow grooves) predominate on B1 track and so does their experimental friction. At this stage, it is unclear whether or not neglecting the thickness inside the groove is physically meaningful. This issue will be addressed again with

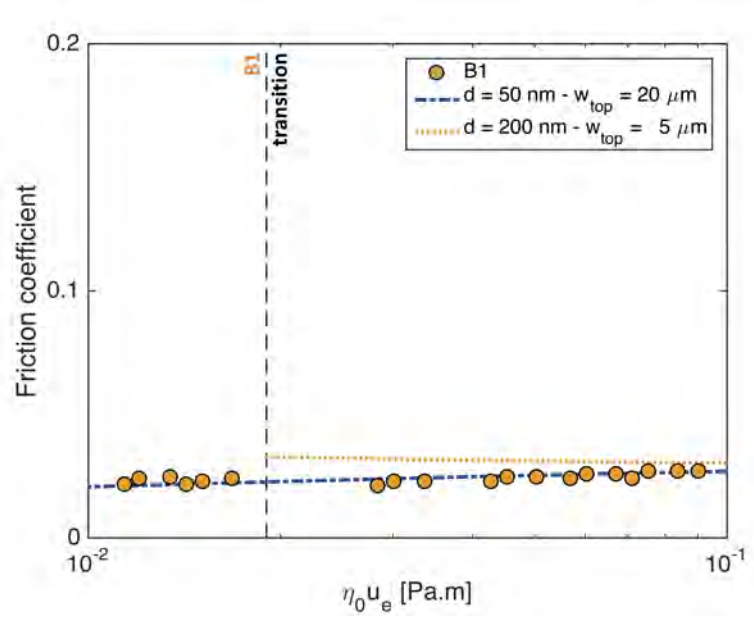

Figure 3.15: Evolution of the friction coefficient, calculated from numerical simulation by neglecting the shearing stress due to the viscous lubricant flow inside the grooves, versus $\eta_0 u_e$. Two groove surfaces are considered: $d = 50$ nm, $w_{top} = 20$ µm and $d = 200$ nm, $w_{top} = 5$ µm. Experimental friction of B1 is reported as well as its mixed/EHL transition.

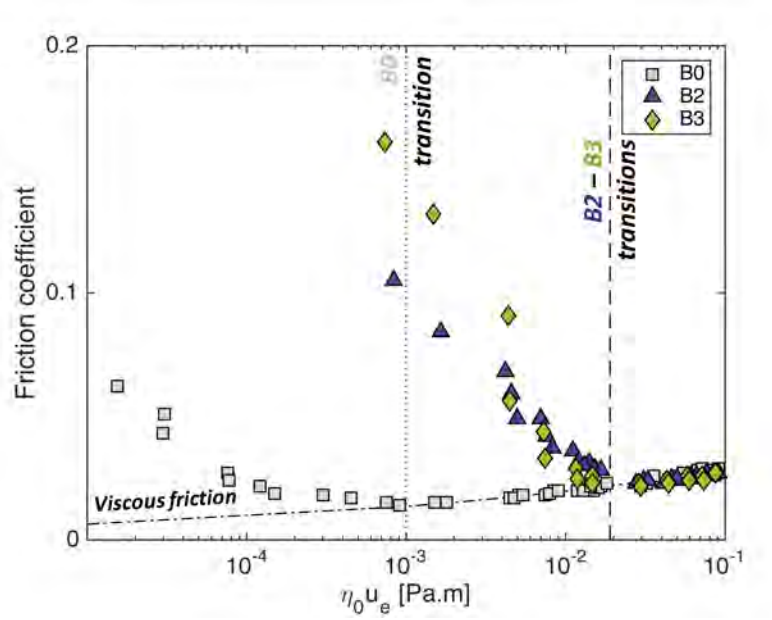

Figure 3.16: Stribeck curves of the smooth surface B0, B2 and B3 at $|\Sigma| = 8\%$, highlighting the mixed/EHL regime transitions and pure viscous friction level.

longitudinal grooves as their track exhibits a larger proportion of narrow tops.

3.5 Experimental longitudinal grooves

3.5.1 Mixed/EHL transition

The Stribeck experiments of Fig. 3.16 show that, the friction and the mixed/EHL regime transition occur at $\eta_0 u_e = 2.1 \times 10^{-2}$ and 1.9×10^{-2} Pa.m, for the two longitudinal groove surfaces, B2 and B3, respectively. The EHL friction values superimpose with those obtained for the smooth surface B0. If the transition remains very close for the groove surfaces, the increasing rate of the friction differs in mixed regime from one surface to another; this point will be discussed later in detail.

3.5.2 Film thickness transition

The lubricant film thicknesses formed with balls B2 and B3 are reported in Fig. 3.17. Because of the presence of grooves - the gap between the groove bottoms

and the disc (resp. groove tops) appear in gray (resp. in color) - , the central film thickness was measured according to the same procedure as that used with ball B1. Fig. 3.17a shows the ratio of the central film thickness measured for balls B2 and B3 over the central film thickness measured for smooth ball B0 versus the angular position of the ball, at $\eta_0 u_e = 3.2 \times 10^{-2}$ and 3.1×10^{-2} Pa.m respectively, i.e. in EHL regime. The ratio of $h_{c,B2}/h_{c,B0}$ is constant at 100% until the angular position of 100°, then it collapses to 43% for the next 150°. The B3 ratio is also roughly constant at 95% until 100° then it drops to 46% for nearly 180°. Fig. 3.17b-c present the evolution of the film thickness distribution (blue and green bold lines), maximal and minimal central film thickness as a function of $\eta_0 u_e$, respectively for B2 and B3. Corresponding interferograms are displayed beside. The maximal (minimal) central film thickness formed with grooved balls B2 and B3 is close to (thinner than) the central film thickness formed with ball B0. It is noteworthy that the film thickness transition is once again detectable on Fig. 3.17b-c and that its value is in agreement with the friction transition determined from the Stribeck curve.

The difference of the maximal and minimal film thickness seems random. For the same reasons as B1, the error and the camera resolution do not allow to conclude on this difference in EHL and mixed regimes.

In mixed regime, the maximal central film thickness of longitudinal groove balls B2 and B3 is below the one of transverse groove ball B1. Thus, the groove orientation clearly affects the lubrication capability in the mixed regime, transverse grooves being more effective than longitudinal grooves. This result in agreement with the literature [75, 76, 67, 77, 113, 114, 115] where authors report lower film thickness with longitudinal roughness than with transverse roughness.

No hard evidence of dimple formation was found for longitudinal grooves. The reason simply relies in the transient Reynolds equation, which correctly describes the present experiments:

$$\frac{\partial}{\partial x}\left(\frac{\rho h^3}{12\eta}\frac{\partial p}{\partial x}\right) + \frac{\partial}{\partial y}\left(\frac{\rho h^3}{12\eta}\frac{\partial p}{\partial y}\right) = u_e\frac{\partial \rho h}{\partial x} + \frac{\partial \rho h}{\partial t} \ . \tag{3.2}$$

For model longitudinal grooves, the topography "viewed" by the contact is not time-dependent. Thus, the EHL film thickness is not function of time anymore and the local squeeze effect contained in the term $\partial\rho h/\partial t$ does not longer exist for longitudinal groove surfaces.

The ratios $h_{c,B2}/h_{c,B0}$ and $h_{c,B3}/h_{c,B0}$ are plotted in Fig. 3.18 versus the respective groove top width, both in EHL at $\eta_0 u_e = 3.2 \times 10^{-2}$ and 3.1×10^{-2} Pa.m. For ball B2, the film thickness is constant, close to the B0 central film thickness for top width larger than a critical value as illustrated in Fig. 3.17.

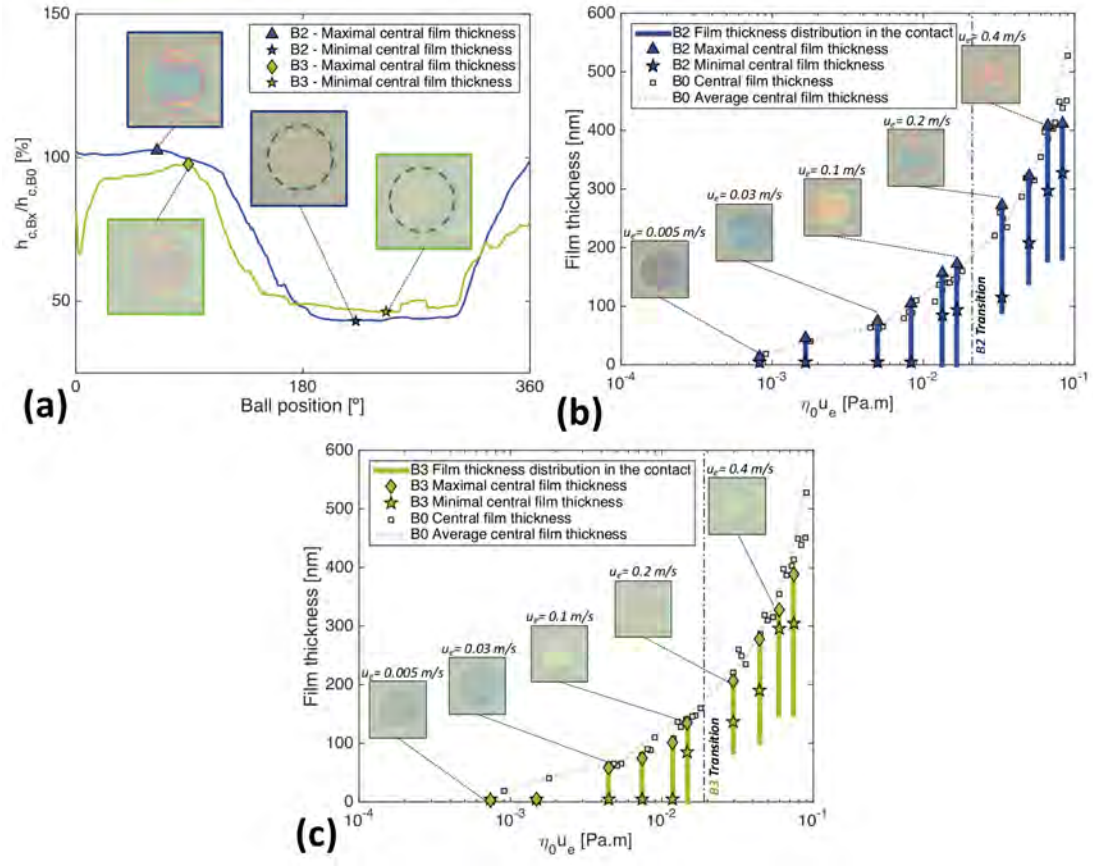

Figure 3.17: Ratio of central film thicknesses of B2 (blue line) and B3 (green line) over B0 respectively at $\eta_0 u_e = 3.2 \times 10^{-2}$ and 3.1×10^{-2} Pa.m along one ball rotation (a) and film thickness of the B2 Stribeck experiments (b) and B3 Stribeck experiments (c) vs. $\eta_0 u_e$ with corresponding 125-μm-radius contact interferograms. The contact edges are stressed with a dash line in the contact interferograms.

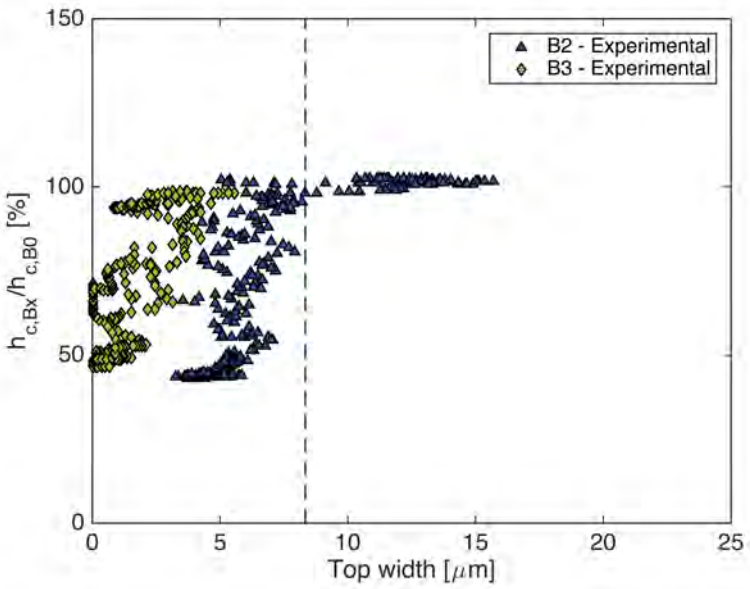

Figure 3.18: Ratio of the central film thickness formed with balls B2 and B3 over that formed with the smooth ball B0 at $\eta_0 u_e = 3.2 \times 10^{-2}$ and 3.1×10^{-2} Pa.m versus their respective groove top width. A critical top width - indicated by the gray dash line - below which the ratios start decreasing, can be defined.

Below this critical value, the film thickness ratio decreases to 40-45%. This critical value is of 8-9 μm. For ball B3, most of the points are gathered in the decreasing part of the plot since top widths are very narrow, beneath 5 μm. The B3 ratio tends to the same minimum and maximum values as B2. For top width smaller than one third of the wavelength, the values of ratio are scattered. This means that the film thickness ratio may no longer be only function of the top widths for longitudinal grooves. Though the groove depth and the groove top width are not independent because of the LASER texturing process (see Fig. 3.1), the way how they are correlated might not be quantitatively the same for balls B2 and B3. This shows, that as for the transverse grooves, the groove depth may have a significant impact on the lubrication process.

3.5.3 EHL friction

This detailed film thickness analysis allows one to apply the method developed for transverse grooves to calculate the viscous friction (see Section 3.4.4). Results are displayed in Fig. 3.19; the average errors are respectively 0.002 for ball B2 and 0.005 for ball B3. Thus the EHL friction coefficient is accurately predicted

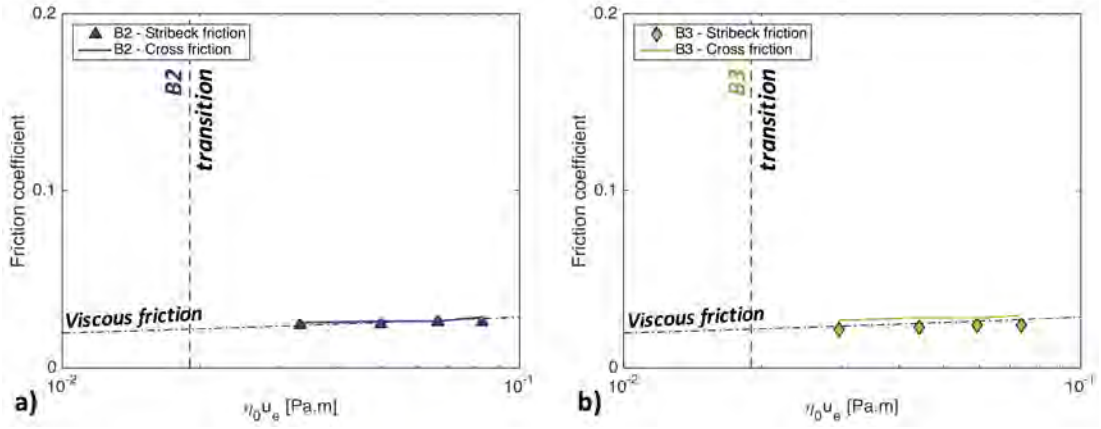

Figure 3.19: Viscous friction predictions for groove surface B2 and B3 assuming the lubricant under pressure follows a Cross law (see Eq. 2.54). These theoretical results are compared to friction measurements from Stribeck experiments in EHL.

for B2 and B3.

The EHL friction coefficient obtained for transverse and longitudinal groove surfaces is the same so the orientation has not impact on it. In the previous part, the physical relevance of neglecting the film thickness inside the groove in the friction prediction was discussed. It yielded that the B1 track is made of few grooves with narrow tops (i.e. few grooves with wide bottoms). Thus, their contribution to friction is not significant. This is confirmed by the experimental measurements. In the case of ball B3, the narrow grooves are predominant over the ball track and thus the film thickness of B3 is lower than that B1 and B0. If the shearing inside the groove was negligible then the EHL friction coefficient of ball B3 would be higher than that of B1 or even B0. Experiments show that the B3 friction remains the same and so the whole film thickness (inside and outside the grooves) is sheared and responsible for the friction dissipation in the contact.

3.6 Groove EHL lubrication mechanisms

Narrow and deep grooves reduce the film thickness whereas wide and shallow grooves do not affect it, for each groove orientation. The "dimple" effect is not very important in EHL for transverse groove, except when the groove tops are wide enough. Moreover, the mixed/EHL transition of transverse and longitudinal grooves is about the same. Therefore the lubrication mechanisms involved with

groove surfaces is supposed to be the same in EHL regardless of these two orientations. Thus the mixed/EHL transition of transverse and longitudinal grooves must be governed by the same physics. It has been shown that this transition is due to the onset of asperity contact therefore, to the increasing intimacy of the antagonist surfaces, i.e. to the reduction of the gap between them.

Carrying out experiments on longitudinal grooves, for $\lambda \in [19,\ 45\ \mu m]$, $d \in [490,\ 970\ nm]$, Guegan et al [87] found that the central average film thickness h_{av}, i.e. the average of both the film thicknesses inside and outside the grooves, was the same as the smooth surface, $h_{c,B0}$, for both $\Sigma = 0\%$ and 50%. Therefore, the grooves do not modify flow rate entering in the contact. As Fig. 3.20 illustrates, the more lubricant a groove can entrap, the closer its top and the disc are. Wider groove tops lead to higher film thickness than narrower one and the groove depth amplifies this phenomenon. Hence shallow grooves with wide tops result in thicker separation distance between the groove top and the disc than deep groove with narrow tops. Thus the relevant roughness parameter may be the total volume v_{groove} inside the grooves defined as:

$$v_{groove} = d \times (\lambda - w_{top}) \ . \tag{3.3}$$

This is investigated using the previous numerical simulations of transverse grooves. This volume correspond to the non-deformed surface. Since it is a line contact simulation, volumes corresponds to meter square. Fig. 3.21 reports the central average film thickness versus v_{groove} for five values of $\eta_0 u_e$ in EHL: 1.9×10^{-2}, 3.1×10^{-2}, 4.9×10^{-2}, 7.9×10^{-2} and 1.0×10^{-1} Pa.m. h_{av} is calculated over the similar window $-a/3 < x < +a/3$ as the experimental film thickness:

$$h_{av} = \frac{3}{2a} \int_{-a/3}^{a/3} h(x) dx \ . \tag{3.4}$$

The value of the smooth central film thickness is also reported ($\square$) for the same operating conditions.

For each $\eta_0 u_e$, h_{av} is higher than the central film thickness formed with a smooth ball. Moreover the groove volume increases h_{av} according to a linear function with the smooth central film thickness as the ordinate at the origin and the slopes slightly depend on $\eta_0 u_e$. In fact, when $v_{groove} \to 0$, the groove surface tends to a smooth one and in this case h_{av} is by definition equal to the central film thickness. As a consequence, the slopes of the linear relations are determined and plotted in dash lines in Fig. 3.21. The slopes δ are respectively 1.3×10^4, 1.1×10^4, 1.0×10^4, 1.0×10^4 and 1.1×10^4 m^{-1} for increasing $\eta_0 u_e$ in EHL. This linear approximation well fits the data. From Fig. 3.21, it can be inferred that the groove volume is a relevant key parameter to describe the lubrication efficiency

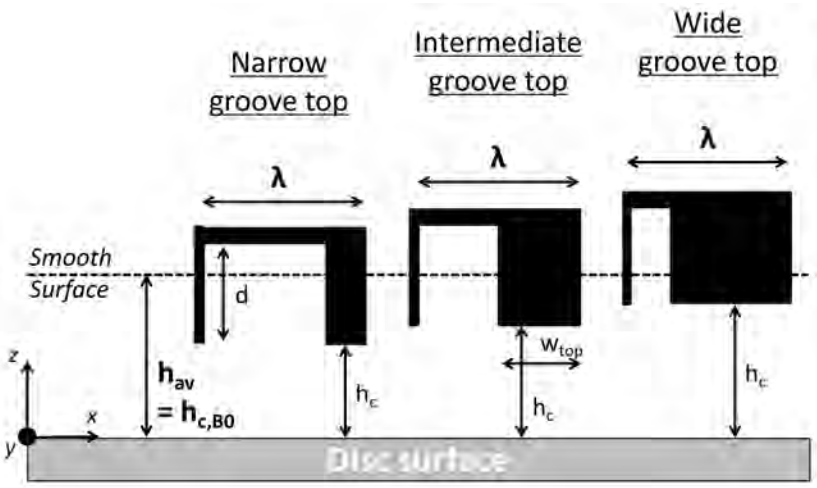

Figure 3.20: Schematic representation of the increasing gap between the groove top and the disc surface as the groove top becomes wider and wider according to experimental results from [87]. The fluid flows in the x direction.

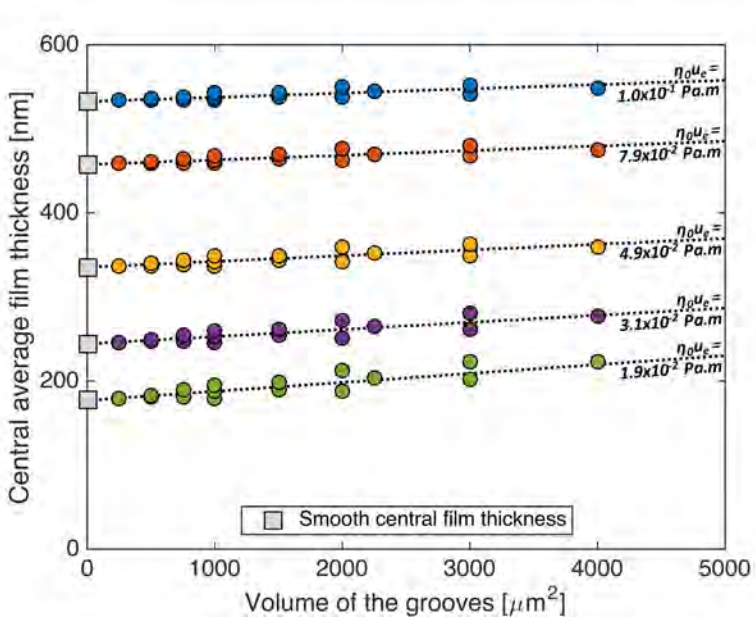

Figure 3.21: Numerical central average film thickness versus the volume of the grooves for five $\eta_0 u_e$ operating conditions and dash lines emphasize their evolution. The value of smooth central film thickness is also reported (□) for these $\eta_0 u_e$.

of the groove surfaces. Indeed it takes into account both groove top width and groove depth which were proved to be significant in groove EHL. Thus, the larger groove volume leads to a slight increase in the central average film thickness.

The consequences of v_{groove} on the central film thickness are now investigated. From Fig. 3.21, h_{av} can be approximated as:

$$h_{av} = h_{c,smooth} + \delta v_{groove} \ . \tag{3.5}$$

From Fig. 3.20 and the amplitude reduction, it also yields:

$$h_{av} = h_c + \frac{\frac{A_d}{A_i} v_{groove}}{\lambda} \ . \tag{3.6}$$

Thus:

$$h_c = h_{c,smooth} + \left(\delta - \frac{A_d}{A_i} \frac{1}{\lambda} \right) v_{groove} \ . \tag{3.7}$$

In the numerical simulations, $\delta \approx 1.0 \times 10^4$ m^{-1} while $1/\lambda = 4.0 \times 10^4$ m^{-1}. Therefore h_c will always be lower than the smooth central film thickness with such wavelength. To increase the film thickness with groove surfaces, the wavelength could be increased so that $\delta > \frac{A_d}{A_i}/\lambda$. The increase of the groove wavelength will also lead to a stronger elastic deformation [86, 68, 69] and so to the reduction of $\frac{A_d}{A_i}$. In addition, when the volume tends to 0, the equation 3.7 shows that the central film thickness tends to that of the smooth ball.

For the chosen wavelength, the mixed/EHL regime transition occurs because narrow tops prematurely decrease the distance between the ball and the disc, leading to a shift of the transition to higher $\eta_0 u_e$ values. Moreover, the narrowest tops of B1, B2 and B3 are of the same order (about few microns). Thus, the minimum film thickness over one rotation for the three balls is expected to be the same. This is confirmed by Fig. 3.4b and 3.17b-c. The regime transition resulting from the strong surface intimacy is likely to occur at the same $\eta_0 u_e$ value. As the portion of narrow tops in B1 and B2 is smaller than on B3, the B3 surface is, in average over a rotation, closer to the disc than B1 and B2. This may explain the friction difference observed in mixed regime. This will be tackled in the following part.

3.7 Mixed friction

Fig. 3.22a reports the friction coefficient of B1, B2 and B3 along one ball rotation versus the corresponding top width at respectively $\eta_0 u_e = 7.8 \times 10^{-4}$, 8.0×10^{-4}

and 7.7×10^{-4} Pa.m, corresponding to the mixed regime. The friction coefficient is clearly a decreasing function of the groove top width. The maximum friction coefficient is 0.2 and is reached with ball B3 when the groove top width is smaller than 5 μm. Meanwhile, the minimum friction seems to stabilize between 0.015 and 0.05 for ball B1 and wider groove tops. As narrower groove causes the film thickness drop, the reduction of the top width brings the ball and the disc closer, increasing the probability of asperity contacts and consequently the friction value. For each groove ball, the mixed friction is found to be higher as the tops get narrower, irrespective of the groove orientation.

In mixed regime, the contact area is supposed to be split into two zones: one works in EHL and the second works in boundary lubrication. Then the friction results from two major contributions: the shearing of the boundary layers, μ_{BL} and the shearing of the pressurized lubricant in EHL, μ_{EHL}. Mixed friction can be modeled as follows,

$$\mu = A_{\%}\mu_{BL} + (1 - A_{\%})\mu_{EHL} \ , \tag{3.8}$$

with $A_{\%}$ the percentage of the Hertzian contact area where asperity contacts occur between the ball and the disc.

In order to measure the boundary friction coefficient, friction experiments were carried out on IRIS tribometer with a smooth ball at $u_e = 0.005$ and 0.01 m/s. A droplet of oil was deposited on the ball surface and then wiped off before the experiment. From several tests at two different speeds, the boundary friction coefficient was measured at 0.26 ± 0.03. As expected, this value is much higher than the friction coefficient values measured with the smooth ball B0 plotted in Fig. 3.2.

From Eq.3.8, the theoretical value of $A_{\%}$ can be calculated: μ_{BL}=0.26 ± 0.03, μ_{EHL} is considered to be equal to that measured with ball B0 at the corresponding sliding velocity and μ is taken from data of Fig. 3.22a. Results are plotted in Fig. 3.22b versus the groove top width for balls B1, B2 and B3. The relative area of asperity contacts diminishes as the groove top width increases. Interferograms corresponding to maximal and minimal groove top widths are reported for the three groove surfaces. To measure the $A_{\%}$ of the grooved balls, the associated static contact was analyzed. From these interferograms, the distribution of the hue parameter of each pixel belonging to the contact areas was determined. The ratio of similar areas detected in a rolling/sliding contact over the total lubricated contact area gave the $A_{\%}$, with a relative error estimated at 2%. Nonetheless the static interferogram of B3 did not allow determining precisely the real contact area. The measured values of $A_{\%}$ are reported on each interferogram obtained with balls B1 and B2 in Fig. 3.22b. The predicted values of the asperity contact

area is in good agreement with these measurements. For ball B3, the dynamic contacts have qualitatively the same shape as the static contact one, thus even if $A_{\%}$ cannot be determined properly, it is likely to be high (over 50%).

The proposed friction model in mixed lubrication regime is able to describe the influence of grooves on the contribution of each component of contact, shearing of the EHL films and interfacial shearing of boundary film, through the asperity contact ratio, $A_{\%}$. The effect of groove orientation does not appear in the model, confirming that the groove orientation is negligible in mixed lubrication friction.

3.8 Conclusions

Experiments were carried out with transverse and longitudinal grooves. They pointed out the influence of the groove top width upon the lubricant film thickness. Narrow groove tops decrease the distance between the ball and the disc whereas wide groove tops keep it the same as that formed with a smooth surface. As a result, the first asperity contacts happen at higher $\eta_0 u_e$. No influence of the groove orientation was found in EHL.

Numerical simulations performed for various transverse grooves geometries, in terms of depth and top width, confirmed the key role of the groove width on the film-forming capability in EHL. They also emphasized the importance of the groove depth. Deep grooves reduce the distance between the ball and the disc while shallow keep it similar to that calculated with a smooth ball.

Using complementary approaches, the groove volume has been introduced as the product of the groove depth times the groove bottom width (equal to the wavelength minus the groove top width). This geometrical parameter has been able to explain the evolution of the average film thickness in the center of the contact. This has allowed us to demonstrate that the groove surfaces manufactured by LASER processing tends to decrease the separation between the ball and the disc. In addition, it theoretically shows that the increase in the groove wavelength should improve the lubrication efficiency.

Also, the grooves have no influence on the EHL friction which was accurately predicted using the viscous shear of a under-pressure Cross-like fluid. No micro-EHL phenomenon during the friction process for $\eta_0 u_e$ values at the neighbourhood of the mixed lubrication/EHL transition was evidenced. Therefore, the film thickness transition and the mixed/EHL transition are the same for the studied grooves.

Finally, in mixed regime the friction coefficient increases due to narrower

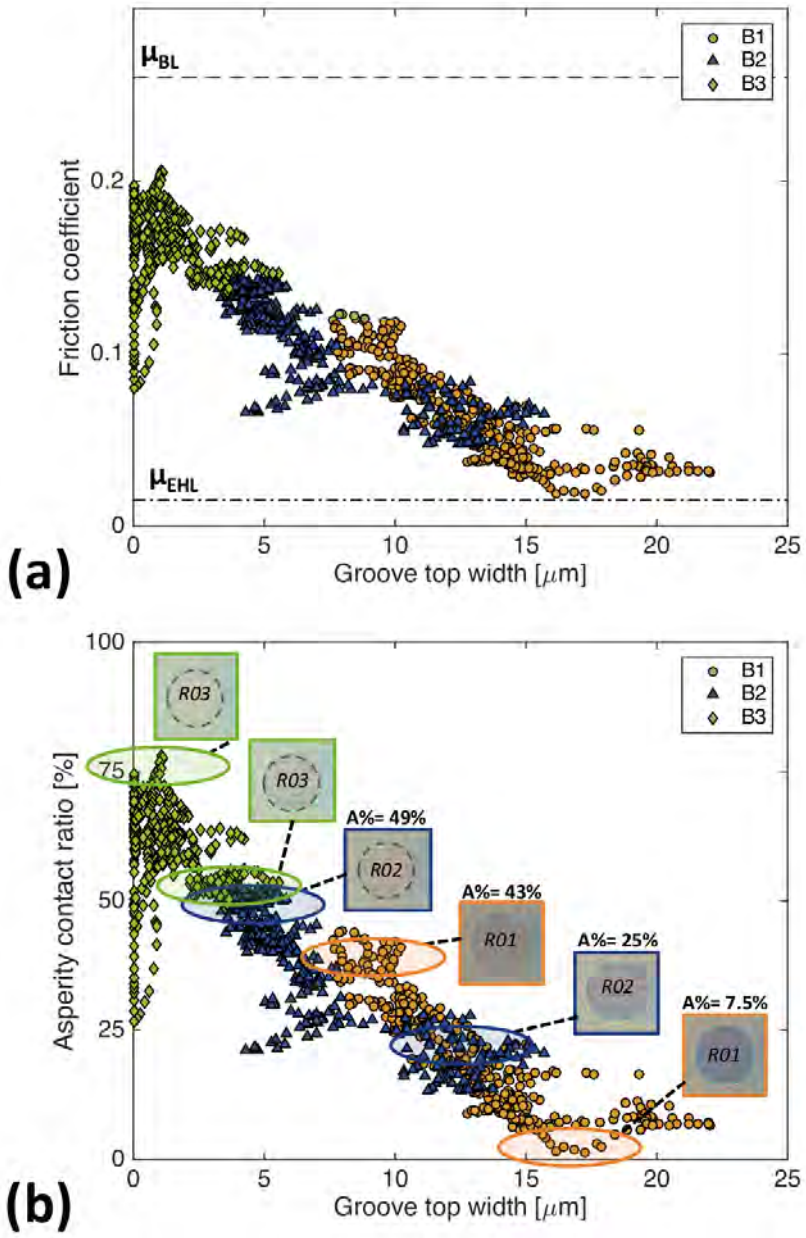

Figure 3.22: Friction coefficient measured with groove balls B1, B2 and B3 along one ball rotation vs. the groove top width, respectively at $\eta_0 u_e = 7.8 \times 10^{-4}$, 8.0 $\times$ 10^{-4} and 7.7 $\times$ 10^{-4} Pa.m, in the mixed lubrication regime, with emphasized μ_{BL} and μ_{EHL} (a) and theoretical asperity contact ratio ($A_{\%}$) vs. the groove top width compared with values of $A_{\%}$ measured on contact interferograms (b). The contact edges are stressed with a dash line in the contact interferograms.

groove tops. The latter induce a film thickness drop resulting in an increasing number of asperity contacts, disregarding of the groove orientation. Local dimples are formed with transverse grooves. While they were negligible in EHL, they become significant in mixed regime leading locally to thicker film than that formed with a smooth surface. Nevertheless, the dimple is found to occur only when the groove tops are wide enough to properly separate the two constrictions formed at its edges.

Chapter 4

Ripple textures

Contents

In the previous chapter, the EHL friction was investigated with groove textures. These rough surfaces were elastically deformed inside the EHL contact due to the pressure of the lubricant. This deformation is mainly dependent upon the wavelength of the surface topography [86, 68, 69]: shorter wavelengths are less deformed than longer wavelengths. Therefore, carrying out experiments with very small wavelength textures presents the advantage of knowing the exact texture shape inside the EHL contact since elastic deformation is negligible.

The development of LASER Surface Texturing (LST) technique has enable the production of self organized nano-texture called LIPPS or ripples [116]. These textures can be considered as sinusoidal surfaces, which wavelength is lower than the micrometer. Thus, no elastic deformation is expected with these ripple textures. This particular behavior is used to study in detail the transition regime from EHL to mixed lubrication in terms of friction and film thickness.

The topographic description of the investigated ripple surfaces is presented. Then experimental Stribeck results at $|\Sigma| = 8\%$ are reported and discussed using the numerical simulations performed with the line contact model. This allows us to explain the origins of friction, in terms of both shear stress and film thickness transitions, through the description of the film thickness evolution governed by the ripple texture.

4.1 Surface topography

The balls were made of AISI 52100-drilled steel with a radius of 9.525 mm. They were polished to reduce their roughness until $S_q < 10$ nm. After polishing, three balls, B4, B5 and B6, were treated with femtosecond LASER irradiations to sculpt periodic ripples on their surface with different orientations (θ_s) toward the sliding direction. Their topography was characterized with a Brücker interferometer with a 0.4 µm/px resolution over a 230x180 μm^2 window and a Brücker Nanoman AFM with a high spatial resolution of 20 nm/px over a window of 10x10 μm^2. As a consequence, the AFM data applies a high-pass filter with a cut-off of 10 µm.

4.1.1 Ripple texture

The three ripple surfaces investigated in this chapter are homogeneous along the ball track. Fig. 4.1a shows AFM surface topographies from which 1D profiles are extracted and plotted in Fig. 4.1b. These profiles confirm that the ripple roughness is very close to a sinusoidal roughness. From these profiles, precise measurements of the average peak-to-valley ripple amplitude, A, the average

ripple wavelength using a Fast Fourier Transform, λ, and the RMS roughness parameters, R_q, were carried out and reported beside. The three surfaces have a similar wavelength, about 800-900 nm which leads to the amplitude reduction $A_d/A_i \approx 99\%$. Therefore, the ripples are expected not to be elastically deformed. The peak-to-valley ripple amplitudes range from 199 nm to 276 nm: the ripples of ball B4 are the highest and those of ball B5 the lowest. Their RMS roughness, measured with the AFM, is respectively 101, 66 and 83 nm: $R_{q,B4} > R_{q,B6} > R_{q,B5}$. For a sinusoidal surface given by:

$$z(x,y) = \frac{A}{2}\sin\left(\frac{2\pi}{\lambda}x\right) \ , \tag{4.1}$$

the following relation stands between the RMS roughness parameter and the amplitude A:

$$R_q = \frac{A}{2\sqrt{2}} \ . \tag{4.2}$$

Multiplying the measured R_q (cf. Fig. 4.1b) by $2\sqrt{2}$ gives a theoretical amplitude of 286, 187 and 235 nm for B4, B5 and B6, which is in agreement with their respective measured amplitude A (cf. Fig. 4.1b). This confirms that ripple textures are correctly modeled with a sinusoidal surface.

4.1.2 Waviness

In addition to the ripple texture, a small waviness, made by the adjacency of the LASER passages, is observed with the optical interferometer measurements of B4, B5 and B6. The interferometer resolution is equal to half of the ripple wavelength. Therefore, the optical interferometer applies a low-pass filter on the topography and gives only information on the waviness of the ripple surfaces. Interferometer measurements are respectively displayed in Fig. 4.2a. 1D profiles are extracted in Fig. 4.2b and their RMS waviness parameter $S_{q,w}$ is shown as well. For balls B5 and B6, the waviness peak-to-valley amplitude is about 20-30 nm. The surface of ball B4 has a rougher waviness, the peak-to-valley is about 50-75 nm. Thus, the waviness amplitude is four to ten times lower than the ripple amplitude. Moreover, $S_{q,w}$ is almost three times lower than R_q yet the same ordering as the ripple textures is found: $S_{q,w,B4} > S_{q,w,B6} > S_{q,w,B5}$. The waviness is then smoother than the ripple texture.

In addition, the Fourier analysis does not emphasize one specific wavelength for the waviness but a series of wavelengths ranging from 10 µm to 20 µm, i.e. about ten times higher than the ripple wavelength. Such wavelength is expected to be reduced from 3% to 20% regarding the entrainment speed [86, 68, 69]. Since

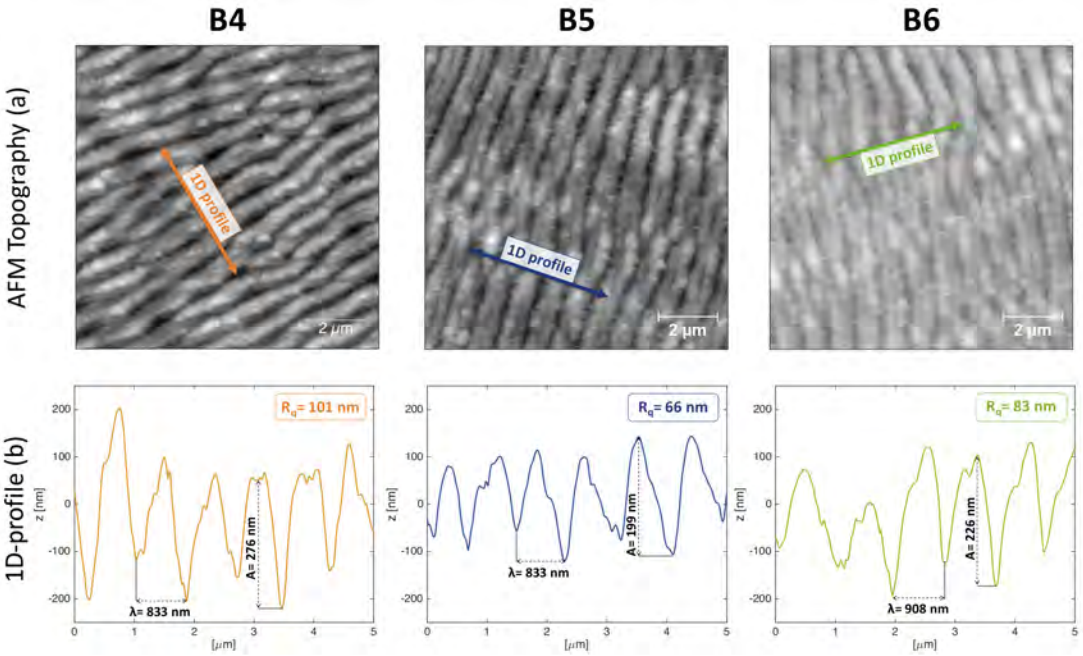

Figure 4.1: AFM topographic images of balls B4, B5 and B6 (a) and extracted ripple 1D-profiles with measured peak-to-valley amplitude A, wavelength λ and RMS roughness R_q (b).

they undergo elastic deformations in EHL, the waviness is expected to be even smoother in the EHL contact than the non-deformed ripple textures.

The zoom of the topography displayed in Fig. 4.2c with a resolution of 100 nm/px shows that the ripples orientation is perpendicular to the waviness orientation. To get the ripples orientation θ_s relative to sliding direction, an interferogram of a dry static contact between each ball and the disc with a 15 N load was analyzed (Fig. 4.2d). It yields that the waviness orientation of balls B4, B5 and B6 are -75°, -23° and 16° respectively. Since the ripples are oriented perpendicular to the waviness, θ_s is 15°, 67° and 106° for balls B4, B5 and B6 respectively.

4.2 Stribeck experiments

4.2.1 Friction transition and friction split

Stribeck experiments at $|\Sigma| = 8\%$ were performed with the three ripple surfaces B4, B5 and B6 and the Stribeck curves are reported in Fig. 4.3. The friction coefficient μ is plotted as a function of $\eta_0 u_e$. The calculated smooth viscous friction (oblique dash line) and the friction coefficient measured for a smooth ball are also indicated for comparison. Vertical dash lines represent the friction regime transitions. As presented in the previous chapter, the mixed/EHL transition is determined as the $\eta_0 u_e$ value corresponding to the change in the slope of the μ - $\eta_0 u_e$ curve. For ripple surfaces, this occurs for $\eta_0 u_e = 2.1 \times 10^{-2}$ Pa.m. The mixed/EHL regime transition is shifted to higher $\eta_0 u_e$ in comparison with the smooth surface. For $\eta_0 u_e > 2.1 \times 10^{-2}$ Pa.m, it is the EHL regime. In this regime, Fig. 4.3 shows that the ripple friction superimposes the smooth friction and the viscous friction. When $\eta_0 u_e < 2.1 \times 10^{-2}$ Pa.m, it is the mixed regime. There the friction starts increasing, becoming higher than the smooth and viscous ones. The ripple friction remains the same until it diverges so that $\mu_{B4} > \mu_{B6} > \mu_{B5}$: the higher the amplitude, the higher the friction. Nevertheless, the onset of the friction split occurs between $\eta_0 u_e = 8.0 \times 10^{-3}$ and 1.2×10^{-2} Pa.m.

4.2.2 Film thickness transition and film collapse

The measurement of the film thickness formed with the ripple surfaces during the Stribeck experiments has to account for the following considerations to be accurate. As the resolution of the camera is of 0.9 μm/px, i.e. of the same order as the ripple wavelength, the image is blurred and the ripples cannot be

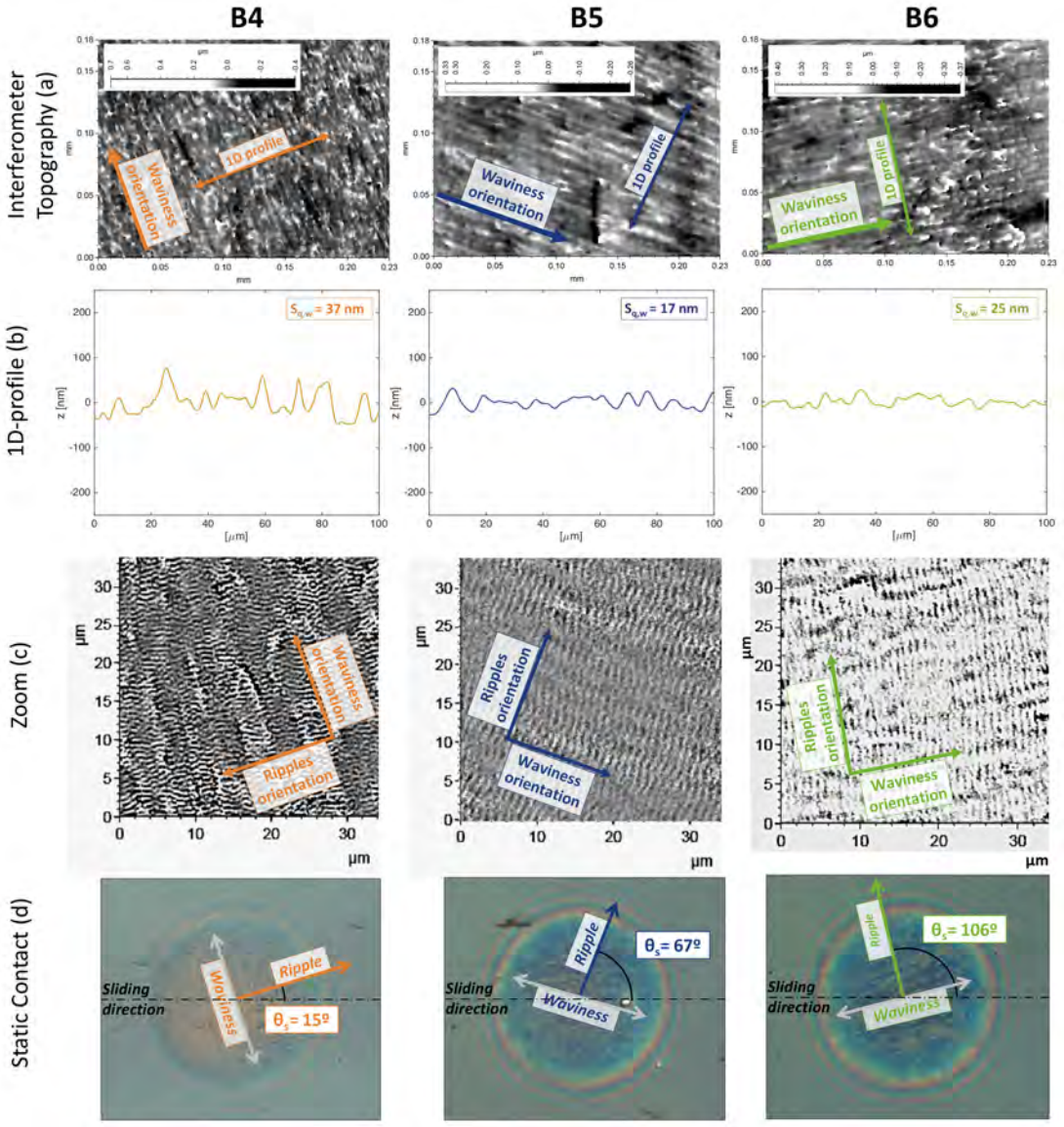

Figure 4.2: Interferometer topographic images of ripples B4, B5 and B6 (a) and extracted waviness 1D-profiles with measured RMS parameter, $S_{q,w}$. Zoom highlighting ripple and waviness orientations (c). IRIS interferograms of static loads (15 N) showing the waviness orientation toward the sliding direction giving the ripple orientation θ_s (c).

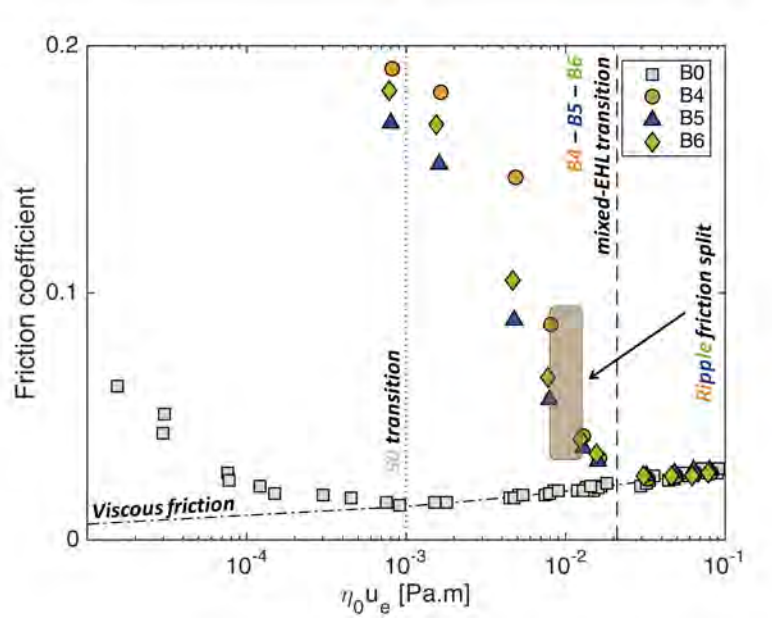

Figure 4.3: Stribeck curves at $|\Sigma| = 8\%$ of the smooth surface B0 and the ripple surfaces B4, B5 and B6 versus $\eta_0 u_e$, highlighting the mixed/EHL transition, the friction split and the calculated smooth pure viscous friction.

distinguished. Yet, the images appear homogeneous as in smooth EHL (see Fig. 4.4). As above-mentioned, such small wavelengths are not elastically deformed in the contact and the surface cannot be completely flattened. Therefore, some parts of the ripple surface must reflect more photons to the camera than other parts, which yields to a predominant local hue value. Thus, the ripple tops are supposed to be the most reflective part for two reasons. First, the incident light is normal to the surface: the more horizontal the surface part, the more reflected the light. Then, for a sinusoidal surface, both tops and bottoms are likely to reflect more the incident light. Nevertheless, Fig. 4.1b shows that ripple bottoms are sharper than the ripple tops. Thereby ripple tops should reflect more photons than any other part of the ripple texture. Second, the light reflected by the ripple bottoms has more probability to be intercepted and reflected by the edges of the bottoms. Hence the measured film thickness deduced from the colour analysis of the interferograms corresponds to the distance between the disc and the ripple tops.

Moreover, the interferogram of the static contact shown in Fig. 4.2d did not allow us to determine a precise calibration function that links the image hue values to the film thickness. The Hertzian theory, classically used for smooth dry contacts, cannot be applied to the ripple contact. To overcome this issue, the

film thickness was measured using a calibration function derived from the interferogram of a static contact between the smooth ball B0 and the disc at the same temperature, with the same lubricant, under the same load and with the same camera setting parameters. To estimate the error induced by this method, the film thickness measurements performed from this calibration curve were compared to film thickness measurements performed from a calibration function obtained with another smooth contact. The maximal difference of film thickness between both measurements was of 20 nm: the error in the ripple film thickness is estimated to be ± 10 nm.

The measured central film thickness between the ripple tops and the disc surface is plotted in Fig. 4.4 versus $\eta_0 u_e$. It corresponds to the value of the averaged film thickness over a 2/3-Hertzian-radius square zone centered on the contact. For each operating conditions $\eta_0 u_e$, the difference between the central film thickness of the three balls (B4, B5 and B6) is of the same order as the error, i.e. ± 10 nm. Thus, it can inferred that the ripple texture orientation has not a significant influence in EHL and that the roughness difference between the ripple surfaces is small enough not to modify the central film thickness results. Only the mean value of the central film thickness over B4, B5 and B6 is reported ($\circ$). For a given $\eta_0 u_e$ value, this central film thickness is always lower than that obtained for the smooth ball. The film thickness distribution in the contact, i.e. the whole range of values taken by the film thickness in the contact, is plotted in bold line for several $\eta_0 u_e$. The maximum of the distribution is reached at the contact center (central film thickness). The IRIS interferograms from B6 are displayed for various operating conditions. For comparison, a gray dot line shows the average evolution of the central film thickness measured for the smooth ball B0. The mixed/EHL transition and the friction split are respectively displayed in dash line and brown zone. A gray zone highlights the range of $\eta_0 u_e$, for which the smooth central film thickness is equal to half of the ripple peak-to-valley amplitudes, $A/2$ i.e. the range of $\eta_0 u_e$ for which the tops of the ripples balls B4, B5 and B6 should theoretically start coming in contact with the smooth disc. It is worth noticing that this range includes the $\eta_0 u_e$ values of the friction split determined in the previous section.

Below 1.6×10^{-2} Pa.m, the minimum film thickness becomes null: the first asperity contacts do happen. This value is lower than the $\eta_0 u_e$ value measured at the friction transition. Thereby, the film thickness transition, corresponding to the first asperity contacts, takes place for $\eta_0 u_e \in [1.6 \times 10^{-2}, 2.3 \times 10^{-2}]$ Pa.m. This is in agreement with the mixed/EHL transition found at $\eta_0 u_e = 2.1 \times 10^{-2}$ Pa.m. However, nothing is assumed about the physical origin of the friction transition (asperity contact or micro-EHL). For $\eta_0 u_e \in [1.0 \times 10^{-2}, 3.2 \times 10^{-2}]$ Pa.m, the ripple film thickness tends to stabilize around the value of 140 nm.

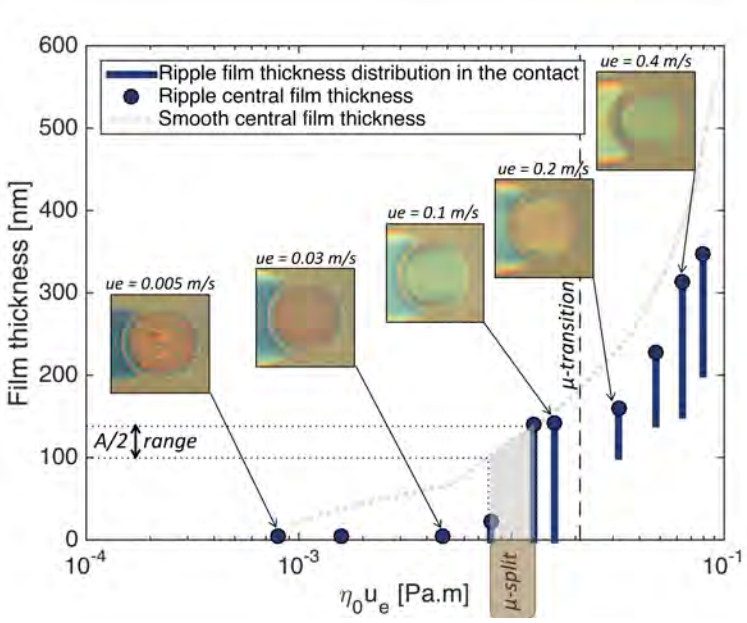

Figure 4.4: Film thickness distribution of the ripple Stribeck experiments at Σ = 8%, central film thickness ($\circ$) and corresponding interferogram (from B6) are reported versus $\eta_0 u_e$. The central film thickness measured for the smooth ball B0 is displayed for comparison. The range of $\eta_0 u_e$ for which the smooth central film thickness is equal to the ripple amplitudes $A/2$, is emphasized. The friction transition and the friction split are also reported.

Then, the central film thickness decreases to only few nanometers for $\eta_0 u_e$ below 1.0×10^{-2} Pa.m. The substantial central film thickness drop occurs for $\eta_0 u_e \in [8.0 \times 10^{-3}, 1.0 \times 10^{-2}]$ Pa.m, where the friction split was detected. Moreover, during this film collapse, values of the smooth central film thickness are close to $A/2$ as Fig. 4.4 illustrates. For representation convenience, only the friction transition and the friction split are reported in the following figures. However, one can bear in mind that the film thickness transition (the film collapse) occurs for $\eta_0 u_e$ values close to that of friction transition (friction split).

4.3 Stribeck numerical simulations

Using the line contact EHL model, the numerical simulations of Stribeck experiments with ripple texture and waviness are performed at $\Sigma = +8\%$. It has been reported that the wavelength is a key parameter in the elastic deformation and so in the lubrication [68, 69]. Hence, the surface wavelength in the line contact simulation must be the same as the surface roughness in the experimental point contact. Moreover, the waviness and the ripple texture are perpendicular so it is not possible to have the two wavelengths on a single topographic 1D profile. Because of these specifications, the following numerical approach is proposed. The ripple texture and the waviness will be simulated separately: this will provide information on the pertinent topographic scale in EHL, or on a possible multi-scale coupling. The numerical ripple textures are either the AFM measured profile (Fig. 4.1b) or its sine wave modeling, allowing to discuss the pertinence of these mathematical function to model the rippled surface. The waviness is the profile obtained from optical interferometer data (Fig. 4.2b). This means that the numerical simulations are equivalent to EHL point contacts with either transverse ripple texture or transverse waviness. To properly compare the numerical results with the experiments, the ripple texture is taken from the balls B5 ($\theta_s = 67°$) and B6 ($\theta_s = 106°$) which are the closest to a transverse ripple texture ($\theta_s = 90°$). On the contrary, the transverse waviness profile is obtained from B4, which waviness is the closest to a transverse one ($\theta_s - 90° = -75°$).

From an experimental profile $z(x)$ of either the ripple texture or the waviness, the numerical surface $r(x,t)$ is defined as:

$$r(x,t) = z\left(x - u_2 t \mod l\right) , \tag{4.3}$$

with l the length of the measured 1D profile chosen so that it is a multiple of the experimental profile wavelength. Hence, this does not affect the periodicity of the topography. For ripple textures, the numerical surface is also modeled with

a sinusoidal function:

$$r(x,t) = \frac{A}{2}\sin\left(2\pi\frac{x-u_2 t}{\lambda}\right) \ , \tag{4.4}$$

B5 and B6 are mathematically modeled with respectively $A = 199$ nm, $\lambda = 833$ nm and $A = 226$ nm, $\lambda = 908$ nm. In these simulations, oil, materials and load parameters are the same as those of the experiments. The film thickness can be null for some values of $\eta_0 u_e$. Since we did not include asperity contact model in the line contact EHL model, only cases with $\forall x, h(x,t) > 0$ are presented. This explains why for some numerical results, the data are not plotted for all the $\eta_0 u_e$ range.

4.3.1 Convergence

In each case, the topography is directly introduced in the contact at $T = 0$. Thus, the program needs to converge to a "stationary" state. The number of time steps required to converge is first determined. As the wavelength of the ripple texture is about 800-900 nm, the EHL equations are solved on a mesh with 8192 nodes over the domain $X \in [-2.5, 1.5]$. Hence, the spatial pitch is $\Delta x \approx 60$ nm, small enough to discretize the ripple texture. On the contrary, the waviness exhibits a wavelength close to that of the groove topography studied in the previous chapter. Thus, the waviness simulations run on a mesh with 512 nodes over the domain $X \in [-2.5, 1.5]$. The convergence of the minimum film thickness is reported in Fig. 4.5a-b versus the dimensionless time step for model ripple texture of B5 (a) and waviness profile of B4 (b), at $\eta_0 u_e = 1.0 \times 10^{-1}$ Pa.m which corresponds to operating conditions of EHL regime. The respective converged value is reported in dash line.

In both case, the numerical simulation convergence is fast. In Fig. 4.5a, the relative error is less than 1% after 10 time steps. The minimum film thickness oscillates with a period of 10 dimensionless time steps which corresponds to 1.1 µs. This is due to the periodicity of the B5 sine wave modeling which wavelength is equal to 833 nm. As the textured surface velocity is $u_2 = 0.5$ m.s^{-1}, the dwell time of one ripple defined as the period of the pattern is $\lambda/u_2 = 1.7$ µs, which magnitude order is equal to the oscillations of Fig. 4.5a. Similar evolutions were found with experimental ripple profiles. For the waviness, Fig. 4.5b shows that the minimum film thickness oscillates with a period of 22 dimensionless time steps, i.e. a period of 0.04 ms. The significant wavelengths of the waviness profile range from 10 µm to 20 µm and the textured surface velocity is $u_2 = 0.5$ m.s^{-1}: $0.02 < \lambda/u_2 < 0.04$ ms. This result is in good agreement with the oscillation period from Fig. 4.5b.

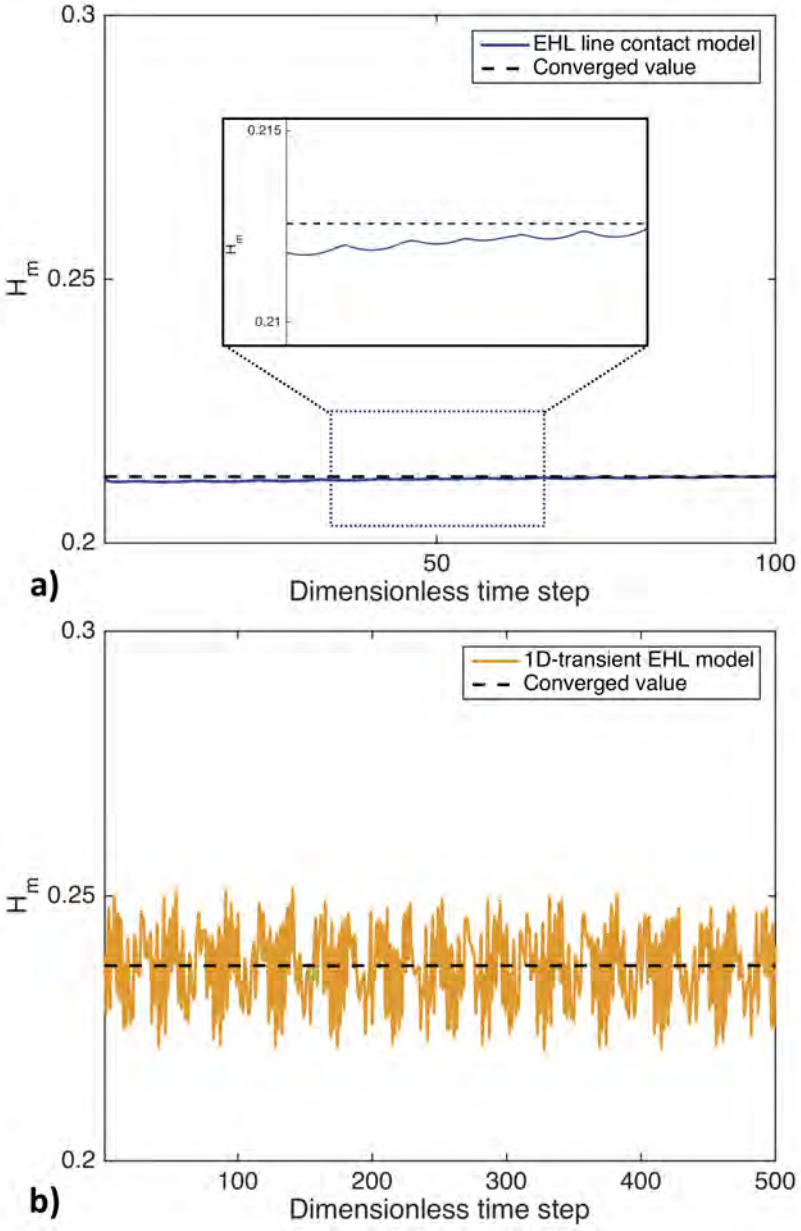

Figure 4.5: Minimum film thickness versus the number of time steps for the ripple texture (a) and the waviness (b) numerical simulations. The respective converged value is emphasized in dash line. A zoom of the convergence is displayed in (a).

In the following, data for ripple textures will correspond to the value of the 10^{th} time step. For the waviness, the oscillation amplitude of the numerical results is significant. Thus, data will be determined as the mean over the last two hundred time steps of a 500-time-step run, i.e. data will be a mean over nine periods. Besides, numerical and experimental data will be represented, respectively, with lines and dots. In the figures, the friction transition and friction split will be reported with vertical dash lines. The corresponding numerical smooth results will be displayed with a full black line and will be referred to h_s.

4.3.2 Central film thickness - h_c

Simulations were run for $\eta_0 u_e$ varying from 1.0×10^{-2} to 1.0×10^{-1} Pa.m with B5 and B6 experimental profiles (ripples), B5 and B6 sine profiles and B4 experimental profile (waviness). As for the experiments, the central film thickness h_c was defined as the distance between the ripple tops and the disc for $-a/3 < x < a/3$. In practice, h_c is determined as the average of the ten lowest film thicknesses over the previous interval. In Fig. 4.6 the numerical central film thickness is reported versus $\eta_0 u_e$ for B4, B5, B6 and the smooth surface. Experimental central film thickness values of B4, B5 and B6 are reported with dots for comparison.

The numerical central film thicknesses of transverse ripples from B5 and B6 is about 100 nm thinner than that formed with the smooth surface. The numerical model predicts that the film thickness formed with the transverse waviness from B4 is, in average, 60 nm thicker than the central film thickness of the transverse ripple textures and so about 40-nm thinner than the smooth central film thickness. The transverse waviness reduces the central film thickness to a lesser degree in comparison to the transverse ripple textures.

In EHL, experimental central film thicknesses measured for balls B4, B5 and B6 are in agreement with the numerical simulations of transverse ripples determined from the B5 and B6 topographies. On the contrary, there is no agreement between the experimental points and the B4 calculations based on its transverse waviness. In mixed regime, the experimental data are close to the calculated smooth central film thickness and are thicker ($\approx$ 100 nm) than the numerical simulations of B5 and B6. There, the asperity contacts observed in the constriction region for experimental point contacts are not predicted with the line contact model: the film thickness is always strictly positive. This would indicates that the occurrence of asperity contacts in the constriction region has a significant impact on the central film thickness with ripple surfaces, leading to a central film thickness equal to the smooth cases. This film thickness rising will be later discussed in detail.

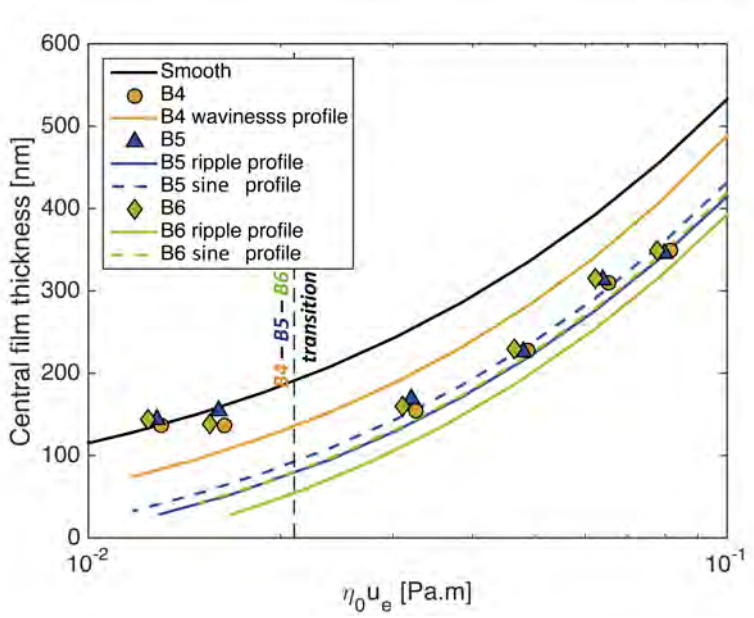

Figure 4.6: Central film thickness versus $\eta_0 u_e$ for B5, B6 ripple profiles, B5, B6 sine profiles and B4 waviness profile. The experimental data of B4, B5 and B6, the numerical smooth central film thickness and the mixed/EHL regime transition are reminded.

Numerical simulations confirm that the film formed with transverse-ripple textured ball is thinner than that formed with a smooth ball above the mixed/EHL transition. They also confirm that the experimental h_c is indeed the distance between the ripple tops and the disc. The waviness of B5 and B6 is negligible in the lubrication mechanisms in EHL. Results from B5 and B6 suggest that the ripple texture is the relevant topographic length-scale in the lubrication of longitudinal ripple texture. The waviness is not the topographic length-scale that governs the EHL process for ball B4, as shown by Fig. 4.6. Again, this indicates that the ripple texture orientation has not a significant influence on the film forming capability of ripple surfaces in EHL.

4.3.3 Ripple sinusoidal modeling

In Fig. 4.6, the central film thickness of the sine profiles are higher than their respective experimental ripple profiles. In average, the difference is respectively equal to 15 nm and 24 nm, for B5 and B6. As an example, Fig. 4.7 shows the film thickness profiles from B5 simulations with the experimental and sine profiles at $\eta_0 u_e = 1.0 \times 10^{-1}$ Pa.m. A zoom is displayed to distinguish the ripple texture. The smooth film thickness is reported for comparison. Both calculated film thickness profiles are close to each other which is confirmed by the detailed profiles in the zoom box. However, the film thickness obtained from the AFM profile can sometimes be lower or higher than the sine wave model. Indeed, the amplitude of the sine wave model is an average over the experimental profile. This explains the slight film thickness difference according to the local variations between the real roughness and the average sine profile. As a result, ripple textures are correctly modeled with a sinusoidal function in terms of film forming capability.

Besides, the zoom in Fig. 4.7 suggests that the smooth central average film thickness $h_{c,s}$ is the average of the film thickness at the center of the contact h_{av}:

$$h_{av} = h_{c,s} \ . \tag{4.5}$$

This relation is tested with other $\eta_0 u_e$ values using experimental and sine profiles of B5 and B6. Fig. 4.8 reports the central average film thickness h_{av} versus $\eta_0 u_e$ for experimental and sine profiles of both B5 and B6. Fig. 4.8 shows that Eq. 4.5 is verified for all these surfaces and conditions.

For sine profiles, Fig. 4.9 illustrates the relation between the central film thickness h_c, the elastically reduced amplitude of the ripple A_d and the central average film thickness h_{av} given by:

$$h_c = h_{av} - \frac{A_d}{2} \ . \tag{4.6}$$

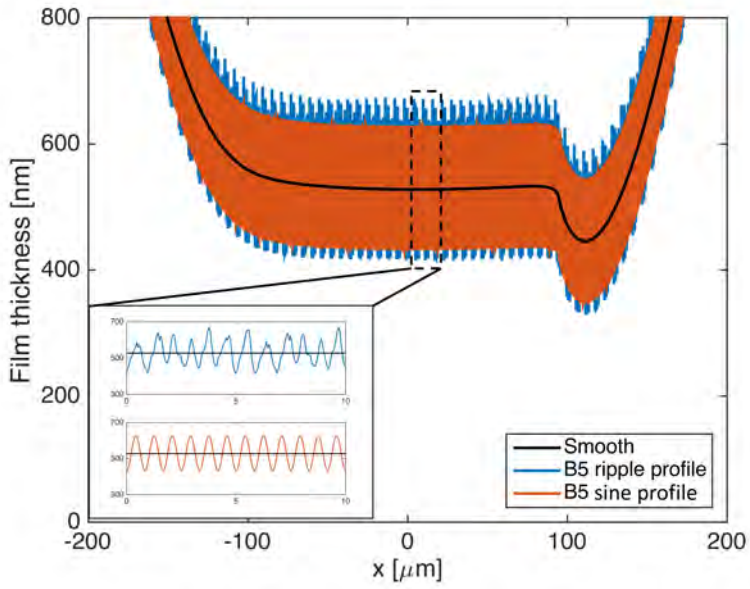

Figure 4.7: Film thickness profile at $\eta_0 u_e$ =1.0 × 10^{-1} Pa.m for the smooth surface, B5 ripple and B5 sine profiles.

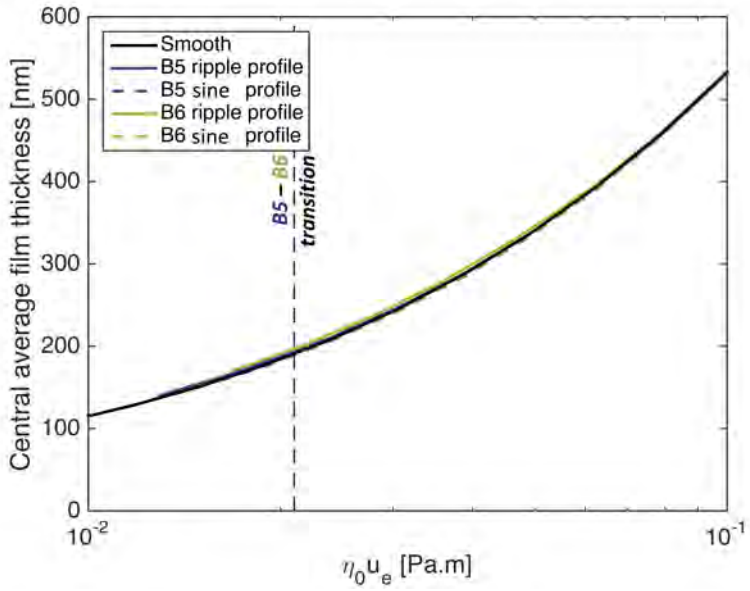

Figure 4.8: Central average film thickness versus $\eta_0 u_e$ for B5, B6 experimental and sine profiles. The smooth central film thickness and the friction transition are reminded.

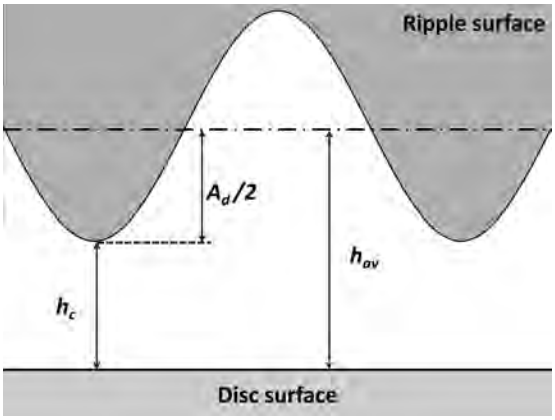

Figure 4.9: Scheme of a ripple sine wave surface inside the contact illustrating the relation between h_c, $A_d/2$ and h_{av}.

Indeed, the central average film thickness is the distance between the disc and the mid plane of the ripple texture. Substituting Eq. 4.5 in Eq. 4.6, it yields:

$$h_c = h_{c,s} - \frac{A_d}{2} \ . \tag{4.7}$$

Eq. 4.7 indicates that for transverse sinusoidal surfaces, the central film thickness is always reduced by half of the ripple deformed amplitude. In Fig. 4.6, h_c of B5 sine profile is always higher than that of B6. The difference is small and equal to 13 nm, in average. Using Eq. 4.7, it yields that:

$$h_{c,B5} - h_{c,B6} = \frac{A_{d,B6} - A_{d,B5}}{2} \ . \tag{4.8}$$

As previously stated, the ripple texture is expected not to be elastically deformed. The amplitude reduction A_d/A_i is calculated from the numerical simulations performed for balls B5 and B6. For $\eta_0 u_e \in [1.0 \times 10^{-2}, 1.0 \times 10^{-1}]$, the amplitude reduction is in average of 98-99% which is in agreement with the theory of amplitude reduction [68, 69]. Ripple texture can then be considered as an undeformed texture:

$$A_d = A \ . \tag{4.9}$$

Using Eq. 4.8 and 4.9: $h_{c,B5} - h_{c,B6} = 13.5$ nm. This calculated value is in agreement with the difference previously determined on Fig. 4.6 and equal to 13 nm. Therefore, the amplitude of the sine profiles is responsible for the difference in the lubrication efficiency between B5 and B6. This difference is slight and close to experimental error magnitude which explains why this cannot be detected experimentally.

	3.2×10^{-2} Pa.m	4.8×10^{-2} Pa.m	6.4×10^{-2} Pa.m	8.0×10^{-2} Pa.m
B4	22%	13%	13%	5%
B5	8%	3%	4%	5%
B6	15%	7%	11%	3%

Table 4.1: Relative error between the experimental central film thickness of B4, B5 and B6 and the formula from Eq. 4.7.

Finally, the central film thickness formula (see Eq. 4.7) is compared to the experimental h_c of B4, B5 and B6 from Fig. 4.6. The relative error is reported in Table 4.1 for the four $\eta_0 u_e$ values in EHL: 3.2×10^{-2}, 4.8×10^{-2}, 6.4×10^{-2} and 8.0×10^{-2} Pa.m. Table 4.1 shows that the relative error is around 10% for $\eta_0 u_e \geq 4.8 \times 10^{-2}$ Pa.m. For $\eta_0 u_e = 3.2 \times 10^{-2}$ Pa.m, the relative error becomes much higher, up to 22% with B4. In fact, the absolute error ranges from 10 to 35 nm, irrespective of $\eta_0 u_e$. Since h_c is lower when $\eta_0 u_e$ decreases, the relative error will increase. Hence, formula from Eq. 4.7 gives a better approximation of the central film thickness for high $\eta_0 u_e$.

4.3.4 Film thickness transition - h_m

Minimum film thickness

Fig. 4.10 reports three IRIS interferograms, respectively at $\eta_0 u_e = 8.0 \times 10^{-3}$ (below the friction split), 1.3×10^{-2} and 1.6×10^{-2} Pa.m (both between the friction split and the film thickness transition). The more orange the color, the thinner the film thickness. Interferograms from Fig. 4.10a-b indicate that the film thickness inside the constriction region is likely homogeneous. Thus, the minimum film thickness on the center line is representative for the minimum film thickness of the constriction region and thus of the whole contact. The EHL line contact model, which is based on the line contact equivalent description, will give the minimum film thickness on the center line. As long as the EHL line contact is equivalent to an EHL point contact with a homogeneous constriction region, the EHL line contact model will predict the correct h_m. With smooth surfaces, this homogeneity decreases as $\eta_0 u_e$ increases. At high $\eta_0 u_e$, the film thickness is much thinner in the side region of the constriction than at its center. Thus, the EHL line contact model will overestimate the minimum film thickness at high $\eta_0 u_e$.

The region where the EHL line contact accurately predicts h_m is investigated. In the meantime, the quantity $h_m + A_d/2$ is calculated. In Fig. 4.11a (4.11b) the

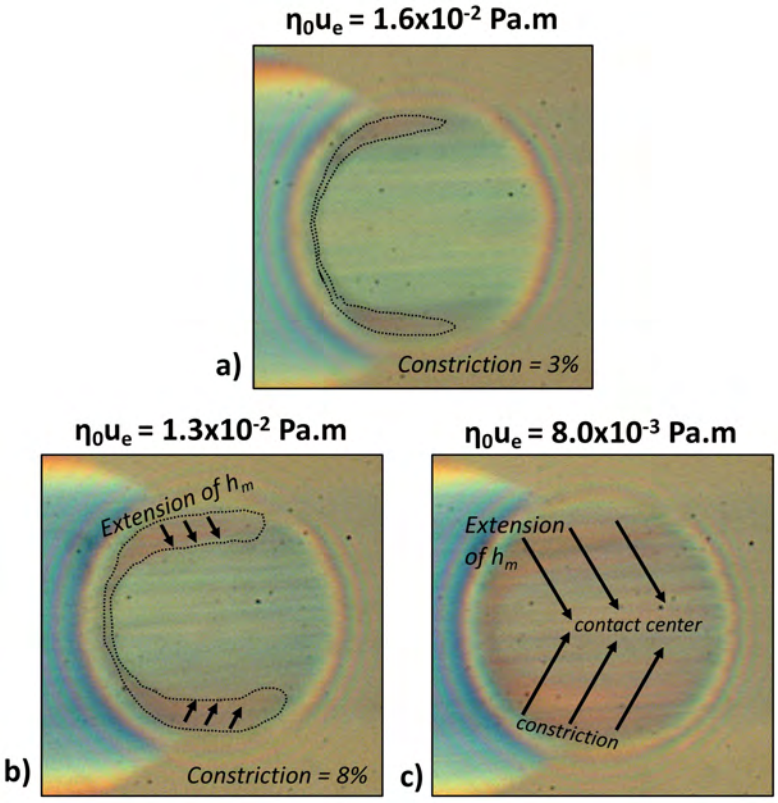

Figure 4.10: IRIS interferograms of B6 contact at three $\eta_0 u_e$ operating conditions emphasizing the minimum film thickness extension and the constriction region.

quantity $h_m + A_d/2$ is plotted versus $\eta_0 u_e$ for B5, B6 experimental and sine profiles and experimental data (B4 waviness profile and experimental data). The calculated amplitude reduction [68, 69] is about 80% for the waviness. The value of A_d is respectively 47, 199 and 226 nm for B4, B5 and B6. The ripple mixed/EHL transition (dash line) and the smooth minimum film thickness (full line) are reminded.

Data from the experimental profiles are slightly lower than those from the sine profiles, which perfectly fit $h_{m,s}$. This difference as previously observed in Fig. 4.7, con be explained by the occurrence of lower and higher amplitudes in the experimental profile than in the sine profile. The $h_m + A_d/2$ values calculated from experimental and sine profiles of balls B5 and B6 are close to that calculated for the smooth case ($A_d = 0$). Then, it can be inferred for transverse ripples that:

$$h_m = h_{m,s} - \frac{A_d}{2} \ . \tag{4.10}$$

In Fig. 4.11a, the experimental quantity $h_m + A_d/2$ of B5 and B6 fits the corresponding numerical values and the smooth minimum film thickness for $\eta_0 u_e \in [1.0 \times 10^{-2}, 5.0 \times 10^{-2}]$ Pa.m. Therefore, the experimental minimum film thickness is correctly predicted on this $\eta_0 u_e$ range. Above, the experimental values are lower than the calculated values. The constriction becomes heterogeneous and h_m occurs in the side region of the constriction. Therefore, the minimum film thickness of the experiments is well described by Eq. 4.10 for $\eta_0 u_e \in [1.0 \times 10^{-2}, 5.0 \times 10^{-2}]$ Pa.m and in particular around the film thickness transition. This means that the first asperity contacts occur for the $\eta_0 u_e$ value corresponding to a smooth minimum film thickness of $A_d/2$ ($= A/2$ here). From the numerical smooth film thickness, $h_{m,s} = A_d/2$ happens respectively for B5 and B6 at $\eta_0 u_e = 2.2 \times 10^{-2}$ and 2.7×10^{-2} Pa.m which is in agreement with the interval of the film thickness transition observed in Fig. 4.4. This prediction remains valid until the so-determined $\eta_0 u_e$ is below 5.0×10^{-2} Pa.m. For $\eta_0 u_e > 5.0 \times 10^{-2}$ Pa.m, Fig. 4.11a shows that:

$$h_m = h_{m,s} - (A_d/2 + \bar{\epsilon}) \ , \tag{4.11}$$

with $\bar{\epsilon}$ a positive number. When $h_m = 0$, the corresponding $h_{m,s}$ from Eq. 4.11 and its related $\eta_0 u_e$ value are higher than those from Eq. 4.10. Thus, if the so-determined $\eta_0 u_e$ with Eq. 4.10 is above 5.0×10^{-2} Pa.m, the actual film transition happens higher than the so-determined $\eta_0 u_e$.

Finally, Fig. 4.11b shows the calculated minimum film thickness for transverse waviness which is always much thicker than the minimum film thickness measured for ball B4. Considering only the transverse waviness profile do not lead to a correct prediction of the B4 minimum film thickness. Again the waviness is not

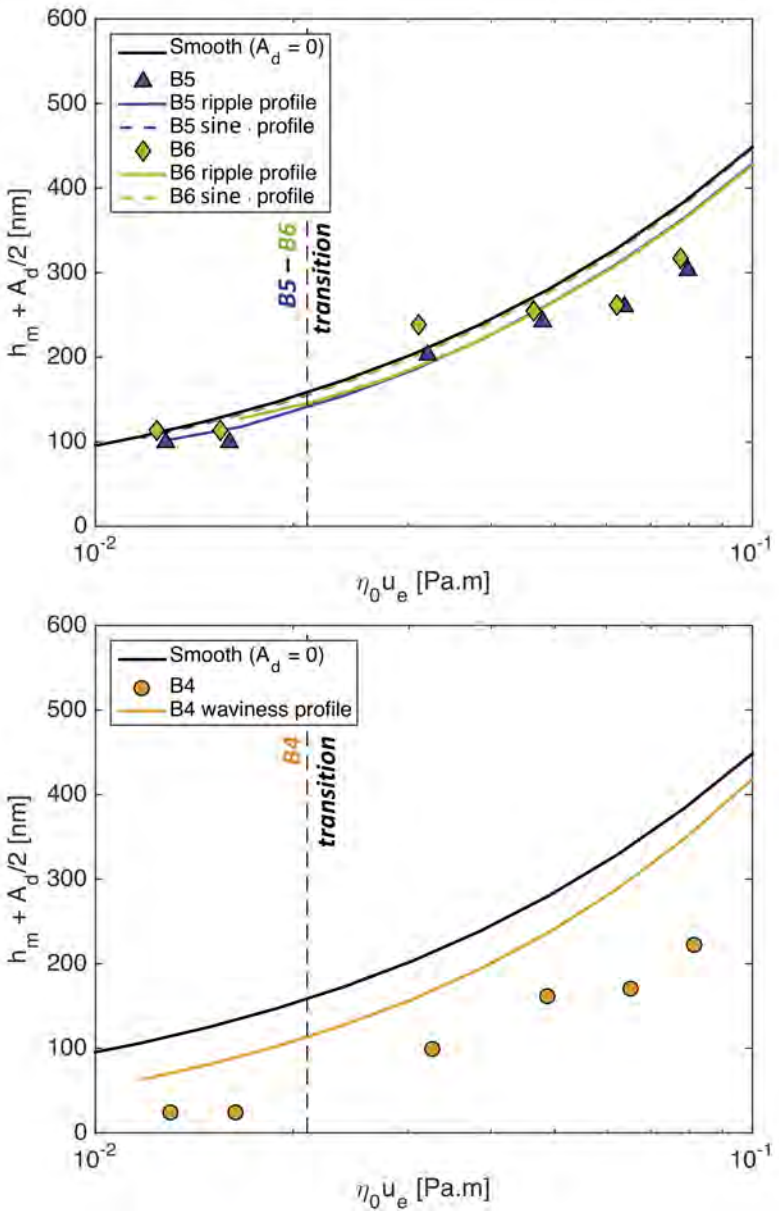

Figure 4.11: Minimum film thickness $h_m + A_d/2$ versus $\eta_0 u_e$ for B5, B6 experimental and sine profiles and experimental data (a). Minimum film thickness $+A_d/2$ versus $\eta_0 u_e$ for B4 waviness profile and experimental data (b). The ripple mixed/EHL transition (dash line) and the smooth minimum film thickness (full line) are reminded.

the significant topographic scale to predict the lubrication with the ripple texture. For the numerical waviness, $h_m + A_d/2$ is always lower than the smooth reference.

Tallian criterion

The Tallian parameter is now investigated as it is usually used to characterize the occurrence of the first asperity contacts. To qualify the wear rate at a given EHL operating condition, Tallian [117] proposed the following parameter Λ_T:

$$\Lambda_T = \frac{\tilde{h}_0}{\sigma} \ , \tag{4.12}$$

with σ, the composite RMS roughness parameter of the two surfaces, defined as:

$$\sigma = \sqrt{R_{q,disc}^2 + R_{q,ball}^2} \ , \tag{4.13}$$

and $\tilde{h}_0$ the uniform EHL film thickness in the contact area As transverse ripple textures are well modeled with sinusoidal surfaces, $\tilde{h}_0$ corresponds to the mean the surface, i.e. h_{av}. Substituting h_{av} from Eq. 4.5, the Tallian parameter yields:

$$\Lambda_T = \frac{h_{c,s}}{\sigma} \ . \tag{4.14}$$

For $\Lambda_T > 3$ the wear was negligible whereas for $\Lambda_T < 3$ the wear started to occur. The criterion $\Lambda_T = 3$ was then considered as the onset of asperity contact. For the smooth surface B0, $R_{q,disc} = R_{q,ball}$ and $\sigma_s = \sqrt{2} R_{q,ball} = 14\ nm$, where σ_s is the composite RMS roughness of the smooth contact. At the transition in Fig. 4.4, $h_{c,s} = 3\sigma_s$. According to the Tallian parameter, the film thickness transition occurs at $\eta_0 u_e = 1.4 \times 10^{-3}$ Pa.m. In the previous chapter, this transition was estimated to happen for $\eta_0 u_e \in [9.0 \times 10^{-4}, 1.8 \times 10^{-3}]$ Pa.m. The Tallian prediction is in agreement with the experimental observations.

The RMS roughness of the ripples is at least six times higher than the smooth surface. Thus, $\sigma_{ripple} \approx R_{q,ripple}$. In the following R_q will stands for $R_{q,ripple}$. Similarly the $\eta_0 u_e$-transitions are determined for B5 and B6 so that the smooth film thickness is equal to $3R_q$. This yields to $\eta_0 u_e = 2.6 \times 10^{-2}$ and 3.3×10^{-2} Pa.m respectively. This is compatible with the film transition found experimentally: $\eta_0 u_e \in [1.6 \times 10^{-2}, 3.2 \times 10^{-2}]$ Pa.m. However, these calculated $\eta_0 u_e$ values indicate that the asperity contacts start closer to 3.2×10^{-2} Pa.m than 1.6×10^{-2} Pa.m. Moreover, in Fig. 4.4 the measured minimum film thickness at $\eta_0 u_e = 3.2 \times 10^{-2}$ Pa.m is equal to 100 nm whereas it is null at 1.6×10^{-2} Pa.m. This indicates that the asperity contacts are much likely to occur at $\eta_0 u_e$ values closer to 1.6×10^{-2} than to 3.2×10^{-2} Pa.m, contrary to what the Tallian criterion predicted. In

addition, experimental and numerical data show that the lubrication behavior of the longitudinal ripple B4 is close to B5 and B6. So the Tallian criteria is also expected to give a good approximation of film thickness transition of ball B4. It yields $\eta_0 u_e = 4.8 \times 10^{-2}$ Pa.m, far to high from experimental observations. For all these reasons, a new definition of the Tallian parameter has to be determined for the ripples.

Tallian empirically defined this parameter from wear observation. So the value of 3 may not stand for every surfaces. The ratio for smooth surfaces of h_c/h_m is numerically determined: $h_c = 6/5 h_m \pm 0.003$, $\forall\ \eta_0 u_e \in [1.0 \times 10^{-4}, 1.0 \times 10^{-1}]$ Pa.m. Thus Eq. 4.14 becomes:

$$\Lambda_T = \frac{6}{5} \frac{h_{m,s}}{R_q} \ . \tag{4.15}$$

Given that the ripples are well modeled with a sinusoidal function, R_q is replaced in Eq. 4.15 with its definition from Eq. 4.2, leading to:

$$\Lambda_T = \frac{6}{5\sqrt{2}} \frac{h_{m,s}}{A} \ . \tag{4.16}$$

At the first film thickness transition, $h_{m,s} = A_d/2$ and $A_d = A$. Thus, the Tallian parameter is equal to $6\sqrt{2}/5 = 1.7$ which is lower than theoretical Tallian value of 3. Yet, it is higher than the Tallian value of 1 corresponding to severe wear and usually associated to the boundary/mixed transition. This value of 1.7 is used to determine the $\eta_0 u_e$-transitions for B4, B5 and B6 as above-presented. This leads respectively to $\eta_0 u_e = 1.9 \times 10^{-2}$, 1.0×10^{-2} and 1.5×10^{-2} Pa.m with experimental smooth central film thickness. These results are in perfect agreement with film thickness transition range observed experimentally: 1.0×10^{-2} to 3.2×10^{-2} Pa.m. This illustrates that the Tallian parameter value of 3 is not universal.

4.3.5 Extension of the constriction region

In Fig. 4.6, it was observed that the central film thickness is equal to the smooth central film thickness minus $A_d/2$ (see Eq. 4.7), above the mixed/EHL transition. Below the film thickness transition and above the film thickness collapse, the central film thickness behaved differently: h_c is almost constant equal to the smooth central film thickness. However, at $\eta_0 u_e = 8.0 \times 10^{-3}$ Pa.m (just below the film thickness collapse), Eq. 4.7 predicts a negative h_c, i.e. asperity contacts happen in the central region of the contact, which is in agreement with the experiments. Therefore, Eq. 4.7 is used to determine the $\eta_0 u_e$ value corresponding to the film

thickness collapse: $h_c = 0$. The similar lubrication behavior of the longitudinal ripple B4 and the importance of the ripple texture in the previous part lead to suppose the same mechanisms for B4, B5 and B6. Given the previous criterion, the film collapse should respectively take place at $\eta_0 u_e = 1.2 \times 10^{-2}$, 9.1×10^{-3} and 1.1×10^{-2} Pa.m, for balls B4, B5 and B6. These values are in correct agreement with the observations placing the onset of the film collapse between 8.0×10^{-3} and 1.2×10^{-2} Pa.m for balls B4, B5 and B6 (see Fig. 4.4).

This film collapse is indeed the consequence of the constriction region extension. The interferogram of Fig. 4.10a shows that asperity contacts start to occur in the constriction region. The region where these contacts happen represents $3 \pm 1\%$ of the total contact area while the central film thickness is equal to 143 nm. Then, this asperity contact region spreads little by little to the contact center when $\eta_0 u_e$ is lowered (see Fig. 4.10b-c). In Fig. 4.10b, the asperity contact region covers $8 \pm 2\%$ of the EHL contact and $h_c = 141$ nm. Fig. 4.10c shows the contact for $\eta_0 u_e = 8.0 \times 10^{-3}$ Pa.m, i.e. just below the film collapse. The minimum film thickness zone extends from the constriction region to the central region. There, the film thickness is no longer homogeneous and asperity contacts occur overall the entire EHL contact.

To explain such phenomenon, the following attempt is proposed. With lower $\eta_0 u_e$, less lubricant flows into the contact. The film thickness is reduced and the surfaces become closer. Thus, the probability of solid contacts occurrence increases and so does the contact stress on the ripple texture. However, as the lubricant pressure was not able to elastically deform the ripple texture, it can be supposed that the pressure, on the asperity contacts, faces the same difficulty to deform the asperity. This assumption seems realistic since the film collapse, which is characteristic from the existence of asperity contacts, is well predicted with the relation $h_c = A_d/2$. As the ripple texture cannot be much deformed when in contact with the disc surface, the overall lubrication merging process between the ball and disc surface is prevented. As a result, the central film thickness is kept constant. Yet the volume of available lubricant diminishes in the contact, therefore the constriction region expands toward the contact center until the central film thickness decreases and becomes null.

4.3.6 Mixed friction and friction split

From Fig. 4.3, the friction split was defined as the $\eta_0 u_e$ value at which the friction coefficient starts being different between the ripple surfaces. For our experiments, it gives $\eta_0 u_e = 1.0 \times 10^{-2}$ Pa.m. Then for $\eta_0 u_e$ higher than 1.0×10^{-2} Pa.m, the rougher the surface, the higher the friction. From 4.4, the onset of the film

collapse occurs at similar $\eta_0 u_e$. Besides, Fig. 4.10a-c has shown that this film collapse is characterized with the sudden onset of asperity contacts in both the center and the constriction regions of the lubricated contact. Above 1.3×10^{-2} Pa.m, the asperity contacts represent less than 10% of the lubricated contact while below, they represent more than 50%. At the film collapse, the intimacy of the ripple texture and the disc strongly increases. As a consequence, the mixed friction is expected to be increasingly discriminated by the surface roughness and to depend on it. Hence, the friction split is supposed to be the consequence of the film collapse although these two phenomena appear for very close values of $\eta_0 u_e$ that cannot be distinguished experimentally with accuracy .

The Stribeck curve is usually plotted versus the dimensionless Hersey number $\mathcal{H}$ defined as:

$$\mathcal{H} = \frac{\eta_0 \omega}{p_{m,Hertz}} \tag{4.17}$$

with ω the rotation frequency and $p_{m,Hertz}$ the mean Hertzian pressure equal to 305 MPa for the experiments. To generalize Stribeck curve to rough contacts, Schipper et al. [118, 14] proposed to plot the Stribeck curve as a function of the Lubrication number $\mathcal{L}$. This dimensionless parameter is defined as follows:

$$\mathcal{L} = \frac{\eta_0 u_e}{p_{m,Hertz} R_a} \tag{4.18}$$

with R_a the arithmetical average of the composite surface profile. Later Diew et al. [60] propose instead the RMS roughness parameter of the composite surface σ, introducing the Modified Hersey number $\tilde{\mathcal{H}}$:

$$\tilde{\mathcal{H}} = \frac{\eta_0 u_e}{p_{m,Hertz} \sigma} \tag{4.19}$$

Since the ripples are far more rougher than the smooth surface, the modified Hersey number becomes:

$$\tilde{\mathcal{H}} = \frac{\eta_0 u_e}{p_{m,Hertz} R_q} \tag{4.20}$$

To confirm the role of roughness in increasing the friction coefficient when $\eta_0 u_e$ decreases, the generalized Stribeck curve from friction measurements (see Fig. 4.3) is plotted versus $\tilde{\mathcal{H}}$ for B4, B5 and B6 in Fig. 4.12. From Schipper, Ter Haar and Emmens' works [14, 119, 120] ,the equation of a generalized Stribeck master curve was proposed:

$$\begin{cases} \mu(\tilde{\mathcal{H}}) = \mu_{BL}\mathcal{F} + \mu_{EHL}\left(1 - \mathcal{F}\right) \\ \mathcal{F} = \dfrac{1}{2}\left[1 - \tanh\left(b \log \dfrac{\tilde{\mathcal{H}}}{H_c}\right)\right] \\ \mu_{EHL} = c\ \tilde{\mathcal{H}}^n \end{cases} \tag{4.21}$$

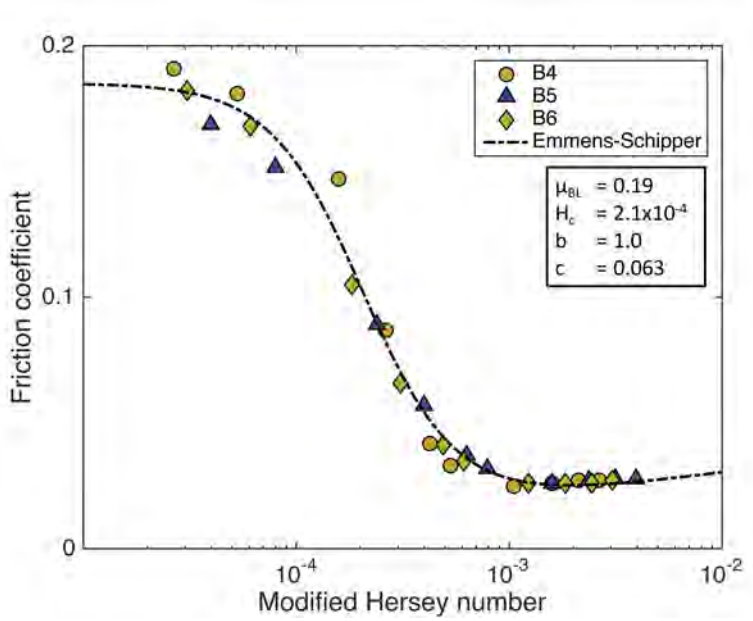

Figure 4.12: Generalized Stribeck curves at $\Sigma = 8\%$ of the ripple surface B4, B5 and B6 versus the dimensionless Hersey number. The master curve deduced from equation 4.21 is plotted and its fitted parameters are reported.

n is determined from the power-law evolution of the friction in the EHL regime. From Fig. 4.3: $n = 0.16$. μ_{BL}, b, c and H_c are constants to fit. Physically, $\mathcal{F}$ represents the relative asperity contact area in the lubricated contact. When $\tilde{\mathcal{H}} = H_c$, then $\mathcal{F} = 0.5$, i.e. half of the contact is in boundary lubrication regime. Locally, the friction is equal to μ_{BL}. From experimental data, the master curve is fitted and its parameters are displayed beside.

Figure 4.12 show that the experimental points measured for balls B4, B5 and B6 all collapse on the master curve deduced from equation 4.21. This means that the ripple orientation is not significant in terms of mixed friction. Moreover the dispersion of the friction in the mixed regime (see Fig. 4.3) is significantly reduced when taking into account R_q. Therefore, the friction response of rippled surfaces is a function of the surface roughness in the mixed regime: the rougher the surface, the higher the friction. This accredits that the sudden increasing intimacy between the ball and the disc (film thickness collapse) will suddenly increase and discriminate the friction (friction split).

In addition, the boundary friction coefficient is found to be equal to 0.19 ± 0.01 which is a little lower than the measured smooth boundary friction in the previous chapter: 0.26 ± 0.03. This difference is not surprising given that the textures can act as an oil reservoir, which might reduce the friction coefficient in boundary

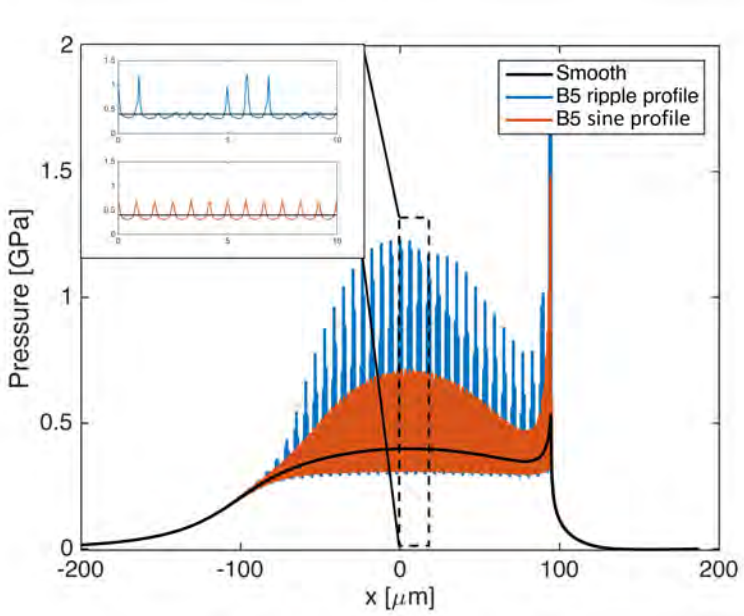

Figure 4.13: Pressure distribution at $\eta_0 u_e$ =1.0 $\times$ 10^{-1} Pa.m calculated for the smooth surface, the ripple ball B5 with its real roughness profile and the ripple ball B5 approximated with a sine profile.

lubrication.

4.3.7 EHL friction and mixed/EHL transition

Thanks to numerical simulations, the physical origins of the mixed/EHL transition (micro-EHL or asperity contact) and the EHL friction were investigated. Fig. 4.13, presents the pressure distribution calculated both with the ripple profile of B5 ripple and the associated sine profile at $\eta_0 u_e = 1.0 \times 10^{-2}$ Pa.m, i.e. at the mixed/EHL transition. A close-up view distinguishes more clearly the pressure variations and the smooth pressure is reminded for comparison.

The pressure variations have the same general shape. Yet, when deduced from the ripple profile, they are sometimes higher or lower in comparison to sinus profile simulation. In fact, as it was shown in Fig. 4.7, the sine profile provides an average amplitude of the ripple profile. In the Reynolds equation, the roughness variations ($\partial h/\partial x$) directly influences the pressure gradient ($\partial p/\partial x$). Higher or lower amplitude would generate higher or lower pressure variations. Nonetheless, the ratio of the mean contact pressure from the sine profile over the mean contact pressure from the ripple profile is equal to 1 ± 0.001 for $\eta_0 u_e \in$

$[1.0 \times 10^{-2}, 1.0 \times 10^{-1}]$ Pa.m. Therefore, the sinusoidal approximation of the ripple texture can be supposed to provide the same under-pressure viscosity and then the same EHL friction considering the pressurized lubricant rheology follows a Cross law. In addition, the ratio of the ripple mean contact pressure over the smooth one is calculated. It also yields that the similar ratio 1 ± 0.001. Hence the ripples do not modify the mean contact pressure.

The Cross friction was calculated in EHL from numerical results as detailed in Chapter 2. An analytical Cross friction μ_{Cross} in EHL was also calculated directly from the experimental central film thickness in Fig. 4.4:

$$\mu_{Cross} = \frac{\mathcal{A}\ \eta(\dot{\gamma})\ \dot{\gamma}}{W}\ , \tag{4.22}$$

with $\mathcal{A}$ the contact area, W the load, η the Cross under-pressure viscosity and $\dot{\gamma}$ the shear rate calculated as:

$$\dot{\gamma} = \frac{u_s}{h_{av}} = \frac{u_s}{h_c + A_d/2}\ , \tag{4.23}$$

h_c is obtained from Fig. 4.4. Since h_c is the same for B5 and B6, A_d is taken as the average peak-to-valley amplitude of the ripple.

The numerical friction of B5, B6 ripple profiles, B5, B6 sine profiles and B4 waviness profile are plotted versus $\eta_0 u_e$ in Fig. 4.14. Analytical Cross friction in EHL is reported ($\star$) as well as experimental measured friction of B4, B5 and B6. For $\eta_0 u_e > 3.2 \times 10^{-2}$ Pa.m, every numerical simulations give the same friction coefficient as the smooth surface and fit the experimental measured data. Besides, the analytical Cross friction is in good agreement with the experimental friction coefficient for $\eta_0 u_e > 3.2 \times 10^{-2}$ Pa.m. It is slightly lower than the experimental measured data. The difference of friction coefficient ranges from 0 to 0.005. It may be attributed to the formula of h_c (see Eq. 4.7) which supposes that the central average film is equal to the smooth central film thickness and that the ripple texture is an uniform sinusoidal surface. Below 3.2×10^{-2} Pa.m, the numerical friction of B5 and B6 starts diverging from the smooth results whereas the numerical friction of B4 keeps superimposing the smooth results. Contrary to the transverse ripples, the transverse waviness does not modify the friction.

In Fig. 4.15, the shear stress in the contact center with the B5 sine wave modeling for $\Sigma = 8\%$ is plotted at 1.1×10^{-2} Pa.m and 1.0×10^{-1} Pa.m, which respectively correspond to conditions with a friction coefficient higher than and equal to the smooth case. The mean shear stress and the smooth shear stress are reported in full and dashed lines. For $\eta_0 u_e = 1.1 \times 10^{-2}$ Pa.m, the mean shear stress is higher than the smooth shear stress whereas for 1.0×10^{-1} Pa.m they are the same. Thus, when $\eta_0 u_e$ decreases, the mean shear stress starts diverging from

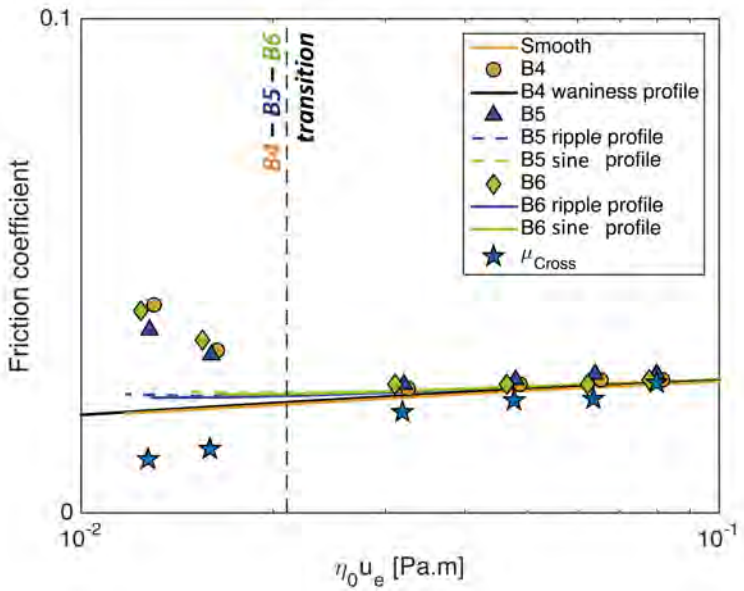

Figure 4.14: Friction of B5, B6 ripple profiles, B5, B6 sine profiles and B4 waviness profile versus $\eta_0 u_e$ at $\Sigma = 8\%$. Experimental friction measurements and calculated friction values from the film thickness modeling and from the measured lubricant film thickness are reported.

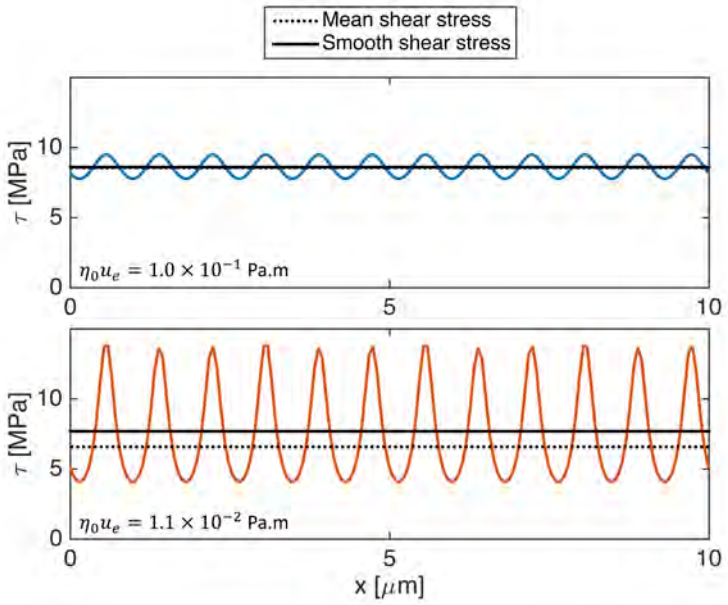

Figure 4.15: Shear stress of B5 with sine wave modeling at the contact center for $\Sigma = 8\%$. The mean shear stress and the smooth shear stress are reported in full and dashed lines.

the smooth reference, becoming higher. The shear stress is a growing function of the shear rate which is equal to:

$$\dot{\gamma}(x) = \frac{u_s}{h(x)} \ . \tag{4.24}$$

With a sine profile, the film thickness h is given by:

$$h(x) = h_{av} + \frac{A_d}{2} \cdot \sin\left(\frac{2\pi}{\lambda} x\right) \ . \tag{4.25}$$

For $A_d/2 \ll h_{av}$, i.e. at high $\eta_0 u_e$ conditions, it yields:

$$\dot{\gamma}(x) \approx \frac{u_s}{h_{av}} \ . \tag{4.26}$$

There, the shear rate is similar to the smooth case. The difference of mean pressure between the ripple simulations and smooth simulations is about 0.1-0.2%. As the mean contact pressure is kept unchanged, the ripple and smooth friction coefficient are the same. At $\eta_0 u_e = 3.2 \times 10^{-2}$ Pa.m, $h_{av} \approx (7/3)A_d/2$ and Eq. 4.26 is still valid. When h_{av} tends to $A_d/2$, the mean shear rate will increase. It yields a higher shear rate and friction coefficient.

Although the numerical transverse ripples increase the friction close to the transition, these numerical results are lower than the experimental values. The difference is respectively equal to 0.016 and 0.009 for $\eta_0 u_e = 1.3 \times 10^{-2}$ and 1.6×10^{-2} Pa.m. In the numerical calculations, no asperity contact was observed in the contact, thus, the friction is purely viscous. From Fig. 4.10a-b, the constriction represents respectively 8% and 3% of the contact for $\eta_0 u_e = 1.3 \times 10^{-2}$ and 1.6×10^{-2} Pa.m, assuming that the shear stress in the constriction region is due to the asperity contacts. The friction from the asperity contacts ($\mu_{BL} = 0.19$) is added to the numerical friction (μ_{EHL}) following the composite law used with the grooves (see Eq. 3.8). The composite friction coefficient yields respectively to 0.037 and 0.029 for $\eta_0 u_e = 1.3 \times 10^{-2}$ and 1.6×10^{-2} Pa.m and the difference with the experiments drops respectively to 0.003 and 0.004. This would indicate that the difference between numerical and experimental friction coefficient is due to the asperity contacts. Although the ripple texture generates micro-EHL effects which occurs below 3.2×10^{-2} Pa.m, their impact magnitude on the friction is far smaller in comparison to the friction due to asperity contacts which strongly raise the friction coefficient. Moreover, the waviness does not produce micro-EHL effects on the investigated $\eta_0 u_e$.

Besides, the analytical Cross friction strongly underestimates the friction coefficient below the mixed/EHL transition: it does not take into account the asperity contact shear stress. However, the analytical Cross friction is also lower than the numerical results. In fact, it approximates the shear rate as the ratio of u_s over h_{av}. As previously pointed out, this approximation is only accurate when $A_d/2 \ll h_{av}$.

To sum up, two phenomena rise around the mixed/EHL transition. Experimental observation shows that the first asperity contacts occur and numerical simulations report micro-EHL effects that increase the shear rate. The numerical results indicate that the micro-EHL effects happen below $\eta_0 u_e = 3.2 \times 10^{-2}$ Pa.m whereas the asperity contacts begin closer to 1.6×10^{-2} Pa.m. However, the micro-EHL effects are so small on the friction coefficient that they are hidden by the asperity contact shear stress.

4.4 Ripple amplitudes

From numerical and experimental data, some relations have been drawn for transverse ripple textures with a peak-to-valley of about 100 nm and a wavelength of about 1 µm. In this part, a twice as small and a twice as high ripple textures were investigated numerically to figure out if these relations still stand with varying amplitude. The numerical simulations were carried out with sine profiles as they

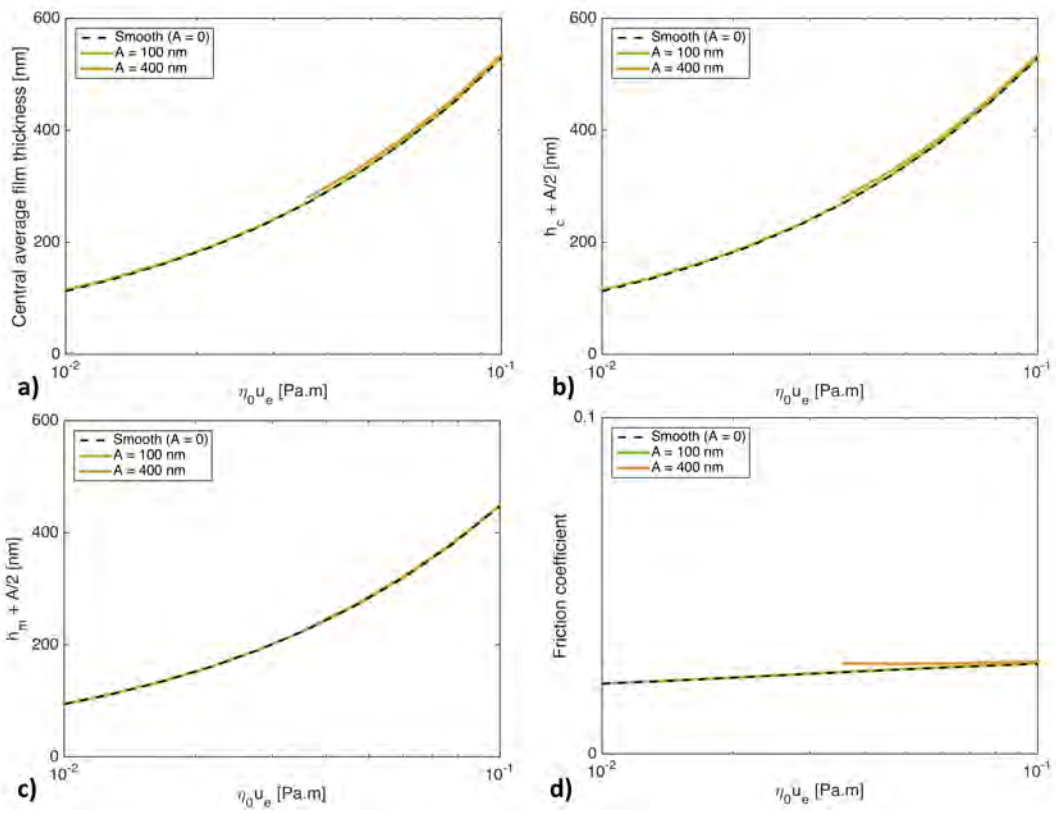

Figure 4.16: Central average film thickness, $h_c + A_d/2$, $h_m + A_d/2$ and friction coefficient versus $\eta_0 u_e$ for ripples with $A = 0$ (smooth), 100 and 400 nm and $\lambda = 1$ μm.

have shown good agreement with the real topographic profiles. The roughness is given by a sinusoidal function as Eq. 4.4 where the wavelength is set to 1 μm and the peak-to-valley amplitudes A are 100 and 400 nm. The central average film thickness, the quantities $h_c + A_d/2$, $h_m + A_d/2$ and the friction coefficient are respectively plotted versus $\eta_0 u_e$ in Fig. 4.16a-d for $A = 0$ (smooth), 100 and 400 nm.

Fig. 4.16a-d show that the amplitude variation produces no change of the investigated quantities: all curves superimpose the smooth surface results. This confirms and extends the previous results:

- the amplitude of the ripple textures does not influence the central average film thickness, $h_{av} = h_{c,s}$ (see Eq. 4.5),

- for the ripples $h_c = h_{c,s} - A_d/2$ and $h_m = h_{m,s} - A_d/2$ (see Eq. 4.7 and 4.10),
- the friction is not a function of A in EHL until $A_d/2 \ll h_{av}$ (see Fig. 4.14).

Moreover, the amplitude reduction is respectively of 97, and 99% for $A = 100$ and 400 nm; the EHL conjunction does not deform the ripple texture, which explains the independence of textured ball/disc gaps with the ripple amplitude A.

Regarding the friction coefficient, below $\eta_0 u_e = 6.0 \times 10^{-2}$ Pa.m and for $A = 400$ nm, it starts diverging from the smooth one. There, $h_{av} \approx 2(A_d/2)$ which is in agreement with the onset of the micro-EHL divergence in the previous section. The EHL friction rises due to similar micro-EHL effects as described in the previous section. For $A = 100$ nm, the friction coefficient is always equal to the smooth one.

4.5 Conclusion

Experimental Stribeck curve at $|\Sigma| = 8\%$ was obtained for three ripples surfaces of similar amplitude with various ripple orientations $\theta_s = 15$, 67 and 106°. The experimental similarity of the EHL friction and the mixed/EHL lubrication between B4, B5 and B6 suggested that θ_s is not significant in these cases. Numerical simulations confirmed this observation. Since the ripple textures are not deformed by the fluid pressure, the elastic deformation might be the same for B4, B5 and B6. Thus, the film thickness equation (see Eq. 2.20) of B4, B5 and B6 is the same except the roughness function $r(x, y, t)$. The different $r(x, y, t)$ functions are sine functions with almost the same wavelength and amplitude, only the orientation is different. Therefore, B4, B5 and B6 share the same pattern, i.e. the same film thickness, yet it is orientated differently. θ_s is not relevant in the lubrication mechanism as there is no elastic deformations of the texture.

Numerical results also demonstrated that the ripple surfaces are well-modeled with a sine function with similar amplitude and wavelength. This emphasized the predominant role of the amplitude of the ripple surfaces compared to that of waviness. In EHL, the ripple lubrication behaves as a smooth contact, which film thickness is decreased by the ripple amplitude $A_d/2$ ($= A/2$ for the ripple texture). This result bears on the fact that the central average film thickness is not modified with the ripples in EHL. The volume of lubricant carried inside the contact does not vary much from a smooth contact to the one with ripples. Nevertheless, the ripple amplitude reduces the film thickness (either central and minimum) leading to the onset of asperity contact responsible for the film thickness transition. The

film thickness transition was found to occur for $h_{m,s} = A_d/2$, corresponding to a critical Tallian parameter value equal to 1.7.

In the previous chapter, the lubricant film thickness of grooved surfaces was modeled as follow:

$$h_c = h_{c,s} + \left(\delta - \frac{A_d}{A_i}\,\frac{1}{\lambda}\right) v_{groove} \tag{4.27}$$

In the ripple case, $h_{av} = h_{c,s}$ so $\delta = 0$. There is no elastic deformation: $A_d/A_i = 1$. And the volume inside the ripple v_{ripple} is:

$$v_{ripple} = \int_0^{\lambda} \frac{A}{2}\left[1 + \sin\left(\frac{2\pi}{\lambda}x\right)\right] dx = \frac{A}{2}\,\lambda \tag{4.28}$$

Therefore using Eq. 4.27 with ripple parameters yields to:

$$h_c = h_{c,s} + \left(0 - 1\,\frac{1}{\lambda}\right)\frac{A}{2}\,\lambda = h_{c,s} - A/2. \tag{4.29}$$

This corresponds exactly to relation found in the present chapter. It demonstrates the pertinence of the formula in Eq. 4.27 and its potential use in optimizing one-dimensional textures.

When $A_d/2 \ll h_{av}$, the average shear rate is not modified by the presence of ripples as $h_{av} = h_{c,s}$ in EHL. Since the mean contact pressure is also not impacted, the ripple friction is equal to the viscous smooth EHL friction. At the mixed/EHL transition, micro-EHL effects increase the shear rate and so the friction coefficient; the mixed/EHL transition is physically due to micro-EHL effects. Then, asperity contact shear stress increasing the friction coefficient. The magnitude of micro-EHL effects is much smaller than the asperity contacts effects. In mixed regime, the friction is discriminated by the roughness through the ripple amplitude. The higher the amplitude, the rougher the surface and so the higher the friction. This difference is significant when the whole film thickness of the EHL contact drops to few nanometers at the film collapse. In fact, below the film thickness collapse, asperity contacts happen over more than 50% of the contact. Thus, the influence of the amplitude is magnified: the film collapse leads to the friction split.

Chapter 5

Cavity textures

Contents

Previous studies on cavity textures [4, 6, 100] showed that these surfaces are able to significantly affect the film thickness and friction in EHL. A cavity texture was investigated here to understand how the friction is affected when the cavity passes through an EHL contact. After the characterization of the cavity topography, experimental Stribeck curves performed at $|\Sigma| = 8$, 25, 50 and 100% are presented and their film thickness distribution is analyzed.

From the transport equation governing the film thickness in low pressure gradient regions, the location of the film thickness genesis is carried out regarding the position of the cavity. The line contact model was used as a complementary tool to qualitatively observe the influence of the cavity roughness and to obtain the pressure disturbance due to the cavity. Finally, the friction difference between the surface with cavities and the smooth surface was studied, investigating the role of the mean pressure inside the EHL contact.

5.1 Topography characterization

The ball made of AISI 52100-drilled steel with a radius of 9.525 mm was used in the experiments. It was polished to reduce its roughness until $S_q < 10$ nm. After polishing, the ball B7 was treated with femtosecond LASER irradiations to dig cavities on its surface. Its topography was measured with a Brucker optical interferometer and is displayed in Fig. 5.1a. The ball track of B7 is composed of one cavity row, oriented along the x direction, i.e. parallel to the entrainment direction. The cavity spacing ΔC_x along the x direction is emphasized. From a single cavity (see Fig. 5.1a), a 1D profile is extracted and displayed in Fig. 5.1b to determine the cavity depth d and diameter $\varnothing$.

As Fig. 5.1a illustrates $\Delta C_x = 250$ µm $= 2a$. Thus, there is always 'one' cavity in the contact, either an entire cavity or two cavity portions equivalent to a single one. The 1D profile in Fig. 5.1b respectively reports a diameter and a maximal depth of $\varnothing = 50$ µm and $d = 10$ µm. The bottom of the cavity is rough with few peaks and valleys. Given the presence of roughness inside the cavity, an upper C1 and lower C2 envelopes are determined from the 1D profile of Fig. 5.1b. According to the mathematical formula proposed by Mourier et al. [4] to model a cavity made with femtosecond LASER:

$$z(x) = d \cdot \cos\left(\frac{\pi}{2}\frac{x}{0.6\varnothing}\right) \exp\left[-2\left(\frac{x}{0.6\varnothing}\right)^2\right] , \tag{5.1}$$

the parameters of the two envelopes, C1 and C2, are determined and plotted in Fig. 5.1b. They have the same diameter $\varnothing = 50$ µm and their depth d are respectively equal to 3.5 and 10 µm.

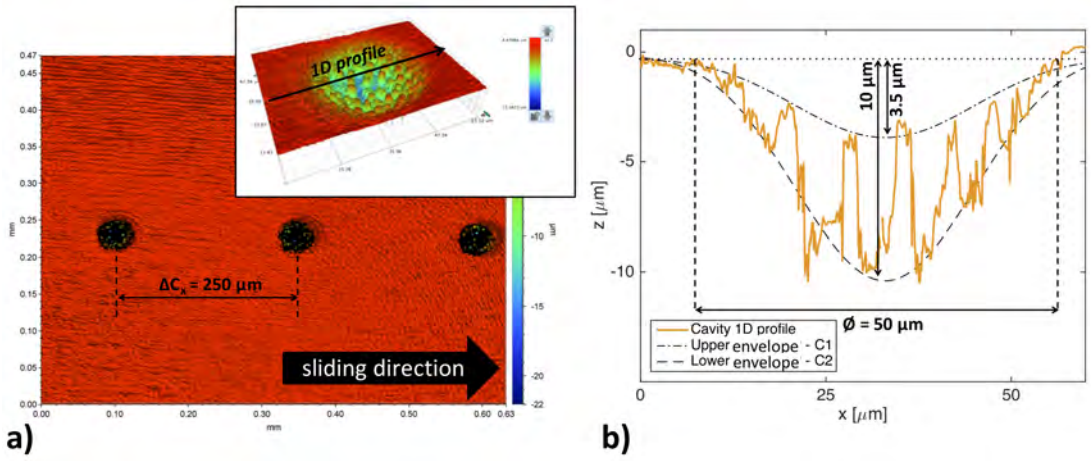

Figure 5.1: 3D-topography images of the ball B7 obtained by optical interferometry (a) with a zoom of a single cavity and the 1D profile extracted from this zoom in (b). The upper C1 and lower C2 envelopes of this profile are plotted with dash lines in (b).

Labels	d (µm)	$\varnothing$ (µm)	ΔC_x (µm)
B7	3.5-10	50	250
C1	3.5	50	-
C2	10	50	-

Table 5.1: Geometrical characteristics of the cavity surface B7 and mathematical profiles C1 and C2 where d, $\varnothing$ and ΔC_x are, respectively, the cavity depth, the cavity diameter and the spacing between two successive cavities.

All the geometrical characteristics of the cavity and the mathematical profiles are summarized in Table 5.1.

5.2 Stribeck experiments

5.2.1 Stribeck curves

Stribeck experiments were carried out with the ball B7 for $|\Sigma| = 8$, 25, 50 and 100%. The friction of B7 is reported in Fig. 5.2a-d versus $\eta_0 u_e$ for the four values of $|\Sigma|$ (Couette friction), $+\Sigma$ and $-\Sigma$. Fig. 5.2a-d also shows the B0 (smooth) friction as a reference. From Fig. 5.2a-d, the following trends are drawn:

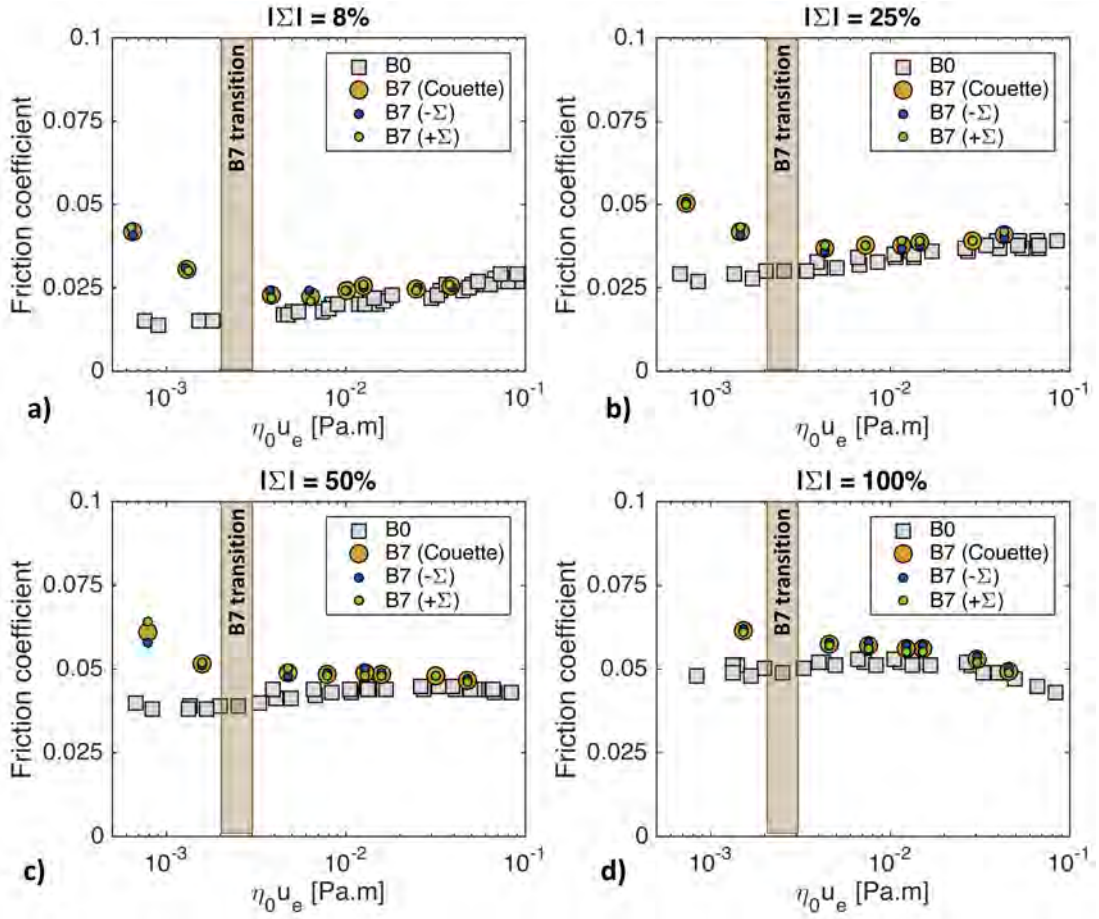

Figure 5.2: Friction coefficients measured for ball B7 versus $\eta_0 u_e$ at $|\Sigma| = 8$ (a), 25 (b), 50 (c) and 100% (d). The range of the mixed/EHL transition for ball B7 along the various SRR conditions is displayed in light brown. The Stribeck curve measured with the smooth ball B0 is indicated.

- no significant difference, on average, is observed between the Couette friction coefficient and the friction coefficients at $+\Sigma$ and $-\Sigma$. Thus, only the Couette friction is considered in the following,
- the friction coefficient measured for ball B7 is slightly higher than that measured for the smooth ball when $\eta_0 u_e > 2.0$ - 3.0×10^{-3} Pa.m,
- for $\eta_0 u_e < 2.0$ - 3.0×10^{-3} Pa.m, the friction coefficient of ball B7 strongly rises.

The mixed/EHL transition is defined as the intersection of the mixed and EHL friction tangents. From Fig. 5.2a-d, this regime transition occurs when $2.0 \times 10^{-3} < \eta_0 u_e < 3.0 \times 10^{-3}$ Pa.m, for $|\Sigma| = 8$, 25 and 50%. For $|\Sigma| = 100\%$, there are not enough data points to accurately determine it. Yet, the shape of the Stribeck curve suggests that the mixed/EHL transition may occur for similar $\eta_0 u_e$ range. For comparison, the smooth mixed/EHL transition is located at $\eta_0 u_e = 1.0 \times 10^{-3}$ Pa.m. The B7 cavity shifts this transition to slightly higher $\eta_0 u_e$ values.

As the sign of Σ does not influence the friction coefficient, the contribution of the Poiseuille flow in the friction is negligible compared to the contribution of the Couette flow. The friction in EHL is viscous and thus proportional to $|\Sigma|$. The increase in SRR significantly affects the friction coefficient magnitude but hardly any on the location of the mixed/EHL transition.

5.2.2 Film thickness distribution

Although no significant difference in terms of friction was found between $+\Sigma$ and $-\Sigma$, the film thickness distribution was sensitive both to the sign of Σ (i.e. the sign of the sliding velocity) and to $|\Sigma|$. To exemplify, representative contact interferograms are reported for minimum and maximum SRR values ($|\Sigma| = 8$ and 100%) at both SRR signs.

Fig. 5.3 shows two contact interferograms for $\eta_0 u_e = 1.8 \times 10^{-2}$ Pa.m at $\Sigma = -8\%$ and -100%. In these images, the cavity is more or less located at the center of the contact. A zone of modified thickness is located around the cavity and can be extended in the upstream direction. The location and the value of the minimum film thickness in the constriction region h_m and the minimum film thickness generated by the cavity h_- are shown. The corresponding central film thickness profiles are also plotted. h_c is determined as the average film thickness at the contact center when the cavity is at the EHL contact edge. Given the resolution of the camera (2.16 μm/px), the cavity slopes cannot be measured and are thus indicated with dash lines.

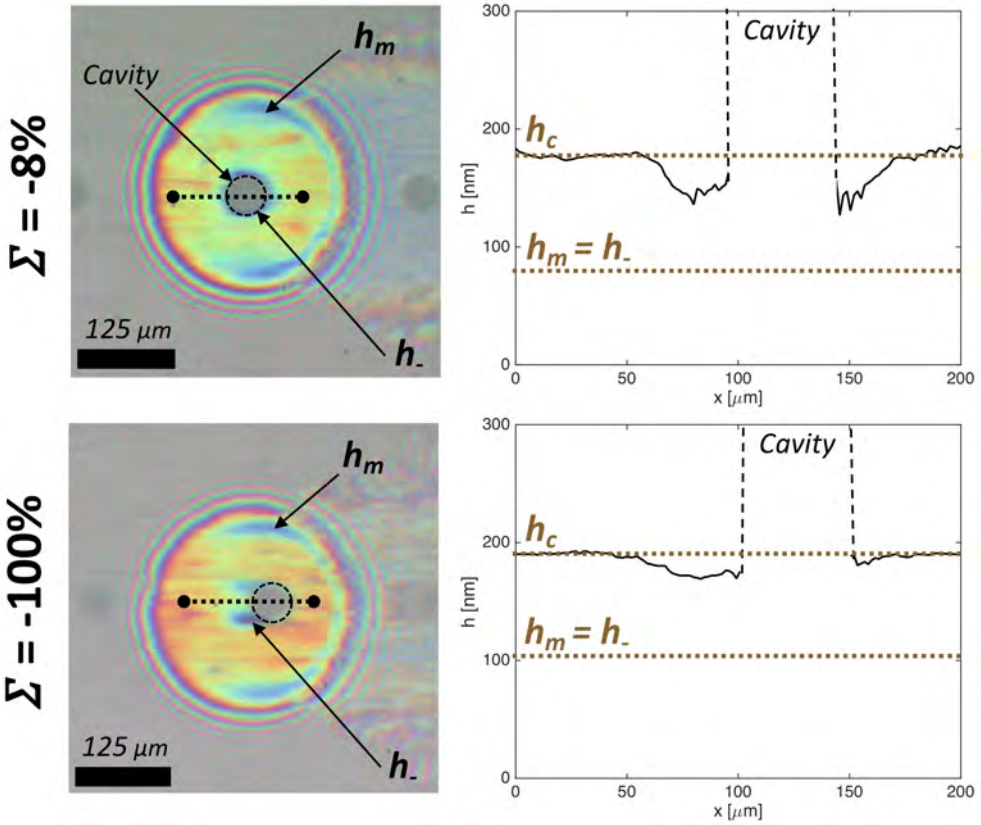

Figure 5.3: Contact interferograms at $\eta_0 u_e = 1.8 \times 10^{-2}$ Pa.m under $\Sigma = -8\%$ and -100%. Their respective central film thickness profile is displayed beside to highlight the film thickness disturbances. The fluid goes from left to right.

For $\Sigma = -8\%$, the central film thickness is equal to 178 nm which is higher than the smooth one $h_{c,s} = 160$ nm in the same working conditions. The minimum film thickness in the constriction region h_m is equal to 77 nm and similar to the minimum film thickness formed in a smooth contact. Moreover, the cavity generates a film thickness modification at its edges. There and for that peculiar position of the cavity inside the contact, the film thickness is reduced. The film thickness reduction can locally reach down to values close to the minimum film thickness h_m. The minimal film thickness reduction is referred to h_-. At $\Sigma = -100\%$, the cavity generates a much higher $h_c = 190$ nm than smooth surfaces which central film thickness is $h_{c,s} = 154$ nm (close to -8% SRR conditions). A film thickness reduction region also spreads in the contact toward the upstream direction. The thickness h_- surrounds the area in which the film thickness distribution is modified by the cavity. h_- and h_m are equal to 102 nm which is higher than the minimum film thickness with smooth surfaces.

In addition, Fig. 5.4 shows two contact interferograms for the same $\eta_0 u_e = 1.8 \times 10^{-2}$ Pa.m but with positive SRR: $+8\%$ and $+100\%$. The corresponding central film thickness profiles are plotted and the cavity slopes are marked with dash lines. For $\Sigma = +8\%$, the film thickness distribution is analog to that obtained with $\Sigma = -8\%$ (h_c and h_m) except that the film thickness reduction region is larger at the cavity front. Over the whole region of film thickness reduction, h_- at $\Sigma = +8\%$ is only 5 nm less than h_- at $\Sigma = -8\%$. Similarly, at $\Sigma = +100\%$ and $\Sigma = -100\%$, the central and minimal film thicknesses are the same. Nonetheless, the film thickness distribution modified by the cavity spreads in the contact toward the downstream direction and leads to a film thickness reinforcement which maximum film thickness is referred to h_+. The film thickness increase is located at the center of the film thickness modifications, with $h_+ = 269$ nm. On its edges, the film thickness reaches $h_- = 66$ nm, much lower than h_- at $\Sigma = -100\%$. On the film thickness profile at $\Sigma = +100\%$, the film thickness is reduced at the cavity rear. Yet the film thickness in the area located at the cavity rear is, in average, close to h_c. This lower film thickness may not be attributed to the cavity influence but to a local nanoscale defect.

In their works, Mourier et al. [96, 121, 97] and Krupka et al. [102, 100, 101] noticed that the film thickness modified by the cavity spreads respectively in the upstream and downstream directions, for negative and positive SRR. This is in agreement with the present observations of B7. In the particular case of pure rolling, they showed that the lubrication modification surrounded the cavity did not spread into the contact. The extension of area, where the local film thickness is modified by the cavity, starts as soon as $\Sigma \neq 0$ and is all the more important that $|\Sigma|$ is high. Thus, the disruption of the local lubricant is low and only concerns a small area confined around the cavity for the very low SRR such as

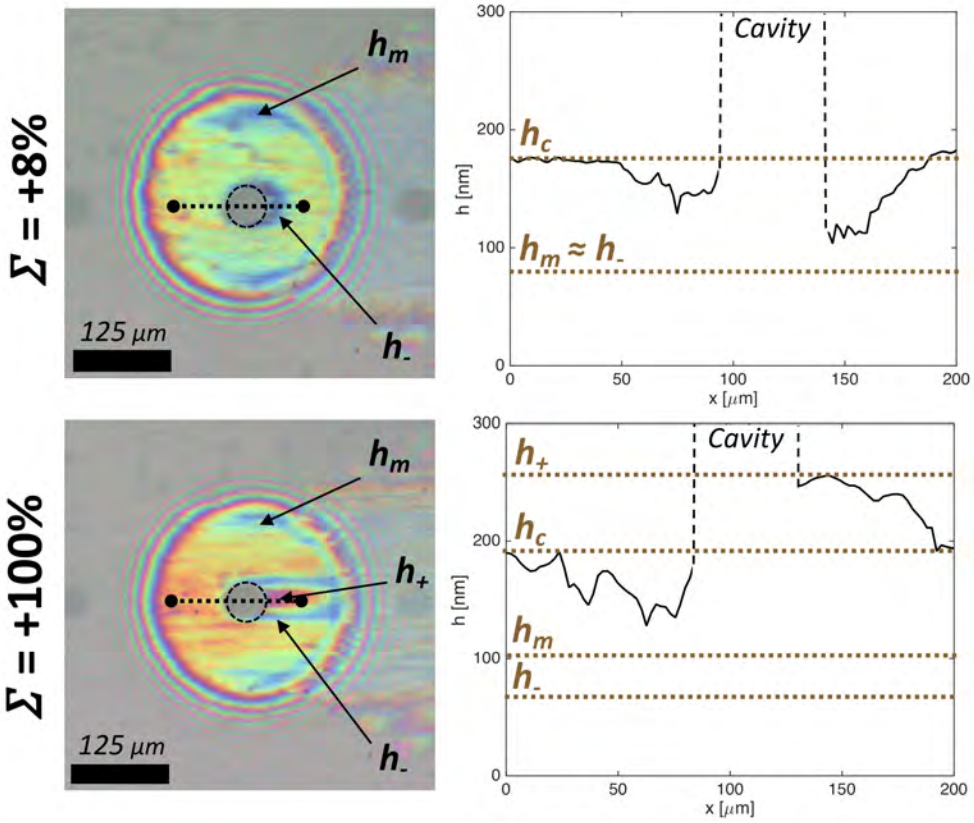

Figure 5.4: Contact interferograms at $\eta_0 u_e = 1.8 \times 10^{-2}$ Pa.m under $\Sigma = +8\%$ and $+100\%$. Their respective central film thickness profile is displayed beside to highlight the film thickness disturbances. The fluid goes from left to right.

$|\Sigma| = 8\%$. In this case, the film thickness distribution differs little from that of a pure rolling contact.

5.2.3 Central and minimal film thickness - h_c and h_m

The measurement of the central and minimal film thicknesses from the previous Stribeck experiments presented in Fig. 5.2, are plotted in Fig. 5.5a-b versus $\eta_0 u_e$ for $|\Sigma| = 8$, 25, 50 and 100%. The smooth central and minimal film thicknesses are marked (□). The B0 and B7 friction transitions are highlighted. The figure confirms that for a wide range of $\eta_0 u_e$, the film thicknesses h_c and h_m measured for ball B7 are slightly higher than that generated by the smooth ball B0. The increase is more significant at high $\eta_0 u_e$. Nonetheless, no general trend on the SRR influence upon h_c and h_m can be drawn over the investigated range of $\eta_0 u_e$ and SRR conditions.

As the minimum film thickness for B7 is similar to that of B0 at the transition, the onset of the asperity contacts in the constriction region with ball B7 should happen at a lower or the same $\eta_0 u_e$ value as the smooth surface B0 (B0 asperity contact onset in the constriction region, coincides with the B0 mixed/EHL transition). However, the B7 mixed/EHL regime transition takes place for all SRR conditions around $\eta_0 u_e = 2.0$ - 3.0×10^{-3} Pa.m which is higher than the $\eta_0 u_e$ value at which the mixed/EHL transition occurs for the ball B0. Therefore, either asperity contacts occurs elsewhere in the contact or micro-EHL effects are able to raise the viscosity and friction, for ball B7.

5.2.4 First asperity contacts

To tackle the onset of the asperity contacts, the thinnest film thickness generated by the cavity h_-, for a given SRR is investigated. h_- is plotted versus $\eta_0 u_e$ for $|\Sigma| = 8$, 25, 50 and 100% in Fig. 5.6. The B7 mixed/EHL transition is reminded with a vertical dash line. Fig. 5.6 shows that h_- is an increasing function of $\eta_0 u_e$. Yet, no general trend comes out on the SRR influence upon h_- though previous contact interferograms of Fig. 5.3 and 5.4 indicated a possible increase of h_- when $|\Sigma|$ rises. Therefore, no significant influence of the SRR on the h_- value is assumed.

Besides, h_- becomes null, for $\eta_0 u_e = 2.0 \times 10^{-3}$ Pa.m and lower values, i.e. just at the B7 mixed/EHL transition. Thus, asperity contacts start occurring in the region where the film thickness is reduced by the cavity. Therefore, if the mixed/EHL transition of ball B7 is supposed to be caused by the onset of the asperity contacts, it is mainly governed by the thinnest film thickness h_-

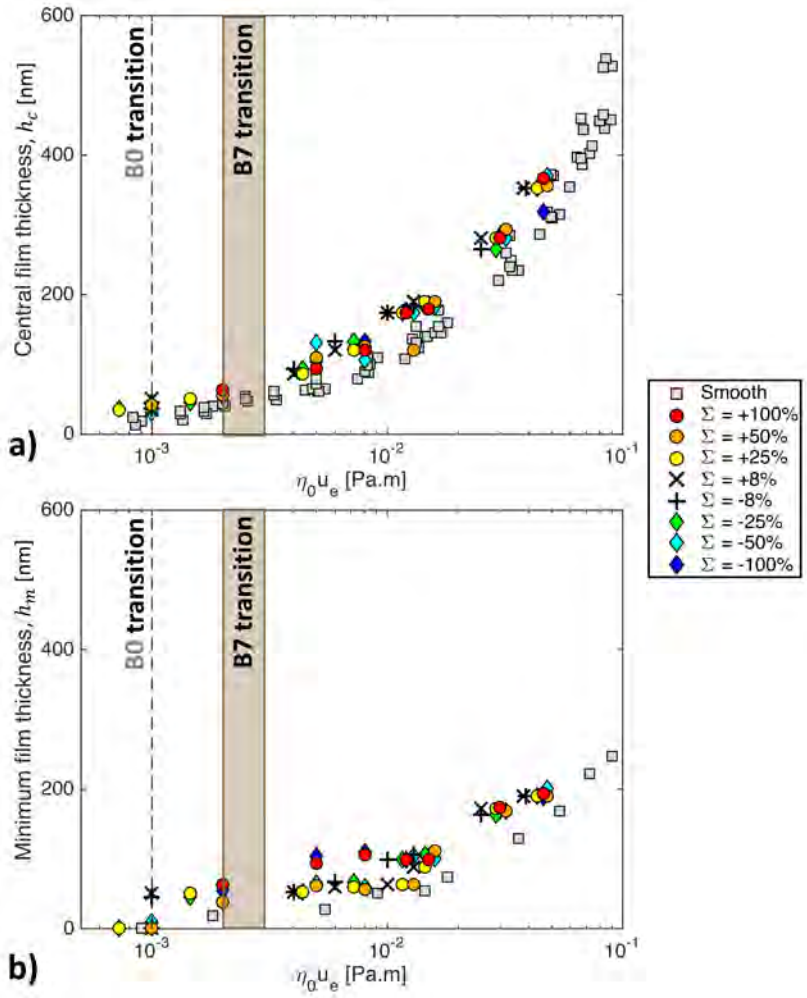

Figure 5.5: Central (a) and minimal (b) film thicknesses formed with ball B7 versus $\eta_0 u_e$ for $|\Sigma| = 8$, 25, 50 and 100%. The B0 and B7 friction transitions and the central and minimal film thicknesses formed with the smooth ball B0 are marked with gray squares.

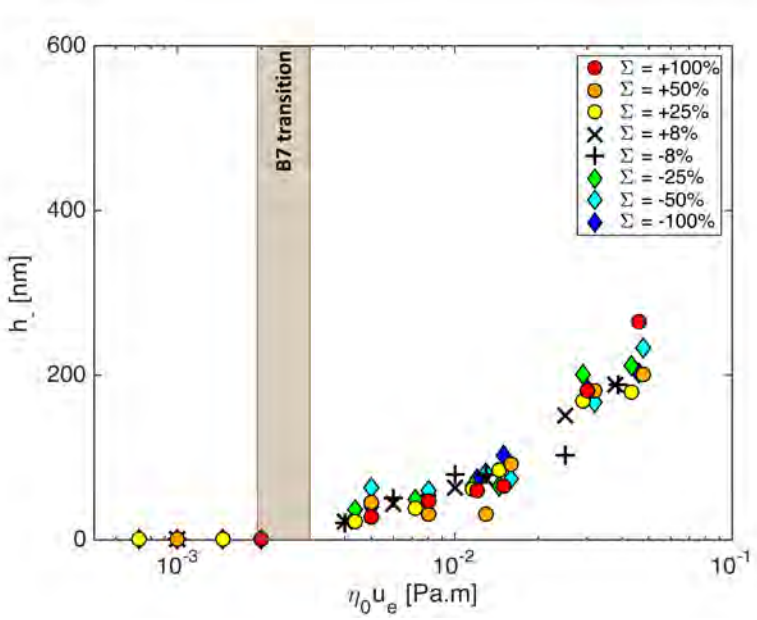

Figure 5.6: The thinnest film induced by the cavity h_- versus $\eta_0 u_e$ for $|\Sigma| = 8$, 25, 50 and 100%. The B7 mixed/EHL transition is shown.

due to the cavity. The independence of the latter versus the SRR explains why the mixed/EHL transition is not strongly influenced by the SRR, as previously observed in the Stribeck curves from Fig. 5.2.

5.2.5 Film thickness reinforcement

Among the several Stribeck experiments, no local film thickness increase above the central film thickness (h_+) was observed for $\Sigma < +25\%$. The capacity of the cavity to locally increase the film thickness in comparison to its central film thickness is determined by plotting the quantity $h_+ - h_c$ (B7 central film thickness) versus $\eta_0 u_e$ for $\Sigma = 8$, 25, 50 and 100% and when the cavity is located at the contact center (see Fig. 5.7). The B7 mixed/EHL transition is highlighted. Substantial film thickness increases occur at high $\eta_0 u_e$ for $\Sigma = +50$ and $+100\%$. Below 3.0×10^{-2} Pa.m, $h_+ - h_c < 10$ nm for $\Sigma = +25$ and $+50\%$. On the contrary, $h_+ - h_c$ ranges from 34 to 123 nm for $\Sigma = +100\%$ until the mixed/EHL transition. Below the mixed/EHL transition no more positive lubrication effect occurs for $\Sigma < +100\%$. As h_c does not significantly depend on the SRR, it is inferred that the higher the SRR, the thicker the h_+.

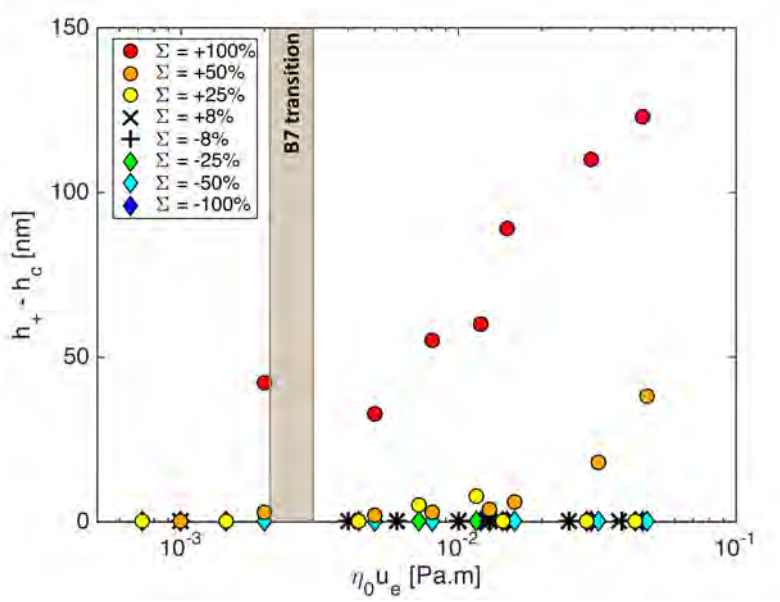

Figure 5.7: $h_+ - h_c$ versus $\eta_0 u_e$, for $|\Sigma| = 8$, 25, 50 and 100%. The B7 mixed/EHL transition is emphasized.

5.3 Influence of cavity geometry and topography

Mourier et al. [4] pointed out the importance of the depth in the ability of the cavity to increase or reduce locally the film thickness. At $\Sigma = +100\%$ and $\eta_0 u_e = 1.2 \times 10^{-2}$ Pa.m, Mourier et al. stated that a cavity, with $\varnothing = 57$ µm and a smooth bottom, is not able to increase the film thickness if its depth d is larger than 2.1 µm. However, the cavities of ball B7 increase the film thickness for such conditions (see Fig. 5.7) whereas their depth, due to the roughness, is between 3.5 and 10 µm. The difference of cavity diameter is not supposed to be significant. According to Mourier et al. for a given depth, a smaller cavity diameter leads to a smaller film thickness increase. Therefore, the cavities of ball B7 ($\varnothing = 50$ µm) would have a lubrication efficiency even weaker than a Mourier's cavity ($\varnothing = 57$ µm) at equivalent depth, i.e. no film thickness increase. The roughness inside the ball B7 was then investigated as a possible reason of the above contradictory observations. Indeed, Ninove et al. [6] experimented a cavity ($\varnothing = 60$ µm) with a heterogeneous rough bottom. One part of the cavity had a mean depth of 0.6 µm and induced, downstream the cavity, a film thickness reinforcement. On the contrary, the other part of the cavity had a mean depth of 0.2 µm and led, downstream the cavity, to a film thickness reduction. Therefore, Ninove et al.

pointed out the possible importance of the cavity roughness.

The line contact model was used to qualitatively compared the cavity profiles C1 and C2 previously described that could be representative of the effects of the cavity shapes and that of B7 from Fig. 5.1b. The cavity bottom of C1 and C2 is smooth whereas it is rough for the B7 profile. Numerical simulations were run on a mesh with 512 nodes over the domain $X \in [-2.5, 1.5]$ at $\Sigma = +100\%$ for $\eta_0 u_e$ values ranging from 1.0×10^{-2} to 1.0×10^{-1} Pa.m. The cavity center position is set to $X = -3$ at $T = 0$. All material and lubricant parameters are equal to that of the experimental conditions. Fig. 5.8a reports the film thickness distribution obtained for the model profiles C1, C2 and the B7 profile when the cavity center is in $X = 0$ for $\eta_0 u_e = 3.6 \times 10^{-2}$ Pa.m. For $\eta_0 u_e < 3.6 \times 10^{-2}$ Pa.m, the film thickness with the B7 profile became negative during the numerical simulations and thus cannot be reported. The numerical smooth film thickness is shown with a dash line for comparison. The maximal film thickness increase h_+, due to the profile cavities C1, C2, the B7 profile and the B7 experiments, minus their central film thickness h_c is plotted versus $\eta_0 u_e$ for $\Sigma = +100\%$, in Fig. 5.8b.

Fig. 5.8a shows a film thickness increase at the cavity front with the model profile C1 and to a lesser degree with C2. On the contrary, the rough cavity from the B7 profile does not increase the film thickness. Moreover, at the cavity rear, the film thicknesses of the model profiles C1, C2 and the B7 profile are reduced as compared to the smooth reference. Fig. 5.8b confirms that C1 provides the best increase among the three cavity profiles. Such as in the experiments with ball B7, C1 reinforces the film thickness whereas below, respectively, 1.3×10^{-2} and 4.6×10^{-2} Pa.m, the C2 and B7 profiles do not increase the central film thickness anymore. The B7 experimental values are, nonetheless, higher than those from the profile C1.

In conclusion, simulations of the C1 profile qualitatively matched the B7 experiments. When considering only the fluid on the upper envelope of the cavity roughness, the numerical simulations better predict the lubrication response of the cavity, i.e. the occurrence of a film thickness increase. Therefore, the roughness of the cavity bottom influences the lubrication of the cavity as previously mentioned by Ninove et al. [6]. The fluid trapped in the roughness of the cavity bottom may act differently than modeled by the Reynolds equation. For example, the assumption stating that the pressure is the same along the z direction may not be valid in this case. To qualitatively predict the tribological response of a rough cavity, one can use only the upper envelope of the cavity bottom roughness. For quantitative predictions, Navier-Stokes' equations might be considered instead.

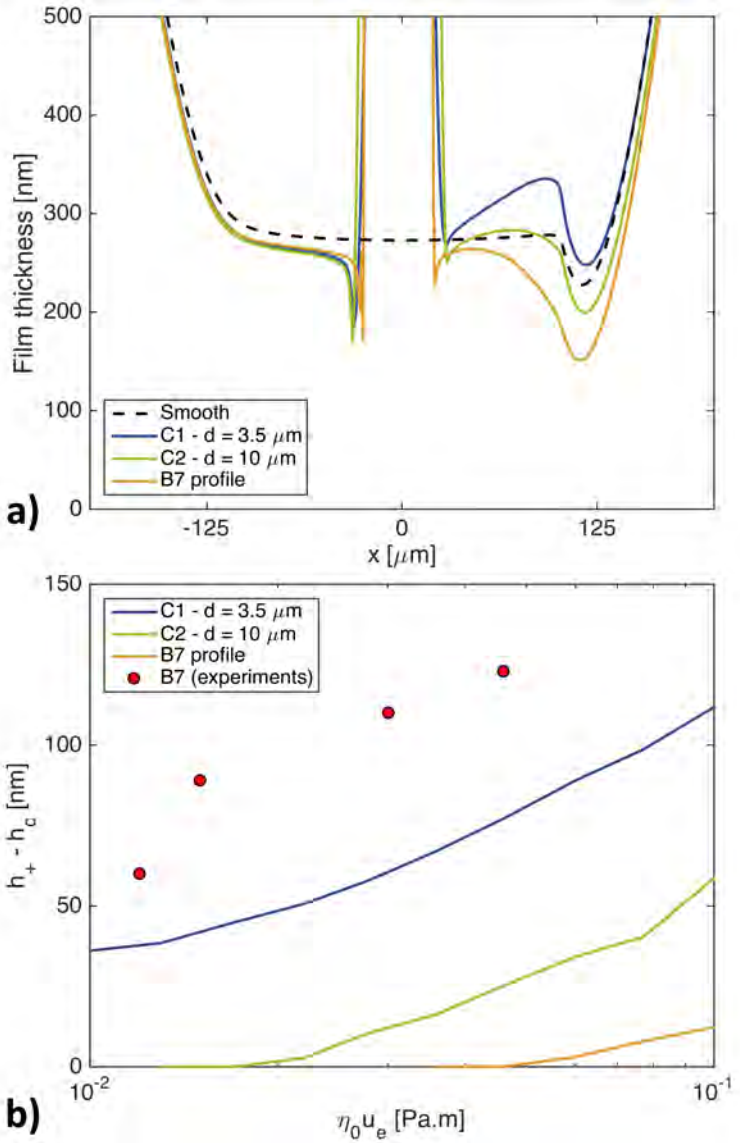

Figure 5.8: Film thickness distributions calculated for the model cavity profiles C1 and C2 and the real B7 cavity profile, when the cavity center is in the center of the contact ($x = 0$) at $\Sigma = +100\%$ and $\eta_0 u_e = 3.6 \times 10^{-2}$ Pa.m. The smooth film thickness profile is displayed with a dash line (a). Maximal film thickness increase h_+ minus the central film thickness h_c versus $\eta_0 u_e$, for C1, C2, B7 cavity profile and B7 experiments at $\Sigma = +100\%$ (b).

5.4 Characteristic thickness distribution of B7 cavity

The geometry shape and the topography are undoubtedly responsible for the film thickness modifications. However, this geometry induces different effects regarding the cavity position (see Fig. 5.9a). A new approach is described in the following to characterize the tribological response of a given cavity and to determine the correlation between the film thickness variations induced by the cavity and the location of the cavity.

With the cavities of ball B7, only positive SRR conditions were able to generate both an increase h_+ and a reduction h_- of the film thickness. Therefore, only positive SRR conditions were carried out in this section, in order to determine the cavity locations leading to film thickness increase and reduction.

5.4.1 Transport equation

As supposed in the Ertel's approach [15], the pressure can be considered as constant in the zone of the contact where no high pressure gradients caused by either the EHL constriction or the cavity are located. In these regions, the Reynolds equation in line contact then becomes a simple transport equation:

$$\frac{\partial h}{\partial t} = -u_e \frac{\partial h}{\partial x} \ . \tag{5.2}$$

It yields on the center line that $h(x, y = 0, t) = h(x - u_e t)$. The film thickness travels at u_e, i.e. at the mean velocity of the fluid flow whereas the cavity runs at u_2. Eq. 5.2 is supposed to be verified on the interval $[\max(-a, x_c(t)), 0.75a]$, with $x_c(t)$ the position of the cavity front at the time t and $x = 0.75a$ a lower estimation of the constriction onset, obtained from contact interferograms (see Fig. 5.3 and 5.4). The film thickness in this region was measured at different times for $\eta_0 u_e = 1.8 \times 10^{-2}$ Pa.m (same conditions as Fig. 5.3) and $\Sigma = +8$, $+25$, $+50$ and $+100\%$.

The images of interferograms (see Fig. 5.9a) were acquired with a high-speed camera when a cavity passes through the contact. The time between two consecutive shots was equal to 312.5 µs. As illustrated in Fig. 5.9a-c, the first image used to characterize the beginning of the passage of the investigated cavity was acquired when the cavity front $x_c(t)$ was located in $-1.5a$. The corresponding time was referred to $t = t_0$. The last image that marks the end of passage of the cavity through the contact was taken when $x_c(t) = 0.75a$, referred to $t = t_{end}$

when the cavity was reaching the constriction region. For $t \in [t_0, t_{end}]$, the position of the cavity front was located at $x_c(t)$ and the film thickness along the center line was measured as follows:

- when the cavity was outside the contact, the measured profile starts from the onset of the Hertzian contact toward the previous cavity ($t = t_0$),
- when the cavity was inside the contact, the profile was measured from the front of the cavity toward the onset of the constriction region ($t > t_0$).

Since the film thickness is supposed to follow Eq. 5.2, the film thickness profiles, at different time t, were rescaled in order to be superimposed and more easily compared (see Fig. 5.10). This is why the film thickness profiles of Fig. 5.10 were plotted in the cavity referential. Thus, the lubricant film thickness was plotted for $\eta_0 u_e = 1.8 \times 10^{-2}$ Pa.m and $\Sigma = +100\%$ versus the rescaling abscissa $\tilde{x}(t)$ defined as:

$$\tilde{x}(t) = [x - u_e t] - [x_c(t_{end}) - u_e t_{end}] = x - x_c(t_{end}) + u_e \times (t_{end} - t) \ . \quad (5.3)$$

Each dot represents the film thickness on an interferogram pixel, with a pixel size of 2.16 μm, at a position $\tilde{x}(t)$ for a given time t. Each color corresponds to a film thickness profile extracted at a time t. The film thicknesses h_c, h_m, h_+ and h_- are reminded with dash lines.

It is remarkable that all points collapse on a single master curve. For $160 \leq \tilde{x}(t) \leq 275$ μm, the film thickness is lower than h_c and corresponds to the cavity-induced film thickness reduction. In Fig. 5.10, the minimal film thickness is equal to 105 nm. As $h_- = 66$ nm is located on the border of the area where the film thickness is modified by the presence of the cavity, it is not observed in Fig. 5.10 which comes from h measurements on the center line of the EHL contact. The maximal film thickness of the master curve is equal to 269 nm, i.e. h_+.

5.4.2 Characteristic film thickness distribution

By using the transport equation, it is possible to retrieve for each thickness value $h(\tilde{x}(t))$ the time and then the location where this film thickness was generated. The characteristic film thickness distribution when the cavity passes in the EHL contact is then plotted. Two cases can occur: $h(\tilde{x}(t))$ was generated either at the front of the cavity or at the entrance of the EHL contact. When the cavity is inside the contact, the transported film thickness is generated at the cavity front $x_c(t)$ whereas it is generated at $x = -a$ when $x_c(t) < -a$. In the first case, the

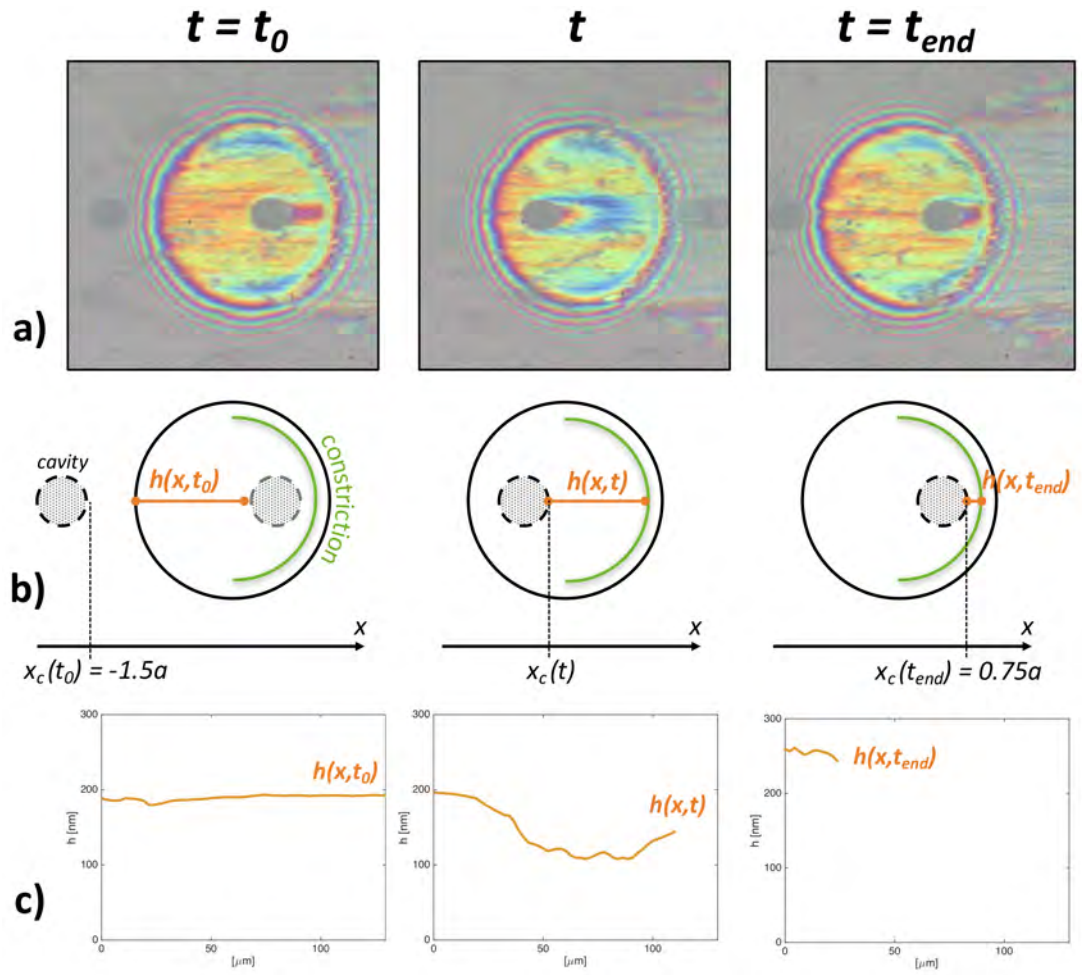

Figure 5.9: Contact interferograms at time t_0, t and t_{end} for $\eta_0 u_e = 1.8 \times 10^{-2}$ Pa.m and $\Sigma = +100\%$ (a). Schemes showing the location of the measured film thickness at t_0, t and t_{end} (b). Measured film thickness profiles at t_0, t and t_{end} (c).

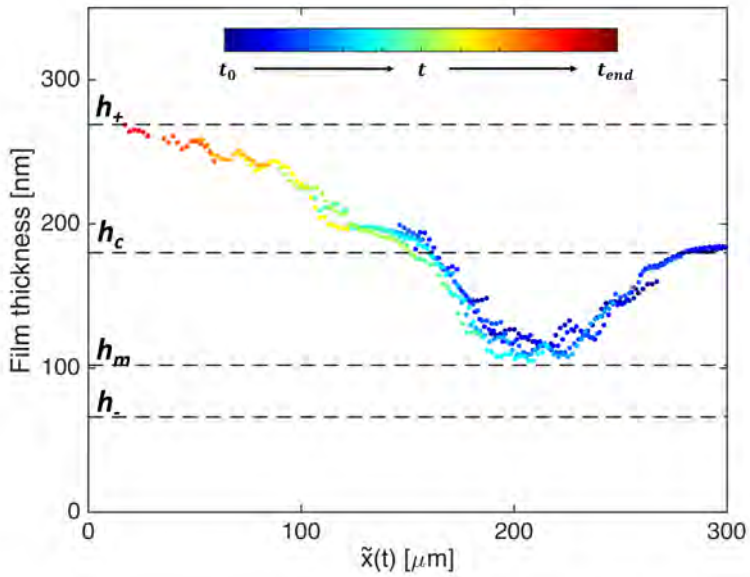

Figure 5.10: Film thickness profiles in the contact between the cavity front and the constriction region versus $\tilde{x}(t)$ for $\eta_0 u_e = 1.8 \times 10^{-2}$ Pa.m and $\Sigma = +100\%$. Each color corresponds to a different time t. h_c, h_m, h_+ and h_- are reminded with horizontal dash lines.

generation of $h(\tilde{x}(t))$ happened at $t_1 = t_{end} - \Delta t_1$ with Δt_1:

$$u_e \Delta t_1 = u_2 \Delta t_1 + \tilde{x}(t) \ , \tag{5.4}$$

and in the second one, the generation of $h(\tilde{x}(t))$ happened at $t_2 = t_{end} - \Delta t_2$ with Δt_2:

$$u_e \Delta t_2 = x_c(t_{end}) + a + \tilde{x}(t) \ . \tag{5.5}$$

The minimal value $\min(\Delta t_1, \Delta t_2)$ from Eq. 5.4 and 5.5, gives the location of the film thickness generation. In Fig. 5.11, the characteristic thickness distribution of B7 is reported: $h(\tilde{x}(t))$ is plotted at $\eta_0 u_e = 1.8 \times 10^{-2}$ Pa.m and $\Sigma = +8$, $+25$, $+50$ and $+100\%$ versus the cavity front position $x_c(t)$ defined by:

$$\begin{aligned} x_c(t) &= x_c(t_{end}) - u_2 \Delta t \ , \\ \Delta t &= \min\left(\frac{\tilde{x}(t)}{u_e - u_2}, \frac{x_c(t_{end}) + a + \tilde{x}(t)}{u_e} \right) \ . \end{aligned} \tag{5.6}$$

Given that $u_2/u_e = 1 - \Sigma/2$, Eq. 5.6 yields:

$$x_c(t) = x_c(t_{end}) - \left(1 - \frac{\Sigma}{2}\right) \cdot \min\left(\frac{2\tilde{x}(t)}{\Sigma}, x_c(t_{end}) + a + \tilde{x}(t) \right) \ . \tag{5.7}$$

For $x_c(t) < -a$, Fig. 5.11 reports the film thickness generated in $x = -a$ versus the cavity front position $x_c(t)$. For $x_c(t) > -a$, Fig. 5.11 shows the film thickness generated in $x = x_c(t)$ versus the cavity front position $x_c(t)$.

When the cavity front is located before $-1.5a$, the film thickness generated in $x = -a$ is not disturbed by the cavity and is equal to h_c. As soon as the cavity front enters the region of the contact inlet defined by the position interval $[-1.5a, -a]$, the film thickness produced in $-a$ starts decreasing. It reaches its minimal value around $x = -a$ except for $\Sigma = +50\%$. At this peculiar SRR, the position of the minimal film thickness is slightly shifted inside the contact. A minimal value of around 65 nm (i.e. close to h_-) is reached for $\Sigma = +8$ and $+50\%$. For $\Sigma = +25$ and $+100\%$, the minimal value is around 100 nm. Then, the film thickness generated at the cavity front starts rising roughly linearly with different slopes, which depend on the SRR. This increase leads to an improvement of the film-forming capability at $\Sigma = +50$ and $+100\%$ by producing a lubricant film thicker than h_c. At $\Sigma = +25\%$ the lubrication barely reaches h_c and at $\Sigma = +8\%$ it is always lower than h_c.

In addition, the slopes measured when the film thickness starts increasing in Fig. 5.11 were plotted versus the SRR in Fig. 5.12. According to the experiments in pure rolling from Mourier et al [4], the cavity causes a slight film thickness reduction when approaching the contact. However, when the dimple passes through

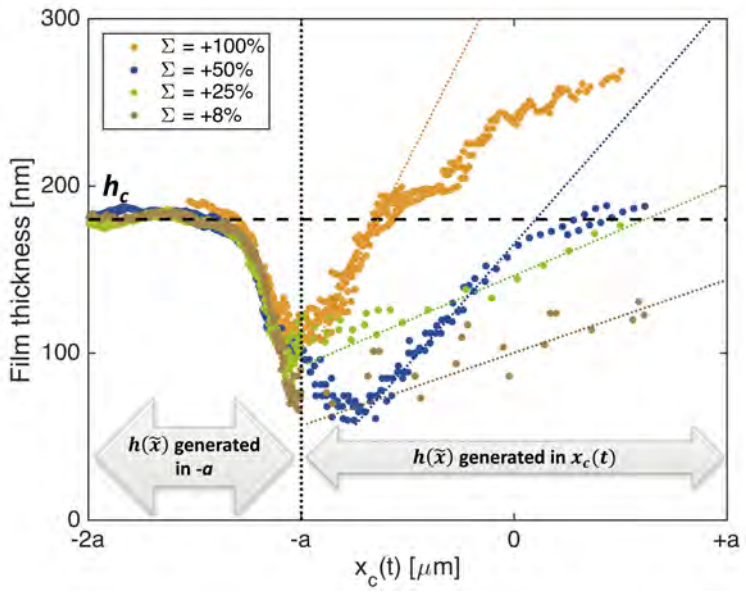

Figure 5.11: Characteristic thickness distribution of B7 according to the position of the cavity front in the contact at $\eta_0 u_e = 1.8 \times 10^{-2}$ Pa.m and for $\Sigma = +8$, +25, +50 and +100%. The curve slopes when the film thickness starts rising are emphasized with dash lines.

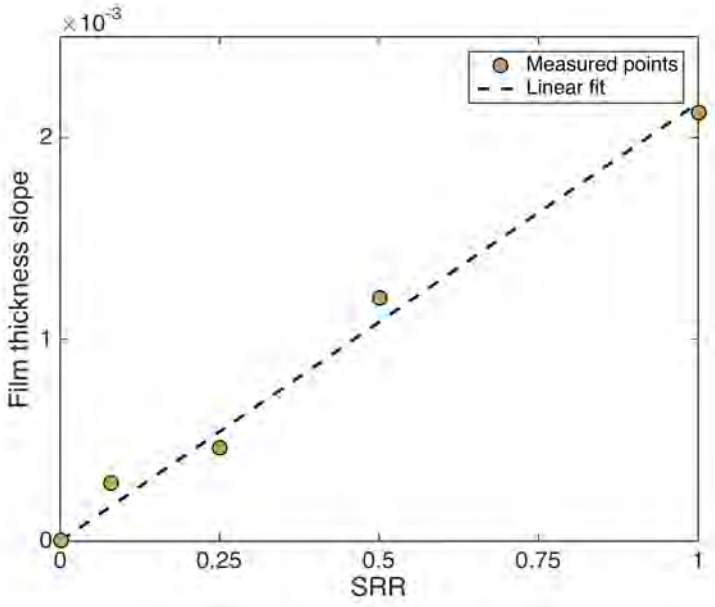

Figure 5.12: Film thickness slopes from Fig. 5.11 versus the SRR at $\eta_0 u_e$ = 1.8 × 10^{-2} Pa.m. The linear fit of the data is reported in dash line.

the contact, the area in which the film thickness is changed remains constant and does not extend downstream. Therefore, the slope for $\Sigma = 0\%$ is null. This peculiar point was added to Fig. 5.12. Then, a linear fit passing by the origin $(0, 0)$ can be used to approximate the curve of Fig. 5.12. It yields that the film thickness slope is equal to 2.2 × 10^{-3} Σ.

To summarize, when the cavity approaches the EHL contact, the generated film thickness in $x = -a$ is reduced to $h_{-a}(\Sigma)$. Then, the film thickness starts rising with a gradient that is an increasing function of the SRR: $f(\Sigma)$. Therefore, when the cavity is inside the contact, the evolution of the film thickness in Fig. 5.11 can be expressed by:

$$\forall x_c(t) \in [-a, a],\ h(\tilde{x}(t)) = h_{-a}(\Sigma) + f(\Sigma) \cdot (x_c(t) + a)\ , \tag{5.8}$$

with $f(\Sigma) = 2.2 \times 10^{-3}\ \Sigma$ at $\eta_0 u_e = 1.8 \times 10^{-2}$ Pa.m. In Eq. 5.8, the film thickness modification produced by the cavity in the contact is the sum of two contributions that both depend on the SRR: the first one, $h_{-a}(\Sigma)$, comes from the inlet (low pressure zone of the contact) and the second one, $f(\Sigma) \cdot (x_c(t) + a)$, comes from the high pressure zone of the contact.

The role of the inlet is to pressurize the fluid so that it is able to separate the moving surfaces by elastically deforming them. Yet, the cavity in the inlet may disrupt this phenomenon leading to a weaker pressurization and thus a weaker

film-forming capacity. On the contrary, the cavity when in the high-pressure zone of contact has a positive effect and enhances the lubricant film thickness more quickly and at a level even higher as the SRR is high. In the contact, the moving cavity can be viewed as a 'local convergent' for a fluid moving at the speed $u_e - u_2 = u_e\Sigma/2$. Therefore, in pure rolling ($\Sigma = 0$), the fluid is static regarding the cavity 'convergent', remaining trapped in the cavity and has no effect on the separation between the surfaces. When the SRR increases, the fluid will exit faster and faster the cavity acting as a 'convergent'. If the required time for the fluid to pass through the cavity 'convergent' is superior or equivalent to the time spent by the cavity in the contact, the lubricant stored in the cavity cannot increase the film thickness much above $h(x = -a)$ as it is the case for $\Sigma = +8\%$. On the contrary, if the required time for the fluid to pass through the cavity 'convergent' is shorter than the dwell time of the cavity in the contact, the film thickness increase can occur ($\Sigma = +25\%$) and may lead to $h_+ > h_c$ for the highest SRR ($\Sigma = +50$ and $+100\%$). The increase of the local film thickness does not only depend on the SRR but also on the cavity depth and shape which both contribute to the pressure drop.

5.4.3 Numerical inlet pressurization

The influence of the cavity upon the inlet pressure was numerically investigated using the equivalent line contact EHL model applied to the mathematical profiles C1 and C2 and measured profile of the cavity. In Fig. 5.13, the evolution of the pressure integral along the inlet $\int_{-2.5a}^{-a} p(x)dx$ is plotted versus the cavity front position $x_c(t)$ for the profile C1, C2 and the B7 profile at $\eta_0 u_e = 3.6 \times 10^{-2}$ Pa.m and $\Sigma = +8$, $+25$, $+50$ and $+100\%$. The inlet pressure integral calculated for the smooth contact is plotted with a horizontal dash line. As the cavity approaches the contact entrance, the pressure inside the convergent keeps decreasing. The inlet pressure integral starts rising around $x = -1.1a$. The SRR has negligible effect on the results. Though the B7 profile reduces the inlet pressure integral to a lesser degree than C1 and C2, the difference is not significant.

Thus, the numerical simulations confirm that, when in the inlet, the cavity lowers the fluid pressure at the contact entrance, reducing the film thickness which then propagates downstream the contact. To prevent the film thickness reduction, the shape of the cavity should be chosen to limit the pressure drop in the inlet.

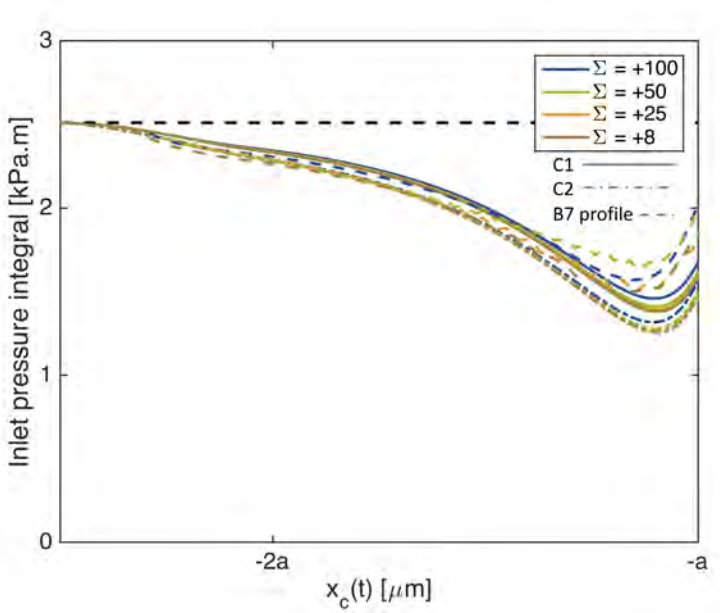

Figure 5.13: Inlet pressure integral $\int_{-2.5a}^{-a} p(x)dx$ versus the cavity front position for profiles C1, C2 and the B7 profile at $\eta_0 u_e = 3.6 \times 10^{-2}$ Pa.m and $\Sigma = +8$, $+25$, $+50$ and $+100\%$. The smooth inlet pressure integral is reported with a horizontal dash.

5.5 EHL friction

In the previous chapter, the shearing of the under pressure viscous fluid was responsible for the EHL friction. Thus, the shear rate $\dot{\gamma}$ and the mean contact pressure p_m are the two main relevant parameters governing the friction. The Stribeck curves experimentally determined for ball B7 and presented in Fig. 5.2a-d reported a higher friction in EHL than that measured for the smooth contact although no friction difference, contrary to film thickness distribution, was observed between the operating condition $-\Sigma$ and $+\Sigma$. Therefore, only similar phenomena happening at both $-\Sigma$ and $+\Sigma$ are supposed to be responsible for the friction increase. Thus, the SRR-dependence of the film thickness modifications outside the cavity and induced by the cavity are not supposed to significantly modify the B7 friction in the Stribeck curves. Hence, the increase of the shear stress cannot be related to a shear rate variation as the film thickness distribution is SRR-dependent contrary to the friction. The shear rates for $-\Sigma$ and $+\Sigma$ conditions are supposed to be similar and close to that of the smooth case, for a given $|\Sigma|$ condition.

Krupka et al. [122] showed that the pressure strongly dropped inside a 1 μm-deep cavity regardless to the sign of the SRR. This local pressure drop can influence the mean contact pressure p_m, i.e. the under-pressure viscosity and thus the shear stress (cf. Chapter 2). In numerical point contact simulations, Mourier et al. [4] showed that this pressure drop depends on the cavity depth: the deeper the cavity, the stronger the pressure drop. In addition, the pressure profile from the previous numerical simulations with profiles C1, C2 and the B7 profile are presented in Fig. 5.14. The pressure profile is plotted for the cavity center at $x = 0$, $\Sigma = +100\%$ and $\eta_0 u_e = 3.6 \times 10^{-2}$ Pa.m. The smooth pressure profile is plotted with a dash line. Fig. 5.14 confirms that the pressure drops inside the cavity. The pressure inside the cavity is equal to 110, 128 and 164 MPa for the profiles C1, C2 and the B7 profile, respectively. The profile with the rough cavity bottom reduces to a lesser degree the pressure inside the cavity. These pressure values were calculated for conditions $1.0 \times 10^{-2} < \eta_0 u_e < 1.0 \times 10^{-1}$ Pa.m at $\Sigma = +100\%$. The pressure drop is not $\eta_0 u_e$-dependent. The influence of the pressure drop on the mean fluid pressure and thus on its viscous friction is investigated next.

For the ball B7, the cavity centers are separated by a distance equal to $2a$. Therefore, there is always a single cavity passing through the EHL contact. This can be either a whole cavity or the portion of the entering cavity plus the complementary portion of the exiting one. Then, the load borne by the EHL contact with ball B7 can be expressed as the sum of the contribution from the mean pressure outside the cavity p_m and the contribution from the mean pressure inside

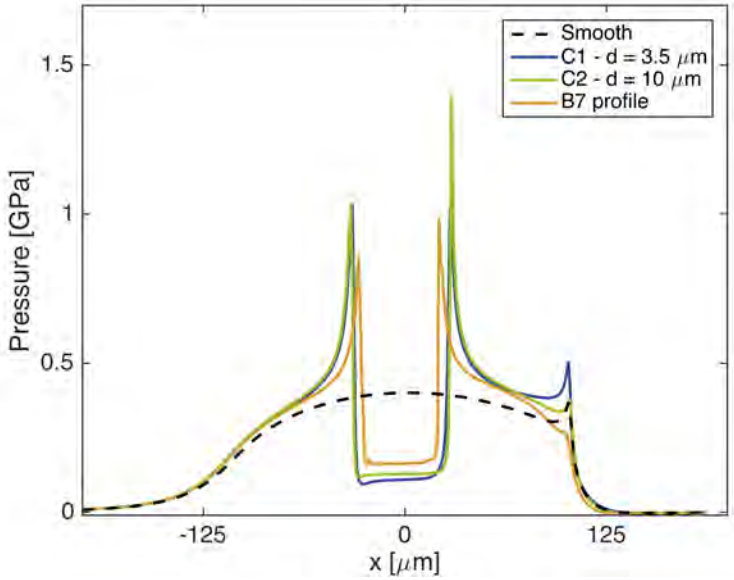

Figure 5.14: Pressure distribution inside the contact for model profiles C1, C2 and the measured B7 profile when the cavity center is in $x = 0$ for $\Sigma = +100\%$ and $\eta_0 u_e = 3.6 \times 10^{-2}$ Pa.m. The pressure distribution calculated for the smooth ball is plotted with dash line.

the cavity $p_{m,cav}$:

$$W = p_m \left[\pi a^2 - \pi \left(\frac{\varnothing}{2} \right)^2 \right] + p_{m,cav}\ \pi \left(\frac{\varnothing}{2} \right)^2 \ . \tag{5.9}$$

All other things being equal, the mean contact pressure of a smooth contact at the mean pressure $p_{m,s}$, is:

$$W = p_{m,s}\ \pi a^2 \ . \tag{5.10}$$

Numerical simulations were run to get the magnitude order of $\chi = p_{m,cav}/p_m$. It yields respectively $\chi = 0.31$, 0.37 and 0.47 ± 0.04 for the profiles C1, C2 and the B7 profile. From Eq. 5.9 and 5.10:

$$p_m = \frac{p_{m,s}}{1 + (\chi - 1) \left(\frac{\varnothing}{2a} \right)^2} \ . \tag{5.11}$$

In the present case $p_{m,cav} < p_m$ then $\chi < 1$, yielding to $p_m > p_{m,s}$. Thus, when the cavity is in the contact, the mean pressure outside the cavity is expected to increase. The pressure distributions reported in Fig. 5.14 confirm this interpretation.

Using the Barus law:

$$\eta_{0/P} = \eta_0 \exp\left(\alpha p\right) \ , \tag{5.12}$$

the ratio of the viscosity inside the cavity $\eta_{0/p_{m,cav}}$ over the viscosity outside the cavity η_{0/p_m} is approximated:

$$\frac{\eta_{0/p_{m,cav}}}{\eta_{0/p_m}} = \exp\left[\alpha (p_{m,cav} - p_m)\right] \ . \tag{5.13}$$

According to the numerical simulations, $|p_{m,cav} - p_m|$ is equal, in average, to 244, 221 and 186 MPa for the profiles C1, C2 and the B7 profile, respectively. Therefore, the viscosity inside the cavity is 164, 103 and 46 times lower than the viscosity outside the cavity, respectively. Hence, the shear stress contribution of the cavity region is negligible and the friction μ is expressed as:

$$\mu = \frac{\tau \left[\pi a^2 - \pi \left(\frac{\varnothing}{2} \right)^2 \right]}{W} \ , \tag{5.14}$$

with τ the shear stress outside the cavity. All other things being equal, the friction of a smooth contact μ_s is:

$$\mu_s = \frac{\tau_s\ \pi a^2}{W} \ , \tag{5.15}$$

with τ_s the shear stress in the smooth contact. Thus,

$$\mu = \mu_s \left[1 - \left(\frac{\varnothing}{2a}\right)^2\right] \frac{\tau}{\tau_s} \ . \tag{5.16}$$

Based on Eq. 2.64, reminded below:

$$\frac{\tau}{\tau_{Hertz}} = \frac{\eta_{0/P}}{\eta_{0/P,Hertz}} \ , \tag{5.17}$$

the EHL friction dissipated by the viscous shearing of lubricant in the contact with ball B7 can be rewritten as a function of the under-pressure viscosities η_{0/p_m} and $\eta_{0/p_{m,s}}$, assuming that the average smooth shear rate is equal to the average shear rate of the ball B7:

$$\mu = \mu_s \left[1 - \left(\frac{\varnothing}{2a}\right)^2\right] \frac{\eta_{0/p_m}}{\eta_{0/p_{m,s}}} \ . \tag{5.18}$$

The theoretical friction μ can then be calculated according to Eq.5.18, from the experimental smooth friction coefficients measured with ball B0 and using the Cross law proposed in chapter 2 to evaluate η_{0/p_m} and $\eta_{0/p_{m,s}}$. In this model, the pressure drop was supposed to be distributed equally in the whole cavity. The theoretical friction coefficient μ is plotted versus $\eta_0 u_e$ for the profiles C1, C2 and the B7 profile at $|\Sigma|$ = 8, 25, 50 and 100% in Fig. 5.15a-d. The mixed/EHL transition and the B7 friction coefficient are marked. Since the experimental friction coefficients in smooth EHL slightly fluctuate (see Fig. 5.2), the theoretical friction curves in Fig. 5.15 behave in the same way. For $|\Sigma|$ = 8, 25, 50 and 100%, Fig. 5.15b-d show that the theoretical friction coefficients with C1, C2 and B7 profiles are in good agreement with the experimental data for $\eta_0 u_e$ above the B7 mixed/EHL transition. This can be explained by the fact that both the mean pressure increase outside the cavity and the pressure drop in the cavity give the correct magnitude of the friction difference between the textured ball B7 and the smooth ball B0. Below the mixed/EHL transition, asperity contacts occur.

5.6 Conclusions

The study of a row of single cavities passing through the EHL contact at different SRR values was carried out. In comparison with a smooth contact, the central film thickness h_c slightly increases and the minimum film thickness h_m of the constriction region remains unchanged. Both are roughly independent of the SRR. The influence of the roughness at the cavity bottom was also highlighted.

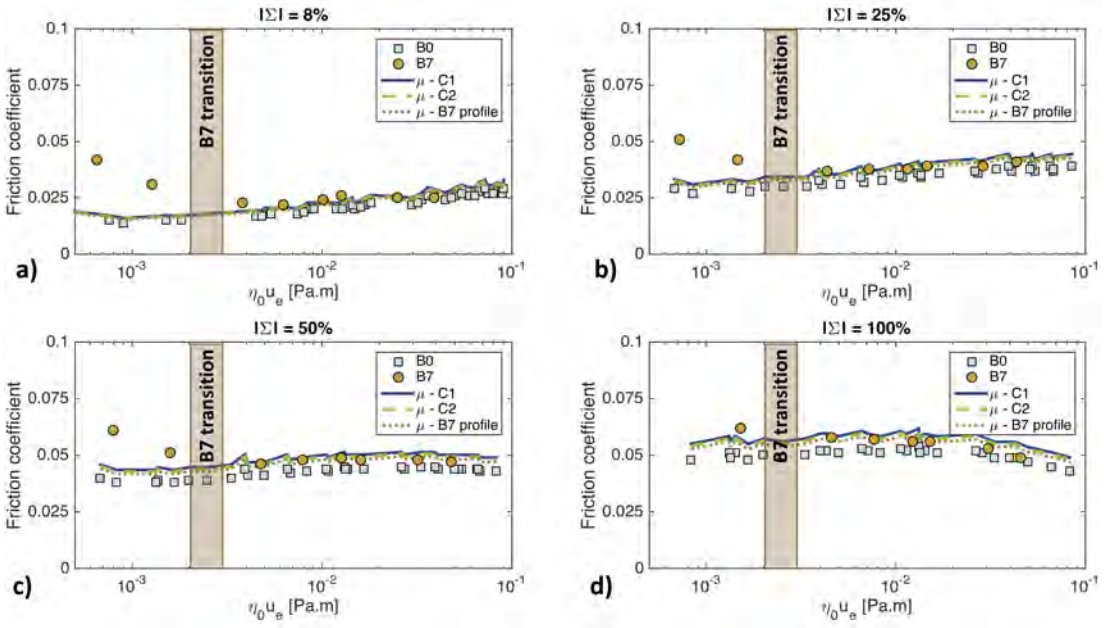

Figure 5.15: Theoretical friction μ from the smooth friction coefficients measured for ball B0 according Eq. 5.18 versus $\eta_0 u_e$ at $|\Sigma| = 8$ (a), 25 (b), 50 (c) and 100% (d) and for the profiles C1, C2 and the B7 profile. The B7 mixed/EHL transition is reported. The B0 (smooth) and B7 friction coefficients are marked.

The upper envelope of the cavity bottom roughness appeared to be significant in the ability of the cavity to reinforce the film thickness.

When the cavity approaches the contact, the inlet pressure starts to decrease which reduces the film thickness at the contact entrance ($x = -a$). Then, this generated film thickness spreads into the contact at the velocity u_e. Thus, the area where the local film thickness is reduced, propagates downstream the cavity when the SRR is positive ($u_e > u_2$), upstream the cavity when the SRR is negative ($u_e < u_2$) and is static regarding the cavity in pure rolling ($u_e = u_2$). The thinnest film thickness h_- generated by the cavity is independent of the SRR and leads to asperity contacts at higher $\eta_0 u_e$ than the smooth surface B0. Thus, the mixed/EHL transition is shifted to higher $\eta_0 u_e$ and remains independent of the SRR conditions.

When the cavity enters the contact, the film thickness in front of the cavity starts rising for positive SRR. The sharpness of the increase depends on the SRR: the higher the SRR, the sharper the increase. As a result, the film thickness in front of the cavity reaches higher (lower) values than h_c at high (low) SRR. For negative SRR, no such film thickness increase was observed for the studied cavity.

The location of the film thickness reduction and the existence of a film thickness increase depend on the SRR sign. Yet, the friction is the same irrespective of the sign of the SRR. Thus, the local modifications of the shear rate induced by the cavity do not significantly influence the average shear rate and the friction coefficient in EHL regime. The investigation of the mean contact pressure disturbances indicates that the cavity most likely increases the pressure of the fluid outside the cavity. Thus, the resulting lubricant viscosity rise increases the EHL friction.

General conclusions

The tribological response of groove, ripple and cavity textures was carried out in EHL and compared to that of a smooth contact. In particular, the friction modifications and their coupling with the film thickness, pressure and asperity contact were investigated as a function of the surface topography. For this purpose, experiments were performed and a transient EHL line contact model was developed, validated and used to simulate the experimental EHL point contacts with equivalent contacts.

The Cross-like fluid rheology under pressure well predicted the shearing of the lubricant inside the EHL contact. For a given fluid, the friction due to the viscous shear stress τ is function of two parameters: the average shear rate $\dot{\gamma}$ and the mean contact pressure p_m. The average shear rate is directly related to the average film thickness. Both the film thickness and the pressure are modified by surface texturing.

The chosen textures induced locally significant film thickness and pressure variations. The groove and ripple textures decreased the film thickness in the constriction region. On the contrary, the cavity texture reduced the film thickness at the vicinity of the cavity. When the SRR increased, this thickness reduction spread downstream (upstream) the cavity for positive (negative) SRR. The intensity of the reduction was enhanced with large texture sizes (depth/amplitude, width/diameter) which is supposed to enhance the side leakage. No effect of the groove and ripple orientations was observed on the film thickness reduction. As a result, the studied textures favored the onset of asperity contacts. Once the first asperity contact occurred, the friction started rising. Local pressure variations with ripple texture were also responsible for an increase of the viscous shear stress (micro-EHL effects) yet its order of magnitude was far lower than that of the asperity contacts.

Furthermore, film thickness reinforcements were locally achieved with the transverse groove and cavity textures. At $|\Sigma| = 8\%$, the periodic transverse groove texture increased the film thickness at the top of the wide grooves. With

the cavity texture, high and positive SRR ($\Sigma = +100\%$) were required to generate an increase in film thickness at the vicinity of the cavity which spread downstream the contact. Experiments and numerical simulations showed that the EHL contact was only sensitive to the upper envelope of the cavity bottom roughness.

Despite the above local film thickness and pressure variations, the groove and ripple textures generated the same average film thickness and mean contact pressure as a smooth contact, regardless of their orientation (transverse or longitudinal), width and depth/amplitude. Therefore, the average viscous shear stress and thus the friction with these textures was equal to that of the smooth contact in EHL.

With the cavity texture, the local modifications of the film thickness distribution did not influence the viscous shear stress. Nevertheless, the pressure dropped inside the cavity and led to an increase of the mean contact pressure outside the cavity and thus of the viscous shear stress. The sensitivity of the viscous shear stress regarding the mean contact pressure was also observed with smooth contact. At high $\eta_0 u_e$, the pressure spread in the inlet region and the mean contact pressure was reduced, thus the friction decreased. The viscous friction is more sensitive to the mean contact pressure variations than to those of the film thickness.

To summarize, this works demonstrates that the Cross-like rheology under pressure predicts the friction in EHL for smooth and textured contacts. Therefore, the choice of the surface texturing, reducing the friction, should take into account the texture influence on both the average film thickness and the mean contact pressure. Then, *what must a surface texture induce, in terms of average film thickness and mean contact pressure variations, to reduce the EHL friction by 5, 10 and 20%?* Two cases are illustrated with the 330 NS oil: the mean contact pressure remains constant (varies) while the film thickness varies (remains constant). From an initial shear stress τ_i, a lower shear stress τ_f is targeted. The shear stress reduction χ_τ is then defined as τ_f/τ_i. The 330 NS oil is modeled with the Cross-like rheology under pressure at 305 MPa.

Film thickness influence

From an initial average shear rate $\dot{\gamma}_i$ in the contact, the required film thickness h_f to get the targeted χ_τ, is determined. The shear rate variation $\chi_{\dot{\gamma}}$ is defined as:

$$\chi_{\dot{\gamma}} = \frac{\dot{\gamma}_f}{\dot{\gamma}_i} = \left(\frac{h_f}{h_i}\right)^{-1} ,$$

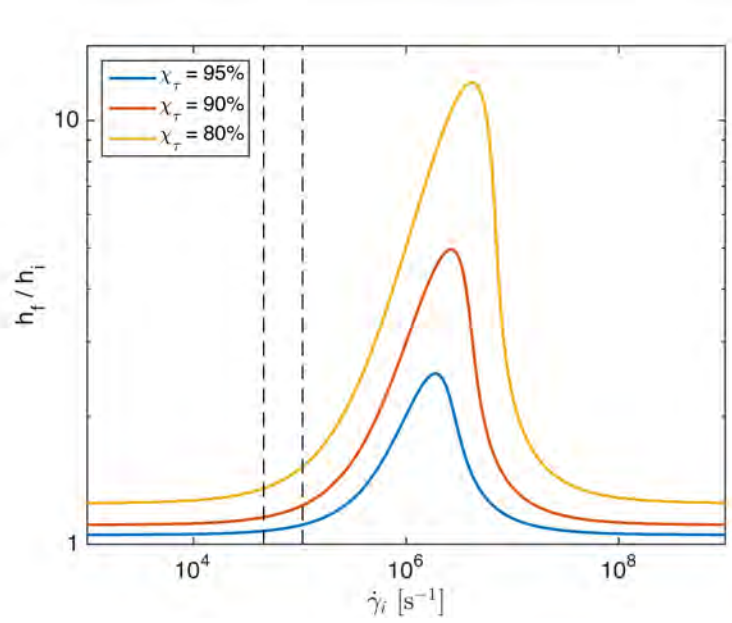

Figure 5.16: Ratio of the film thickness h_f required to get χ_τ over the initial film thickness h_i versus the initial shear rate $\dot{\gamma}_i$. Three values of χ_τ are investigated: 95, 90, and 80%. The shear rate range of the smooth experimental at $|\Sigma| = 8\%$ is emphasized with dash lines.

where $\dot{\gamma}_f = u_e\Sigma/h_f$ and h_i is the initial average film thickness ($\dot{\gamma}_i = u_e\Sigma/h_i$). The shear stress reduction, χ_τ is then expressed for a given mean contact pressure by:

$$\chi_\tau = \frac{\dot{\gamma}_f\ \eta(\dot{\gamma}_f)}{\dot{\gamma}_i\ \eta(\dot{\gamma}_i)} = \chi_{\dot{\gamma}} \frac{\eta(\chi_{\dot{\gamma}}\ \dot{\gamma}_i)}{\eta(\dot{\gamma}_i)}\ .$$

The shear rate variation $\chi_{\dot{\gamma}}$ is calculated for three values of the χ_τ, 95, 90 and 80%. In Fig. 5.16, the film thickness ratios h_f/h_i are plotted versus $\dot{\gamma}_i$ for the three values of χ_τ. The shear rate range of the smooth experiments at $|\Sigma| = 8\%$ presented in this work is delimited with vertical dash lines (from 4.6×10^4 to 1.1×10^5 s^{-1}).

In Fig. 5.16 illustrates, h_f/h_i decreases for low and high initial shear rates since the viscosity becomes independent of the shear rate. Therefore the relationship between the shear stress and shear rate variations becomes:

$$\chi_\tau = \chi_{\dot{\gamma}} = \left(\frac{h_f}{h_i}\right)^{-1}\ .$$

For intermediate $\dot{\gamma}_i$, the reduction of the shear rate will increase the viscosity. As the shear stress is the product of the shear rate times the viscosity, the shear

stress reduction will require a significant shear rate reduction and thus similar film thickness enhancement. To achieve the $\chi_\tau = 95$, 90 and 80% of the smooth experiments performed at $|\Sigma| = 8\%$, the surface texture must keep the mean contact pressure at 305 MPa and increased by 8-12, 15-23 and 36-52% the film thickness, respectively.

Mean contact pressure influence

From an initial mean contact pressure p_i, the required mean contact pressure p_f to reach the targeted χ_τ, is calculated. The mean contact pressure variation χ_p is defined as:

$$\chi_p = \frac{p_f}{p_i} \ .$$

From the Roelands' equation, the shear stress reduction χ_τ is defined as for a given average shear rate:

$$\chi_\tau = \frac{\eta_{0/P_f}}{\eta_{0/P_i}} = \frac{\exp\left\{(\ln\eta_0 + 9.67)\left(-1 + \left(1 + \frac{p_f}{p_0}\right)^{z_\alpha}\right)\right\}}{\exp\left\{(\ln\eta_0 + 9.67)\left(-1 + \left(1 + \frac{p_i}{p_0}\right)^{z_\alpha}\right)\right\}} \ .$$

Thus:

$$\chi_p = \frac{p_0}{p_i}\left\{\left[\frac{\ln\chi_\tau}{\ln\eta_0 + 9.67} + \left(1 + \frac{p_i}{p_0}\right)^{z_\alpha}\right]^{1/z_\alpha} - 1\right\}$$

In Fig. 5.17, χ_p is plotted versus p_i for the three targeted shear stress reductions χ_τ: 95, 90 and 80%. η_0, z and p_0 are the same as in the experiments.

In Fig. 5.17, χ_p tends to 99.7, 99.3 and 98.5% at high values of p_i (close to 1 GPa) for $\chi_\tau = 95$, 90 and 80%, respectively. The higher the initial pressure, the closer p_i and p_f. At high pressure the piezo-viscosity leads to very high viscosity through an exponential law. Hence, a small pressure reduction will induce a significant viscosity variation and friction change. To achieve a friction reduction of 5, 10 and 20% of the smooth EHL friction, the surface texture has to keep the same average film thickness and lower the mean contact pressure by 0.8, 1.7 and 3.6%, respectively.

Relation to the surface texture

These two cases exemplify the huge sensitivity of the friction regarding the mean contact pressure of the sheared fluid. Nevertheless, to change the mean contact pressure, a texture has to modify the pressure distribution. Thus, the film thickness distribution will be affected and potentially the average film thickness.

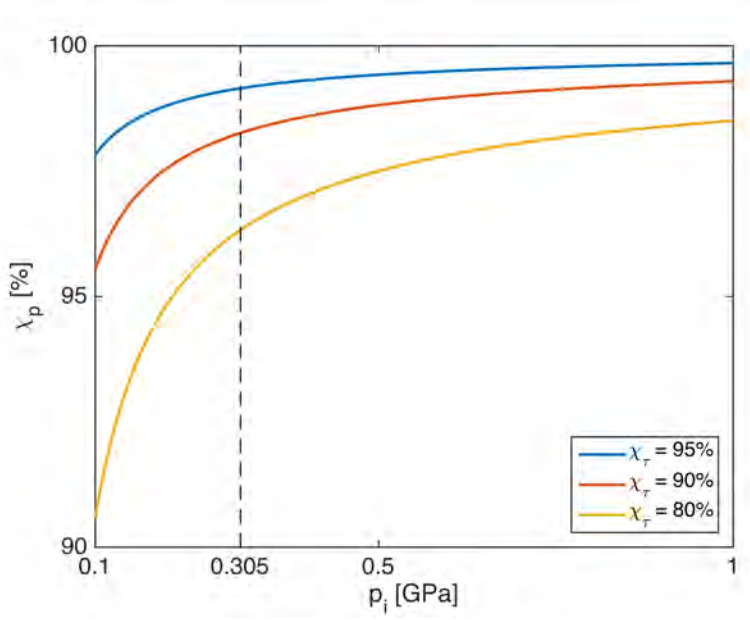

Figure 5.17: Mean contact pressure variations χ_p versus the initial mean contact pressure p_i for the three shear stress reduction ratios: 95, 90 and 80%. The mean contact pressure of the experiments is emphasized with a dash line.

Optimizing the surface texturing to reduce the friction with a base oil, requires a fine knowledge of complex coupling that the geometry induces between the pressure and the film thickness distributions. Thus, the use of multiple textures inside a contact might be a way to control this coupling. As shown with the cavity texture, the EHL contact might not be sensitive to the whole roughness of the cavity bottom, but for example only to the upper envelope. This also opens up the way to multi-scale effect investigations with surface texturing.

An other way to reduce the friction, but with an additivated oil, could be to take advantage of the onset of asperity contacts due to deep and large textures. These textures will locally decrease the film thickness and the boundary friction from the asperity contact will replace locally the viscous one. Increasing the number of asperity contacts might lead to a friction reduction if the shear stress of asperity contacts is lowered by the oil additives, promoting boundary lubrication.

Bibliography

[1] K. Holmberg, P. Andersson, and A. Erdemir. Global energy consumption due to friction in passenger cars. *Tribology International*, 47:221–234, 2012.

[2] D.B. Hamilton, J.A. Walowit, and C.M. Allen. A theory of lubrication by micro-irregularities. *Journal of Basic Engineering, Series D*, 88(1):177–185, 1966.

[3] I. Etsion, Y. Kligerman, and G. Halperin. Analytical and experimental investigation of laser-textured mechanical seal faces. *Tribology Transactions*, 42:511–516, 1999.

[4] L. Mourier. *Optimisation des contacts elastohydrodynamiques par la microtexturation de surface*. PhD thesis, Ecole Centrale de Lyon, France, 2007.

[5] F. Brémond. *Lubrification des contacts sous-alimentés : apport de la microtexturation de surface*. PhD thesis, Ecole Centrale de Lyon, France, 2012.

[6] F.-P. Ninove. *Texturation de surface par LASER femtoseconde en régimes elastohydrodynamique et limite*. PhD thesis, Ecole Centrale de Lyon, France, 2011.

[7] H. S. Patir, N.and Cheng. An average flow model for determining effects of three-dimensional roughness on partial hydrodynamic lubrication. *Journal of Lubrication Technology*, 100(1):12–17, 1978.

[8] A. A. Lubrecht. *The numerical solution of the elastohydrodynamically lubricated line and point contact problem, using multigrid techniques*. PhD thesis, University of Twente, The Netherlands, 1987.

[9] C.H. Venner. *Multilevel Solution of the EHL Line and Point Contact Problems*. PhD thesis, University of Twente, The Netherlands, 1991.

[10] T. Woloszynski, P. Podsiadlo, and G.W. Stachowiak. Evaluation of discretisation and integration methods for the analysis of hydrodynamic bearings with and without surface texturing. *Tribology Letters*, 51(1):25–47, 2013.

[11] A. Guzek, P. Podsiadlo, and G.W. Stachowiak. Optimization of textured surface in 2d parallel bearings governed by the reynolds equation including cavitation and temperature. *Tribology Online*, 8(1):7–21, 2013.

[12] P. Podsiadlo and G.W. Stachowiak. Directional multiscale analysis and optimization for surface textures. *Tribology Letters*, 49(1):179–191, 2013.

[13] S.Y. Poon and D.J. Haines. Frictional behaviour of lubricated rolling-contact elements. *Proceedings of the Institution of Mechanical Engineers*, 181(1):363–389, 1966.

[14] D.J. Schipper. *Transitions in the lubrication of concentred contacts*. PhD thesis, University of Twente, The Netherlands, 1966.

[15] G.E. Morales-Espejel and A.W. Wemekamp. Ertel-grubin method in elastohydrodynamic lubrication - a review. *Proceedings of the Institution of Mechanical Engineers, Part J: Journal of Engineering Tribology*, 222(1):15–34, 2008.

[16] B. J. Hamrock and D Dowson. *Ball Bearing Lubrication - The Elastohydrodynamics of Elliptical Contacts*. Wiley-Interscience, New-York, 1981.

[17] T. Almqvist and R. Larsson. The navier-stokes approach for thermal ehl line contact solutions. *Tribology International*, 35(3):163–170, 2002.

[18] M. Hartinger, M.-L. Dumont, S. Ioannides, D. Gosman, and H. Spikes. Cfd modeling of a thermal and shear-thinning elastohydrodynamic line contact. *Journal of Tribology*, 130(4), 2008.

[19] A.A. Lubrecht, W.E. ten Napel, and R. Bosma. Multigrid, an alternative method for calculating film thickness and pressure profiles in elastohydrodynamically lubricated line contacts. *Journal of Tribology*, 108(4):551–556, 1986.

[20] A.A. Lubrecht, W.E. ten Napel, and R. Bosma. Multigrid, an alternative method of solution for two-dimensional elastohydrodynamically lubricated point contact calculations. *Journal of Tribology*, 109(3):437–443, 1987.

[21] B.J. Hamrock and D. Dowson. Isothermal elastohydrodynamic lubrication of point contacts - 1. theorical formulation. *Journal of Lubrication Technology*, 98 Serie F(2):223–229, 1976.

[22] B.J. Hamrock and D. Dowson. Isothermal elastohydrodynamic lubrication of point contacts - 2. ellipticity parameter results. *Journal of Lubrication Technology*, 98 Serie F(3):375–383, 1976.

[23] B.J. Hamrock and D. Dawson. Isothermal elastohydrodynamic lubrication of point contact. part iii - fully flooded results. *Journal of Lubrication Technology*, 99(2):264–276, 1977.

[24] C.H. Venner, W.E. ten Napel, and R. Bosma. Advanced multilevel solution of the ehl line contact problem. *Journal of Tribology*, 112(3):426–432, 1990.

[25] C.H. Venner and W.E.t. Napel. Multilevel solution of the elastohydrodynamically lubricated circular contact problem part 1: Theory and numerical algorithm. *Wear*, 152(2):351–367, 1992.

[26] C.H. Venner and W.E.t. Napel. Multilevel solution of the elastohydrodynamically lubricated circular contact problem part 2: Smooth surface results. *Wear*, 152(2):369–381, 1992.

[27] A. Brandt and A.A. Lubrecht. Multilevel matrix multiplication and fast solution of integral equations. *Journal of Computational Physics*, 90(2):348–370, 1990.

[28] H. Okamura. A contribution to the numerical analysis of isothermal elastohydrodynamic lubrication. *Proceedings of the 9th Leeds-Lyon Symposium on Tribology*, pages 313–320, 1983.

[29] M.J.A. Holmes, H.P. Evans, T.G. Hughes, and R.W. Snidle. Transient elastohydrodynamic point contact analysis using a new coupled differential deflection method part 1: Theory and validation. *Proceedings of the Institution of Mechanical Engineers, Part J: Journal of Engineering Tribology*, 217(4):289–304, 2003.

[30] M.J.A. Holmes, H.P. Evans, T.G. Hughes, and R.W. Snidle. Transient elastohydrodynamic point contact analysis using a new coupled differential deflection method part 2: Results. *Proceedings of the Institution of Mechanical Engineers, Part J: Journal of Engineering Tribology*, 217(4):305–322, 2003.

[31] H.P. Evans and T.G. Hughes. Evaluation of deflection in semi-infinite bodies by a differential method. *Proceedings of the Institution of Mechanical Engineers, Part C: Journal of Mechanical Engineering Science*, 214(4):563–578, 2000.

[32] W. Habchi, I. Demirci, D. Eyheramendy, G. Morales-Espejel, and P. Vergne. A finite element approach of thin film lubrication in circular ehd contacts. *Tribology International*, 40(10-12):1466–1473, 2007.

[33] W. Habchi, D. Eyheramendy, P. Vergne, and G.E. Morales-Espejel. A full-system approach of the elastohydrodynamic line/point contact problem. *Journal of Tribology*, 130(2):1–10, 2008.

[34] H. Eyring. Viscosity, plasticity, and diffusion as examples of absolute reaction rates. *The Journal of Chemical Physics*, 4(4):283–291, 1936.

[35] T. Gillespie. An extension of goodeve's impulse theory of viscosity to pseudoplastic systems. *Journal of Colloid Science*, 15(3):219–231, 1960.

[36] M.M. Cross. Rheology of non-newtonian fluids: A new flow equation for pseudoplastic systems. *Journal of Colloid Science*, 20(5):417–437, 1965.

[37] Pierre J. Carreau. Rheological equations from molecular network theories. *Transaction of the Society of Rheology*, 16(1):99–127, 1972.

[38] D. Tabor. *Gases, Liquids and Solids*. Cambridge University Press, 1991.

[39] T. Ree and H. Eyring. Theory of non-newtonian flow. i. solid plastic system. *Journal of Applied Physics*, 26(7):793–800, 1955.

[40] C.F. Goodeve. A general theory of thixotropy and viscosity. *Transactions of the Faraday Society*, 35:342–358, 1939.

[41] M.M. Cross. Polymer rheology: Influence of molecular weight and polydispersity. *Journal of Applied Polymer Science*, 13(4), 1969.

[42] A. Powell. The influence of the molecular size distribution within a liquid on the viscous flow of the liquid. *Polymer*, 7(2):91–97, 1966.

[43] M.M. Cross. Kinetic interpretation of non-newtonian flow. *Journal of Colloid and Interface Science*, 33(1):30–35, 1970.

[44] A.S. Lodge. Constitutive equations from molecular network theories for polymer solutions. *Rheologica Acta*, 7(4):379–392, 1968.

[45] K.L. Johnson and J.L. Tevaarwerk. Shear behaviour of elastohydrodynamic oil films. *Proceeding of the Royal Society of London Series A*, 356(1685):215–236, 1977.

[46] J.L. Tevaarwerk. *The shear of elastohydrodynamic oil films*. PhD thesis, University of Cambridge, U.K., 1976.

[47] K.L. Johnson. Non-newtonian effects in elastohydrodynamic lubrication. *Proceedings of the 19th Leeds-Lyon Symposium on Tribology*, pages 15–26, 1993.

[48] Scott Bair and W.O. Winer. Shear strength measurements of lubricants at high pressure. *Journal of Lubrication Technology*, 101(3):251–257, 1979.

[49] Scott Bair and W.O. Winer. Rheological model for elastohydrodynamic contacts based on primary laboratory data. *Journal of Lubrication Technology*, 101(3):258–265, 1979.

[50] Y. Liu, Q.J. Wang, W. Wang, Y. Hu, D. Zhu, I. Krupka, and M. Hartl. Ehl simulation using the free-volume viscosity model. *Tribology Letters*, 23(1):27–37, 2006.

[51] S. Yasutomi, S. Bair, and W.O. Winer. Application of a free volume model to lubricant rheology. 1 - dependence of viscosity on temperature and pressure. *Journal of Tribology*, 106(2):291–303, 1984.

[52] B. Jacod. *Friction in Elastohydrodynamic Lubrication*. PhD thesis, University of Twente, The Netherlands, 2002.

[53] R.-T. Lee and B.J. Hamrock. A circular non-newtonian model: Part i-used in elastohydrodynamic lubrication. *Journal of Tribology*, 112:386–496, 1990.

[54] A.A. Elsharkawy and B.J. Hamrock. Subsurface stresses in micro-ehl line contacts. *Journal of Tribology*, 113(3):645–655, 1991.

[55] Jacobson B. On the lubrication of heavily loaded spherical surfaces considering surface deformations and solidification of the lubricant. *Acta Polytechnica Scandinavica, Mechanical Engineering Series*, (54), 1970.

[56] B.O. Jacobson. *Rheology and Elastohydrodynamic Lubrication*. Elsevier Science, 1991.

[57] J. Stahl and B.O. Jacobson. A non-newtonian model based on limiting shear stress and slip planes - parametric studies. *Tribology International*, 36(11):801–806, 2003.

[58] P. Ehret, D. Dowson, and C.M. Taylor. On lubricant transport conditions in elastohydrodynamic conjunctions. *Proceedings of the Royal Society A: Mathematical, Physical and Engineering Sciences*, 454(1971):763–787, 1998.

[59] H. Spikes and Z. Jie. History, origins and prediction of elastohydrodynamic friction. *Tribology Letters*, 2014.

[60] M. Diew, A. Ernesto, J. Cayer-Barrioz, and D. Mazuyer. Stribeck and traction curves under moderate contact pressure: From friction to interfacial rheology. *Tribology Letters*, 57(2), 2015.

[61] A. Ernesto, D. Mazuyer, and J. Cayer-Barrioz. From full-film lubrication to boundary regime in transient kinematics. *Tribology Letters*, 59(1), 2015.

[62] J.A. Greenwood and G.E. Morales-Espejel. The behaviour of real transverse roughness in a sliding ehl contact. *Tribology Series*, 25(C):227–236, 1993.

[63] J.A. Greenwood and G.E. Morales-Espejel. The behaviour of transverse roughness in ehl contacts. *Proceedings - IMechE: Part J, Journal of Engineering Tribology*, 208(J2):121–132, 1994.

[64] G.E. Morales-Espejel, C.H. Venner, and J.A. Greenwood. Kinematics of transverse real roughness in elastohydrodynamically lubricated line contacts using fourier analysis. *Proceedings of the Institution of Mechanical Engineers, Part J: Journal of Engineering Tribology*, 214(6):523–534, 2000.

[65] G.E. Morales-Espejel, P.M. Lugt, J. Van Kuilenburg, and J.H. Tripp. Effects of surface micro-geometry on the pressures and internal stresses of pure rolling ehl contacts. *Tribology Transactions*, 46(2):260–272, 2003.

[66] C.J. Hooke, K.Y. Li, and G. Morales-Espejel. Rapid calculation of the pressures and clearances in rough, rolling-sliding elastohydrodynamically lubricated contacts. part 1: Low-amplitude, sinusoidal roughness. *Proceedings of the Institution of Mechanical Engineers, Part C: Journal of Mechanical Engineering Science*, 221(5):535–550, 2007.

[67] C.C. Kweh, H.P. Evans, and R.W. Snidle. Micro-elastohydrodynamic lubrication of an elliptical contact with transverse and three-dimensional sinusoidal roughness. *Journal of Tribology*, 111(4):577–584, 1989.

[68] C.H. Venner, F. Couhier, A.A. Lubrecht, and J.A. Greenwood. Amplitude reduction of waviness in transient ehl line contacts. *Tribology Series*, 32:103–112, 1997.

[69] A.A. Lubrecht, D. Graille, C.H. Venner, and J.A. Greenwood. Waviness amplitude reduction in ehl line contacts under rolling-sliding. *Journal of Tribology*, 120(4):705–709, 1998.

[70] P. Sperka, I. Krupka, and M. Hartl. The behavior of surface roughness in ehl contacts under small slide to roll ratios. *Tribology Letters*, 47(3):357–366, 2012.

[71] S. De Silva, J.C. Anderson, and J.A. Leather. Model rough surfaces in elastohydrodynamic lubrication. *Thin Solid Films*, 96(1):1–8, 1982.

[72] C.J. Hooke. Surface roughness modification in ehl line contacts - the effect of roughness wavelength, orientation and operating conditions. *Tribology Series*, 36:193–202, 1999.

[73] L. Chang, A. Jackson, and M.N. Webster. Effects of 3-d surface topography on the ehl film thickness and film breakdown. *Tribology Transactions*, 37(3):435–444, 1994.

[74] M.J. Patching, H.P. Evans, and R.W. Snidle. Micro-ehl analysis of ground and superfinished steel discs used to simulate gear tooth contacts. *Tribology Transactions*, 39(3):595–602, 1996.

[75] A. Jackson and A. Cameron. An interferometric study of the ehl of rough surfaces. *ASLE Transactions*, 19(1):50–56, 1976.

[76] L.D. Wedeven and C. Cusano. Elastohydrodynamic film thickness measurements of artificially produced surface dents and grooves. *ASLE Transactions*, 22(4):369–381, 1979.

[77] A.A. Lubrecht, W.E. Ten Napel, and R. Bosma. Influence of longitudinal and transverse roughness on the elastohydrodynamic lubrication of circular contact. *Journal of Tribology*, 110(3):421–426, 1988.

[78] C.H. Venner and A.A. Lubrecht. Numerical analysis of the influence of waviness on the film thickness of a circular ehl contact. *Journal of Tribology*, 118(1):153–161, 1996.

[79] J. Seabra and D. Berthe. Elastohydrodynamic point contacts part ii: Influence of surface speeds, surface waviness and load on the contact behaviour. *Wear*, 130(2):319–335, 1989.

[80] M.J.A. Holmes, H.P. Evans, and R.W. Snidle. Analysis of mixed lubrication effects in simulated gear tooth contacts. *Journal of Tribology*, 127(1):61–69, 2005.

[81] H.P. Evans and R.W. Snidle. A model for elastohydrodynamic film failure in contacts between rough surfaces having transverse finish. *Journal of Tribology*, 118(4):847–857, 1996.

[82] P. Ehret, D. Dowson, and C.M. Taylor. Waviness orientation in ehl point contact. *Tribology Series*, 31:235–244, 1996.

[83] M. Kaneta, T. Yamada, and J. Wang. Micro-elastohydrodynamic lubrication of simple sliding elliptical contacts with sinusoidal roughness. *Proceedings of the Institution of Mechanical Engineers, Part J: Journal of Engineering Tribology*, 222(3):395–405, 2008.

[84] P. Ehret, D. Dowson, and C.M. Taylor. Time-dependent solutions with waviness and asperities in ehl point contacts. *Tribology Series*, 32:313–324, 1997.

[85] I. Krupka, P. Perka, M. Hartl, S. Xue Jin, and C. Xiao Yang. Effect of real longitudinal surface roughness on lubrication film formation within line elastohydrodynamic contact. *Tribology International*, 43(12):2384–2389, 2010.

[86] C.H. Venner and A.A. Lubrecht. Transient analysis of surface features in an ehl line contact in the case of sliding. *Journal of Tribology*, 116(2):186–193, 1994.

[87] J. Guegan, A. Kadiric, and H. Spikes. A study of the lubrication of ehl point contact in the presence of longitudinal roughness. *Tribology Letters*, 59(1), 2015.

[88] P. Sperka, I. Krupka, and M. Hartl. The effect of surface grooves on film breakdowns in point contacts. *Tribology International*, 102:249–256, 2016.

[89] T. Hirayama, M. Ikeda, T. Suzuki, T. Matsuoka, H. Sawada, and K. Kawahara. Effect of nanotexturing on increase in elastohydrodynamic lubrication oil film thickness. *Journal of Tribology*, 136(3), 2014.

[90] M. Kaneta, T. Sakai, and H. Nishikawa. Effects of surface roughness on point contact ehl. *Tribology Transactions*, 36(4):605–612, 1993.

[91] M. Kaneta, N. Tani, and H. Nishikawa. Optical interferometric observations of the effect of moving transverse asperities on point contact ehl films. *Tribology Series*, 41:101–109, 2002.

[92] C. Cusano and L.D. Wedeven. The influence of surface dents and grooves on traction in sliding ehd point contacts. *ASLE Transactions*, 26(3):306–310, 1983.

[93] B. Jacod, C.H. Venner, and P.M. Lugt. Influence of longitudinal roughness on friction in ehl contacts. *Journal of Tribology*, 126(3):473–481, 2004.

[94] F. Ali, M. Kaneta, I. Krupka, and M. Hartl. Experimental and numerical investigation on the behavior of transverse limited micro-grooves in ehl point contacts. *Tribology International*, 84:81–89, 2015.

[95] M.-S. Suh, Y.-h. Chae, S.-s. Kim, T. Hinoki, and A. Kohyama. Effect of geometrical parameters in micro-grooved crosshatch pattern under lubricated sliding friction. *Tribology International*, 43(8):1508–1517, 2010.

[96] L. Mourier, D. Mazuyer, A.A. Lubrecht, and C. Donnet. Transient increase of film thickness in micro-textured ehl contacts. *Tribology International*, 39(12):1745–1756, 2006.

[97] L. Mourier, D. Mazuyer, F.-P. Ninove, and A.A. Lubrecht. Lubrication mechanisms with laser-surface-textured surfaces in elastohydrodynamic regime. *Proceedings of the Institution of Mechanical Engineers, Part J: Journal of Engineering Tribology*, 224(8):697–711, 2010.

[98] I. Krupka and M. Hartl. Experimental study of microtextured surfaces operating under thin-film ehd lubrication conditions. *Journal of Tribology*, 129(3):502–508, 2007.

[99] I. Krupka, M. Vrbka, and M. Hartl. Effect of surface texturing on mixed lubricated non-conformal contacts. *Tribology International*, 41(11):1063–1073, 2008.

[100] I. Krupka and M. Hartl. The effect of surface texturing on thin ehd lubrication films. *Tribology International*, 40(7):1100–1110, 2007.

[101] I. Krupka and M. Hartl. Effect of surface texturing on very thin film ehd lubricated contacts. *Tribology Transactions*, 52(1):21–28, 2009.

[102] I. Krupka, M. Hartl, L. Urbanec, and J. Cermak. Single dent within elastohydrodynamic contact - comparison between experimental and numerical results. *Proceedings of the Institution of Mechanical Engineers, Part J: Journal of Engineering Tribology*, 221(6):635–644, 2007.

[103] C. J. A. Roelands. *Correlational aspects of the viscosity-temperature-pressure relationship of the lubricating oils*. PhD thesis, University of Technology Delft, The Netherlands, 1966.

[104] D. Dowson and G. R. Higginson. *Elasto-hydrodynamic lubrication, The fundamentals of roller and gear lubrication*. Pergamon, Oxford, Great Britain, 1966.

[105] G. Nijenbanning, C.H. Venner, and H. Moes. Film thickness in elastohydrodynamically lubricated elliptic contacts. *Wear*, 176(2):217–229, 1994.

[106] H. Moes. Optimum similarity analysis with applications to elastohydrodynamic lubrication. *Wear*, 159(1):57–66, 1992.

[107] S.R. Wu. A penalty formulation and numerical approximation of the reynolds-hertz problem of elastohydrodynamic lubrication. *International Journal of Engineering Science*, 24(6):1001–1013, 1986.

[108] V. Chauveau, D. Mazuyer, F. Dassenoy, and J. Cayer-Barrioz. In situ film-forming and friction-reduction mechanisms for carbon-nanotube dispersions in lubrication. *Tribology Letters*, 47(3):467–480, 2012.

[109] A. Ernesto, D. Mazuyer, and J. Cayer-Barrioz. The combined role of soot aggregation and surface effect on the friction of a lubricated contact. *Tribology Letters*, 55(2):329–341, 2014.

[110] B.O. Jacobson and B.J. Hamrock. Non-newtonian fluid model incorporated into elastohydrodynamic lubrication of rectangular contacts. *Journal of Tribology*, 106(2):275–284, 1984.

[111] H.A. Spikes. Mixed lubrication - an overview. *Lubrication Science*, 9(3):221–253, 1997.

[112] Jinn-an Shieh and Bernard J. Hamrock. Film collapse in ehl and micro-ehl. *Journal of Tribology*, 113(2):372–377, 1991.

[113] P. Yang, J. Cui, M. Kaneta, and H. Nishikawa. Influence of a surface bump or groove on the lubricating performance and dimple phenomena in simple sliding point ehl contacts. *Journal of Tribology*, 126(3):466–472, 2004.

[114] N. Ren, D. Zhu, W.W. Chen, Y. Liu, and Q.J. Wang. A three-dimensional deterministic model for rough surface line-contact ehl problems. *Journal of Tribology*, 131(1):1–9, 2009.

[115] L.-M. Chu, W.-L. Li, J.-R. Lin, and Y.-P. Chang. Coupled effects of surface roughness and flow rheology on elastohydrodynamic lubrication. *Tribology International*, 43(1-2):483–490, 2010.

[116] H.J. Leamy, G.A. Rozgonyi, T.T. Sheng, and G.K. Celler. Periodic regrowth phenomena produced by laser annealing of ion-implanted silicon. *Applied Physics Letters*, 32(9):535–537, 1978.

[117] T.E. Tallian. On competing failure modes in rolling contact. *ASLE Transactions*, 10(4):418–439, 1967.

[118] D.J. Schipper, P.H. Vroegop, and A.W.J. de Gee. Prediction of lubrication regimes of concentrated contacts. *Lubrication Science*, 3(3):191–200, 1991.

[119] R. Haar Ter. *Friction in sheet metal forming.* PhD thesis, University of Twente, The Netherlands, 1996.

[120] W. C. Emmens. *Tribology of flat contacts and its application in deep drawing.* PhD thesis, University of Twente, The Netherlands, 1997.

[121] L. Mourier, D. Mazuyer, A.A. Lubrecht, C. Donnet, and E. Audouard. Action of a femtosecond laser generated micro-cavity passing through a circular ehl contact. *Wear*, 264(5-6):450–456, 2008.

[122] I. Krupka, M. Vrbka, M. Vaverka, R. Poliscuk, and M. Hartl. Effect of surface dents on contact pressure in elastohydrodynamic contacts. *Proceedings of the Institution of Mechanical Engineers, Part J: Journal of Engineering Tribology*, 223(4):683–693, 2009.